MODAL ANALYSIS OF LASER VIBRATED STRUCTURES

A thesis submitted

by

Wayne Reginald Philp

for the degree of

DOCTOR OF PHILOSOPHY

Department of Applied Physics
Victoria University of Technology

1993

In bringing before you some discoveries made by Mr. Sumner Tainter and myself, which have resulted in the construction of apparatus for the production and reproduction of sound by means of light, it is necessary to explain the state of knowledge which formed the starting point of our experiments.

I shall first describe that remarkable substance 'selenium,' and the manipulations devised by previous experimenters; but the final result of our researches has widened the class of substances sensitive to light vibrations, until we propound the fact of such sensitiveness being a property of all matter.

We have found this property in gold, silver, platinum, iron, steel, brass, copper, lead, antimony, german-silver, Jenkin's metal, Babbitt's metal, ivory, celluloid, gutta-percha, hard rubber, soft vulcanised rubber, paper, parchment, wood, mica, and silvered glass; and the only substances from which we have not obtained results, are carbon and thin microscope glass.

We find that when a vibrating beam of light falls upon these substances they emit sounds, the pitch of which depends upon the frequency of the vibratory change in light.

Alexander Graham Bell. On the production and Reproduction of Sound by Light.
Read before the American Association for the Advancement of Science, Boston, August 27, 1880

Declaration

I, **Wayne Reginald Philp**, declare that the thesis titled,

Modal Analysis of Laser Vibrated Structures,

is my own work and has not, been submitted previously, in whole or in part, in respect of any other academic award.

W.R. Philp,

dated the 11th day of October, 1993

Acknowledgments

I would most like to thank my supervisor, the Head of the Applied Physics Department at Victoria University of Technology, Professor David Booth, for guidance and discussion in all matters of this research. I am also most grateful to Dr Nigel Perry for helpful discussions on mathematical matters and to Associate Professor Ken Peard, Dr Michael Linthwaite, Dr Stephen Collins and Mrs Elisabeth Grove for criticism of this thesis. In addition, I wish to thank all the other academics, technicians, administrative staff and fellow postgraduate students in the department for their willing assistance and friendship.

I am greatly indebted to Victoria University of Technology for the provision a Postgraduate Scholarship.

Finally I thank my wife Sharon, for always placing my needs and dreams before her own.

Abstract

This thesis describes the laser irradiation of metallic structures to excite mechanical vibrations within those structures. As found by other authors, single high-power laser pulses ablate the irradiated surface material and may impulsively excite structural vibration; however, the use of laser power densities above the ablation threshold causes significant surface damage. This work extends current optical excitation techniques by demonstrating that a single laser pulse, with a power density below the surface ablation threshold, can also efficiently induce flexural vibration in a structure. The mechanism of excitation is shown to be consistent with the production of a photothermally-induced bending moment at the site of the laser irradiation. These sub-ablative photothermal excitation techniques do not damage the structure in any way.

A Fourier analysis of the temporal behaviour of transverse vibrations caused by laser excitation, enables the measurement of frequencies corresponding to the modes of free vibration (modal analysis). These modal frequencies are determined by the size, shape, elasticity and structural integrity of the vibrating structure. Changes in one or more of these parameters can be detected by means of measured changes in the modal frequencies. Hence, modal analysis can be used to non-destructively test for changes in these structural parameters.

Much of the work described in this thesis was carried out, using a single sub-ablative laser pulse of relatively high power, to excite structures with dimensions measuring tens of centimetres. The single laser pulse efficiently excited free vibration of these structures and modal signatures were recorded over a frequency range of about 2 Hz to 2 kHz. The efficiency of this form of excitation suggested that it would be possible to excite the same structures with very much less laser power, and so this has also been investigated. It was found that simple structures of significant size could be easily excited using repetitive pulses from a low-power diode laser and the efficiency of

excitation was shown to depend on the ratio of the diode laser modulation frequency to the thermal characteristic frequency of the structure. Measurements are reported for modulation frequencies between about 20 Hz and 1.5 kHz. The use of repetitive sub-ablative pulses from diode lasers is not totally new as they have previously been used to oscillate small microresonant sensors; however, to the best knowledge of this author, no previous results have been reported using diode lasers to excite large structures of the type used in this thesis. The excitation of large structures, using single sub-ablative laser pulses, is also novel and has not been previously reported.

The laser excitation and non-destructive testing techniques developed in this thesis are of considerably more practical value if they are made totally remote to the structure. For this reason, non-contact optical sensors were used to detect and measure the surface vibrations. This has the added advantage of not loading the structure with the sensor and thus modifying the modal frequencies of free vibration. Two innovative, non-contact, all-fibre optical vibration sensors have been designed and constructed to monitor a small area of the vibrating structure. The first of these was an intensity-modulated proximity sensor to detect amplitudes of vibration greater than a few micrometres. The second was an interferometric device, which was capable of detecting nanometre displacements over a bandwidth of several tens of kilohertz.

The modal analysis of laser vibrated structures enables the totally remote and accurate measurement of frequencies characteristic to those structures. Measured shifts in these modal frequencies have been used to non-destructively test for changes in physical dimension and structural integrity due to fatigue caused by severe and repeated stretching. These measured frequency shifts have also been used with simple structures to indicate the presence of cross-sectional damage due to both cracks and slots. The use and limitations of laser excitation and non-contact sensing techniques have been investigated by applying them to a range of cantilevers and a large truck-wheel rim.

Contents

Chapter 1

Introduction

1.1 An overview of this thesis

A costly and common cause of mechanical failure in industry, and heavy machinery in general, is structural fatigue damage due to protracted stress and vibration. Fatigue damage is caused by the gradual propagation of small cracks within a structure subjected to cyclic stress, which eventually results in fracture and failure of that structure.[Liebowitz, 1969] However, unless these cracks are large or externally evident, it is often difficult to determine the fatigue state or the serviceability of the structure without extensive and sometimes destructive testing.[Temple, 1988]

A simple form of non-destructive testing has long been used to reliably determine the status of railway wheels while they were still in service; namely, the "Wheel Tap Test". The test requires that an experienced inspector strike each wheel of a train along its length, listen attentively to the resultant "ring", and compare that to the "ring" of the previous wheel. An off-pitch "ring", or an abnormally rapid reduction in the sound intensity, indicated a damaged or defective wheel. If the inspector's memory were to be replaced by a digital signal analyser, his ear by a sensitive transducer and his hammer by a laser pulse, one may achieve the measurement and comparison of vibrational frequencies (modal analysis of the "ring") which are indicative of the wheel's structural integrity (or changes in the other parameters on which the modal frequencies depend). In this manner, the inspector's subjective assessment could be quantified.[Bray et al. 1973, Nagy et al. 1978]

Many of the techniques developed in the field of modal analysis over the past 20 years have sought to accurately measure the modal frequencies of free vibration for a structure, and to explain observed shifts in those frequencies in terms of defect or damage to that structure. This form of analysis is, when practicable, very attractive since it provides in the same manner as the "Wheel Tap Test", a rapid and routine means of assessing structural integrity. However, two practical limitations in the usual application of modal analysis for non-destructive testing (NDT) are;

i. imprecise impulsive excitation techniques (traditionally, hitting or shaking) which allow the energy delivered to the test-structure to vary between successive trials, and
ii. invasive vibration sensing methods which significantly load light-weight structures by physical contact during vibration, require special preparation or modification of the structure's surface and can alter the modal frequencies being measured.

The aim of the research described in this thesis was to assess the potential of optical methods, for overcoming the limitations mentioned above, by attempting to develop new non-contact excitation and sensing techniques for modal analysis of reasonably large structures.

The work began as an off-shoot of research conducted within the Faculty of Engineering at this university. The engineering research program sought to develop better truck wheels by;

i. creating conditions of protracted stress and fatigue in Mercedes-Benz truck wheel rims,
ii. gauging the extent of fatigue damage using modal and finite element analysis methods, and
iii. suggesting and testing modifications which reduced fatigue damage.

Some of these matters were referred to the Department of Applied Physics; in particular, the investigation of non-invasive techniques for excitation and sensing. If such techniques were to provide an accurate modal signature of the test-structure, an assessment of structural integrity could be achieved without loading the structure with sensing and excitation equipment. Non-contact excitation and sensing could also facilitate in-situ automatic checking during the fatigue process.

Laser irradiation of the structure seemed an ideal means by which to excite vibration. Koss and Tobin (1983) demonstrated that when a single high-power laser pulse was directed at the surface of a simple metallic structure, the surface material was rapidly ejected as a molten/gaseous spray or vapour (ablated). The momentum transferred to the ablated material resulted in an impulsive reaction to the irradiated structure, which caused it to vibrate. The advantages of this technique, when compared to simply hitting the structure, are that;

i. if the laser energy is constant, the energy delivered to the irradiated structure is well-defined and repeatable,

ii. the site of the laser-produced impulse can be directed so as to selectively enhance or suppress a particular mode of flexural vibration, and

iii. beam (pulse) splitting techniques can be employed to excite the structure at multiple points simultaneously.

However, two major disadvantages are that the ablative laser excitation damages the surface of the structure and that the impulse generated by the excitation is not repeatable due to cumulative damage. The ablative mechanism, for the excitation of a cantilever, is depicted schematically in figure 1.1.1.

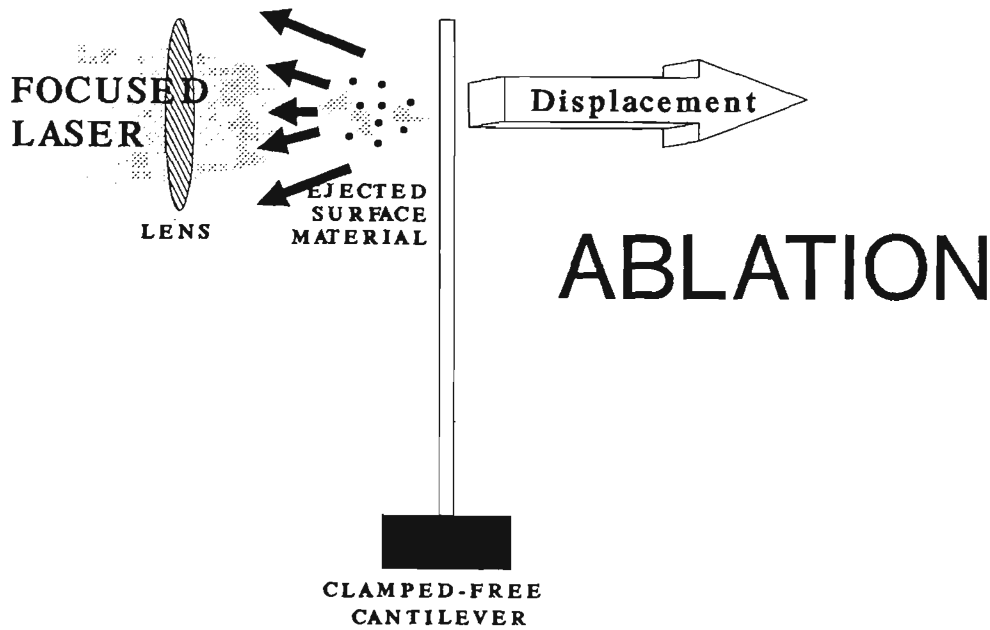

Figure 1.1.1 Displacement of a cantilever by surface ablation.

A laser pulse, depending on its power density, has been shown to heat an irradiated surface and cause that surface to rapidly boil, bend or bulge.[Ready, 1971] The response of the structure to these three actions differs in that: boiling of a small area of the surface results in an impulsive displacement of the structure, localised bending causes the whole structure to flex, and rapid transient bulging of a small shallow region will produce shock-waves within the structure. Each of these actions will elicit a mechanical response and so excite the structure in some way. The photothermal excitation of laser-irradiated structures may therefore be described within three regimes; ablation of the material surface (as already described), flexing due to deformation of the structure as a whole, and photoacoustic shock-wave generation within the material bulk. The dominance of one regime over another, and therefore the mechanism by which the structure is excited, is determined by the intensity and duration of the laser irradiation.

The last of the three regimes is that of photoacoustic shock-wave generation. This occurs when the laser has a short pulse length (typically nanoseconds) and a power density below the surface ablation threshold of the irradiated material. A thermoelastic stress wave is generated as the heated layer expands and compresses the adjacent cooler material.[Tam 1986, Hutchins 1988] This "photoacoustic effect" may be used to generate ultrasonic pulses but, since this has little affect on the flexural free vibration of the structure as a whole, the photoacoustic regime is of little importance to this thesis, except as a related form of NDT.

The work described in this thesis began with duplication of the results reported by Koss and Tobin (1983) and Edwards, Tobin and Koss (1983) using a single 40 J Nd:glass laser pulse with full width at half maximum (FWHM) duration of 600 μs incident upon a 315 mm × 12 mm × 254 μm stainless steel clamped-free cantilever. In order to detect and record the laser-induced structural vibrations, a non-contact fibre-optic vibration sensor was designed and constructed to replace the strain gauge bridge used by these workers. This fibre-optic sensor provided a significant improvement in its ease of use and accuracy when compared to that of the strain gauges. The surface-mounted strain gauges required careful preparation of the cantilever and the necessary adhesive and wiring loaded the flimsy structure and altered its flexural modes of vibration. After repeating Koss and Tobin's techniques, this work was extended by investigating the effect of systematic reduction in the laser power density (thereby minimising the damage caused to the surface) while still exciting the irradiated structure. In so doing, it was found that the cantilever could be excited without any damage to the surface at all. It was discovered during the course of this early work that the stainless steel cantilever, and other steel and aluminium cantilevers of similar geometries, were efficiently excited to flexural vibration using a single laser pulse with a power density well below the ablation threshold of the irradiated material. Experiments were conducted to identify and confirm the nature of the mechanism of physical excitation caused by this low power density excitation. Unfocused pulses from the Nd:glass laser with a power density of approximately 1.3×10^5 W.cm^{-2} were used to excite flexural vibration in both aluminium and steel cantilevers, and by way of contribution to the engineering project, also a 57 kg Mercedes-Benz steel truck wheel rim. The power density of each laser pulse was well below the ablation threshold of the irradiated material and so the laser pulse did not provide an impulse to the structure. The absence of impulsive forces was confirmed using a low boiling-point alloy target attached to a sensitive piezoelectric force transducer.

The effect of the unfocused laser pulse can be understood in terms of the second of the outlined photothermal excitation regimes; namely, flexing due to deformation of the structure as a whole. When the laser irradiation has a power density below the ablation threshold of the material, and a relatively long pulse duration (about a millisecond), photothermal deformation due to thermal expansion in the surface and sub-surface material causes the structure to bend and flex at the irradiation site. This photothermal deformation produces a localised transient bending moment which results in a time dependent angular displacement of the structure and consequent flexural vibration. The development of a thermal model to describe this transient bending moment, and the solution to the equation of motion for vibrations in a simple cantilever driven by this excitation (in which the natural frequencies of vibration are reduced by damping to give the modal frequencies of oscillation), are a significant part of this work. The dependence of the amplitude for each excited modal frequency on the dominant frequency in the Fourier spectrum of this bending moment is also discussed. This model of photo-thermoelastic flexing can also be used to explain results obtained from experiments in which, by varying the location of the site of sub-ablative laser excitation, the amplitude of vibration for different modal frequencies could be changed relative to one another. The action of photothermal flexing is simply illustrated schematically in figure 1.1.2.

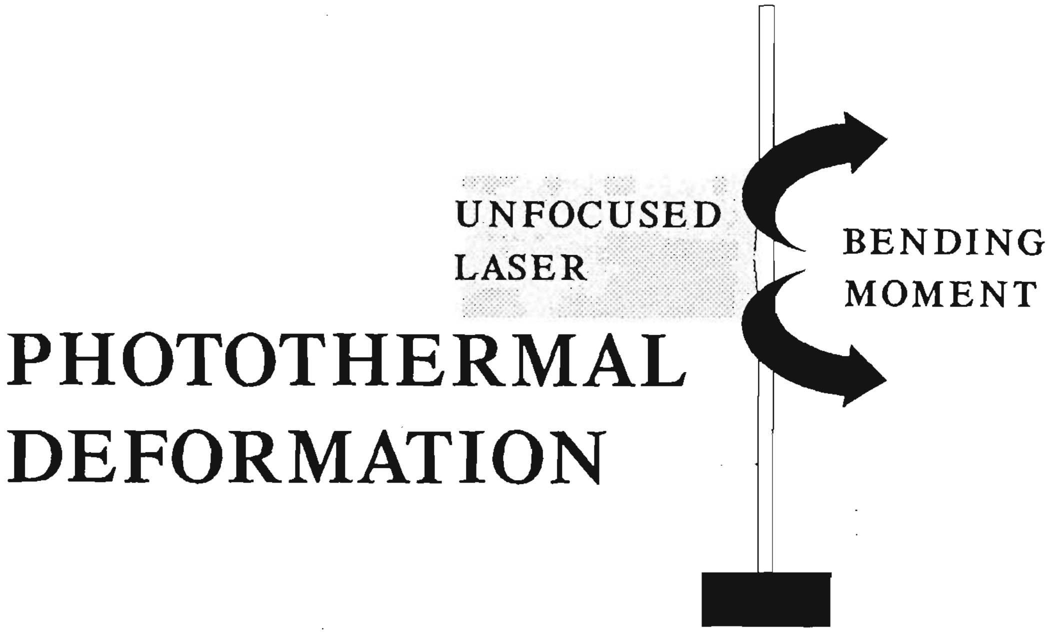

Figure 1.1.2. Illustration depicting the mechanism by which a single laser pulse induces photo-thermoelastic flexing.

Most of the measurements described in this work were derived from the laser irradiation and excitation of clamped-free cantilevers. Cantilevers were chosen as test-structures because the geometric simplicity of their transverse modal oscillations, and the ease with which the natural frequencies of vibration could be calculated, greatly aided in the process of elucidating the mechanism responsible for the observed physical excitation.

Once the mechanism of photo-thermoelastic flexing was understood, it was possible to greatly reduce the laser power required to excite structural vibration. A particular structural resonance may be photo-thermally driven by matching the pulse-repetition-rate of chopped irradiation from a CW laser, and therefore also the frequency of forced thermoelastic flexing, to a selected resonant frequency of the structure. In this manner, a 15 mW diode laser was shown to excite the same aluminium cantilever previously excited by the 40 J Nd:glass laser pulse (having approximately 60 kW average power). The cantilever was driven to resonance by irradiating its surface with pulsed light from the diode laser and the small displacements of the cantilever were detected using a sensitive stabilised interferometric sensor, which was specifically built for this purpose. The interferometric sensor was an all-fibre design, which used an in-fibre phase modulator to compensate for thermal drifts and fading effects in the optical paths, and thereby stabilise the output sensitivity. The first five resonances of the aluminium cantilever were excited using a single 15 mW diode laser and measured using the interferometric sensor. Greater resonant amplitudes were achieved by using two or three synchronously pulsed diode lasers. These were positioned so as to irradiate sites along the cantilever length corresponding to the bending moment antinodes of the specific resonance excited. The remote applications of this technique were demonstrated by optically exciting and monitoring the cantilever at a range of one metre through an intervening glass window.

An important aspect of this work for both single and repetitive pulse excitation, is the modal analysis of the resulting vibrations to determine the modal frequencies of free vibration. These frequencies are characteristic of the test-structure. The vibration of the structure was recorded over an interval of time and these vibration profiles were then Fourier-transformed to provide frequency spectra (modal signatures) unique to those structures. The first five modes of free vibration were accurately determined for selected cantilevers using both a single unfocused high-power laser pulse and a series of repetitive low-power pulses from the diode laser(s). In the case of the truck rim, the first ten modes of vibration were measured using the same single-pulse laser irradiation technique used to excite the cantilevers.

The use and limitations of single-pulse and repetitive-pulse laser excitation techniques have been investigated by applying them to a range of cantilever and other structures. Experiments were conducted to try to fatigue a series of aluminium strips which could then, in turn, be mounted as clamped-free cantilevers. A universal testing machine was used to periodically stretch these strips between 20 and 95 percent of their ultimate tensile stress for up to 10,000 stretching cycles. This is not an ideal way to try to produce cracks in samples, however equipment was not available to provide millions of fatigue tension cycles at low stress (as is usually the case in accelerated stress fatigue). The severity of the stretching technique, which was considered necessary to cause any significant fatigue to the test-samples over a relatively short period of time (hours or days), permanently lengthened the test-samples. This elongation, and the consequent change in shape and size, was found to account for most of the observed changes in the modal signatures of the test-samples. Another test-sample was sought which had been subjected to internal damage by accelerated fatigue at tension levels within the limits of elastic deformation for that structure. Such a sample was procured from the Hawker De Havilland Aircraft Corporation in the form of a Macchi Aircraft wingspan section, and this had been fatigue-stressed over several million cycles until a bisecting lateral crack had propagated over 90% of its breadth. Modal frequency shifts resulting from this crack were investigated using optical excitation and sensing techniques, as well as with conventional tapping and microphone methods.

Further investigation of the use of single-pulse laser excitation techniques for the detection of crack damage in structures was carried out using thin slots to simulate the effects of cracks. Additional aluminium test-samples were subjected to controlled damage as slots of constant width and varying depth were cut laterally across the face of these samples. Modal signatures were recorded at each stage of damage and it was found that the severity of damage could be easily identified from the measured frequency shifts. The magnitude of the change in a particular modal frequency has been shown to depend on the location of the cross-sectional damage with respect to the nodes and antinodes of that mode.

These non-destructive laser excitation techniques, when used in conjunction with non-contact fibre-optic vibration sensors, enabled totally remote excitation and sensing of structural vibrations. These techniques may find commercial application in the remote detection of variations in size, shape, mass or structural integrity of mass-produced items or otherwise inaccessible structures. The quality control of mass-produced items on a "go/no go" basis may be determined in-situ by comparing the modal signature gained from a object under test with that obtained from a standard or ideal object. Furthermore, the light needed for excitation or sensing may be directed from a remote location through a transparent barrier, or channelled directly to the structure via an optical fibre. The optical system is therefore ideally suited to the remote testing of structures within difficult, physically isolated or hazardous environments.

This research has endeavoured to characterise sub-ablative laser excitation by identifying the mechanisms by which it can efficiently cause simple structures to vibrate, demonstrating the effect using both high and very low power lasers together with appropriately-designed optical sensors, and presenting modal analysis for NDT as a relevant application of these methods.

1.2 Some methods of non-destructive testing

The laser excitation and optical sensing techniques described in this thesis have been applied to the field of non-destructive testing and evaluation. Before further discussion of this application is developed, it may be useful to briefly review this broad field and examine the technologies that the modal analysis of the laser vibrated structures, described in this thesis, may complement.

Non-destructive testing (NDT) techniques enable the integrity of a structure under investigation to be evaluated without damage to that structure. The techniques of NDT vary widely in their complexity and portability; for example, surface crack detection may require either a simple inspection using a coloured dye or a thorough microscopic investigation. The selection of the most appropriate technique depends on the quality and reliability required by the inspection, the nature of the physical parameters under examination and the accessibility of the structure to be tested. The field of NDT includes an extensive range of technologies and a wide selection of equipment, varying in cost and sensitivity. Several excellent reviews of the field have been published.[Frost 1979, Bryant and McIntire 1985, Tam 1986, Hull and John 1988, Adams and Cawley 1988] The following is a summary of the more common inspection techniques used for NDT.

Optical inspection includes the use of filters, geometrical optics and coherent fibre-optic cables to visually assess structural integrity by examination of the material surface. Photographic and holographic techniques (visible, ultraviolet and infra-red) are also within this category. Although optical inspection is the simplest, quickest and cheapest means of assessing structural integrity, these techniques cannot, in general, detect sub-surface defects. Recent developments, however, in coherent gradient sensing methods using lateral shearing interferometry (shearography)[Tippur, 1992] have reported the detection of sub-surface disbonding and cracking.

Liquid penetrant inspection is used to highlight surface cracks or defects in metals, glassware, plastics or glazed ceramics. When a coloured or fluorescent liquid is applied to a carefully prepared surface, capillary action enables the dye to penetrate below the surface through cracks or pores. After the surface has been cleaned of excess liquid, cracks and porous damage may be highlighted with visible or ultraviolet illumination. Unfortunately, since this technique relies ultimately on optical inspection, liquid penetrant inspection is also limited to surface analysis.

Magnetic particle inspection may be appropriate for ferromagnetic materials in the detection of surface and, in the case of smooth surfaces, near-surface defects. By passing an electric current through the test-structure or by permeating it with a magnetic field, cracks or flaws, at or near the surface, will cause discontinuities in the external magnetic field known as "field leakage". Powdered magnetic particles (dry or in solution) are applied to the surface of the structure and these align in the direction of the magnetic field. The field lines and leakage fields emanating from defects may be examined by visual surface inspection of the patterns formed by the powder.

Eddy current inspection techniques are a powerful, industrially established and versatile means of detecting surface and some sub-surface defects in ferromagnetic and paramagnetic materials. This method of NDT is achieved by scanning the material surface with a transducer consisting of two solenoids; one to generate an oscillating magnetic field, the other to detect small induced eddy currents within the material. Eddy currents are secondary or induced currents produced in a conductor by a time dependent change in the external magnetic field. The opposing fields generated by the eddy currents produce a back e.m.f. in the sensing solenoid and hence a change in the effective impedance of that solenoid. A crack or flaw in the test-structure, which is directly below the transducer, will cause a localised disturbance in the internal and surface eddy currents of that structure and thereby change the impedance of the sensing solenoid. By monitoring the impedance of the sensing solenoid as it is scanned over the surface of the structure, defects can be located and mapped in some detail.

Radiographic inspection requires that a structure under test be probed with a source of penetrating sub-atomic particles or electromagnetic radiation. The main techniques include; fluoroscopy (transient images viewed on a fluorescent screen), xeroradiography (latent images formed on electrostatically charged plates and then reproduced on paper), radiography (images produced on radiation sensitive film or paper), radiation gauging (electronic detection of radiation), and computerised tomography (computer-aided two or three-dimensional images constructed from data obtained by radiation gauging). Thermography, spectroscopy, electron microscopy, neutron scattering and X-ray/γ-ray diffraction are all examples of technologies used by radiographic NDT.

Acoustic emission inspection is a passive form of NDT. A structure is subjected to imposed stresses and strains whilst highly sensitive transducers monitor any internal acoustic emissions. Cracking (cracks as short as 2×10^{-4} mm), deformation and micro-yielding result in the emission of acoustic frequencies from 50 kHz to 10 MHz as stress is released by further crack growth or dislocation movement. The location of a defect may be determined by the use of a transducer array and the analysis of signal delays. The growth of larger cracks or flaws creates acoustic emissions of greater intensity and thus can provide early warning of impending structural breakdown. This technique can be used to monitor structures under continual strain (for example; aircraft, bridges, mountings, and pressure vessels) and guard against catastrophic failure.

Ultrasonic inspection is the main means of internal defect detection used on the workshop floor. Internal and surface defects can be located and assessed by the analysis of 0.5 to 20 MHz stress waves transmitted through a material of known elastic properties. Ultrasonic pulses are normally generated by a piezoelectric crystal in a series of short bursts, and the crystal can then passively detect echoed signals in-between these periods of active pulse generation. The ultrasonic stress waves within the material exhibit all the normal effects seen in wave propagation; namely, partial transmission and reflection, refraction, interference and attenuation. Ultrasonic pulses may be reflected at cracks and dislocations, scattered as a result of impurities or voids and refracted due to changes in material density. Transmitted and reflected ultrasonic pulses can therefore be used to indicate the size and location of cracks, impurities or voids in most homogeneous materials. Thickness measurements can be made using a simple ultrasonic pulse-echo technique where typical thickness readings range from 1 mm to 1 m, with an accuracy of 0.02% [Hull and John, 1988] and in theory, flaw detection is possible within the pulse-echo detection range of the ultrasound testing unit. Direct contact ultrasonic inspection can be used to measure thinning due to corrosion in steel to a typical accuracy of 0.01 mm for thicknesses greater than 0.5 mm and if delayed coupling is provided by immersing the object in water, an accuracy of 0.003 mm is possible for thicknesses between 0.1 mm and 50 mm.[Krautkrämer and Krautkrämer 1990]

Laser-generated ultrasonic techniques employ a single laser pulse (typically with a pulse length measuring tens of nanoseconds), or a rapid series of laser pulses, to quickly heat the irradiated surface material and momentarily cause it to expand. Thermoelastic shock-waves are thereby created, which travel away from the irradiation site at frequencies typically between 10 MHz and 50 MHz, and these are usually detected using standard PZT mechanically-coupled sensors. Alternatively, electrostatic or electromagnetic acoustic transducers (ESATs or EMATs), bulk or fibre interferometers and laser-Doppler velocimeters may be used as non-contact detectors to monitor tiny displacements of the material surface. The largest of these displacements are caused by normal pulse echoes from the surfaces of the test-sample. However, lesser displacements may be also be detected from reflections off internal structural flaws or the arrival of surface acoustic waves. The interaction of laser-generated surface acoustic waves with surface/sub-surface defects is an area of current interest in ultrasonic testing. Optically generated and detected ultrasonic inspection techniques are potentially more powerful than conventional techniques for the remote characterization of defects in both metallic and composite materials at elevated temperatures or when direct mechanical contact is impractical. However, the absolute measurement sensitivity of interferometers is below that of resonant piezoelectric sensors.

Modal inspection techniques require that a structure be induced to display flexural modes of free vibration by either direct shaking or hitting of that structure. Frequency spectra derived from the time record of the vibration profile of an excited structure, represent a modal signature unique to the elastic properties and physical dimensions of that structure. Structural vibration may be detected with simple contact sensors or remotely by non-contact optical, radiometric, ESAT or EMAT devices. When the modal signature gained from an undamaged structure is compared with that of a structure containing cracks or flaws, differences in the modal frequencies may indicate a change in the elastic constants or boundary conditions of the damaged structure. In the simplest case, this comparison provides an indication of the total integrity of the structure under test. In geometrically simple structures, numerical reduction of the frequency shifts for a series of modes can also gauge the extent and location(s) of the damage. Modal inspection is also applicable to both metal and composite structures. Examples follow in the next section.

1.3 A summary of previous work on photothermal excitation

When a laser pulse of sufficient power density irradiates an opaque surface, the electromagnetic radiation is absorbed in a thin layer of material, which causes a rapid rise in the surface temperature. The heat generated at the surface is the cause of thermoelastic excitation,[Parkus 1968, Ready 1971] which can be classified into three distinct regimes; **ablation** of the material surface, **photoacoustic shock-wave generation**, and flexing of the structure due to **photo-thermoelastic deformation**. The following is a summary of the current literature on these photothermal excitation regimes and a discussion of relevant detection techniques.

Ablation.

If the rate of temperature increase in the surface layers is sufficient, vapour and molten material are rapidly ejected from the surface. Ablation of the material surface results in momentum transfer to the ejected material and a reactive impulse to the irradiated structure. The onset of impulsive forces, as a result of this removal of surface material, is referred to as the ablation threshold. The impulse derived from the ablation of surface material depends on the energy of the laser pulse, the reflectivity of the surface, the surface area irradiated, the thickness of the structure, the laser pulse duration and the thermal conductivity of the irradiated material.[Ready, 1971] Ablation of an aluminium surface is typically achieved using a laser power density of about 10^7 W.cm^{-2}. [Ready 1965, 1971 and 1974] Impulse production by laser-induced surface ablation has been demonstrated with a variety of metals in vacuum and in air. [Askar'yan et al. 1963, Jones 1971, O'Keefe and Skeen 1972, Fox and Barr 1973, Lowder et al. 1973, Ready 1974]

Koss and Tobin (1983) showed that a pulsed laser system, directed at an easily ablated target attached to a structure's surface, could be used to impart significant impulsive forces to that structure and thereby induce transverse vibration. They used a cantilever structure and strain gauges to detect the induced vibrations. Edwards, Tobin and Koss (1983) then extended this study by considering simultaneous dual-pulse excitation, mode suppression and mode isolation by careful choice of irradiation sites and excitation of plates as well as cantilevers. Koss and Tobin (1983) reported a 6 millipercent energy conversion efficiency (photonic to mechanical) using a 1.5 J, 400 μs Nd:glass laser pulse to ablate a bismuth target attached to a ballistic pendulum. Earlier work by Koss (1980) had used a TEA CO_2 laser with a lead target to achieve an energy conversion efficiency of 1.6 millipercent. Koss and Tobin (1983) also reported a specific impulse (the impulse provided per unit of laser energy) of 250 μN.s/J for bismuth and that the mechanical energy transfer was proportional to the laser pulse energy raised to a power in the range 2.5 to 2.9

At even higher laser power densities (typically 10^9 W.cm^{-2} for aluminium, using a Q-switched laser system[Ready, 1982]), the vaporised material may also absorb significant laser energy which gives rise to laser-supported detonation.[Pirri et al. 1972, Lowder and Pettingill 1974] Laser-supported detonation provides an impulse to the irradiated structure both as momentum is transferred to the ablated material, and by the shock-waves generated immediately above the surface as this ablated material is ionised. Several authors have investigated the specific impulse delivered to an aluminium target upon laser-supported detonation of aluminium vapour in air: Hettche et al. (1973) used 100 - 700 J, 15 - 50 μs CO_2 laser pulses (power density 10^7 - 10^8 W.cm^{-2}) to obtain a specific impulse of 50 - 78 μN.s/J, Lowder and Pettingill (1974) achieved 50 μN.s/J using a 50 J, 15 μs pulsed CO_2 laser with a power density of about 10^8 W.cm^{-2} (decreasing to 25 μN.s/J using 300 J), and Hora (1973) obtained 20 μN.s/J with a 15 J, 250 ps Nd:glass laser having very high power densities of the order 10^{14} W.cm^{-2}.

The impulse produced upon laser-induced ablation of an irradiated surface may be used to displace a supported structure and cause it to vibrate. This has achieved transverse mechanical oscillation in elastic membranes,[Alexander and Nurmikko, 1973] steel cantilevers or plates, [Koss and Tobin 1983, Edwards et al. 1983] and clamped disks.[Crosbie et al., 1986] The disadvantage of this technique as a means of excitation for NDT is that surface damage results from the ablation process. There can also be a slight degree of damage, although rarely visible, from a single sub-ablative laser pulse if there is any surface modification by the elevated temperature;[Clark and Emmony, 1989] however for practical purposes, this damage is not significant. Alternatively, ablative targets can be attached to the material surface,[Koss and Tobin, 1983] but these load and modify the flexural modes of free vibration. Moreover, in many situations, the application of ablative targets is impractical.

Photoacoustic shock-wave generation.

The "photoacoustic effect" (production of sound by light) was first reported by Alexander Graham Bell in his examination of audible sounds produced by focused and chopped sunlight incident upon a selenium surface.[Bell, 1880] The production of brief intense light from a pulsed ruby laser in 1960 renewed interest in this effect[White R.M. 1963, Gournay 1966, Brienza and DeMaria 1967] and subsequently led to the development of laser-generated ultrasonic inspection techniques for sub-surface defect detection.[Kubota and Nakatani 1973, Felix 1974, Kohanzadeh et al. 1975, Wellman 1978, Budenkov and Kaunov 1979, Krautkramer 1979, Scruby and Drain 1990]

When a laser pulse has a power density below the ablation threshold of the irradiated surface, and is of short duration (typically tens of nanoseconds,[Tam, 1986] although picosecond measurements have also been reported[Heritier and Seigman, 1983]), the rate at which heat is generated at the surface can be much faster than the rate at which that heat may be dissipated by thermal conduction. Stresses are created in the surrounding bulk as the heated layer expands and exerts pressure on the adjacent cooler material. Thermoelastic stresses,[Bushnell and McCloskey 1968, Peercy et al. 1970, Hartman et al. 1972] generated at the site of irradiation, result in the propagation of both bulk compression[White R.M. 1963 and 1971, Carome et al. 1964, Anderholm 1970, Yang L.C. 1974] and shear waves[Lee and White 1968, Ledbetter and Moulder 1979] through the material. Ellipsoidal Rayleigh waves, containing both longitudinal and shear displacements, may be detected as displacements along the surface of the structure.[Keller and Karal 1960, Lehfeldt and Höller 1967] The shear and Rayleigh waves are of importance when studying the effect of surface cracks.[Aindow et al. 1982 and 1983]

Analysis of the ultrasonic waveforms generated by these photothermal waves has been used to indicate the presence of slots,[Bondarenko et al., 1976] sub-surface voids,[von Gutfeld and Melcher, 1977a&b] the quality of microwelds,[Bar-Cohen, 1979] surface cracks,[Cooper et al., 1986] laminations[Crosbie et al., 1986] and sub-surface cracks.[Bruinsma, 1987] Other significant contributions to this field of laser-generated ultrasonics include; low-energy generation and detection of photoacoustic pulses using 20 - 210 μJ, 6 ns laser pulses,[Bourkoff and Palmer C.H., 1985] the use of modulated CW laser sources to provide ultrasonic excitation,[Ash et al., 1990] materials characterisation,[Green 1985 and 1987, Hutchins and Tam 1986, Scala and Doyle 1991] generation of two-dimensional acoustic beams for biomedical tomography,[von Gutfeld, 1980] crack and surface/sub-surface flaw detection,[Aindow et al. 1979, 1980, 1981, 1982, 1983 and 1984, Dewhurst et al. 1982, Dewhurst 1983, Hutchins and Nadeau 1983, Nadeau and Hutchins 1984, Hutchins et al. 1981a,b,c&d, Hutchins 1988, Scruby et al. 1980, Cielo et al. 1985, Konstantinov et al. 1989] theoretical development of photoacoustic dynamics[Rosencwaig and Gersho 1976 , Lui 1982, Lai and Young 1982, Kino and Stearns 1985, McDonald and Wetsel 1988] and the development of fibre-optic delivery systems for beam steering and directional analysis.[Vogel and Bruinsma 1987, Vogel et al. 1987, Bruinsma 1987, Le Brun and Pons 1987, Burger et al. 1987, Bruinsma and Jongeling 1989] Reviews describing photoacoustic action at laser irradiated surfaces have also been published.[Tam and Coufal 1983, Tam 1989, Matthias and Dreyfus 1989]

Several authors have written reviews on transducer applications in photoacoustic ultrasonic detection.[Frost 1979, Sache and Hsu 1979, Tam 1986] Some of these transducers include; piezoelectric crystals, ceramics and films,[White, 1963] strain gauges,[Hartman et al., 1972] gas-microphones,[Rosencwaig and Gersho, 1976] electrostatic or capacitance devices (ESAT),[Hutchins and Macphail, 1985] electromagnetic devices (EMAT),[Budenkov and Kaunov 1979, Hutchins et al. 1986] laser probe beam deflection,[Sontag and Tam, 1986] interferometers,[Palmer 1973, Bondarenko et al. 1976, Palmer et al. 1977, Yoneda et al. 1980, Monchalin 1985] and fibre-optic interferometers.[Bowers 1982 , Vogel and Bruinsma 1987] The work of Monchalin and his co-workers in the remote broadband interferometric detection of ultrasound by optical sideband stripping using a bulk-optic confocal Fabry-Perot cavity in reflection at 1.06 μm[Monchalin et al., 1989] and two-wave mixing in a photorefractive crystal[Ing and Monchalin, 1991] has also been significant. These authors have reported interferometric detection of laser-generated ultrasound with a bandwidth from about 1 kHz to 100 MHz. Some, less direct, sensing methods include holographic techniques,[von Gutfeld and Vigliotti, 1983] pulsed photothermal radiometry[Tam and Sullivan, 1983] and Bragg scatter of laser light by very high frequency acoustic waves with wavelengths comparable to visible light.[Williams, 1984]

Photo-thermoelastic deformation.

For laser power densities below the ablation threshold and longer pulse duration, where thermal diffusion processes can play a significant role, photothermal deformation of the irradiated material may excite flexural vibration. A single laser pulse (typically of 0.1 - 1 ms duration), or an intensity modulated laser beam, may cause significant surface heating and localised thermal expansion. The radiation absorption, and hence the magnitude of the effect, can be enhanced by prior blackening of the target surface.[Fox 1974, Hane et al. 1988b] The differential heating and expansion through the depth of the material causes the surface to deform,[Karner et al., 1985] which generates a localised bending moment at the irradiation site.

The term "Drum Effect"[Charpentier et al. 1982, Rousset et al. 1983a&b, Rousset et al. 1985] was initially used to described the unwanted influence of thermoelastic flexing of thin plate samples in photoacoustic experiments using gas microphones to determine the thermal diffusivities of metals. This effect was later employed by Hane et al. (1988), using a chopped low-power diode laser (25 mW at 830 nm), to periodically flex a 12 mm diameter, 80 μm thick glass disk which had been circumferentially mounted. These authors also used the diode laser system to resonate both a 16 mm × 7 mm × 300 μm stack of three 100 μm thick glass plates and a 18 mm × 18 mm × 38 μm silicon wafer glued to an 80 μm thick glass slide (both targets mounted as clamped-free cantilevers) for the detection and definition of sub-surface laminations or holes.[Hane et al., 1988a&b] Forced resonance was shown to be very effective for improving the sensitivity in mapping defects in plate-like samples. Hane and Hattori (1990) have described the experimental characteristics of a thermoelastically bent layered plate using a theoretical model based on a temperature moment caused by thermal wave propagation.

Photothermal deformation has also been used to vibrate micromechanical resonators for fibre-optic sensing.[Andres et al. 1986, Uttamchandani et al. 1987, Jones et al. 1988, Kozel et al. 1990] Etched silicon bridge microresonators, with metallic coatings to enhance thermal expansion upon laser irradiation,[Falconer 1987] and tiny single and dual tine metallic cantilevers[Jones et al., 1989] have been monitored in ways which include interferometric vibration sensors.[Langdon and Lynch, 1988] Small frequency changes in the resonant oscillation frequencies of the cantilever microresonators occur with change in external parameters such as pressure and temperature.[Hockaday et al., 1990] Thus, microresonators can be used as sensors.

Many of the methods used for detecting transverse structural vibrations at acoustic frequencies are the same as those mentioned earlier for detecting ultrasonic shock-waves. Examples include holography,[Aprahamian and Evensen, 1970] capacitance variation with proximity (ESAT),[Adams and Bacon, 1973] microphones[Adams and Coppendale, 1976] and piezoelectric accelerometers.[Nagy et al., 1978] Other methods which have been used for structural vibrations include strain gauges,[Koss and Tobin, 1983] Doppler velocimetry[Buchhave 1975, Cookson and Bandyopadhyay 1978, Halliwell 1979] and a variety of non-interferometric fibre optic sensors.[Legace and Kissinger 1977, Cook and Hamm 1979, Chitnis et al. 1989, Dakin and Culshaw 1989, Perlin 1989, Philp et al. 1992]

Bulk and fibre-optic interferometric sensors have been described by many authors.[Deferrari et al. 1967, Drain et al. 1977, Bowers 1982, Lewin et al. 1985, Laming et al. 1986, Waters and Mottier 1986, Jacob et al.1988, Takada et al. 1990, Koch and Ulrich 1990] Interferometers are extremely sensitive devices since they respond to optical path changes which are a small fraction of a wavelength. However, particularly with fibre interferometers, this sensitivity produces its own problems in that fluctuations in ambient parameters (particularly temperature) randomly affect the path difference between the two beam paths of the interferometer and the output signal undergoes unpredictable fading.[Jackson and Jones, 1989] Furthermore, as the phase shift due to the measurand is detected, changes in source intensity and frequency, and the polarisation states of the interfering beams, also cause unpredictable variations.[Sudarshanam, 1992] To overcome these unwanted effects, demodulation techniques have been devised for dynamic phase shift measurement in both bulk-optic and fibre-optic interferometry. Such techniques include:

i. Heterodyne interferometry, where the optical frequencies in the signal and reference arms have a constant difference of some tens of MHz, and the output is a phase modulated difference frequency signal which can be electronically demodulated by RF circuitry.

ii. Active homodyne interferometry, where the signal and reference arms have the same optical frequency and active feedback phase modulation is used to bias the interferometer at the quadrature point. At this point the phase difference is biased at 90° and sensitivity is a maximum as the slope of the intensity/phase curve is a maximum.

iii. Passive homodyne interferometry, where two output signals are derived with a constant $\pi/2$ phase difference which can then be processed to yield the induced differential phase shift of the interferometer. These demodulation techniques, unlike the active homodyne system, may be performed without feedback to an active element in the optical paths.[Koo et al., 1982] Phase-shift measurements have been achieved by using a 3×3 directional coupler as the optical mixer of a Mach-Zehnder interferometer in conjunction with electronic processing.[Koo et al. 1982, Jackson and Jones 1989] These measurements are also possible from the spectral-analysis of a frequency-filtered Michelson interferometer (manually biased at quadrature whilst sensing simple harmonic surface oscillations) using J_1(max), J_n(null), J_1/J_2, J_1/J_3 Bessel function methods or Bessel recurrence relation methods.[Deferrari et al. 1967, Sudarshanam 1992]

Kobayashi and Shudong (1988) constructed a bulk-optic frequency-modulated heterodyne interferometer for remotely measuring the range and vibrational displacement of both specular and diffuse surface reflectors. Surface displacements of about 1 nm were detected for specular objects at a range of 2 m. Yoshino (1989) also produced a heterodyne-type interferometric displacement sensor using polarisation maintaining optical fibre and a frequency-stabilised He-Ne laser at 633 nm which was subjected to a transverse magnetic field. This laser produced two simultaneous outputs separated by the Zeeman splitting of about 300 kHz. Thus, the heterodyne-type interferometer was based on the two coherent frequencies generated directly from the same laser. Yoshino reported a measurement precision of about 1 nm for periodic displacement of a piezoelectric mirror shaker (minimum detectable phase shift (MDPS) ~ 2×10^{-3} radian). These sensitivities are consistent with calculations which show that typical heterodyne shot-noise-limited systems have a MDPS of about 2 milliradian over a 1 kHz bandwidth for a SNR of 1.[Sudarshanam, 1992]

Extreme sensitivity has been achieved with bulk-optic active homodyne interferometry and also, to a lesser degree, using glass fibre optical paths. Yoneda et al. (1980) reported an unconventional He-Ne laser interferometer which used the two first-order beams from a diffraction grating and lens combination to give reference and sensing beams which were very close together and thus relatively insensitive to differential vibration and thermal effects. The interferometer was held at quadrature using a piezoelectric compensator to vary the path length in the reference arm. Using this system, the minimum detectable vibration amplitude of an oscillating quartz crystal plate was found to be 3×10^{-14} m with a final noise bandwidth of 0.017 Hz. Jackson et al. (1980) reported a stabilised He-Ne fibre-optic Mach-Zehnder interferometer, which was biased at quadrature using a piezoelectric stretcher in the reference fibre to remove low frequency drifts. A similar piezoelectric stretcher was used in the signal arm with 100 turns of fibre to produce controlled phase shifts varying down to about 10^{-7} radian. The measurand in this case was the extension in path length caused by the minute diameter expansion of the stretcher. This interferometer was able to detect periodic diameter changes of approximately 1×10^{-13} m over a 30 Hz bandwidth (MDPS $\sim 2 \times 10^{-6}$ rad/$\sqrt{\text{Hz}}$) at 1 kHz. The active homodyne-type Michelson interferometer used in this thesis is not as sensitive as that reported by Jackson et al. (1980) because a fibre-air-fibre optical path was incorporated into the interferometer design to enable non-contact surface vibration detection. The optical path from glass-fibre to open-air, and back again into fibre after specular reflection, significantly reduced optical power in the signal arm (reducing the SNR) and so limited the output sensitivity to 1.2×10^{-2} rad over a 30 kHz bandwidth (7×10^{-5} rad/$\sqrt{\text{Hz}}$) at 100 Hz. This MDPS was determined for a SNR of 10 and is therefore a fairly conservative measurement.

Passive homodyne interferometers using Bessel function methods, are limited in practical applications to a MDPS of about 0.01 radian,[Sudarshanam, 1992] whereas passive homodyne interferometers based on 3 × 3 directional couplers are reported to have a MDPS of about 3 x 10^{-6} rad/√Hz at 1 kHz.[Koo et al. 1982 and 1983] Recently, a passive demodulation scheme using a 3 × 3 directional coupler as the optical mixer was used in a Mach-Zehnder fibre interferometer with a MDPS of 2.20 × 10^{-4} rad/√Hz at 600 Hz. Under these conditions the maximum detectable phase shift was 140 radian and so the dynamic range was 116 dB.[Brown et al., 1991] The maximum and minimum detectable phase shifts decreased in proportion to the inverse of the operating frequency. 4 × 4 directional couplers have been fabricated[Mortimore, 1990] and should soon be commercially available. These couplers provide four optical outputs, where each successive output fibre experiences a phase retardance of 90° to that of the previous branch. Hence, two output signals may be chosen with a constant $\pi/2$ phase difference, which then greatly simplifies the processing required to demodulate the optical output of the homodyne interferometer.[Niemeier and Ulrich, 1986]

The application of modal analysis techniques for non-destructive testing and evaluation has been described by many authors. In one of the earlier reports of modal analysis for NDT, Spain et al. (1964) demonstrated the application of simple modal comparison to crack-test crankshafts and brake pedals. Other significant contributions (taken chronologically) include: the testing of steel plates taken from a ship's hull,[White, 1971] railway wheels,[Bray et al. 1973, Nagy et al. 1978] carbon and glass fibre/epoxy plates,[Adams et al., 1975] aluminium bars and camshafts,[Adams et al. 1978, Cawley and Ray 1988] aluminium plates and reinforced plastic plates, [Cawley and Adams 1978 and 1979a&b, Cawley et al. 1985] circular plates,[Eastep and Hemmig, 1982] and pistons or pulleys.[Cawley, 1985 and 1987] None of the above authors used non-contact optical techniques to excite the structures. The modal analysis of these, and more complicated structures for NDT, has progressed with the development of mathematical models for predicting the effect of damage on the modal frequencies. These models have treated cantilever beams,[Davis et al. 1972, Kitching et al. 1975, Sanderson and Reid 1976] plates and cylindrical bars,[Bentham and Koiter, 1973] welded joints,[Chondros and Dimarogonas, 1980] shafts, [Sanderson and Kitching 1978, Dimarogonas and Papadopoulos 1983] and other simple structures comprising a combination of these.[Akgün et al. 1984, Ju 1986, Ju et al. 1982 and 1983, Ju and Mimovich 1988, Wang et al. 1984] Analysis techniques using Fast Fourier Transforms,[Gaukroger et al., 1974] finite element analysis,[Yuen, 1985] the maximum entropy method,[Romberg et al., 1984] the transfer matrix method[Sato, 1983] and the fracture hinge method[Ju et al., 1982] have all been used to investigate the vibration of structures with abrupt changes of cross-section due to cracks, slots or flaws. These analysis techniques apply to large, as well as to small structures, as was demonstrated by the modal analysis of an off-shore oil platform excited by wave action.[Vandiver 1977, Yang J. et al. 1974, Rogers 1987]

This thesis is concerned with the ablative and photo-thermoelastic flexing regimes described. The summary of photoacoustic ultrasonic inspection was given in order to highlight methods of laser excitation and delivery of that excitation, the type of defects that may be detected using ultrasonic investigation and the non-contact vibration detection used to sense the small (usually less than a few nanometres) vibrations on the surface of the sample. Most of the detectors used for ultrasonic or modal analysis could have been used for this work. However, electromagnetic interference in electrical sensors such as EMAT or ESAT due to charging or discharging the laser flashtube power supply, and the requirement for a non-loading, non-contact sensor, led naturally to the decision to develop an all-fibre optical detection system.

Although there has been considerable recent interest in the field of microresonator excitation and sensing, to the knowledge of this author, repetitively pulsed diode lasers have not been previously used to excite the type of large structures described in this work. It is also claimed that a single laser pulse, with a laser power density below the ablation threshold of the irradiated material, has not been previously used to excite large structures (cantilevers and truck rims) for the purpose of modal analysis. It is believed that these aspects of this work are therefore quite novel.

Chapter 2

Experimental laser excitation and sensing systems

This chapter describes three experimental arrangements for the excitation and sensing of laser-induced structural vibrations. The first of these arrangements was used for single laser pulse measurements using ablative and photothermal flexing techniques to excite cantilevers. Two cantilevers were chosen to exhibit very different modal frequency characteristics. The selected structures were a 300 mm × 12 mm × 3 mm aluminium clamped-free cantilever (cantilever A) and a 315 mm × 12 mm × 254 μm stainless steel (shim) clamped-free cantilever (cantilever S), the latter being the same as that used by Koss and Tobin (1983). These cantilevers were then irradiated with a single 40 J pulse from a Nd:glass laser. It was sometimes necessary to split the Nd:glass laser pulse into two beams so that the laser could irradiate a cantilever at two locations simultaneously. Initially, strain gauges were used to detect the laser-induced transverse vibration of these cantilevers, but these gauges suffered from difficulties in reproducibly attaching them to the cantilevers. The mass of the gauge, glue and associated wires produced a slight shift in the modal frequencies. In addition, the large sensing area of the strain gauge bridge resulted in poor spatial resolution and therefore also reduced the frequency resolution upon Fourier analysis. A non-contact fibre-optic vibration sensor (proximity sensor, see section 2.1.3), was developed to overcome these complications. The cantilevers, detection system and bulk-optics were mounted on a vibration isolated table to help remove unwanted building vibration effects.

The vibrations profiles were stored as signal-amplitude verses time records on a Philips 250 MS/s dual channel storage oscilloscope (4096 data points), and then down-loaded to a small computer where they were transformed to the frequency domain using a Fast Fourier Transformation (FFT) routine.[Ellis, 1988] During the latter part of this work, a Tektronix digital signal analyser (DSA 602), with real-time FFT display, was available which enabled the direct storage of vibration data (up to 32,768 data points) and frequency spectra. The data retrieval, FFT processing (for use with the Philips oscilloscope), integration, vibration modelling, thermal modelling, Euler-Bernoulli modal distribution modelling and plotting routines used in this work, were written by this author.

The second experimental arrangement used a single 40 J pulse from the Nd:glass laser to excite free vibration in a 57 kg, 50.8 cm diameter steel truck wheel rim suspended horizontally by twelve springs attached to an overhead mount. A Brüel & Kjaer Type 8200 calibrated accelerometer was used to detect structural vibrations of the rim since the large inherent sway of the hanging rim made the use of the fibre-optic proximity sensor impractical. After laser excitation, the suspension system allowed the structure to develop a fairly large low-frequency sway (~ 1 mm), which precluded the use of the proximity sensor since this needed to be located about 0.2 mm from the vibrating surface (see section 2.1.3). A more rigid mounting system for the truck rim would have solved this problem, but this was not attempted because modal data for unclamped oscillation was required to allow predicted modal frequencies (already obtained, using finite element analysis, before conducting the experiment) to be compared with the measured modal frequencies. The rim vibrations were recorded and processed on the Tektronix DSA 602 analyser.

The third experimental arrangement used an all-fibre stabilised interferometer (interferometric sensor, see section 2.2.2) and the Tektronix DSA 602 analyser to measure the resonant frequencies of cantilever A and other cantilever structures with plate-like dimensions. For these measurements, the structures were irradiated with repetitive pulses from a single low-power (15 mW r.m.s) diode laser directed at various locations along the front surface. The sites of laser irradiation were chosen to optimise the efficiency of photo-thermoelastic flexing and the pulse-repetition-rate was then adjusted to achieve resonance of the cantilevers. An additional one or two diode lasers were, on some occasions, used to synchronously irradiate several sites to enhance a particular resonance. To demonstrate the remote sensing applications of this system, the diode lasers and interferometric sensor were removed to a distance of 1 m from cantilever A and a 3 mm thick glass window was placed in the optical paths.

2.1. Single pulse laser excitation

2.1.1 The Nd:glass laser

The laser used for single-pulse excitation measurements used a 460 mm long Nd^{3+} doped glass rod, excited by dual linear close-coupled Xenon flashtubes triggered simultaneously. An EG&G model 581 calibrated radiometer measured the output energy of the laser pulse repeatedly at 38 to 40 J. The Nd:glass laser pulse had a wavelength of 1.06 μm, a pulse length of 600 μs FWHM and an unfocused spot diameter at the target of 8 mm (referred to hereafter as an "unfocused laser pulse"). The power density of the unfocused laser pulse at the target was approximately 1.3×10^5 W.cm^{-2}. A 1 mW visible He-Ne CW laser beam was directed so as to pass through the central axis of the Nd:glass optical cavity as an aid in aiming the irradiation point of the Nd:glass system. A typical output trace of the normal mode laser pulse is shown in figure 2.1.1.

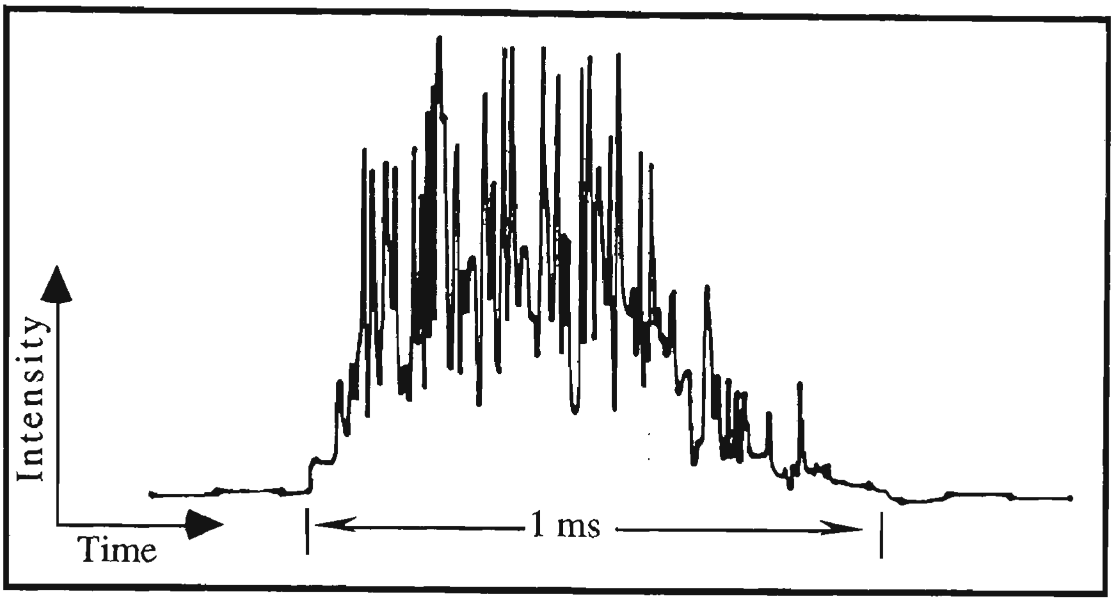

Figure 2.1.1. Profile of the unfocused Nd:glass laser pulse

2.1.2 Contact vibration sensors

Standard vibration sensors include strain gauges, microphones, accelerometers and optical detectors, all of which have specific advantages and disadvantages. These vibration sensors can be divided into two categories; contact and non-contact. Although the major emphasis of this work is on non-contact sensors, some contact ones were also used. The sections which follow provide details of all the sensors employed in this work.

2.1.2.1 The strain gauge bridge

A strain gauge exploits the dependence of the resistance of a wire on its geometry. A small wire grid is bonded to a flexible backing material, sheathed and then attached to the vibrating surface.

A signal is derived from the change in resistance of the wire grid due to changes in the length and diameter of the wire as it stretches with the surface to which it is bonded. Four TML PL-10-11 strain gauges (length 10 mm, resistance 120 Ω and gauge factor 2.07) were attached to the surfaces of both cantilevers A and S with an epoxy resin adhesive and connected to form a Wheatstone bridge. The strain gauges were arranged in a signal-enhancing configuration whereby two strain gauges acted in compression whilst the two on the opposite side of the cantilever were in tension. The out-of-balance signal from the bridge was monitored and amplified. The effective sensing area of the strain gauge bridge was approximately 100 mm^2. An illustration of the arrangement is given in figure 2.2.1.

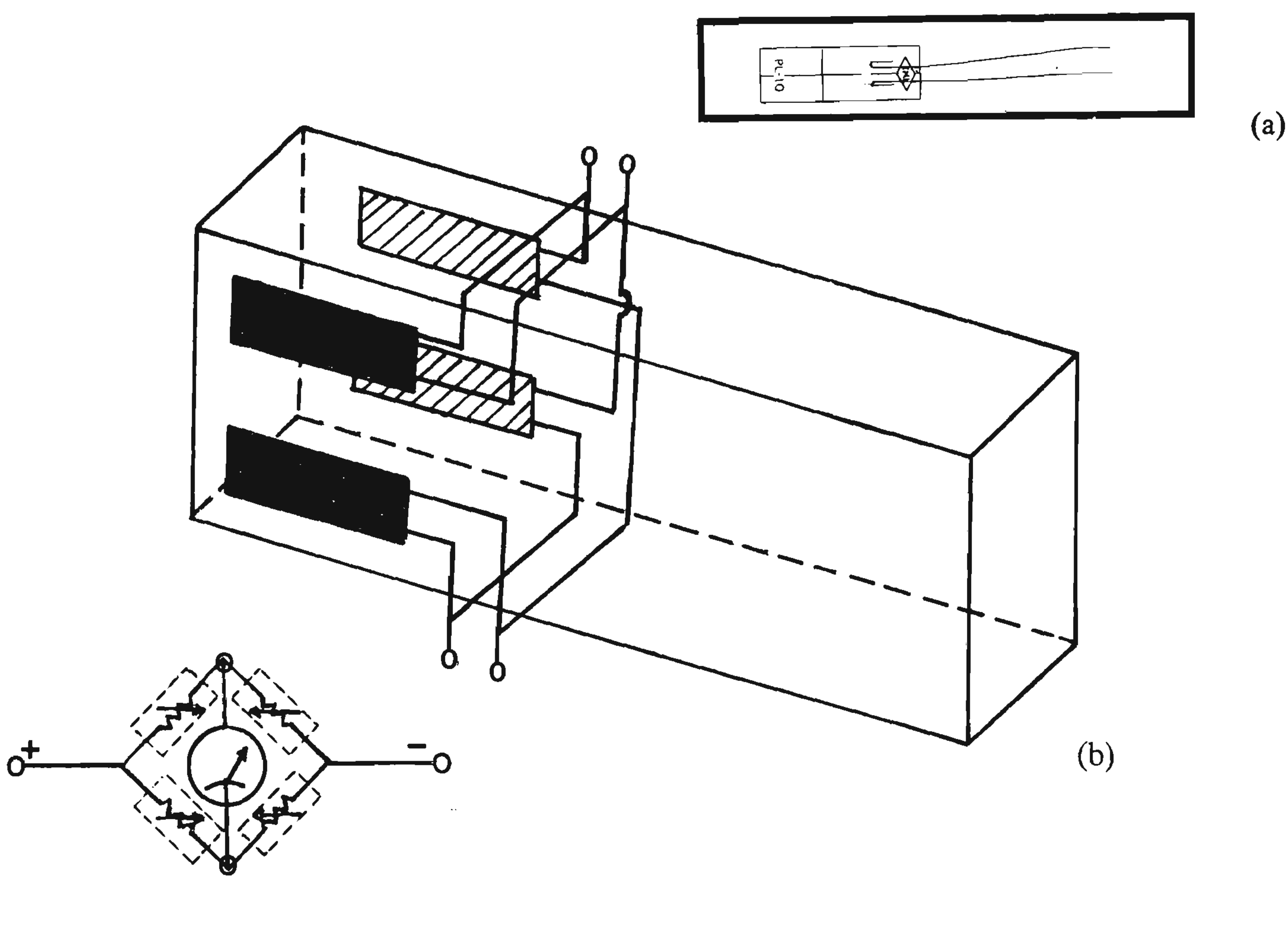

(c)

Figure 2.1.2.1. Wheatstone bridge strain gauge configuration. (a) An individual strain gauge, (b) arrangement of the strain gauges on the cantilever, and (c) the electrical connection of the four strain gauges.

2.1.2.2 The accelerometer

A Brüel & Kjaer type 8200 calibrated piezoelectric accelerometer was used for impulse investigations and to monitor the vibrating surface of the large truck rim. The mass of the accelerometer (excluding co-axial connections) was 21 g. The accelerometer can be seen in plate 4.1 of chapter 4, attached (using an adhesive paste) to the nearest side of a hanging truck wheel rim and trailing a slim co-axial cable connected to the processing electronics situated on the same table which supports the rim.

2.1.3 A non-contact fibre-optic vibration sensor

A fibre-optic vibration sensor [Philp et al., 1992] (proximity sensor) was developed as a non-invasive non-contact alternative to the strain gauges and accelerometer. This optical proximity sensor was used to investigate the modal frequencies of cantilevers A and S in an electromagnetically noisy environment which restricted the use of some standard electrical detectors. A schematic diagram of the proximity sensor, used for vibration frequency measurements, is shown in figure 2.1.3.1.

The light source, used in this sensor, was a Hewlett-Packard HFBR-1404 820 nm LED which was square-wave (on/off) modulated at a frequency of 1 MHz (1000 times greater than the frequencies under investigation) and launched into a 50/125 μm multimode optical fibre at a power level of -17.6 dBm. The modulated light was passed through a 50:50 multimode directional coupler and directed onto a vibrating structure. Some reflected light from the structure was coupled back into the fibre, where it was detected by a Hewlett-Packard HFBR-2406 PIN photodiode module. Changes in the separation between the fibre tip and the vibrating surface caused changes in the intensity of the light re-entering the fibre. Intensity variation in the reflected light resulted in modulation of the square wave at the flexural displacement frequencies of the vibrating structure.

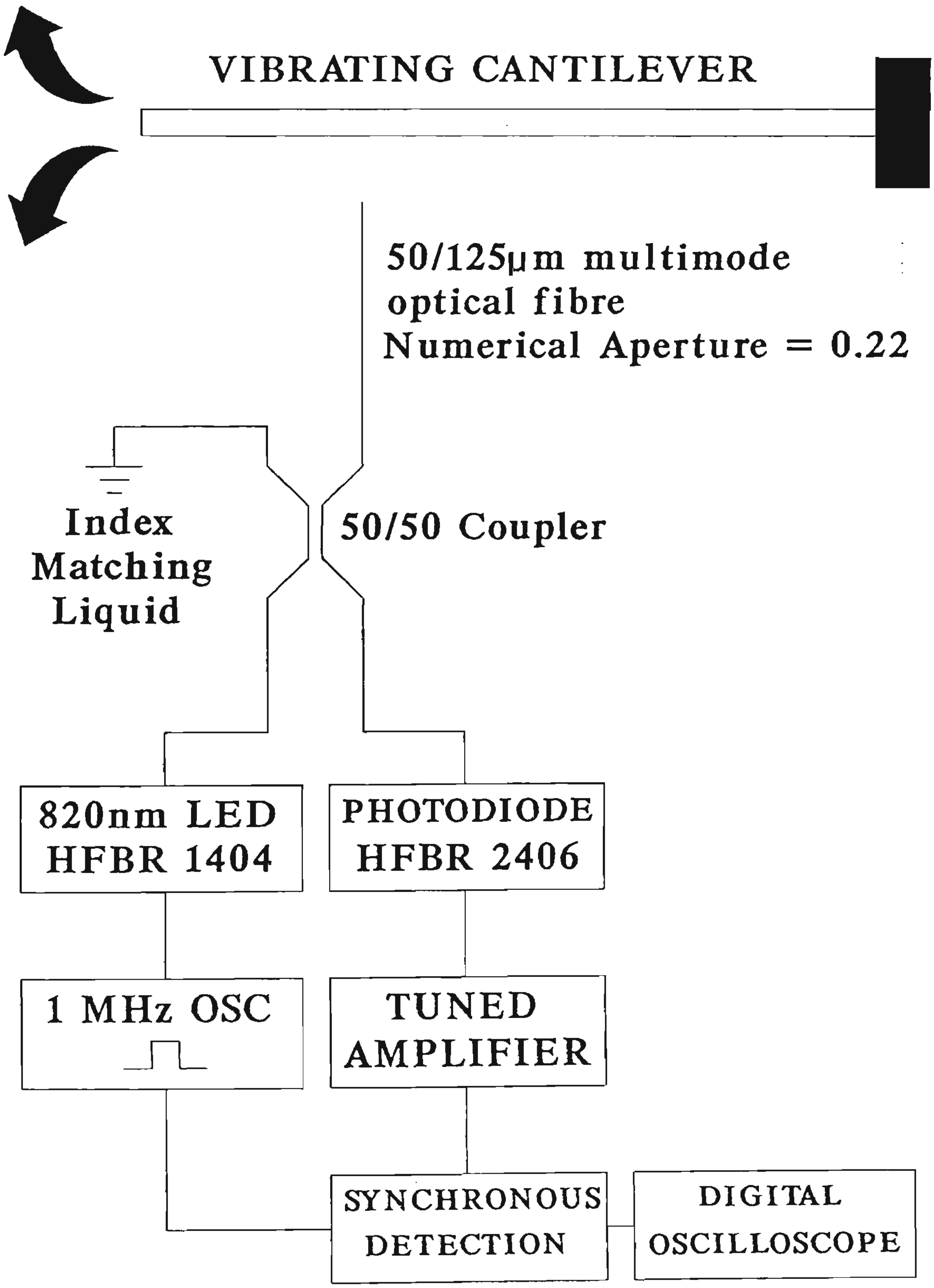

Figure 2.1.3.1. Schematic diagram of the proximity sensor

A synchronous detection circuit was used to improve the signal-to-noise ratio of the basic optical sensor. The intensity-modulated signal from the photodiode was amplified by an LM733 operational amplifier tuned to 1 MHz and then synchronously detected using a CD4010 quad bilateral switch operating as a balanced mixer. The reference signal for the synchronous detection was supplied by the same signal generator used to modulate the LED. No phase compensation was necessary in the synchronous detection as phase shifts were negligible for modulation frequencies below 1 MHz, since the optical and electrical paths were shorter than a few metres. The output from the synchronous circuit was filtered using a low-pass filter which had a cut-off frequency of 20 kHz. The output noise level was 1.8 mV peak-to-peak. The signal-to-noise ratio of the PIN photodiode module was improved after the synchronous detection circuit by a factor of ten, from about 3:1 to 30:1. The circuit diagram for the synchronous detection circuit is shown in figure 2.1.3.2.

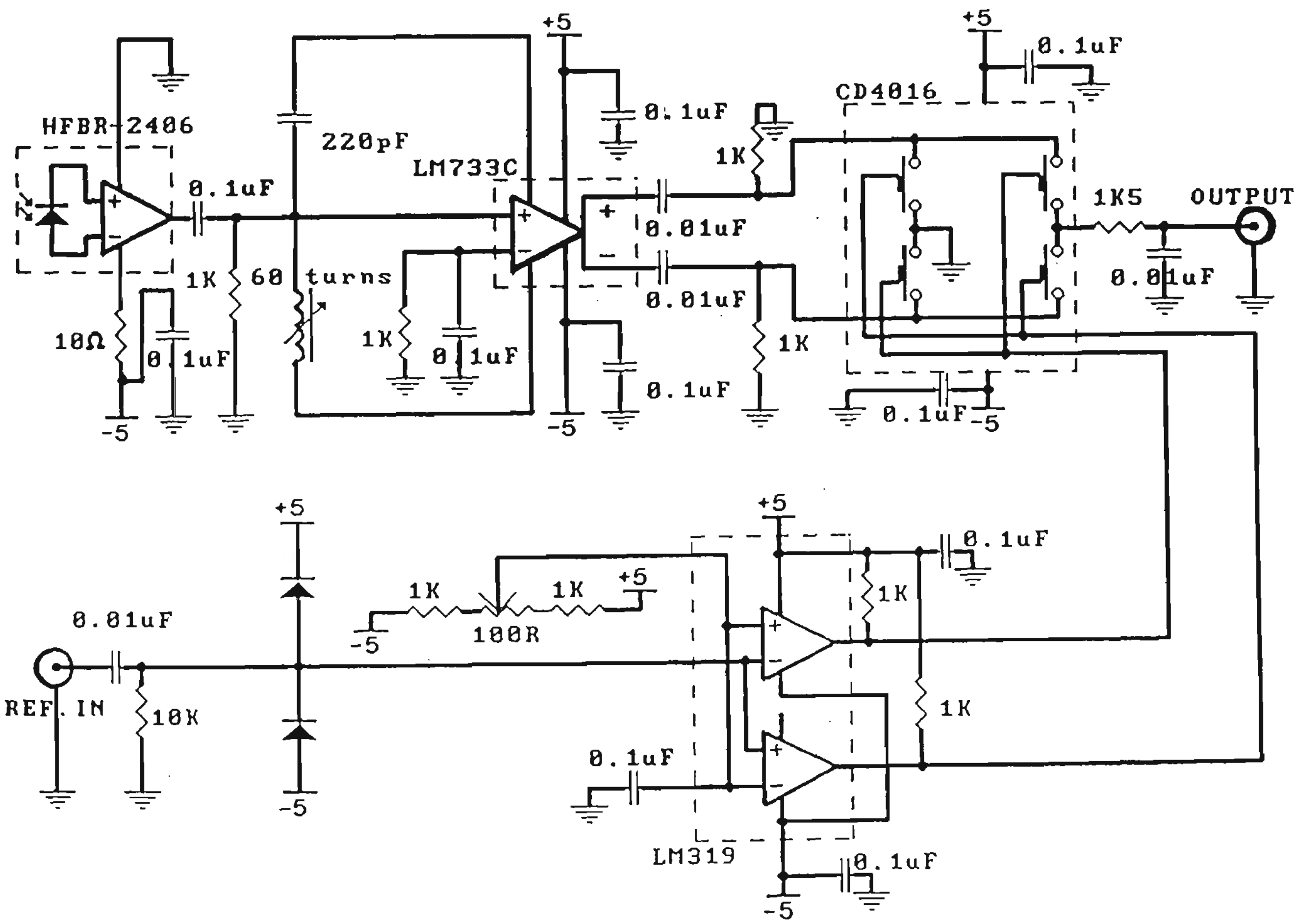

Figure 2.1.3.2. Circuit diagram of the synchronous detector

The physical variables which determine the optical power coupled back into the fibre include the reflectivity and proximity of the surface, the angle of incidence of the light, the numerical aperture of the sensing fibre and the launched optical power.[Perlin, 1989] For vibration frequency measurements, the cause of the signal variation is not important, so long as the intensity of the return signal is modulated at the vibration frequency. For the cantilever structures and experimental arrangement described in this thesis, the variations in power coupled back into the fibre are principally due to variations in the probe to surface distance caused by vibration.

Figure 2.1.3.3 shows the output signal from the proximity sensor as a function of proximity for normal incidence on a variety of reflective surfaces; namely, a front-surfaced mirror, a polished (buffed) steel surface and a clean unpolished aluminium (as extruded) surface. This data was obtained by mounting the surface on a micrometer screw and varying the distance between the fibre tip and the reflective surface. The reflected light intensity from the surface is inversely proportional to the square of the distance and hence the detector output did not vary linearly with displacement. Displacement amplitudes up to about 0.2 mm could be detected with reasonable linearity from an unprepared aluminium surface, but displacements in excess of this level produced signal distortion. The minimum detectable amplitudes were determined from the measured signal noise and the slope of the curves in figure 2.1.3.3. Displacements of 1 μm for the mirror, and 4 μm for buffed steel and unpolished aluminium surfaces, were detected for a sensor proximity of approximately 50 μm.

Figure 2.1.3.4 shows the vibration profile and the modal frequencies for cantilever A using a strain gauge bridge. Figure 2.1.3.5 provides the same information for an identical cantilever (without strain gauges) using the proximity sensor at a point 60 mm from the clamped end. The difference in the vertical scales for the two figures is not significant as quite different sensors are compared.

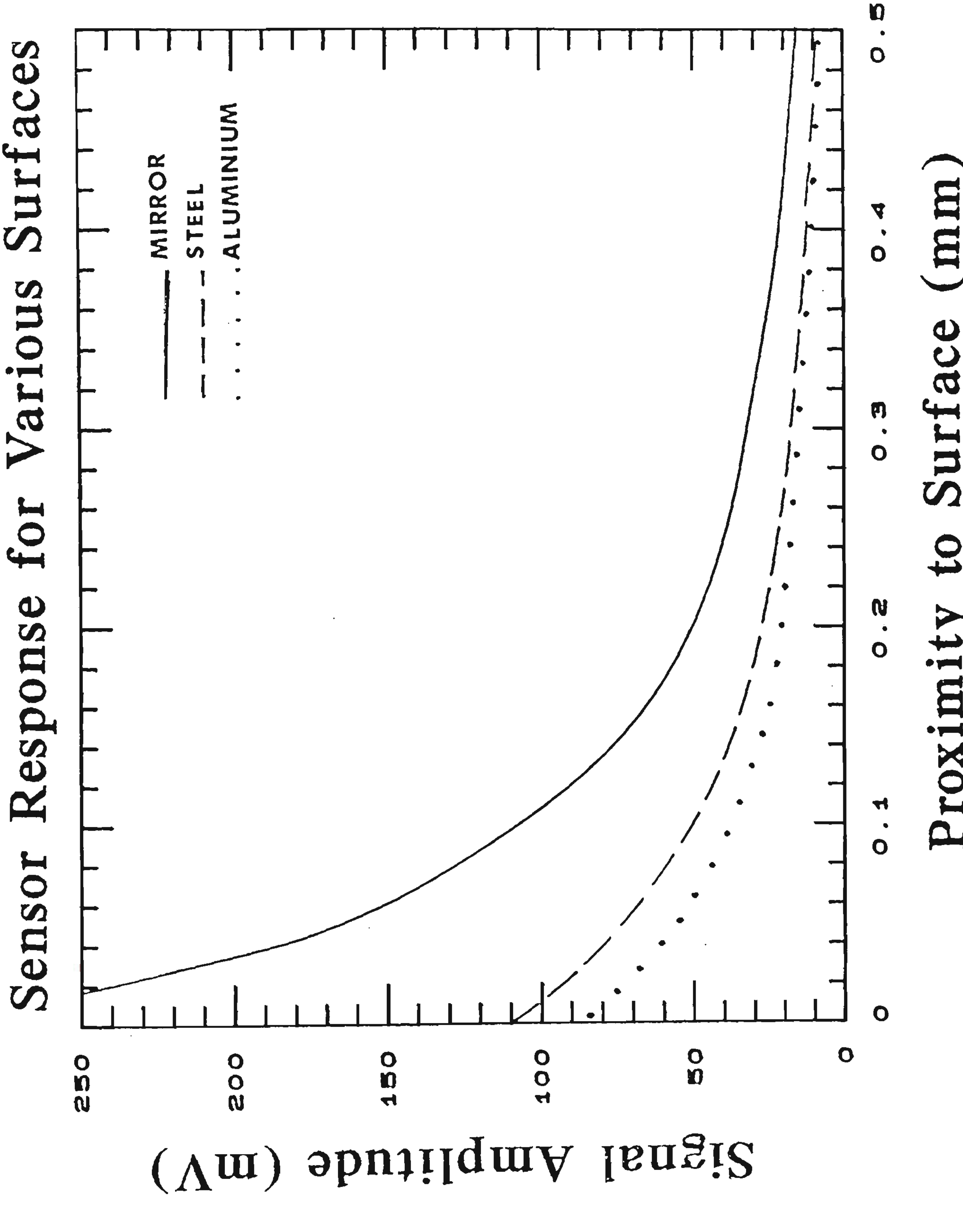

Figure 2.1.3.3. Proximity sensor output for various reflective surfaces

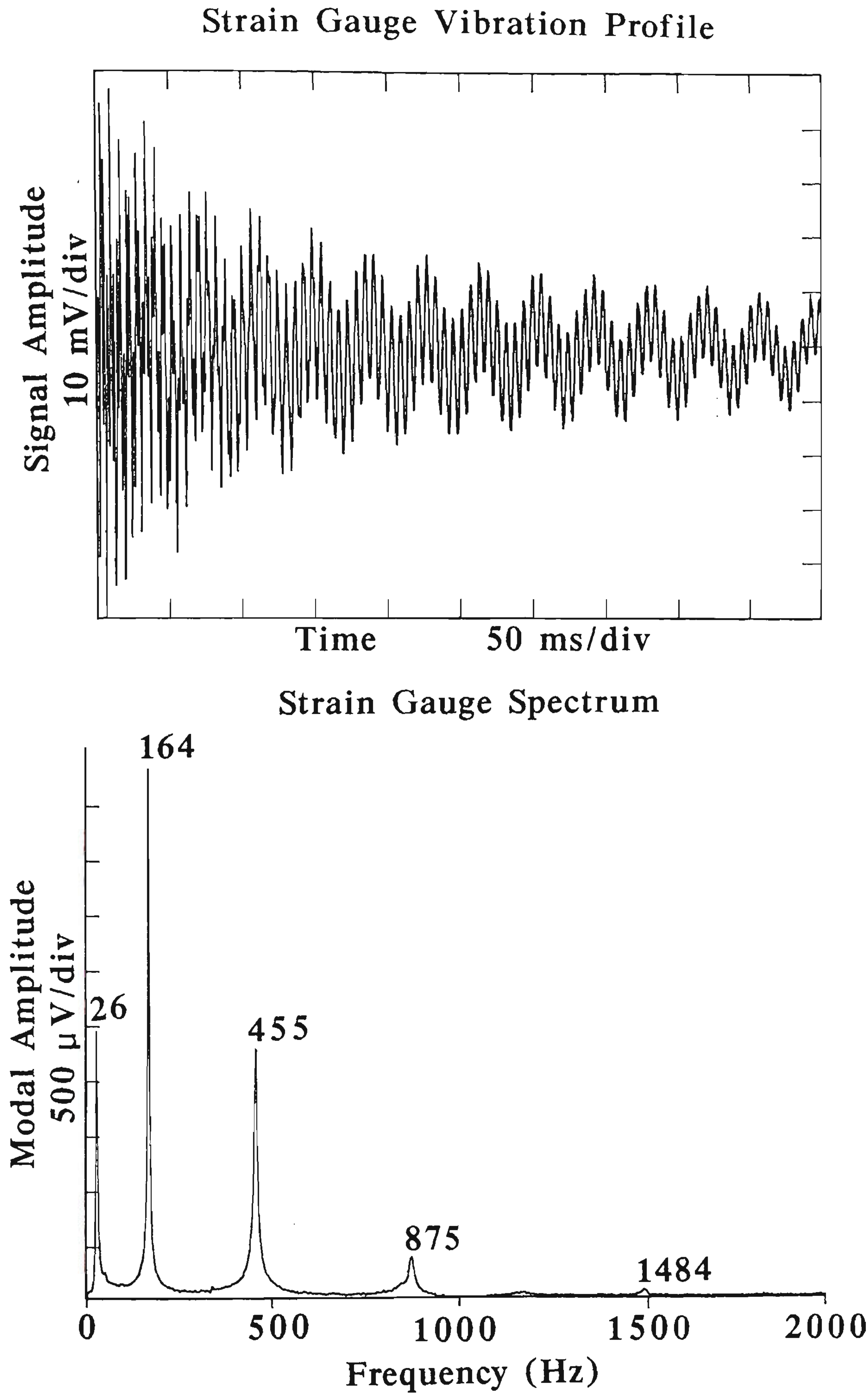

Figure 2.1.3.4. Vibration profile and frequency spectrum of a laser-excited aluminium cantilever as detected by a strain gauge bridge

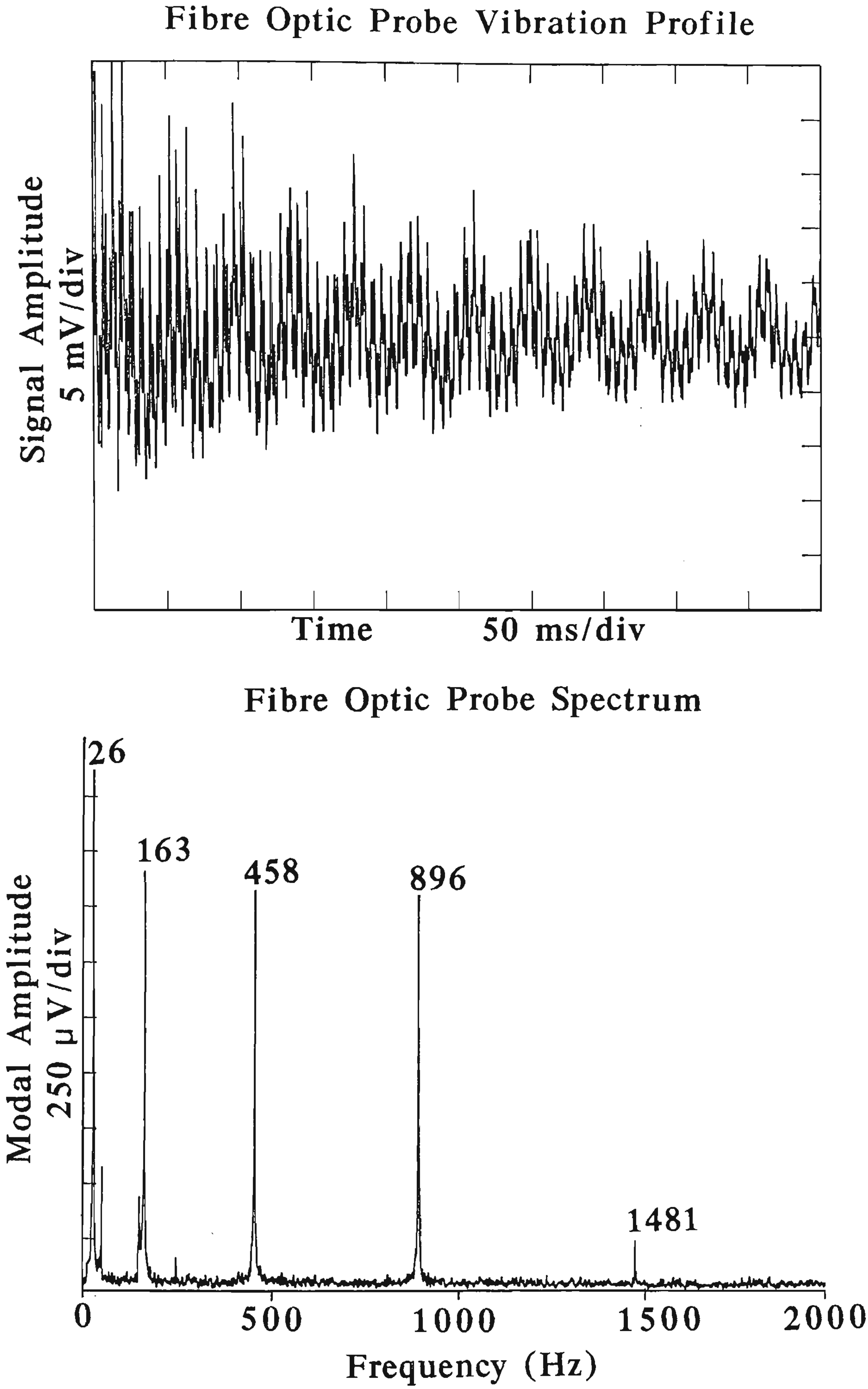

Figure 2.1.3.5. Vibration profile and frequency spectrum of a laser-excited aluminium cantilever as detected by the fibre-optic proximity sensor at a distance of 0.2 mm from the cantilever's surface

Asymmetry, due to the large amplitude of vibration, is evident in figure 2.1.3.5. These non-linear effects produced additional harmonics in the acoustic spectrum but did not affect the frequencies of the vibrational modes. The first five modal frequencies for the aluminium cantilever were calculated from Euler's equation of free vibration (see section 3.1) to be 26 Hz, 163 Hz, 457 Hz, 896 Hz and 1482 Hz, and these agree well with the measured values in the figure.

For the small vibration amplitudes excited, the variation in angle of incidence of the probe beam on the surface is less than a few minutes of arc. For surfaces such as unpolished aluminium, the diffuse reflection makes the sensor signal relatively insensitive to the small bending effects caused by flexural vibrations. In the aluminium cantilever, the variations in surface tilt can be estimated from the vibration amplitude and distance between nodes. In the most pronounced case (mode 5), there are four nodes over the 30 cm length of the cantilever and so the distance between a node and an antinode is about 43 mm. From the recorded signal amplitudes of around 10 mV (corresponding to approximately 0.02 mm), the angle of the surface normal to the line of the probe fibre is about 0.03°. The effect of this on the recorded vibrations (especially considering the acceptance angle of the optical fibre (N.A. ~ 0.2)) is negligible.

A comparison of the frequency profiles gained from the two transducers clearly demonstrates the enhanced frequency precision and resolution gained with the optical sensor. The agreement between the measured and calculated frequencies is better and the spectral peaks are much narrower. The area illuminated by the fibre-optic sensor was only about 7×10^{-3} mm^2, which is very much smaller than that of the strain gauges (effective area approximately 100 mm^2). Hence, the proximity sensor allowed much greater spatial resolution and more accurate modal frequency determination than was possible with the strain gauges. Loading effects due to the mass of the wiring and the adhesive must also be considered when using the strain gauges.

2.2 Repetitive diode laser excitation

2.2.1 Description of the diode lasers

Three 40 mW 810 nm Sharp LT016MD diode lasers were individually set in X-Y-Z positioners and the light from each was focused by a ×20 microscope objective onto the target surface. The output power of each diode laser was controlled by a Sharp IR3C01 Laser Diode Driver IC, with automatic power control, which operated via a feedback loop from an internal photodiode power monitor to control the laser diode drive current. This is shown in figure 2.2.1. The diodes were square wave modulated (chopped) using a TTL drive signal.

Since the average power of a chopped output is half the peak power, in order not to exceed a peak output of 30 mW from the diode laser (the maximum power rating of the diode was 40 mW), the CW power of the diodes was restricted to 15 mW. The laser diode drive circuits of several identical units could be triggered simultaneously and modulated by the same TTL drive signal. When three diode lasers were used, each laser was synchronously pulsed with a repetition-rate determined by the TTL modulation frequency.

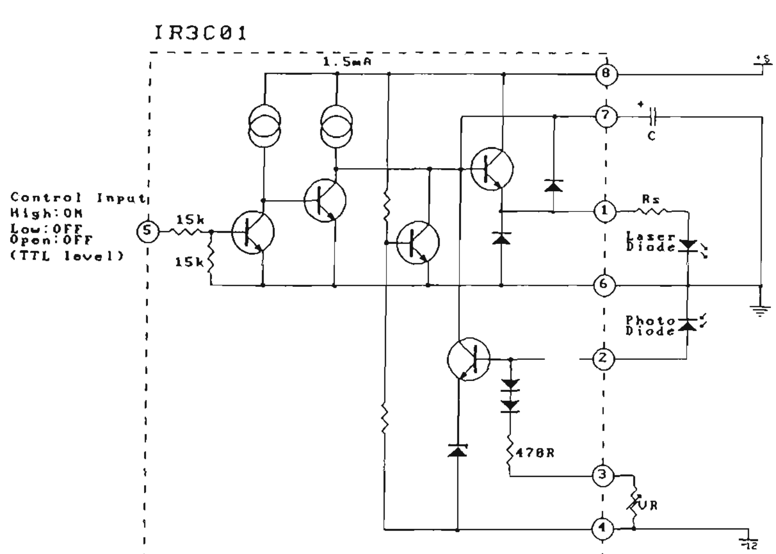

Figure 2.2.1. Laser diode drive circuit (Sharp IC IR3C01)

2.2.2 An all-fibre stabilised interferometer

In order to detect surface vibrations caused by low-power (diode laser) excitation of structures, an improvement in the detection sensitivity of about three orders of magnitude over that of the proximity sensor (described in section 2.1.3) was required. To achieve this improvement, a stabilised fibre-optic interferometer was designed and developed which exhibited a resolution of a few nanometres. A schematic diagram of the interferometer used for vibration measurement is shown in figure 2.2.2.1.

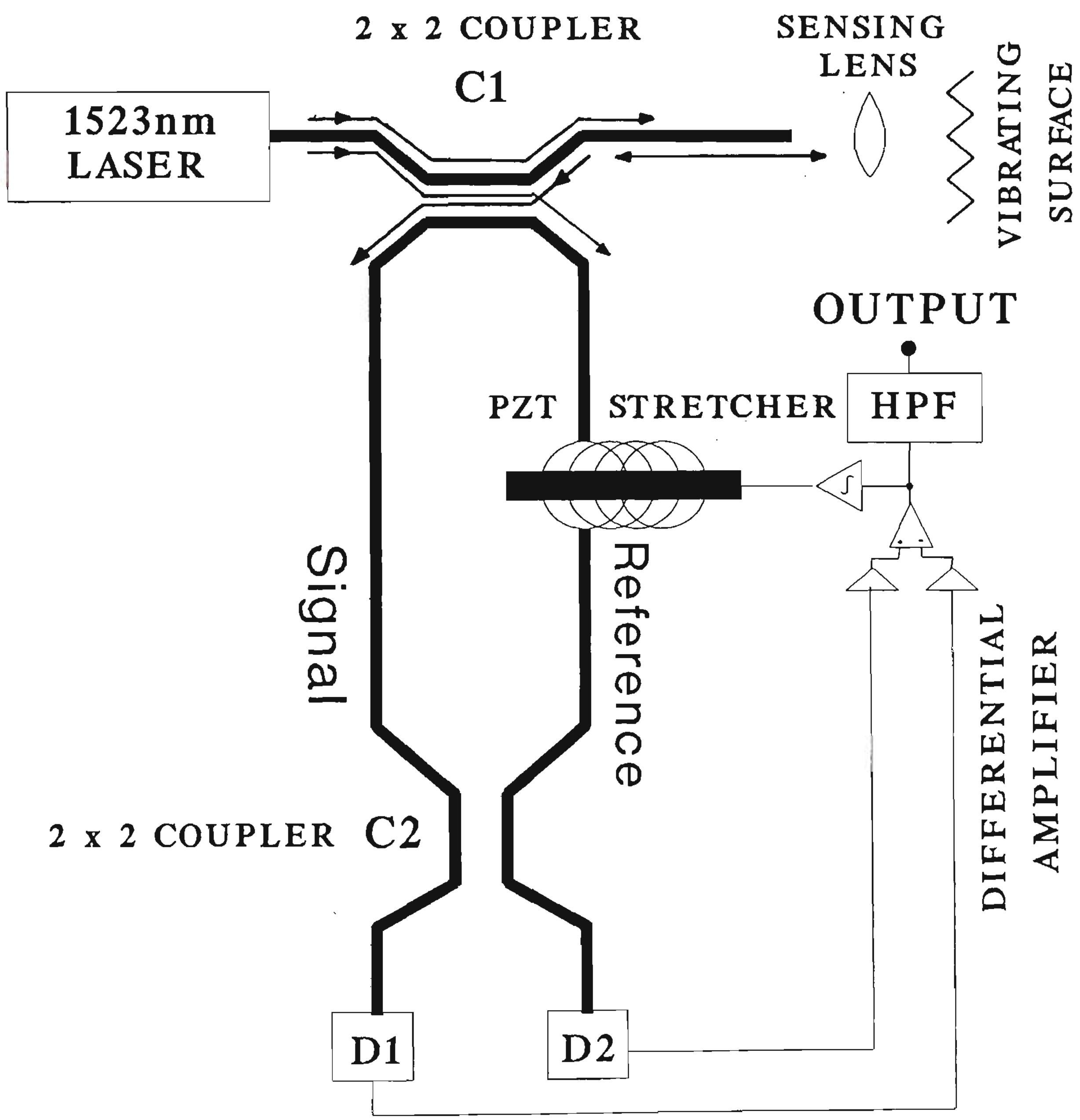

Figure 2.2.2.1 The all-fibre stabilised interferometer

The interferometer is an all-fibre design, using variations in the open-air path length between an output arm of a 2 × 2 directional coupler and the reflective surface of a vibrating test-sample, as the measurand. Light from a 1523 nm He-Ne laser, with a nominal output power of 1.2 mW and a coherence length of about 75 cm, was launched into one input arm of a single-mode 2 × 2, 1550 nm, directional coupler (C1), which divided the launched optical power into signal and reference branches as shown in the diagram. The reflected light from the vibrating surface was also divided in C1 to give modulated light in the signal arm. The signal and reference beams were then mixed using a second 2 × 2 directional coupler (C2). The optical power in the reference arm was attenuated using a few small radius turns of the fibre to approximately match the optical power to that of the signal arm and thus give high-contrast interference. Any change in separation between the sensing fibre tip and the vibrating reflective surface varied the path length of the signal branch with respect to the reference branch, causing intensity modulation of the output. Altering the signal path-length by half a wavelength modulated the output over its full range. The 1523 nm He-Ne laser source was chosen for this interferometer because it had a very long coherence length which was suitable for use with long air paths and also because it was compatible with standard 1550 nm single-mode couplers.

The operation of the interferometer can be analysed using a similar approach to that of Jackson and Jones (1989), whereby the electric field at each detector can be described by:

$$\tilde{E}_1(t) = k_{1t}k_{1c}k_{2t}\, e^{i\phi_a}\, \tilde{E}_0(t-\tau_a) + k_{1c}k_{2c}\, e^{i\phi_b}\, \tilde{E}_0(t-\tau_b) \qquad \text{eq. 2.2.2.1}$$

and

$$\tilde{E}_2(t) = k_{1t}k_{1c}k_{2c}\, e^{i\phi_a}\, \tilde{E}_0(t-\tau_a) + k_{1c}k_{2t}\, e^{i\phi_b}\, \tilde{E}_o(t-\tau_b) \ . \qquad \text{eq. 2.2.2.2}$$

Subscripts a and b refer to the signal and reference arms respectively. $k_{i(t \text{ or } c)}$ is the coupler co-efficient for the i^{th} directional coupler and subscript, t, denotes the transmitted beam in that coupler and c, the coupled beam. ϕ_a and ϕ_b are the phase retardance of the signal and reference arms respectively. $E_0(t)$ is the amplitude of the time dependent electric field of the source $\tilde{E}_0(t)$. τ_a and τ_b are the propagation times from the source to the second directional coupler via the signal and reference arms respectively. For simplicity, losses in the open air path are ignored and 100% reflection is assumed at the vibrating surface.

The coupled arm of an ideal 50:50, 2 × 2 directional coupler experiences a 90° phase retardance with respect to that of the direct (transmitted) arm. These phase shifts result in the signal being 90° ahead of the reference at one detector (D1) and 90° behind the reference at the other detector (D2). Thus, for this arrangement, the two detector outputs are 180° out of phase.

The irradiance observed at each detector (Π_i) may be evaluated using

$$\Pi_i = <\tilde{E}_i \cdot \tilde{E}_i^*> , \qquad \text{eq. 2.2.2.3}$$

where < > denotes time averages over one period of the field, * the complex conjugate and the constants involved in this expression have been ignored. It is convenient to assume that C1 and C2 are ideal 50:50 directional couplers even though the laser wavelength used is slightly off their design wavelength. Therefore, since k_{it} is real and k_{ic} is imaginary (90° phase shift), we can write $k_{ic} = ik'_{ic}$ and $ik'_{ic} = ik_{it} = ik_i$ (here the dashed terms are real and $k_{ic}' = k_{it} = k_i$ for an ideal 50:50 directional coupler). The irradiance at the two detectors can be stated as:

$$\Pi_1(t) = k_1^2 k_2^2 \, [<E_0^2(t-\tau_b)> + k_1^2 <E_0^2(t-\tau_a)> + 2k_1 \sin(\phi_a - \phi_b) \, \Re e[<\tilde{E}_0(t-\tau_a) \cdot \tilde{E}_0^*(t-\tau_b)>]] \qquad \text{eq. 2.2.2.4}$$

and

$$\Pi_2(t) = k_1^2 k_2^2 \, [<E_0^2(t-\tau_b)> + k_1^2 <E_0^2(t-\tau_a)> - 2k_1 \sin(\phi_a - \phi_b) \, \Re e[<\tilde{E}_0(t-\tau_a) \cdot \tilde{E}_0^*(t-\tau_b)>]] \, . \qquad \text{eq. 2.2.2.5}$$

These expressions may be simplified if we assume zero attenuation and reflection losses so that $<E_0^2(t - \tau_a)>$ and $<E_0^2(t - \tau_b)>$ are the source irradiance coupled into the input fibre (Π_0) and note that the degree of coherence (Γ) of the source is given by :

$$\Gamma(\tau_a - \tau_b) = <\tilde{E}_0(t-\tau_a) \cdot \tilde{E}_0^*(t-\tau_b)>/\Pi_0 . \qquad \text{eq. 2.2.2.6}$$

Thus,

$$\Pi_1 = k_1^2 k_2^2 \Pi_0 [(k_1^2 + 1) + 2k_1 |\Gamma| \sin(\phi_a - \phi_b)] , \qquad \text{eq. 2.2.2.7}$$

and

$$\Pi_2 = k_1^2 k_2^2 \Pi_0 [(k_1^2 + 1) - 2k_1 |\Gamma| \sin(\phi_a - \phi_b)] . \qquad \text{eq. 2.2.2.8}$$

The irradiance at the two detectors is shown therefore to be always antiphase. The sine term arises in the last two equations (rather than the usual cosine term) because the "ϕ" terms in the equation do not include the additional phase shifts generated in the couplers. For this reason, the term (ϕ_a - ϕ_b) is referred to as the non-coupler phase difference (NCPD). Periodic change in the path length of the open-air gap, due to vibration of the reflective surface, modulates the NCPD between the signal and reference beams at C2 and so varies the output irradiance according to the sine of the NCPD modulation.

The sensitivity of the interferometer to small phase changes in the signal beam depends greatly on the quiescent NCPD. The slope of the irradiance as a function of phase difference is proportional to cos (ϕ_a - ϕ_b). Thus the slope, and hence the sensitivity of the interferometer, is a maximum for a quiescent NCPD of 0 (modulo π) and a minimum for a quiescent NCPD of $\pi/2$ (modulo π). When the interferometer is at maximum sensitivity, it is said to be at the quadrature point. Usually however, the interferometer will drift away from the quadrature point because of seemingly random temperature changes which vary the refractive index of the fibre and hence the NCPD at the mixing coupler. As the quiescent point drifts, the instrument sensitivity varies and the modulation amplitude of the output irradiance may unpredictably fade.

Since the variations in the signals at the two detectors are always antiphase, subtraction of these signals in a differential amplifier produces a difference signal of reasonably constant amplitude. Any noise which is common (in-phase) to both outputs is significantly reduced in the difference signal. The effect of low-frequency thermal drifts, which are not common to both the signal and reference paths, can be countered by stretching the reference arm to introduce a bias phase which then maintains the instrument at the quadrature point.

A phase modulator was constructed from a piezoelectric cylinder (PZT-5H Vernitron, USA) of dimensions 5.1 cm (outer diameter), 4.6 cm (inner diameter), and 7.6 cm (length) wrapped with 200 turns of single-mode fibre.[Davies and Kingsley 1974, Kingsley 1975 and 1978, Jackson and Jones 1989, Pickelmann 1987 and 1990] This PZT cylinder had a resonance at approximately 55 kHz, and so the phase modulator behaved as a linear device at the low frequencies used to drive the cylinder (units or tens of Hertz). The output signal from the differential amplifier was delivered as a correction signal to the PZT cylinder via an integrator as shown schematically in figure 2.2.2.1. The output of the integrator was constant when its input was zero and this occurred only when the two inputs to the differential amplifier were equal. Since the two inputs were always antiphase, the integrator output was steady only when the interferometer was biased at the quadrature point. Hence, the phase modulator in the reference path maintained the quiescent NCPD at the quadrature point. The output of the interferometer was taken via a high-pass filter (>75 Hz) from the input to the integrator and the half power bandwidth of the electronics was measured to be from 70 Hz to about 30 kHz. For detection of low-frequency structural oscillations of about 100 Hz or below (specifically, vibrational frequencies of 26 Hz, see section 4.2), it was necessary to disconnect the feedback loop and compensate, as best as possible, for "fading" by averaging the output signal amplitude over several vibration records. A circuit diagram for the differential amplifier, integrator, high-pass filter and piezoelectric cylinder is shown in figure 2.2.2.2.

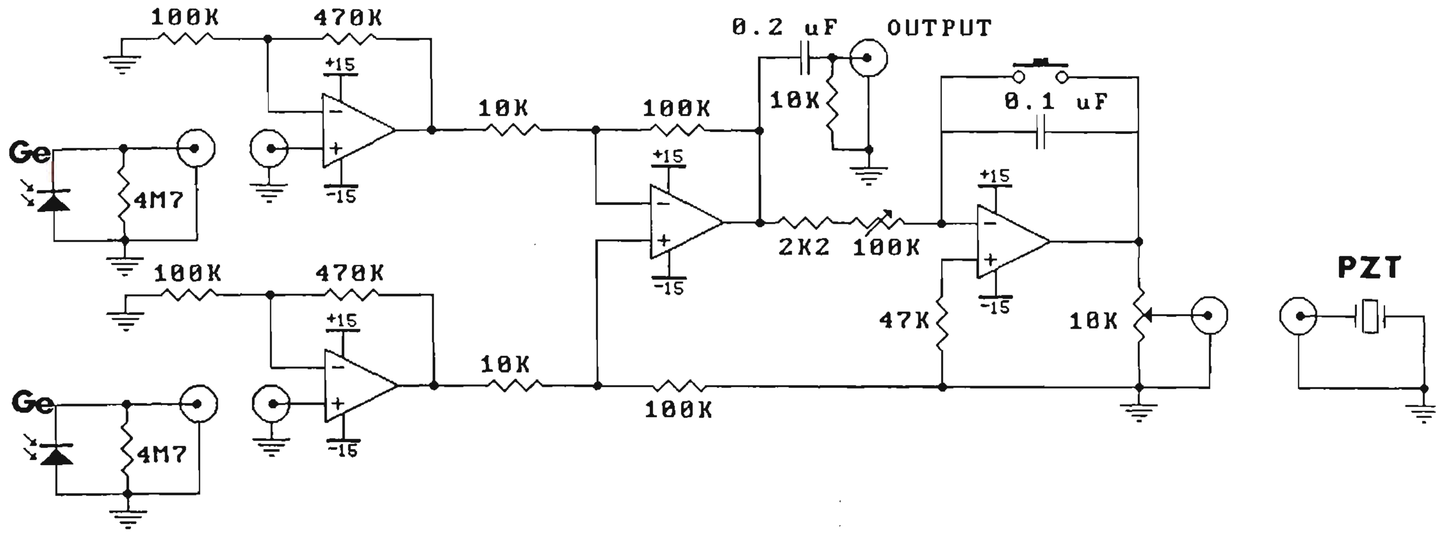

Figure 2.2.2.2. Circuit diagram for the differential amplifier, filters and PZT cylinder.

The interferometer was calibrated using two different techniques; firstly, using a magnetostrictive oscillator (which was itself calibrated using a bulk-optic Michelson interferometer) and secondly, using a mirror mounted on a PZT shaker. The first method used a mirror attached to a 25 cm long, 3 mm diameter polycrystalline nickel rod under magnetostrictive influence as the vibrating element in the fibre interferometer. When an oscillating magnetic field was applied to the nickel rod (by passing a sinusoidal current through a solenoid which surrounded it), the rod expanded and relaxed under magnetostriction. The magnetostrictive mirror shaker was first calibrated using a bulk-optic Michelson interferometer operating at 546 nm as shown in figure 2.2.2.3. A 10 V_{p-p} (off-set by +10 V dc) 10 Hz sine wave applied to the solenoid produced a 10 Hz oscillation of the attached mirror with an amplitude of about one eighth of a fringe shift in the Michelson interferometer (12% ± 5% of a fringe shift). The large uncertainty in this value was due to observation of the fringe shift by eye. This fringe shift corresponded to about 30 nm aftermost-to-foremost excursion (full-cycle displacement) of the mirror attached to the nickel rod.

The magnetostrictive oscillator was then used with the fibre interferometer and driven by a 10 V_{p-p}

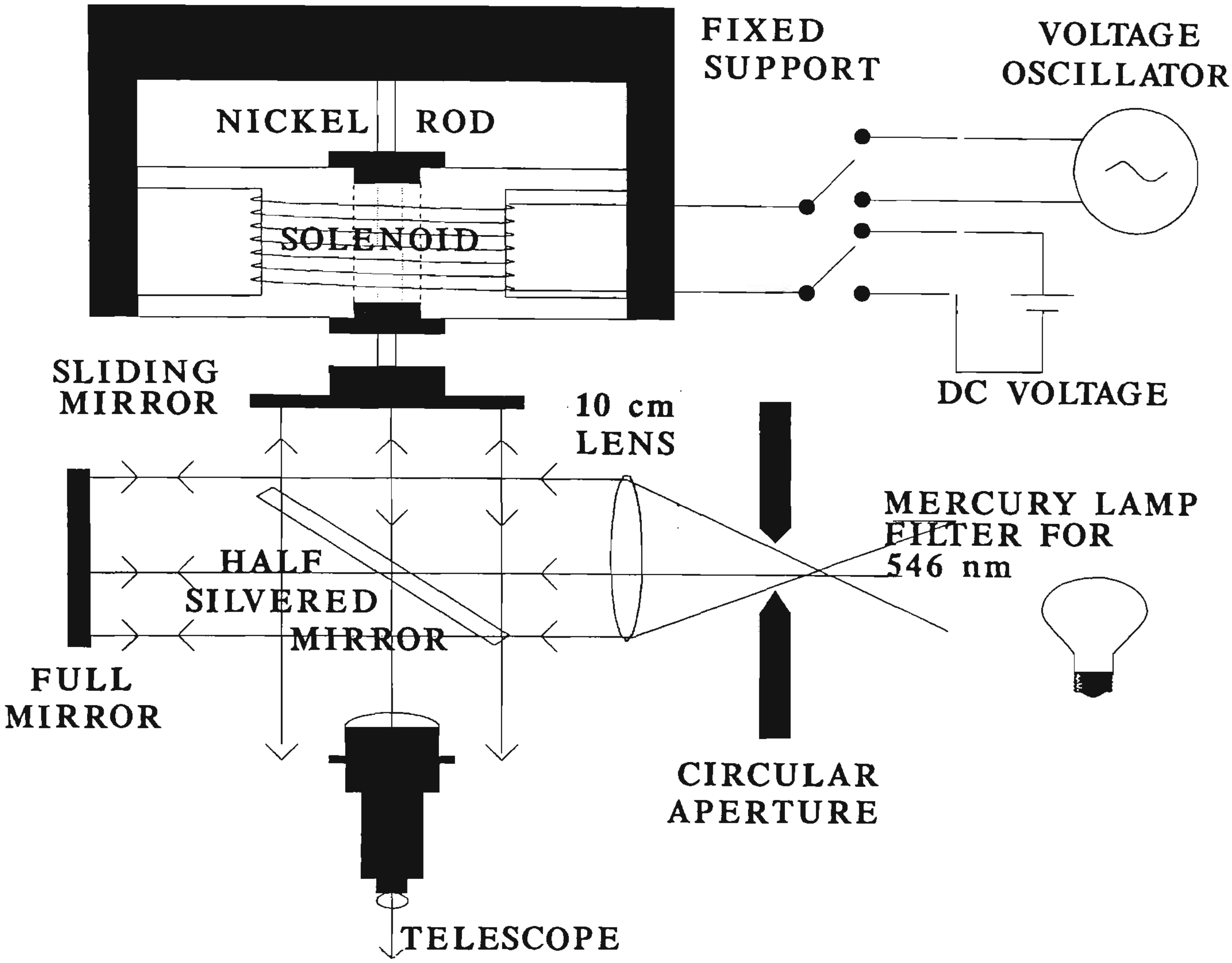

Figure 2.2.2.3. Arrangement for calibrating the magnetostrictive oscillator

sine-wave signal at 2 kHz (a full-cycle displacement of approximately 30 nm was assumed to apply at this frequency also). The output of the fibre interferometer was processed by the Tektronix DSA 602 digital signal analyser in real-time FFT mode. The ac drive signal to the solenoid was decreased until the 2 kHz spectral line was only 10 dB above the broad-band background noise of the interferometer. 10 dB was considered to be the minimum signal-to-noise for reasonable operation of the interferometer. If a linear relationship is assumed between the potential applied to the solenoid and the displacement of the mirror (since the applied voltage is directly proportional to the magnetic field and therefore to the magnetostrictive extension), the interferometer was sensitive to full-cycle displacements of the mirror of approximately 3 nm (an observed mirror amplitude of 1.5 nm). The results are presented in table 2.2.2 .

CALIBRATION TRIAL USING THE MAGNETOSTRICTIVE OSCILLATOR		
Drive signal to the solenoid.	Full-cycle displacement of the mirror attached to the magnetostrictive oscillator.	Amplitude of the 2 kHz spectral line after FFT of the interferometer output.
10 V_{p-p} at 10 Hz	Observed ~ ⅛th fringe shift ~ 30 nm	
10 V_{p-p} at 2 kHz	Assumed ~ 30 nm	30 dB above noise
3 V_{p-p} at 2 kHz	Approximately 10 nm	20 dB above noise
1 V_{p-p} at 2 kHz	Approximately 3 nm	10 dB above noise

Table 2.2.2. Calibration data for the magnetostrictive oscillator and interferometer.

In order to ensure that the output from the interferometer was not due to electromagnetic pick-up in the PZT cylinder of the interferometer, an opaque slide was placed in the open-air path of the interferometer while the signal to the solenoid was maintained at 10 V_{p-p} at 2 kHz. The 2 kHz spectral line was then measured at 2 dB above noise, and so the detected signals (table 2.2.2) were due to optical modulation.

The second, more precise calibration of the interferometer used a Lutz-Pickelmann piezoelectric mirror shaker (PZMS) type MB-ST-500/3 (resonant frequency > 5 kHz; 500 V dc gives 3 μm displacement). The PZMS was biased at +250 V dc and modulated using a 300 V_{p-p} sine wave at 100 Hz. A total shift of 5 fringes was observed in the interferometer output over the 10 ms period of modulation. Thus the full-cycle displacement of the mirror corresponded to a 2½ fringe change in the interferometer (forward 2½ and back 2½) and the amplitude of oscillation to a 1¼ fringe change. Since the optical path change in the interferometer is twice that of the mirror, at a wavelength (λ) of 1523 nm, a 1¼ fringe shift in the interferometer corresponded to a mirror amplitude of 950 nm. The observed mirror amplitudes at 200 V_{p-p}, 180 V_{p-p}, 110 V_{p-p} and 40 V_{p-p} were 760 nm (4 fringes total), 575 nm (3 fringes), 380 nm (2 fringes) and 190 nm (1 fringe) respectively. For all of the above measurements, the peak-to-peak signal amplitude of the interferometer output was steady at 2.15 V. For drive signals less than 40 V_{p-p}, the peak-to-peak signal amplitude of the interferometer output was observed to decrease as mirror amplitudes of less than $\lambda/8$ were detected.

With the interferometer locked into the quadrature condition so that the NCPD was maintained at π, the amplitude of the output signal, V(t), is given by:

$$V(t) = A/2 \sin(\pi + \phi(t)), \qquad \text{eq. 2.2.2.9}$$

where $\phi(t)$ is the modulation-induced phase shift due to the vibrating surface as a function of time and A ($A = 2V_{max}$ when $\phi(t) = \pm \pi/2$) is the maximum peak-to-peak signal amplitude at the output of the interferometer as shown in figure 2.2.2.5. For any phase modulation about the quadrature point less than $\phi = \pm \pi/2$, the observed peak-to-peak signal amplitude for that phase modulation (B) is given by

$$B = A/2 \sin(\pi - \phi) - A/2 \sin(\pi + \phi), \qquad \text{eq. 2.2.2.10}$$

which can be simplified to

$$\phi = \mathrm{Sin}^{-1}(B/A). \qquad \text{eq. 2.2.2.11}$$

By comparing the reduced peak-to-peak signal amplitude for a mirror oscillation of less than one total fringe with the peak-to-peak amplitude (in this case 2.15 V) of an oscillation of one or more fringes, the phase shift may be calculated. The phase shift is related to the mirror amplitude, s, by $\phi = 4\pi s/\lambda$. Therefore, the mirror amplitude may be determined using:

$$s = \lambda/4\pi \ \mathrm{Sin}^{-1}(B/A). \qquad \text{eq. 2.2.2.12}$$

Frequency spectra of the interferometer output were produced for PZMS drive voltages less than 10 V_{p-p} and the amplitude of the 100 Hz spectral line was measured (in dB) with respect to the background noise. The minimum mirror amplitude that could be detected by the interferometer (when the 100 Hz spectral line was 10 dB above the background noise), was calculated from the interferometer output signal using equation 2.2.2.12 to be 1.1 nm when the drive voltage was 0.3 V_{p-p}. Figure 2.2.2.6 shows a calibration plot of the calculated mirror amplitudes (for amplitudes less than $\lambda/8$ using equation 2.2.2.12) verses the PZMS drive voltages. A linear fit to this data, together with a minimum PZMS drive voltage of 0.3 V_{p-p}, gives a minimum measurable mirror amplitude of 1.3 ± 0.4 nm. This result corresponds to an amplitude sensitivity of 5 nm/V or a MDPS of 1.2×10^{-2} radians based on a conservative criterion for signal detection in a practical system (a SNR of 10 dB) rather than the usual criterion of a SNR of 1.

The bandwidth of this intereferometer was effectively limited by the bandwidth of the detector electronics (30 kHz). The noise in the system was mainly due to the Ge detectors and the following electronics since isolating the optical input did not significantly affect the noise level. Noise due to path imbalance was minimized by matching the path lengths of the signal and reference beams (to within 1 cm) for an open-air path of 15 cm. Given that the nominal coherence length of the Melles-Griot laser was 75 cm, there was no significant variation in fringe contrast with small variation in the target range. If a signal-to-noise ratio of 2 is assumed to be the practical limit of this system, the minimum detectable displacement amplitude was found to be 0.3 nm and the MDPS was 2.4 mrad (that is, the noise floor was equivalent to a phase shift of 1.2 mrad) when using the FFT display with a spectral range of 2 kHz and an effective bandwidth of 0.6 Hz.

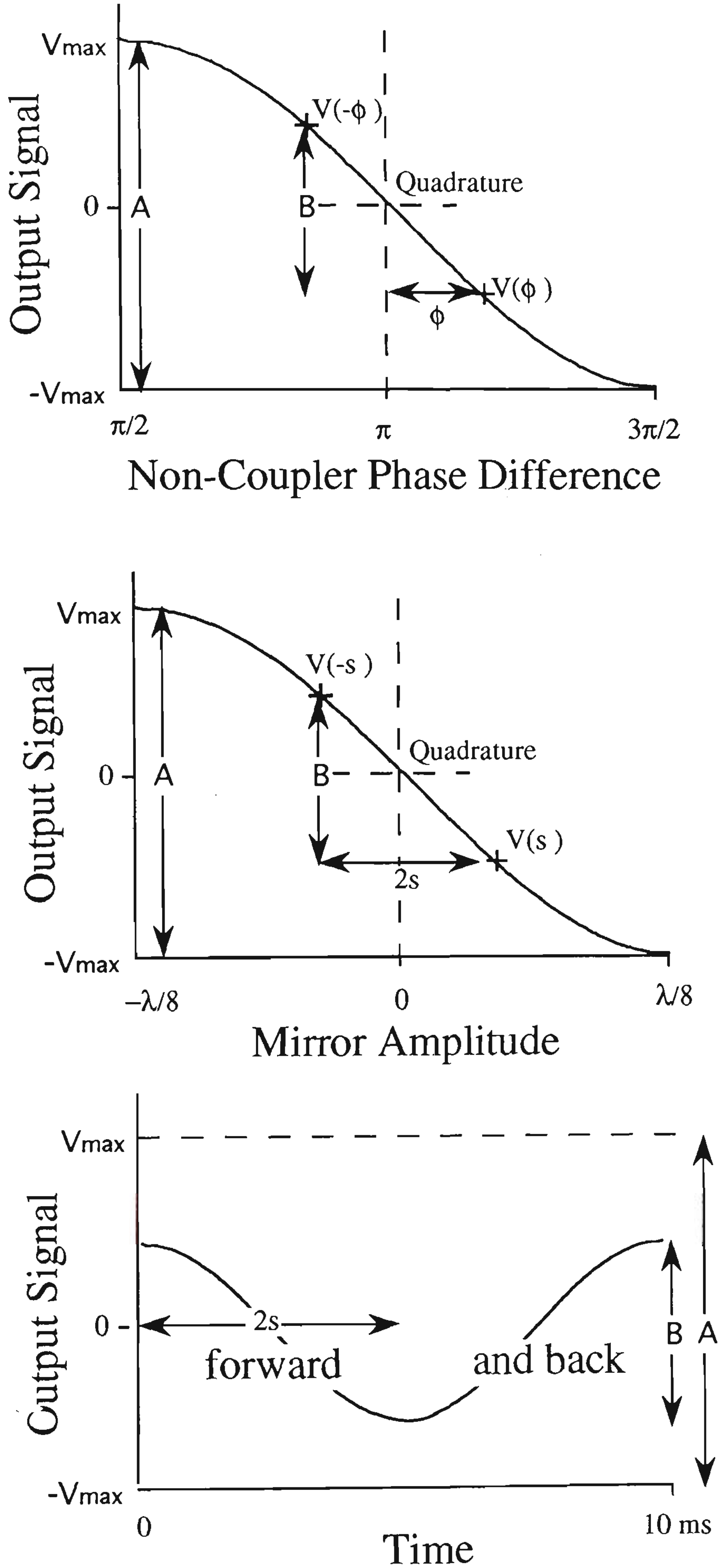

Figure 2.2.2.5 Phase modulation about the quadrature condition.

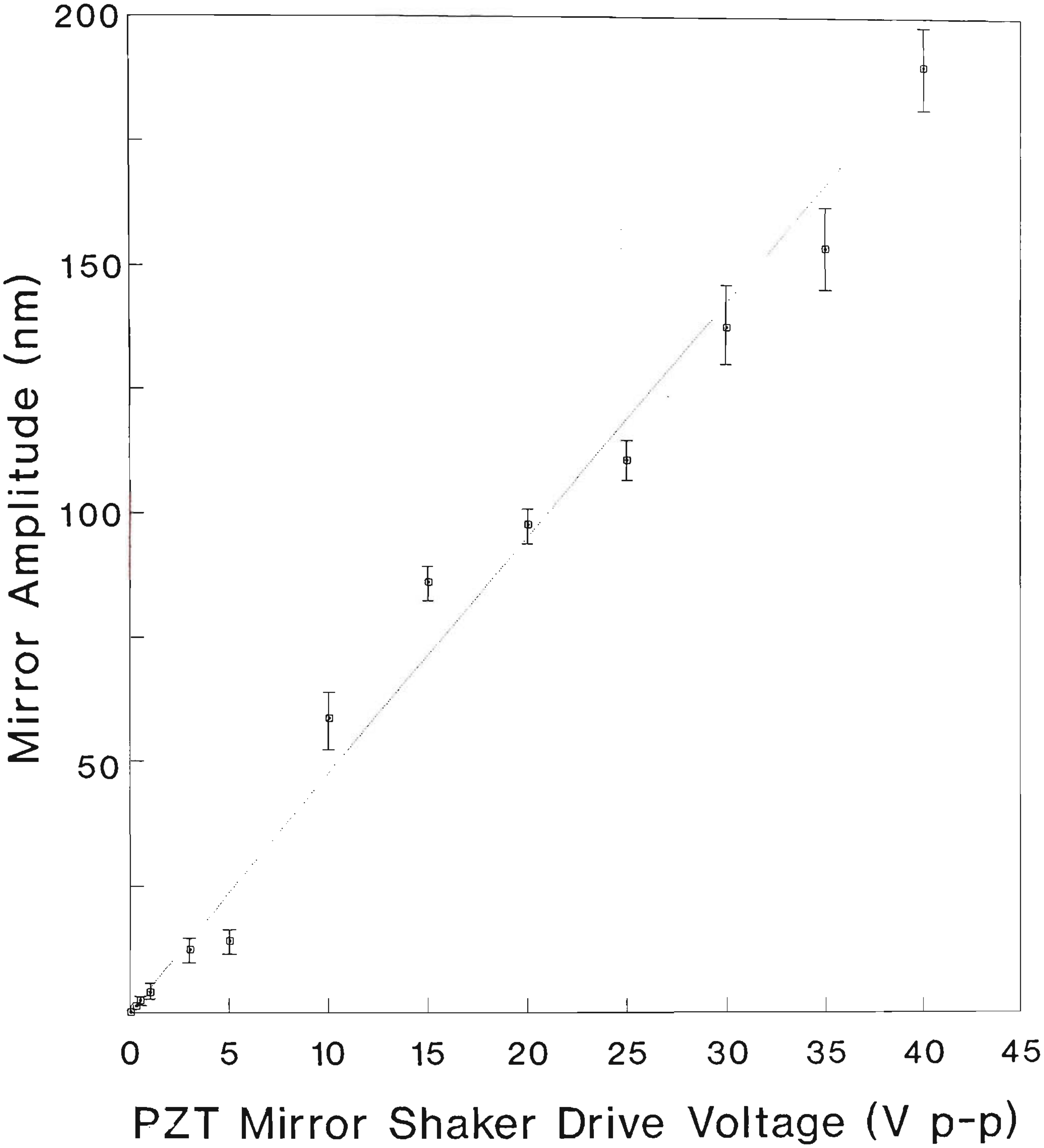

Figure 2.2.2.6 Calibration curve for the piezoelectric mirror shaker

Chapter 3

Laser-induced structural vibration

3.1 Laser-induced structural vibration by ablation

Initial experiments sought to duplicate the results of laser-induced structural vibration (by ablation) reported by Koss and Tobin (1983) and Edwards, Tobin and Koss (1983). A simple "shim" stainless steel clamped-free cantilever, with a full strain gauge bridge as the vibration sensor, was irradiated with a 40 J Nd:glass laser pulse focused onto a small low boiling-point alloy target affixed to the cantilever's surface. The modal signatures, gained by FFT analysis of the strain gauge records, were then compared with those of the above workers. The major variation in the experimental arrangement was the use of a 40 J, 600 μs (FWHM) Nd:glass laser pulse to irradiate the cantilever rather than the 1.5 J, 400 μs Nd:glass system used by Koss and Tobin.

Cantilever S was excited by the Nd:glass laser pulse focused to a spot diameter of approximately 0.5 mm (power density ~ 3×10^7 $W.cm^{-2}$) onto about half a gram of Pb-Sn solder attached to the cantilever surface. Koss and Tobin indicated that the low boiling-point alloy (in their case, bismuth) served to increase the impulse experienced by the cantilever upon ablation. In our case, the solder was not necessary to provide an impulse to the cantilever, since the power density of the focused laser pulse was well above the ablation threshold for stainless steel (see section 3.2 to follow). However, if the solder was not used, the laser pulse blew a hole through the shim. The Nd:glass laser, lens and clamped cantilever target were mounted on a vibration isolated table.

The output of the amplified strain gauge bridge was digitally recorded for 5 seconds following the laser irradiation and stored by a Philips 250 MS/s oscilloscope (10 bit, 4096 data points). Irradiation of the solder at a location 250 mm from the clamped-end (0.78 × cantilever length), caused the free-end of cantilever to deflect by about 15 mm. This initial displacement caused the cantilever to exhibit flexural free vibration. An example of a recorded vibration profile and the frequency spectrum derived from FFT analysis of this profile, are shown in figure 3.1.1. At least two vibrational modes (oscillation frequencies) are clearly visible in the upper time record (figure 3.1.1(a)). The Fourier spectrum of this record (figure 3.1.1(b)) shows four significant peaks corresponding to the first four modes of vibration together with a small peak at 50 Hz which is attributed to electrical noise.

The natural modal frequencies of the clamped-free shim cantilever can be theoretically calculated, using the method known as the Bernoulli-Euler theory. [Prescott 1924, Bishop and Johnson 1960, Thomson 1966, Vierck 1979] This method assumes that vibration occurs in-vacuo, there is an absence of loss, the system is elastic and its force-displacement characteristics linear, the maximum displacement is small, both rotatory inertia and shear displacements due to vibrational forces are negligible, deformation due to gravity is negligible, the cantilever length is large compared with the cross-sectional area, and vibration occurs in one of the principal planes of bending.[McLachlan, 1951]

(a)

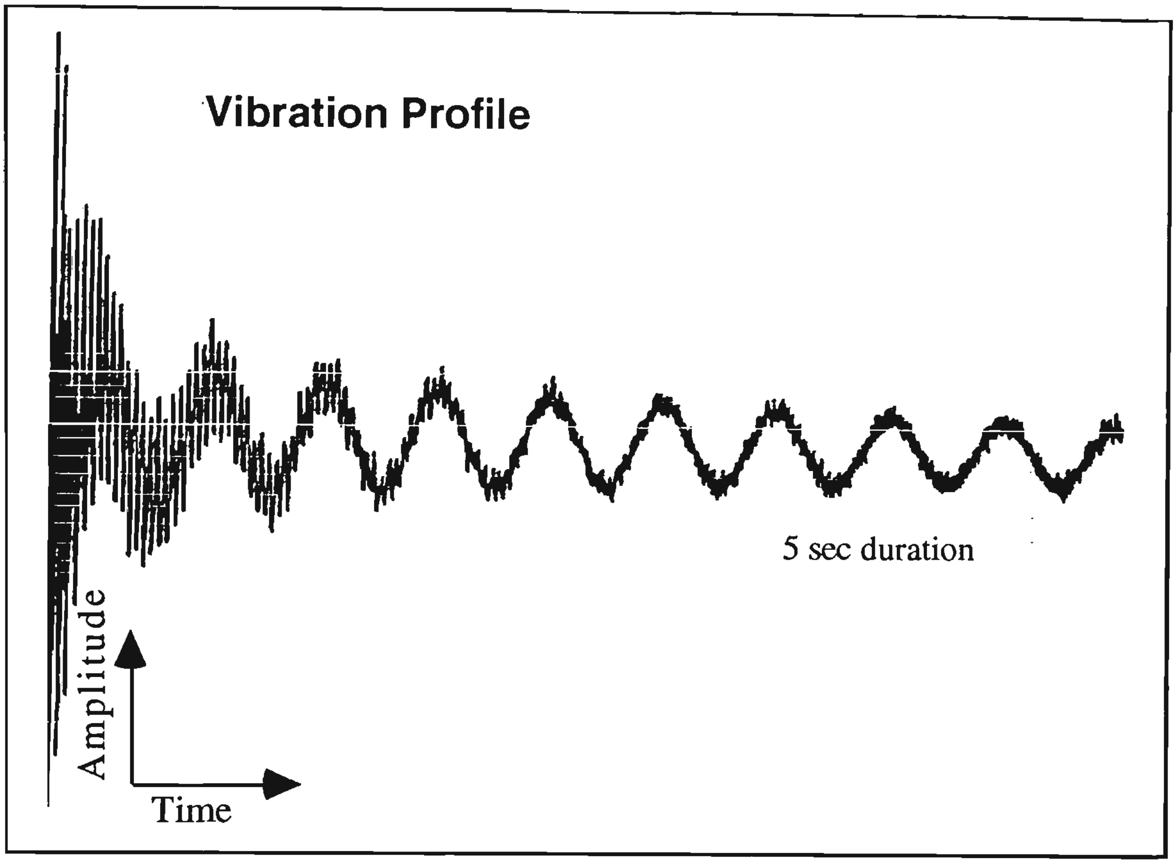

(b)

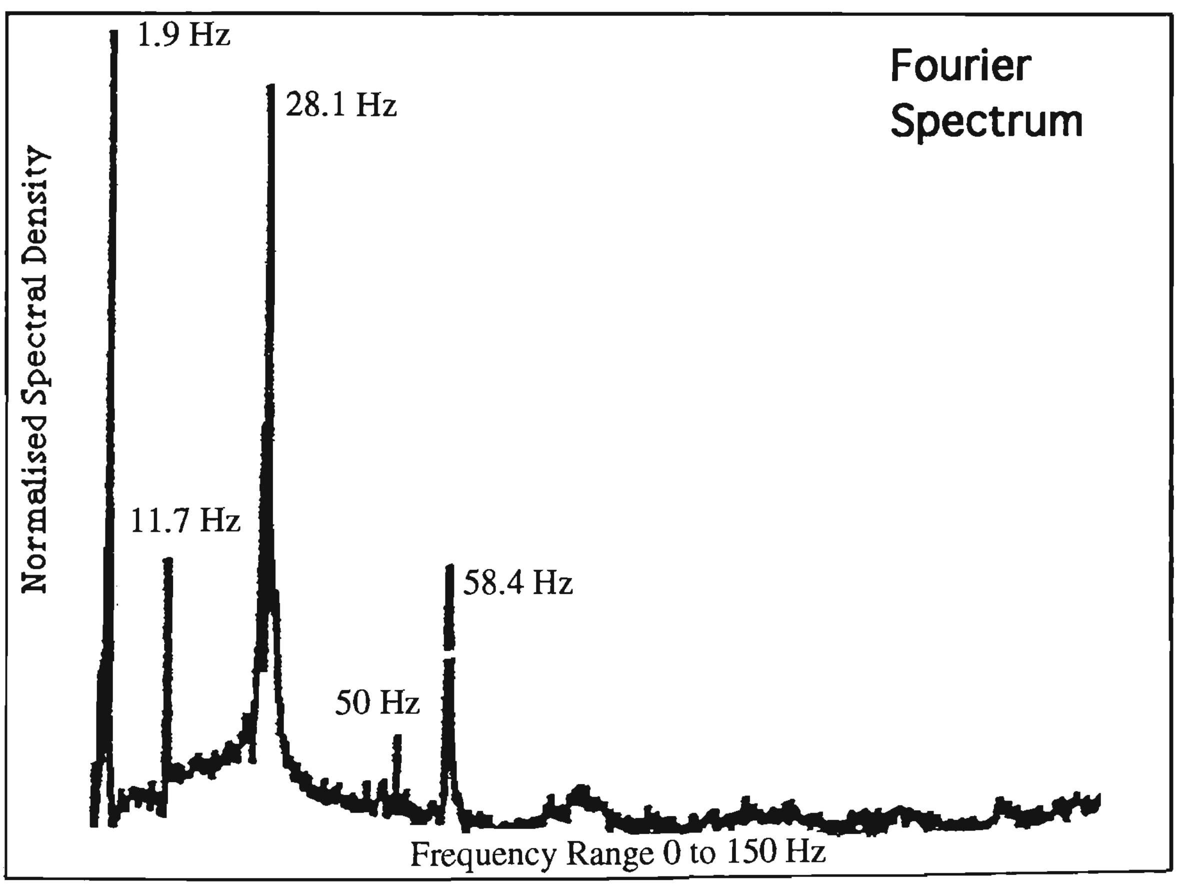

Figure 3.1.1. (a) Vibration profile and (b) derived frequency spectrum of the laser-excited stainless steel shim cantilever.

The natural frequencies and the spatial distribution of modes along a vibrating cantilever are derived by considering the transverse displacement (y) of a small element in length (dx) at a given distance (x) from the left-hand end of a uniform rectangular bar of given length (L), cross-sectional area (**A**), width (b), thickness (h), elastic modulus (E), second moment of area (I), and density (ρ), as illustrated in figure 3.1.2(a). The shear force (S) and the bending moment (M) act on the length element as indicated in figure 3.1.3 (b).

(a)

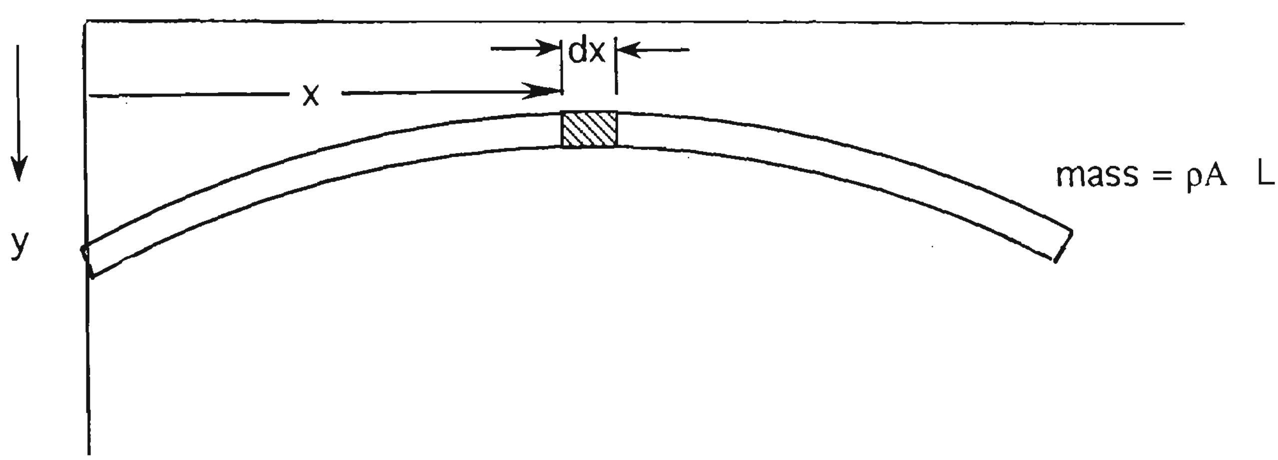

(b)

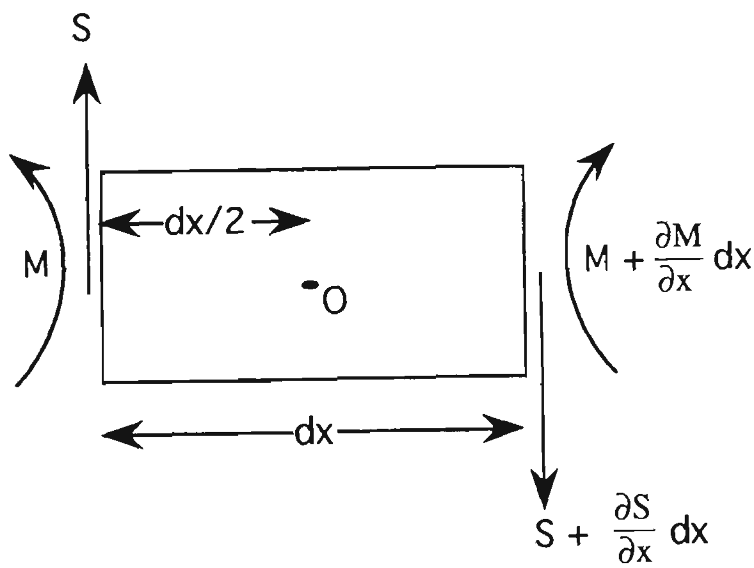

Figure 3.1.2. (a) A cantilever deflected transversely and (b) the applied forces and moments which act on an element of length dx within the deflected cantilever.

If moments (clockwise positive) are taken about an axis through O, and higher-order terms in dx are neglected, then

$$S = - \frac{\partial M}{\partial x} . \qquad \text{eq. 3.1.1}$$

Summing the forces in the y direction (down the page) gives,

$$\frac{\partial S}{\partial x} = \rho A \frac{\partial^2 y}{\partial t^2}$$

which, upon substitution of equation 3.1.1, yields

$$\frac{\partial^2 M}{\partial x^2} = - \rho A \frac{\partial^2 y}{\partial t^2} . \qquad \text{eq. 3.1.2}$$

The same length element, under static loading, is shown in figure 3.1.3. G - N is the neutral plane (mid-plane) and the element is bent about the centre of curvature (⊙). All slopes and bending angles are considered to be small. The perpendicular cross-section (CD) has been re-orientated to its original position, so that all rotation is shown by the deviation of A'B' from the original section AB. The change in slope for the mid-plane is $(d^2y/dx^2)dx$. δ is the total extension (AA'), which is equal in magnitude to the compression (BB'), and occurs at a distance $h/2$ = A'N from the mid-plane. Using equal angles, $(d^2y/dx^2)dx = \delta/(h/2)$, and so $d^2y/dx^2 = (\delta/dx)/(h/2)$. Therefore, using the fact that the strain ε is δ/dx,

$$\frac{d^2 y}{dx^2} = \frac{\varepsilon}{h/2} . \qquad \text{eq. 3.1.3}$$

By applying Hooke's law for elastic conditions ($E = \sigma/\varepsilon$, where σ is the stress) and the bending-stress relation ($\sigma = M\chi/I$, [Halstead et al., 1961] where χ is the distance from the mid-plane) to equation 3.1.3, then

$$M = EI \frac{d^2 y}{dx^2} , \qquad \text{eq. 3.1.4}$$

and thus the bending moment is shown to be directly proportional to d^2y/dx^2 .

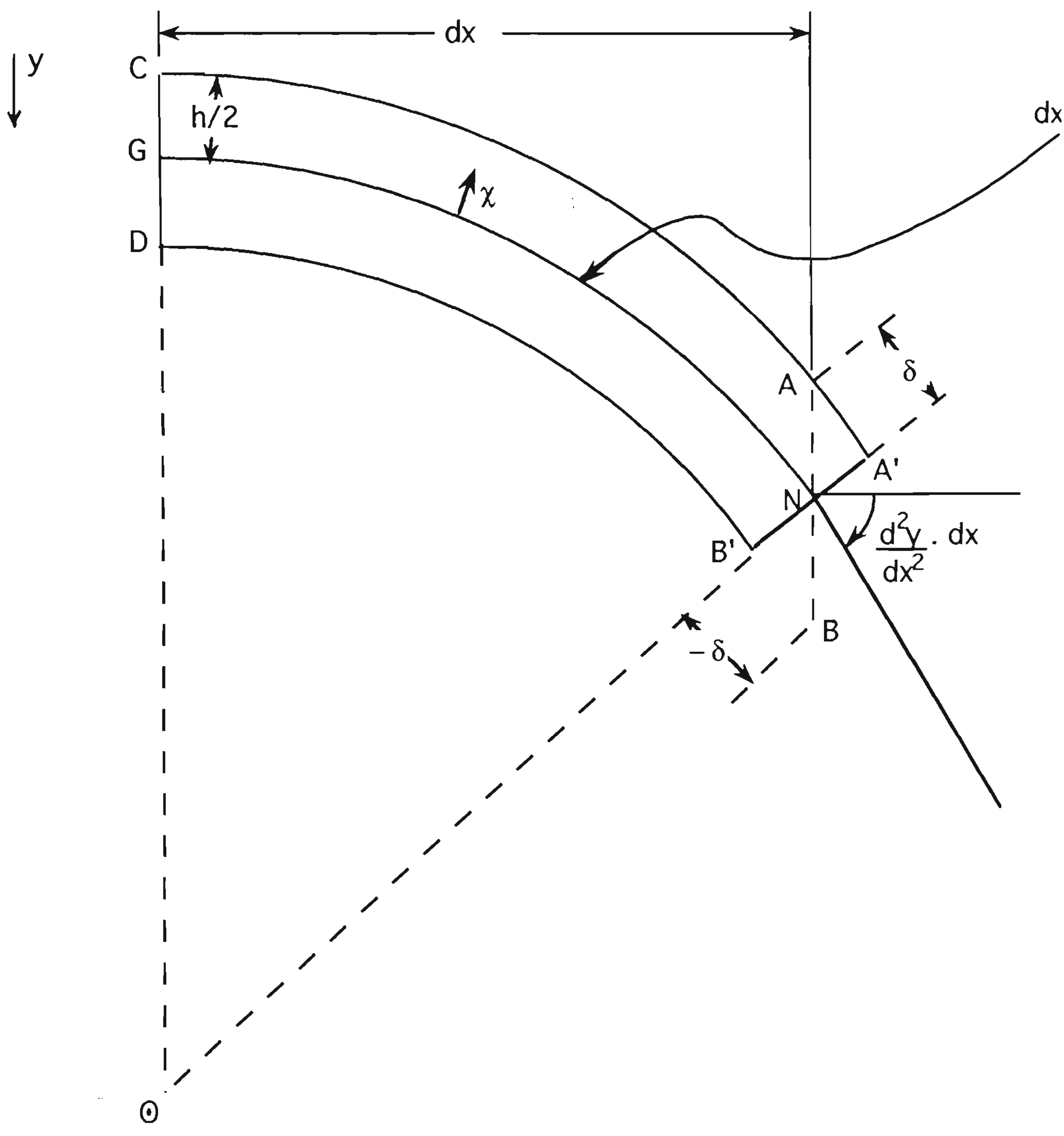

Figure 3.1.3. Schematic diagram of an element of length (dx) under static bending

Similarly, from equation 3.1.1,

$$S = -EI\frac{d^3y}{dx^3} \propto \frac{d^3y}{dx^3} . \qquad \text{eq. 3.1.5}$$

For a freely vibrating cantilever, where the displacement is a function of both position and time, substituting $-\partial S/\partial x = \partial^2 M/\partial x^2 = EI\,(\partial^4 y/\partial x^4)$ into equation 3.1.2 yields

$$\frac{\partial^4 y}{\partial x^4} + \frac{\rho A}{EI}\frac{\partial^2 y}{\partial t^2} = 0 , \qquad \text{eq. 3.1.6}$$

which is the general equation for the transverse flexural vibration of a thin uniform beam. The second moment of area for a rectangular bar with the axis through the centroid is[Parker et al., 1974]

$$I = \frac{bh^3}{12} , \qquad \text{eq. 3.1.7}$$

which upon substitution into equation 3.1.6, gives

$$\frac{\partial^4 y}{\partial x^4} + a^4\frac{\partial^2 y}{\partial t^2} = 0, \quad where \ a = \sqrt[4]{\frac{12\rho}{Eh^2}} . \qquad \text{eq. 3.1.8}$$

This is in the general form of Euler's differential equation, which has a general solution[Vierk, 1979]

$$y(x,t) = (A\sinh\beta_n x + B\cosh\beta_n x + C\sin\beta_n x + D\cos\beta_n x)\,(\alpha_{1n}\sin\omega_n t + \alpha_{2n}\cos\omega_n t), \qquad \text{eq. 3.1.9}$$

where ω_n is the angular vibration frequency, A, B, C and D are general constants and α_{1n}, α_{2n} and β_n are constants dependent on the mode number (n) for n = 1, 2, 3, 4.... The spatial term,

$$A\sinh\beta_n x + B\cosh\beta_n x + C\sin\beta_n x + D\cos\beta_n x,$$

is called the characteristic function[Bishop and Johnson, 1960] and describes the relative amplitude of a specific modal displacement at any position along the length of the cantilever. The harmonic term,

$$\alpha_{1n}\sin\omega_n t + \alpha_{2n}\cos\omega_n t ,$$

is reduced to α_{2n} at time, t, equals zero. The relationships between the general constants in the characteristic function are found for a clamped-free cantilever by applying boundary conditions at time t = 0. That is, at x = 0, the displacement and slope ($\partial y/\partial x$) are zero and at x = L, the bending moment ($\propto \partial^2 y/\partial x^2$) and stress ($\propto \partial^3 y/\partial x^3$) are also zero.

Since

$$y(x,0) = \alpha_{2n} (A\sinh\beta_n x + B\cosh\beta_n x + C\sin\beta_n x + D\cos\beta_n x) \;, \qquad \text{eq. 3.1.10(a)}$$

$$\partial y(x,0)/\partial x = \alpha_{2n}\beta_n (A\cosh\beta_n x + B\sinh\beta_n x + C\cos\beta_n x - D\sin\beta_n x) \;, \qquad \text{eq. 3.1.10(b)}$$

$$\partial y^2(x,0)/\partial x^2 = \alpha_{2n}\beta_n^{\,2} (A\sinh\beta_n x + B\cosh\beta_n x - C\sin\beta_n x - D\cos\beta_n x) \qquad \text{eq. 3.1.10(c)}$$

and $$\partial^3 y(x,0)/\partial x^3 = \alpha_{2n}\beta_n^{\,3} (A\cosh\beta_n x + B\sinh\beta_n x - C\cos\beta_n x + D\sin\beta_n x) \;, \qquad \text{eq. 3.1.10(d)}$$

equations 3.1.10(a) and 3.1.10(b) are simplified by the boundary conditions at $x = 0$ to be

$$y(0,0) = 0 = B + D \text{ and } \partial y(0,0)/\partial x = 0 = A + C.$$

Substituting $-D = B$ and $-C = A$ into equations 3.1.10(c) and 3.1.10(d) at $x = L$ gives,

$$\partial^2 y(L,0)/\partial x^2 = 0 = A(\sinh\beta_n L + \sin\beta_n L) + B(\cosh\beta_n L + \cos\beta_n L)$$

and $$\partial^3 y(L,0)/\partial x^3 = 0 = A(\cosh\beta_n L + \cos\beta_n L) + B(\sinh\beta_n L - \sin\beta_n L).$$

Therefore, $$A = -B(\cosh\beta_n L + \cos\beta_n L)/(\sinh\beta_n L + \sin\beta_n L) \qquad \text{eq. 3.1.11}$$

and also $$A = -B(\sinh\beta_n L - \sin\beta_n L)/(\cosh\beta_n L + \cos\beta_n L). \qquad \text{eq. 3.1.12}$$

These equations can be further simplified by taking the quotient of equations 3.1.11 and 3.1.12 and applying the identities

$$\cosh^2\beta_n L - \sinh^2\beta_n L = 1 \text{ and } \sin^2\beta_n L + \cos^2\beta_n L = 1.$$

The quotient reduces to

$$\cosh\beta_n L \cos\beta_n L + 1 = 0, \qquad \text{eq. 3.1.13}$$

which may be solved graphically, as shown in figure 3.1.5, to yield :

$\beta_1 L = 1.875$ $\quad\beta_2 L = 4.694$ $\quad\beta_3 L = 7.855$ $\quad\beta_4 L = 10.996$

$\beta_5 L = 14.137$ $\quad\beta_6 L = 17.279$ $\quad\beta_7 L = 20.420$ $\quad\beta_8 L = 23.420$

$\beta_{8+k} L \simeq \beta_8 L + k\pi$, where $k = 1,2,3.....$

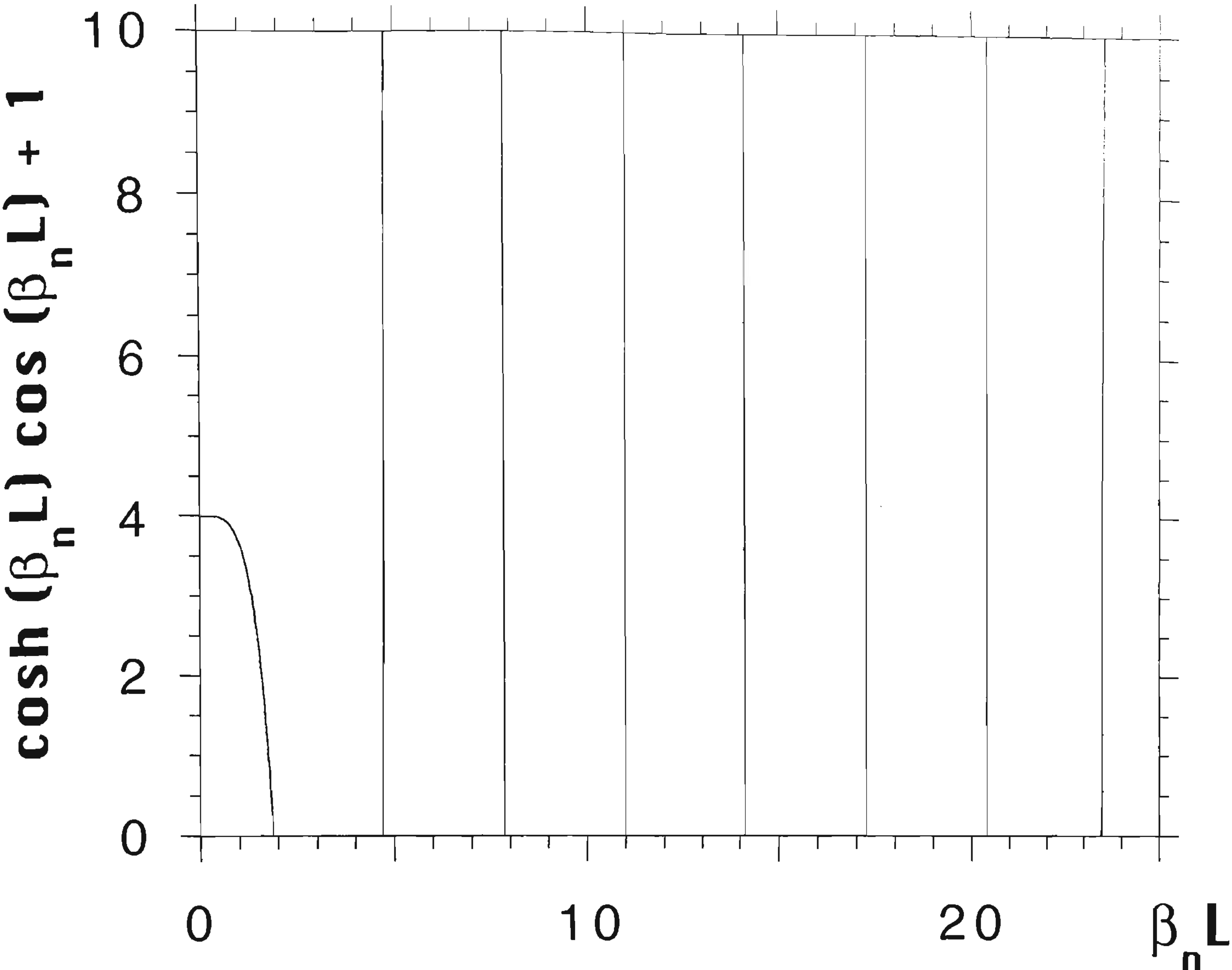

Figure 3.1.5. Graph of $\cosh\beta_nL \cos\beta_nL + 1$ vs. β_nL.

The harmonic term of the displacement is related to β_n by the relationship

$$\beta_n^2 = a^2 \omega_n , \qquad \text{eq. 3.1.14}$$

where $a^2 = [12\rho/(Eh^2)]^{1/2}$. So,

$$\beta_n^2 = \omega_n[12\rho/(Eh^2)]^{1/2}. \qquad \text{eq. 3.1.15}$$

The angular frequencies are therefore

$$\omega_n = \beta_n^2 h \sqrt{\frac{E}{12\rho}} = (\beta_n L)^2 \frac{h}{L^2} \sqrt{\frac{E}{12\rho}} \qquad \text{eq. 3.1.16}$$

and the natural frequencies of flexural vibration may be calculated using

$$f_n = (\beta_n L)^2 \frac{h}{2\pi L^2} \sqrt{\frac{E}{12\rho}} . \qquad \text{eq. 3.1.17}$$

Returning to the experimental investigation of the vibrational modes for cantilever S, the theoretical values were calculated from equation eq. 3.1.17 for an unloaded cantilever (7.6 g) and a loaded cantilever of 10.6 g mass. These values were then compared to the experimental results, shown in figure 3.1.1(b), and also to those published by Koss and Tobin (1983). These values are presented in table 3.1.1.

MODE	EXPERIMENTAL RESULTS (THIS WORK)	PUBLISHED RESULTS (KOSS & TOBIN)	CALCULATED VALUES (7.6 g)	CALCULATED VALUES (10.6 g)
MODE 1	1.9 Hz	2.0 Hz	2.1 Hz	1.8 Hz
MODE 2	11.7 Hz	12.4 Hz	13.3 Hz	11.2 Hz
MODE 3	28.1 Hz	34.0 Hz	36.7 Hz	30.9 Hz
MODE 4	58.4 Hz	68.9 Hz	72.0 Hz	60.7 Hz

Table 3.1.1. Experimental, published and calculated modal frequencies for cantilever S .

The mass of the cantilever and strain gauge bridge was first determined from the density of the steel (7,800 kg.m^{-3}) to be 7.6 g; however, after weighing the cantilever, it was found that adhesive, solder, strain gauges and wiring had loaded the cantilever to a total mass of 10.6 g. Although no attempt was made to define the load distribution along the length of the cantilever, the revised calculations agree reasonably well with the observed values . Irrespective of the difficulties with accurate calculation, this method of excitation and Fourier data analysis certainly enabled the accurate measurement of modal frequencies for this type of vibrating cantilever.

At this stage of the discussion, it is convenient to return to the theoretical argument and discuss more fully the irradiation site (0.78 × cantilever length; 0.78L) chosen by Koss and Tobin (1983).

Now that the characteristic numbers ($\beta_n L$) have been numerically evaluated, the expression for A in terms of B (see equations 3.1.11 and 3.1.12) reduces to A being equal to the product of B and some mode-dependent constant, which we shall simply call, U. For clamped-free vibration

$$A = -B(\cosh\beta_n L + \cos\beta_n L)/(\sinh\beta_n L + \sin\beta_n L) = BU, \qquad \text{eq. 3.1.18}$$

where $U = -(\cosh\beta_n L + \cos\beta_n L)/(\sinh\beta_n L + \sin\beta_n L)$. Therefore, equation 3.1.9 becomes

$$y(x,t) = \alpha_{2n}B[U(\sinh\beta_n x - \sin\beta_n x) + \cosh\beta_n x - \cos\beta_n x]\cos[(\beta_n L)^2\, h/L^2\, \{E/(12\rho)\}^{1/2}]t.$$

eq. 3.1.19

By assigning a value to $y(L,0)= y_L$, where y_L is the initial displacement of the cantilever end, and introducing another mode dependent constant W, y(x,t) may be evaluated for each specific mode of vibration. If,

$$y(L,0) = y_L = \alpha_{2n}B(U(\sinh\beta_n L - \sin\beta_n L) + \cosh\beta_n L - \cos\beta_n L) = \alpha_{2n}B\, W^{-1},$$

where $W^{-1} = U(\sinh\beta_n L - \sin\beta_n L) + \cosh\beta_n L - \cos\beta_n L$, the time-dependent displacement relationship may be expressed as

$$y(x,t) = y_L W[U(\sinh\beta_n x - \sin\beta_n x) + \cosh\beta_n x - \cos\beta_n x]\, \cos[(\beta_n L)^2\, h/L^2\, \sqrt{\{E/(12\rho)\}}]t$$

and in the general case for unit length,

$$y(x/L,t) = y_L W[U\{\sinh(\beta_n L)(x/L) - \sin(\beta_n L)(x/L)\} + \cosh(\beta_n L)(x/L) - \cos(\beta_n L)(x/L)]\cos[(\beta_n L)^2 h/L^2 \sqrt{\{E/12\rho\}}]t$$

eq. 3.1.20

An HP-Basic routine was used to plot the solution to equation 3.1.20 at t = 0 (hereafter referred to as the displacement profile). The first, second and third derivatives of this displacement profile for a clamped-free cantilever were also plotted. These plots are presented in figures 3.1.6 and 3.1.7. The first, second and third derivatives describe the slope profile, bending moment profile (equation 3.1.4), and shear stress profile (equation 3.1.5) respectively. The positions of the nodes and antinodes of the displacement profile for the first five modes of free vibration in a clamped-free cantilever and the nodes and antinodes of the first three derivatives of that displacement profile are summarised in table 3.1.2.

NODES	Mode 2	Mode 3	Mode 3	Mode 4	Mode 4	Mode 4	Mode 5	Mode 5	Mode 5	Mode 5
y(x)	0.78L	0.50L	0.86L	0.36L	0.64L	0.90L	0.28L	0.50L	0.72L	0.92L
$\partial y/\partial x$	0.48L	0.29L	0.69L	0.22L	0.50L	0.78L	0.17L	0.39L	0.61L	0.83L
$\partial^2 y/\partial x^2$	0.22L	0.14L	0.50L	0.10L	0.36L	0.64L	0.08L	0.28L	0.50L	0.72L
$\partial y^3/\partial x^3$	0.53L	0.31L	0.71L	0.22L	0.50L	0.78L	0.17L	0.39L	0.61L	0.83L

ANTI-NODES	Mode 2	Mode 3	Mode 3	Mode 4	Mode 4	Mode 4	Mode 5	Mode 5	Mode 5	Mode 5
y(x)	0.48L	0.29L	0.69L	0.22L	0.50L	0.78L	0.17L	0.39L	0.61L	0.83L
$\partial y/\partial x$	0.22L	0.14L	0.50L	0.10L	0.36L	0.64L	0.08L	0.28L	0.50L	0.72L
$\partial^2 y/\partial x^2$	0.53L	0.31L	0.71L	0.22L	0.50L	0.78L	0.17L	0.39L	0.61L	0.83L
$\partial^3 y/\partial x^3$	0.78L	0.50L	0.86L	0.36L	0.64L	0.90L	0.28L	0.50L	0.72L	0.92L

Table 3.1.2. Node and antinode locations for the first five modes of flexural free vibration for the y(x) displacement profile and its first three derivatives.

When a cantilever is made to vibrate by displacement at some point along its length, the positions of the nodes and antinodes for any particular mode of vibration may be calculated directly from figure 3.1.6(a) and a knowledge of the total cantilever length. The physical shape of the cantilever at any instant is the sum of all the modal displacements at that time.

(a)

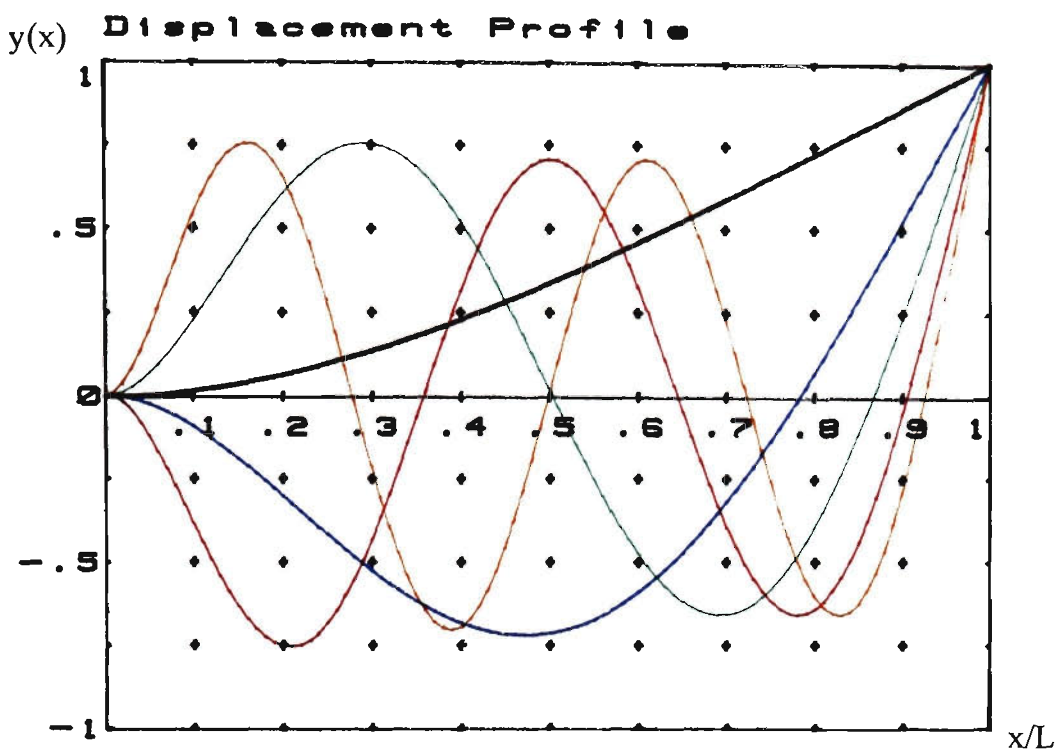

CLAMPED-FREE CANTILEVER

(b)

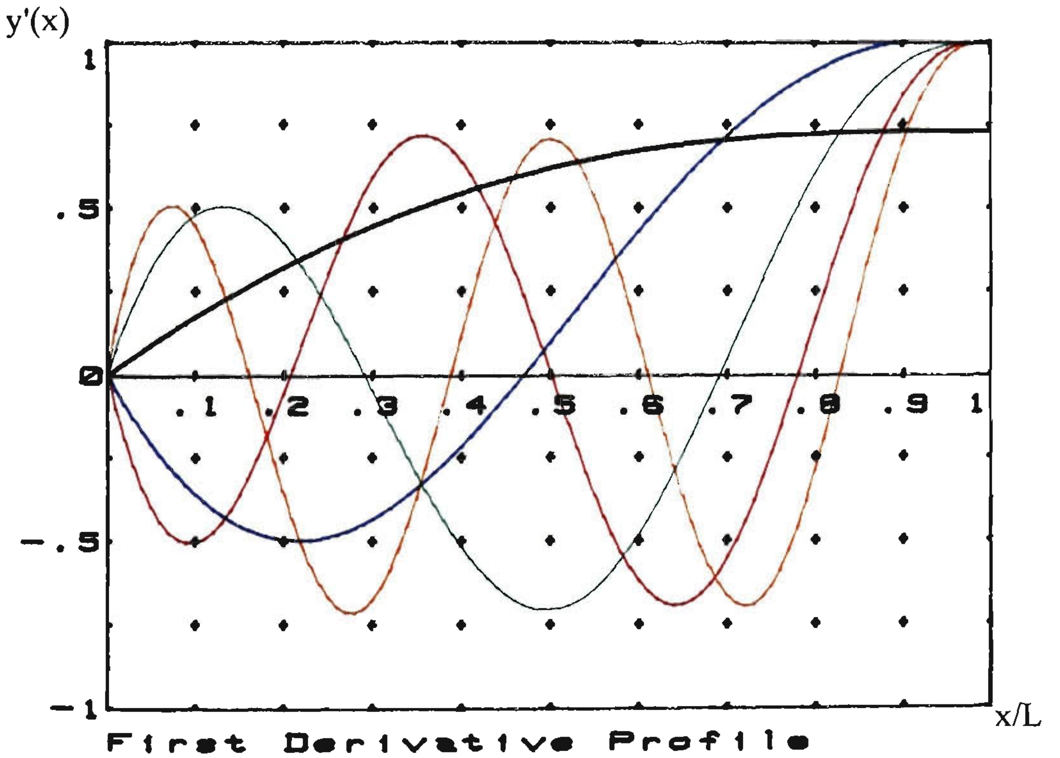

Mode 1-Black, Mode 2-Blue, Mode 3-Green, Mode 4-Red, Mode 5-Orange.

Figure 3.1.6. (a) Displacement profile y(x) and
(b) its first derivative $\partial y/\partial x$ for a clamped-free cantilever.

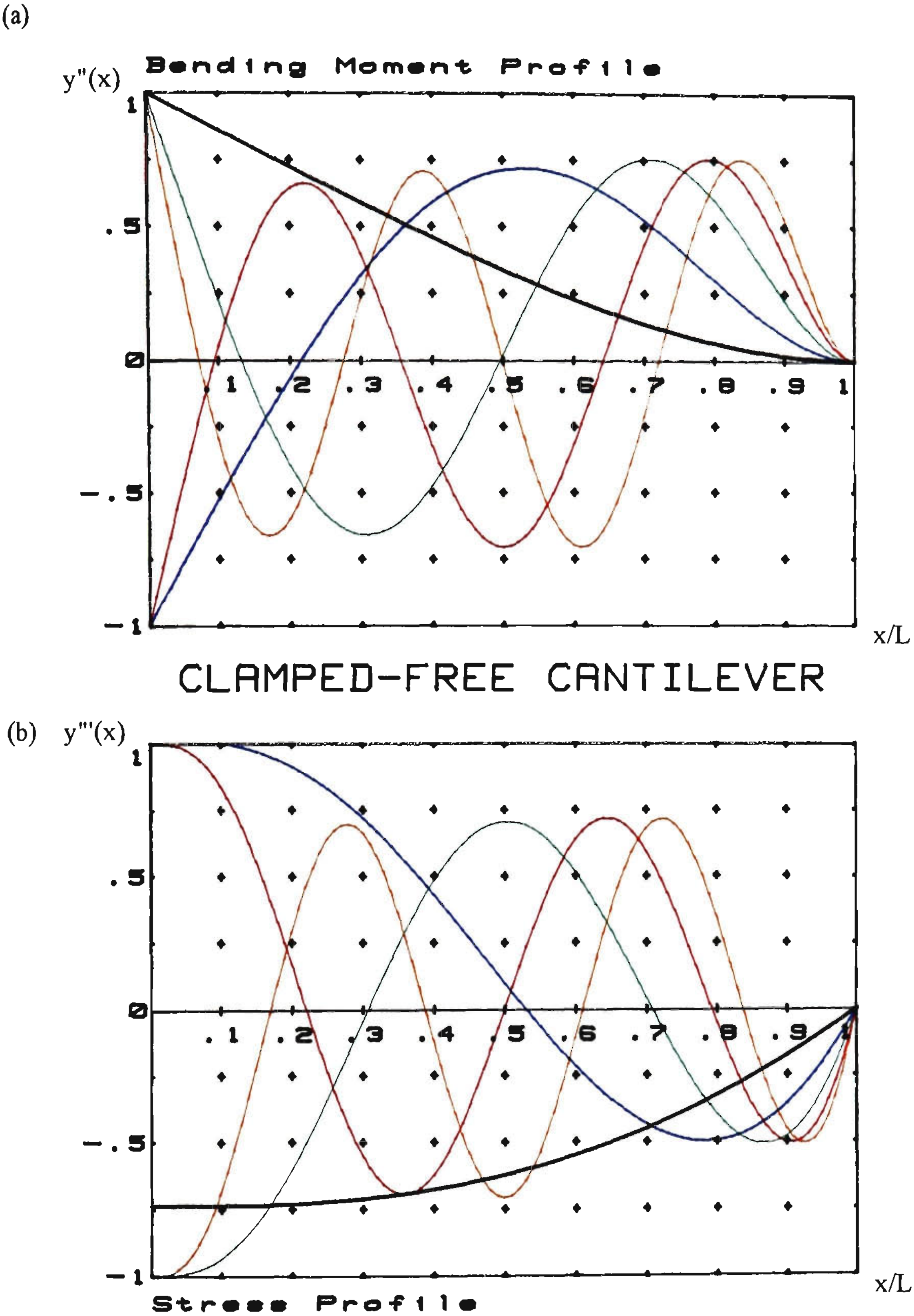

Mode 1-Black, Mode 2-Blue, Mode 3-Green, Mode 4-Red, Mode 5-Orange.

Figure 3.1.7. (a) Bending moment profile $\partial^2 y/\partial x^2$ and
(b) stress profile $\partial^3 y/\partial x^3$ for a clamped-free cantilever.

A single focused laser pulse was used to excite flexural vibration in the cantilever by ablation of the solder target. In order to excite as many vibrational modes as possible, the initial excitation should be at a position which is not close to a node of any of the lower-order modes (in this case, modes one to five). Inspection of the displacement profile (figure 3.1.6(a)) indicates that an impulse applied to the region just below 0.70L will simultaneously excite the first five modes of vibration.

The irradiation site of 0.78L was chosen by Koss and Tobin (1983) to preferentially excite vibration in the first, third, fourth and fifth modes but to suppress vibration in the second mode, since 0.78L is the node of the second mode. It is seen in figure 3.1.1 (also excited at 0.78L) that the spectral density of the second mode of vibration (amplitude of the spectral peak at 11.7 Hz) was significantly less than that of the first and third modes. Koss and Tobin further demonstrated that the third vibrational mode could be preferentially suppressed by irradiating the cantilever at 0.86L, and this was also confirmed experimentally. Successful mode suppression has been demonstrated (as reported by Koss and Tobin) upon high-power laser irradiation at nodes of the displacement profile. This is consistent with a mechanism of excitation in which an impulsive displacement is produced at the irradiation site upon ablation of the material surface. This will be examined in greater detail in section 3.3.3.

3.2 The ablation threshold

Having observed the action of a laser-induced impulse directed at some of the calculated nodes and antinodes of the modal displacement profile for a clamped-free cantilever, the generation of impulsive forces was examined in greater detail. The Nd:glass laser was used to irradiate Wood's alloy (consisting of 50% Bi, 24% Pb, 14% Sn and 12% Cd) and aluminium (6063 T5) targets attached to a calibrated force transducer. Wood's alloy was chosen for its low boiling temperature (~300°C) which, under the available irradiation conditions, would provide a relatively large impulse to the force transducer when vaporised by the laser pulse. The impulse provided to these two materials, upon high power density laser irradiation, could be caused by either radiation pressure or surface ablation, or a combination of both these mechanisms.

The effect of radiation pressure can be estimated from the transfer of momentum from laser photons to the irradiated structure. The momentum (p) of a single photon of wavelength, λ, and energy, **E**, is given by

$$p = \mathbf{E}/\mathbf{c} = \mathbf{h}/\lambda = 6.25 \times 10^{-28} \text{ kg.m.s}^{-1} \text{ per photon.} \qquad \text{eq. 3.2.1}$$

A 40 J pulse of light at 1.06 μm contains 2.1×10^{20} ($40\lambda/\mathbf{hc}$) photons. A pulse from the Nd:glass laser could, if all photons were absorbed by the target, provide a total photon momentum of 1.3×10^{-7} kg.m.s^{-1}, or an impulse of the same magnitude, to the target. The photon impulse of 0.1 μN.s corresponds to a specific impulse of about 2.5 nN.s/J which is very small compared to the specific impulses measured in this work (between approximately 1 and 50 μN.s/J) and also those reported by others. Other published values, for irradiation levels well below the threshold for laser supported detonation, include 250 μN.s/J for bismuth[Koss and Tobin, 1983] and approximately 3 μN.s/J for bare aluminium.[Jones 1971, O'Keefe and Skeen 1972] Hence, the effect of photon momentum is negligible and the measured impulses are most likely due to the ablation of the target material.

The specific impulse delivered to a structure by the laser-induced ablation of its surface has been estimated by a highly simplified analysis recently proposed by Jing (1992). In this analysis the absorbed laser energy rapidly melts, and then vaporises, a small volume of material near the surface. The vaporised material is then assumed to be ejected from the surface as a conical gaseous plume travelling at a speed equal to the mean thermal velocity of the atoms. The analysis assumes that the vaporised material is homogeneous and behaves like an ideal gas, thermal conduction is restricted to a thin layer of depth h_s below the surface, and the time delay between irradiation and vaporisation is negligible (at 10^7 W.cm^{-2} the time to reach the surface boiling temperature in aluminium is 0.27 μs [Ready, 1971]).

The ablation threshold of a laser irradiated material depends on the optical power density of the irradiation as a function of time (F(t)), the temperature dependent reflectivity of the surface (R(T)), the thermal conductivity (K), the boiling temperature of the material (T_b) and the specific/latent heats (specific heat, c, latent heat of fusion, l_f and latent heat of vaporisation, l_v). When a solid body is partially vaporised and produces an expanding mass of vapour, the solid will experience a time dependent force (H(t)). By Newton's second law, this is related to the momentum (p), mass (m_g) and steady state velocity (v_{ss}) of the vapour by

$$H(t) = \frac{\partial p}{\partial t} = \frac{\partial(m_g v_{ss})}{\partial t} = v_{ss}\frac{\partial m_g}{\partial t} . \qquad \text{eq. 3.2.2}$$

This expression can be further developed by considering the v_{ss} and $\frac{\partial m_g}{\partial t}$ terms separately.

The steady state velocity of the vapour is determined by equating its kinetic energy to its average thermal energy;

$$\frac{1}{2}m_w v_{ss}^{\ 2} = \frac{3}{2}R_g T_b , \qquad \text{eq. 3.2.3}$$

where $\mathbf{R_g}$ is the gas constant and m_w is the molecular weight. Hence,

$$v_{ss} = J\sqrt{\frac{3R_g T_b}{m_w}} , \qquad \text{eq. 3.2.4}$$

where J is a reduction factor such that $0 < J < 1$. This factor is introduced to reduce the average expansion velocity of the gas, since v_{ss} is not unidirectional and perpendicular to the surface.

The $\partial m_g/\partial t$ term can be estimated by applying the principle of conservation of energy. For a steady state situation in which surface material is being continuously vaporised, the surface temperature will be maintained at the boiling temperature and the rate of heat absorption (Q) is equal to the power required to vaporise the material plus the rate of heat loss due to thermal conduction. The optical power per unit area absorbed at the surface (the optical power available for heating) is given by (1-R(T)).F(t), where (1-R(T)) is the temperature dependent optical absorption co-efficient. Hence, the rate of heat absorption over an area (**A**) can be written as

$$Q = \frac{\partial m_g}{\partial t}\{ c(T_b - T_0) + l_f + l_v \} + K A \frac{(T_b - T_0)}{h_s} = A\,(1-R(T))\,F(t)\ , \qquad \text{eq. 3.2.5}$$

and therefore,

$$\frac{\partial m_g}{\partial t} = A\ \frac{\{(1-R(T))\,F(t) - K\frac{(T_b-T_0)}{h_s}\}}{\{ c(T_b-T_0) + l_f + l_v \}}\ . \qquad \text{eq. 3.2.6}$$

Substituting equations 3.2.4 and 3.2.6 into 3.2.2 yields an expression for the reaction force at the surface

$$H(t) = v_{ss}\frac{\partial m_g}{\partial t} = J\ A\sqrt{\frac{3R_gT_b}{m_w}}\ \{\frac{(1 - R(T))\,F(t) - \frac{K(T_b-T_0)}{h_s}}{c(T_b-T_0)+l_f+l_v}\}\ , \qquad \text{eq. 3.2.7}$$

which reduces to

$$\frac{H(t)}{A} = J\ k\ [F(t) - N]\ , \qquad \text{eq. 3.2.8}$$

where J**k** is the momentum transfer co-efficient or specific impulse and N is the power loss per unit area due to thermal conduction. The value for **k** may be calculated , when J = 1, using

$$k = \frac{1 - R(T)}{c(T_b - T_0) + l_f + l_v}\sqrt{\frac{3R_gT_b}{m_w}}\ . \qquad \text{eq. 3.2.9}$$

The numerical values used in calculating the specific impulse are summarised in table 3.2.

Quantity		Aluminium	Wood's Alloy
T_b	(K)	2.72×10^3	6×10^2
m_w	($kg.mol^{-1}$)	2.69×10^{-2}	2.2×10^{-1}
c	($J.kg^{-1}.K^{-1}$)	9.00×10^2	2×10^2
l_f	($J.kg^{-1}$)	3.97×10^5	5×10^4
l_v	($J.kg^{-1}$)	1.10×10^7	7×10^5
R(T) at 1064 nm		0.8	0.8

$\mathbf{R_g}$ = 8.315 $J.mol^{-1}.K^{-1}$

Table 3.2 Data used in calculation of **k**.

The specific impulse was calculated from equation 3.2.9 and the data in table 3.2 to be 23 μN.s/J for aluminium and 6×10^2 μN.s/J for Wood's alloy.

In addition to its dependence on **k**, the specific impulse also depends on the reduction factor, J, which allows for the fact that all the vapour is not ejected perpendicular to the surface and hence the effective steady state velocity of the expanding vapour will be less than the kinetic theory value. Plate 3.2 clearly shows the vapour plume produced by surface ablation of a steel target after irradiation with a focused Nd:glass laser pulse. In addition to the vapour plume, the plate also shows that molten globules of steel are also ejected from the surface. This effect, which is not allowed for in the simple calculation above, will further alter the value of the specific impulse.

Having estimated the specific impulse produced upon ablation of aluminium and Wood's alloy using the simplified model above, the values of the specific impulse for these materials were experimentally determined. For these measurements, the laser pulse was focused by a 12 cm focal length lens to yield a spot diameter of 0.5 mm at the target with an estimated power density

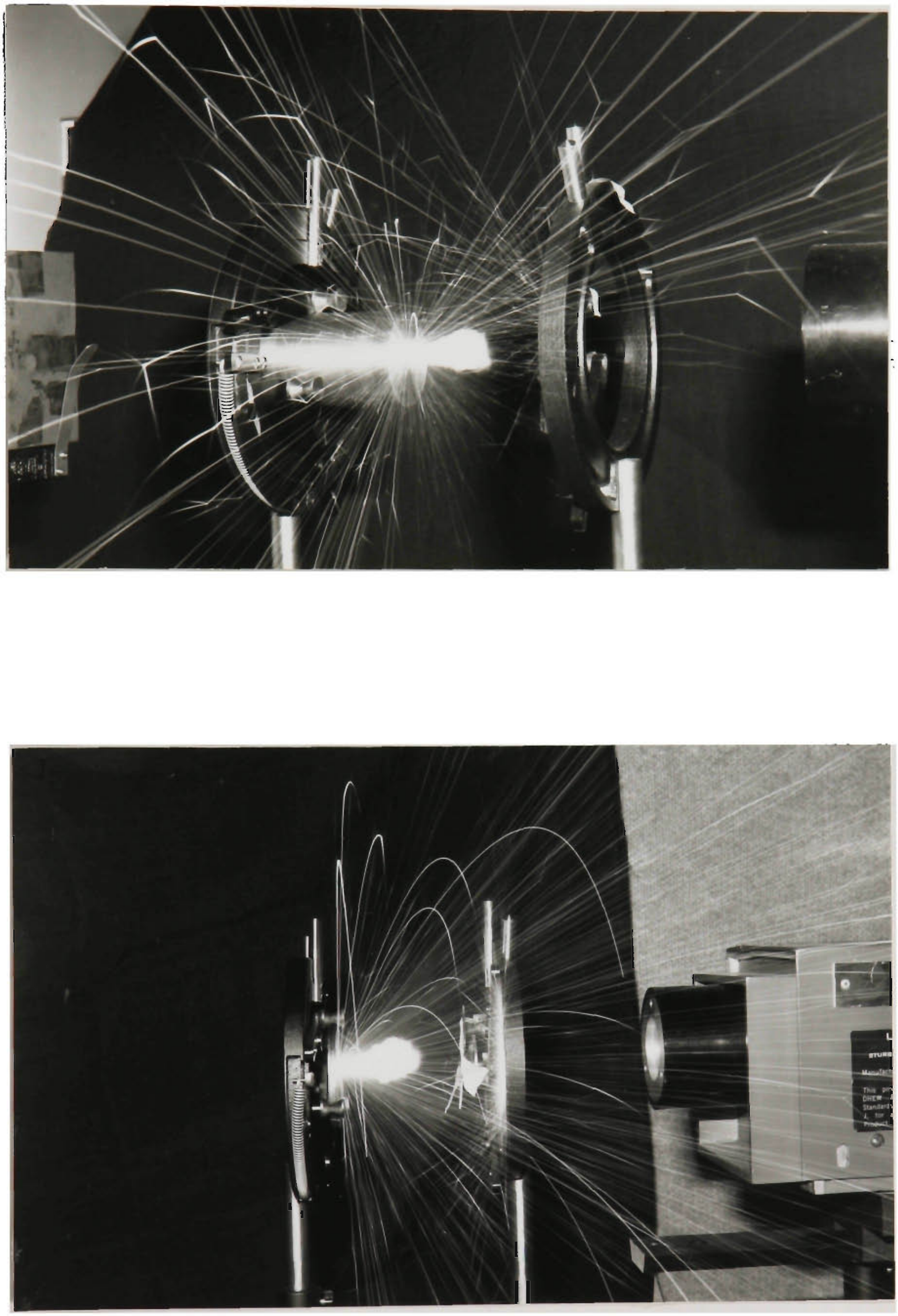

Plate 3.2. Laser-generated ablation at a steel surface.

of 3×10^7 W.cm^{-2}. For a laser pulse duration of 600 μs FWHM, the threshold for ablation of aluminium has been shown to be approximately 10^7 W.cm^{-2}.[Pirri et al., 1972] The aluminium target was fitted directly to the calibrated force transducer (Brüel & Kjaer 8200 accelerometer with calibration constant 100 mV = 1 N) and the Wood's alloy was contained in a 1 cm^2 cavity in a steel capsule mounted directly on the force transducer. The surface of each target (Wood's alloy and aluminium) was blackened with a water-based ink to minimise surface reflection of the laser pulse. The spot diameter at the target was systematically reduced from 5 mm to 0.5 mm, and then expanded again to 5 mm, by focusing and then defocusing the target lens. In this manner, power densities between approximately 1×10^5 W.cm^{-2} and 3×10^7 W.cm^{-2} were achieved at the irradiated surface. The impulse profiles for Wood's alloy and aluminium are presented in figures 3.2.1 and 3.2.2 respectively.

Specific impulses of 53 μN.s/J for Wood's alloy and about 0.7 μN.s/J for aluminium were obtained by numerical integration of these force-time profiles obtained using the calibrated force transducer. The value obtained for aluminium is subject to some considerable uncertainty due to the obvious ringing in the force-time profile. These experimental values are about an order of magnitude smaller than those predicted using equation 3.2.9. This difference can readily be accounted for by a reduced value of J and uncertainty in the assumed reflectivity of the surface. Thus it seems reasonable to assume that vibrational excitation on ablation is due to the impulsive reaction of the ablated material. Impulsive forces were not detected for spot diameters greater than 4 mm in Wood's alloy (5.3×10^5 W.cm^{-2}) and 0.8 mm in aluminium (1.3×10^7 W.cm^{-2}). A laser spot diameter of 8 mm (1.3×10^5 W.cm^{-2}), for the unfocused Nd:glass system used in subsequent measurements, certainly did not produce any measurable impulsive forces in aluminium or Wood's alloy. This is not surprising, since the power density is so much below the ablation threshold. A similar comment would apply to steel (ablation threshold approximately 10^6 W.cm^{-2} [Ready, 1982]).

WOOD'S ALLOY TARGET ON FORCE TRANSDUCER

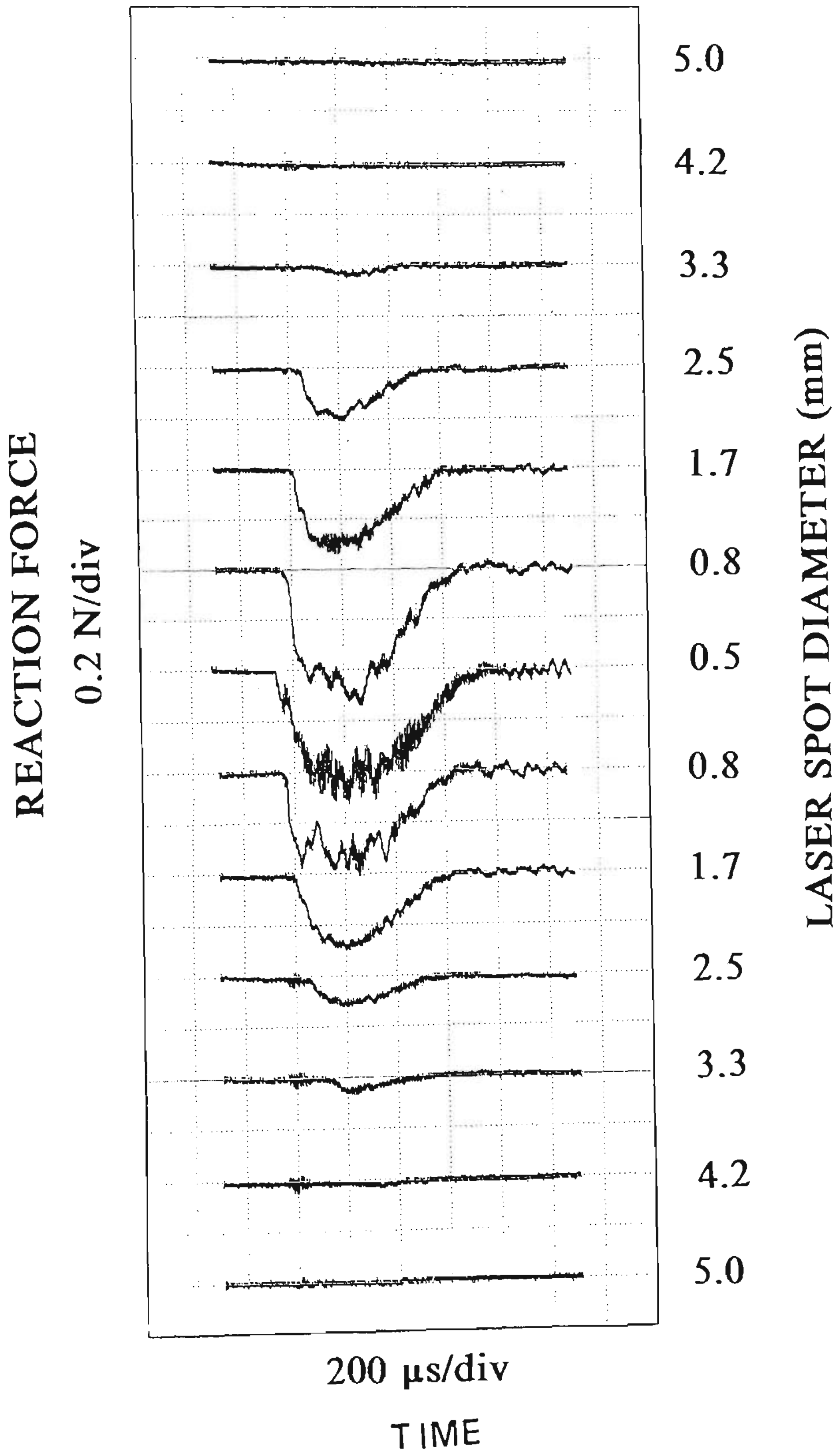

Figure 3.2.1. The impulsive reaction delivered to a Wood's alloy target as a result of laser irradiation at various spot diameters.

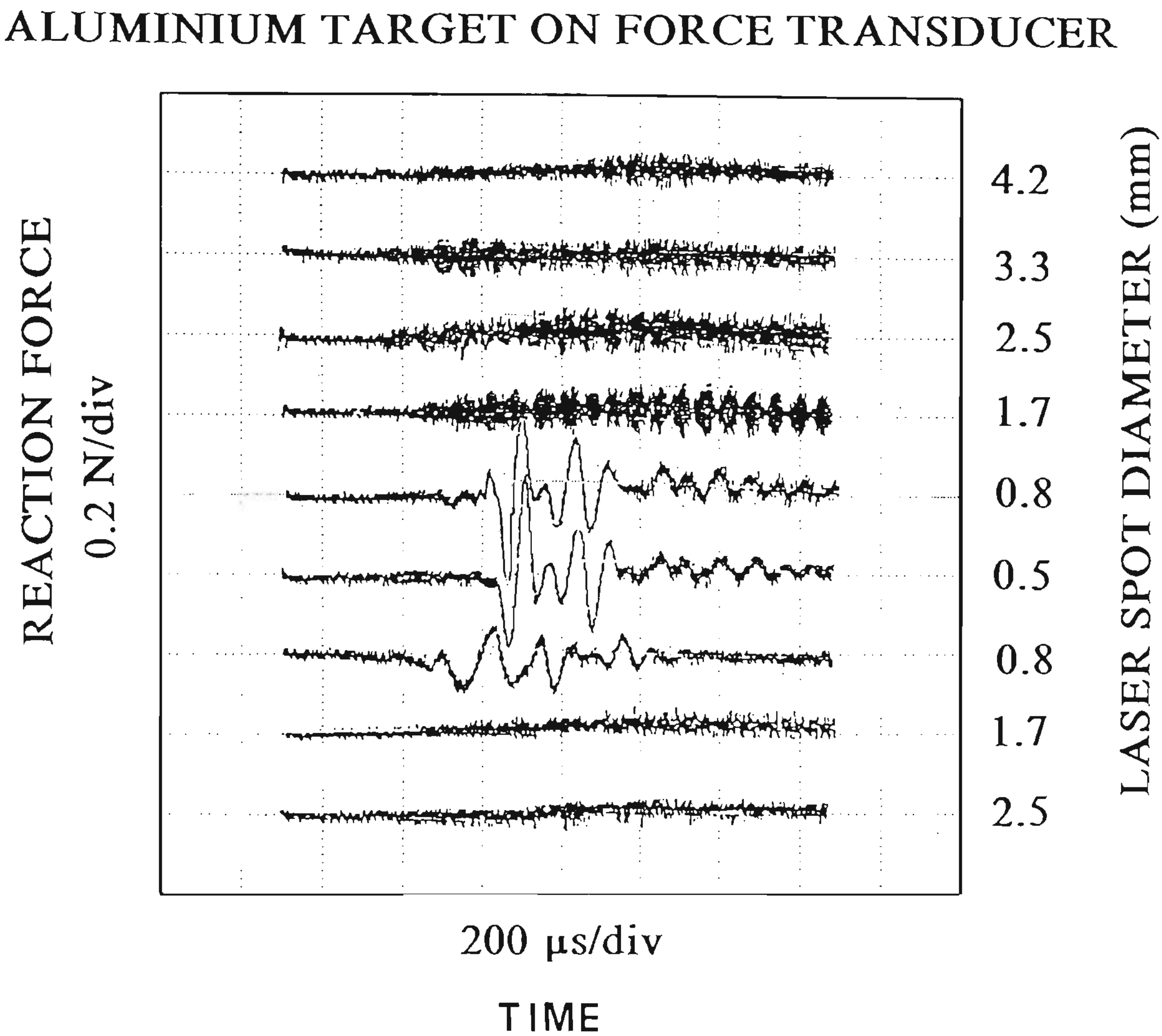

Figure 3.2.2. The impulsive reaction delivered to an aluminium target as a result of laser irradiation at various spot diameters.

A simple experiment was conducted to demonstrate the ability of a small impulse (approximately 2×10^{-3} N.s) to excite even massive structures. The force transducer was placed in-between the Wood's alloy target and a 57 kg, 50.8 cm diameter truck wheel rim (suspended horizontally from an overhead mount by twelve springs) and irradiated at the maximum power density of the laser system as before. Figure 3.2.3 records the impulse produced by laser irradiation of the Wood's alloy target and the vibration of the massive truck rim which followed. The three time bases illustrate the initial impulse to the rim (250 μs/div), the initial vibration of the rim (1 ms/div) and the free vibration which followed (100 ms/div).

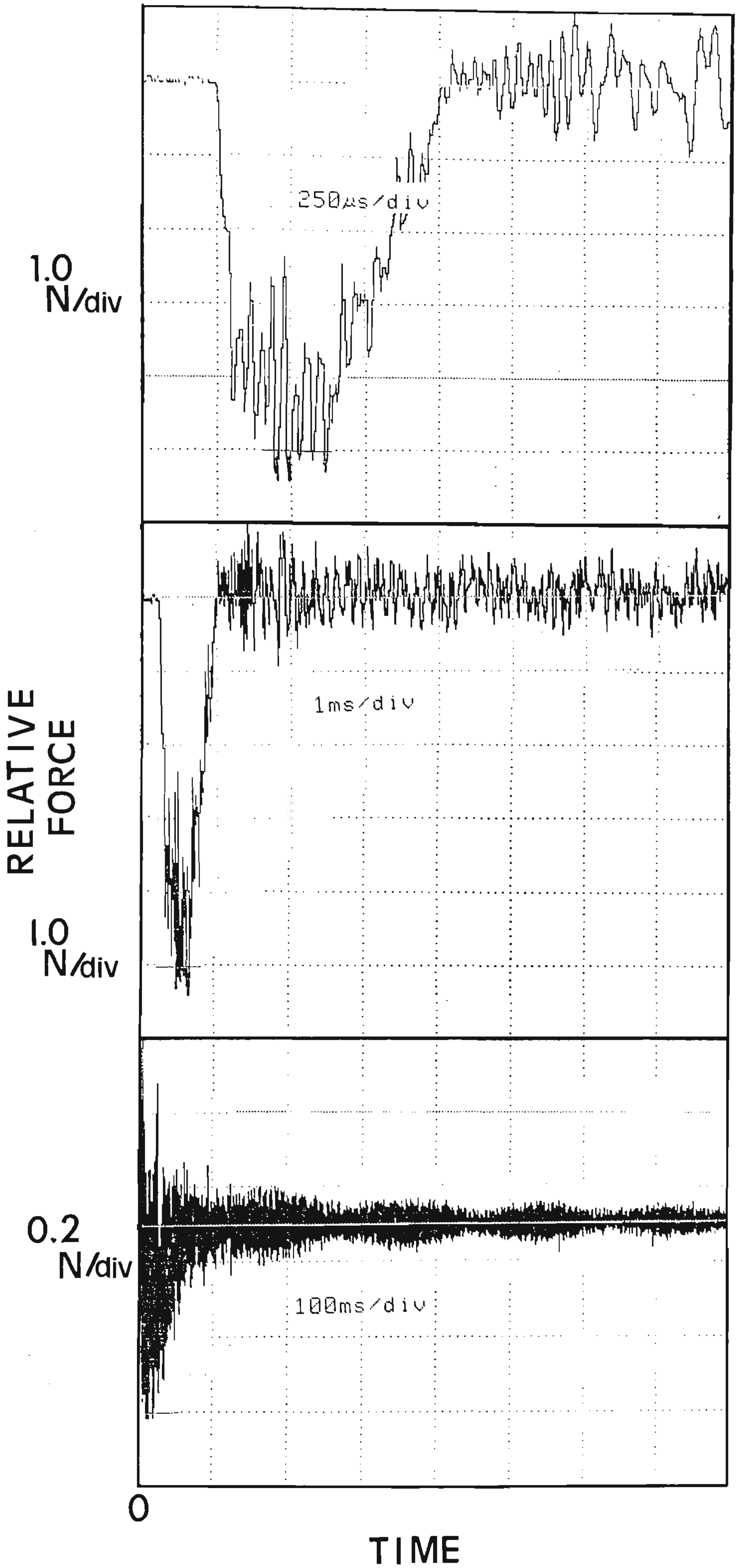

Figure 3.2.3. Laser excitation (flux density 3×10^7 W.cm^{-2}) of a 57 kg wheel rim by irradiating a small Wood's alloy target coupled to its surface through a PZT force transducer

3.3 Laser stimulation of structural vibration using power densities below the surface ablation threshold

Experiments were conducted to identify the mechanism by which simple cantilevers could be excited to free vibration after irradiation by a single sub-ablative laser pulse. Since the power density of the unfocused pulse was well below the ablation threshold of the irradiated materials, the excitation could not be attributed to an ablative impulse (section 3.2). Direct observation of a flexing cantilever for the first few milliseconds during, and after, unfocused laser excitation and scrutiny of the irradiation sites found to suppress or enhance specific vibration modes, indicated that a transient bending moment was most likely to have initiated the flexural vibration.

3.3.1 Excitation and sensor locations for efficient modal analysis in cantilevers

The spectral density (the height of a spectral peak measured as dB above noise) of any specific mode of vibration in a clamped-free cantilever was measured from the Fourier analysis of the vibration record obtained after irradiation with an unfocused laser pulse. This spectral density was observed to change significantly with variation in both the site of irradiation and the location of the proximity sensor. Tests were therefore conducted to determine the optimum laser excitation and sensing positions. The unfocused Nd:glass laser was used to irradiate cantilever A at positions between 10 mm and 290 mm from the clamp in intervals of 10 mm. This process was repeated for positions of the proximity sensor at 10 mm intervals over the same range.

Variation in the location of the proximity sensor, whilst maintaining a fixed irradiation site, revealed that the spectral density of the first vibrational mode increased markedly as the fibre-optic sensor was moved further from the clamped-end of the cantilever. This was expected since the cantilever displacement must be greatest at the free-end. Likewise, the second mode dominated the region around the centre of the cantilever. These effects tended to reduce the amplitude of the peaks corresponding to the fourth and fifth vibrational modes. The larger cantilever deflection necessitated a relatively large probe-to-surface separation and this reduced the sensor sensitivity for small amplitude vibrations. By choosing a sensor position close to the clamped-end of the cantilever, the detected modal amplitudes of the first and second vibrational modes were reduced whilst the third, fourth and fifth modes were most clear. The first five modes of free vibration were best detected when the fibre optic vibration sensor was placed at 0.20L. This experimental detection site agrees with the modal displacement profile shown in figure 3.1.6(a), where the sensor position is not close to a displacement node for any of the first five modes of vibration.

The proximity sensor was placed at 0.20L. When the region of the cantilever between 0.75L and 0.90L was irradiated, all of the first five vibrational modes were clearly detected in the FFT (the problem with other locations is that the fifth mode tends to be very weak). Detailed irradiation of this region indicated an optimum position, for clearest definition of the first five modes of vibration, at 0.85L. The optimum excitation and detection conditions for all of the first five natural modes of vibration were therefore achieved when the laser was directed onto a blackened surface at 0.85L with the fibre-optic sensor located at 0.20L. Blackening of the surface with a water-based felt pen increased the light absorption at the surface and improved the thermal excitation gained from the unfocused pulse. Although the black ink was partially vaporised upon laser irradiation, the impulse produced by this action upon irradiation by the unfocused laser was insignificant (as shown previously in figure 3.2.1).

This investigation also revealed that the irradiation sites for effective suppression or enhancement of a selected vibrational mode did not correspond to the location of nodes (suppression) or antinodes (enhancement) for that mode, in the mode displacement profile (figure 3.1.6(a)). Instead, it was found that a specific mode of vibration could only be effectively suppressed, with respect to the other vibrational modes, when the cantilever was irradiated at sites which corresponded to nodes of the second derivative of the displacement profile (Figure 3.1.7(a)). Similarly, enhancement of a specific mode of vibration was achieved only when the laser irradiation was directed at the antinodes of the second derivative of the displacement profile. As an example, the point of most efficient modal excitation for all of the first five modes of natural vibration was found experimentally to be 0.85L, a point of excitation which, according to the displacement profile, should have selectively suppressed the third mode of vibration, had the excitation been impulsive.

These observations gave a strong clue to the mechanism of excitation, since the second derivative is proportional to the bending moment at each point (equation 3.1.4). This is examined much more fully in the sections which follow. Before that, it is useful to examine the early development of the vibration during, and for the first few milliseconds after, laser irradiation.

3.3.2 Time domain profile of laser vibrated cantilevers

Cantilevers A and S were excited by a single unfocused Nd:glass laser pulse at 0.85L and monitored with the proximity sensor at 0.20L. The laser irradiation should result in thermal expansion of the surface material and bending of the cantilever as a whole about the irradiation site. The laser-induced flexing was recorded as a function of time, using the Tektronix DSA 602. The concept of an induced bend at the irradiation site is depicted in figure 3.3.2.1 and the experimental arrangement used for this investigation is shown schematically in figure 3.3.2.2.

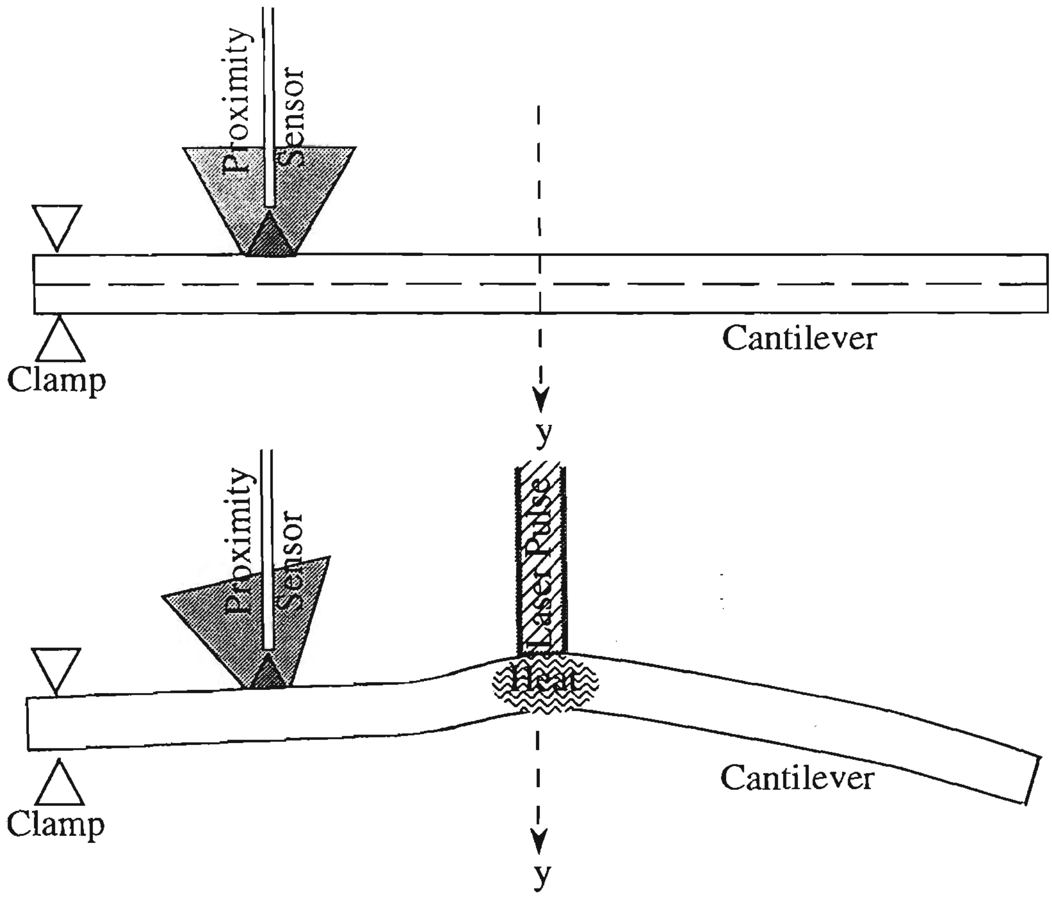

Figure 3.3.2.1. Schematic diagram showing the laser-induced bending of a clamped-free cantilever.

The simultaneous temporal behaviour of both the laser pulse and vibration profiles of two cantilevers are shown in figures 3.3.2.3 (aluminium) and 3.3.2.4 (steel). The upper record in each figure shows the flexing of the cantilever during the period of laser irradiation, whereas the lower two records show the vibration of the cantilever shortly after the initial excitation. In both the aluminium and the steel cases, the cantilever is seen to deflect in the latter stage of the laser pulse, and to oscillate thereafter. It is also apparent that the aluminium cantilever is more efficiently excited to free vibration than the steel cantilever since the initial oscillations are more regular (this will be discussed in greater detail in section 3.4). The rise time (1/e×peak to peak) and fall time (peak to 1/e×peak) of the initial deflection were measured from these traces as; 0.50 ms (Rise) and 0.45 ms (Fall) for cantilever A, and 0.34 ms (Rise) and 0.26 ms (Fall) for cantilever S. The initial oscillations have frequencies of about 400 Hz and 600 Hz for cantilevers A and S respectively.

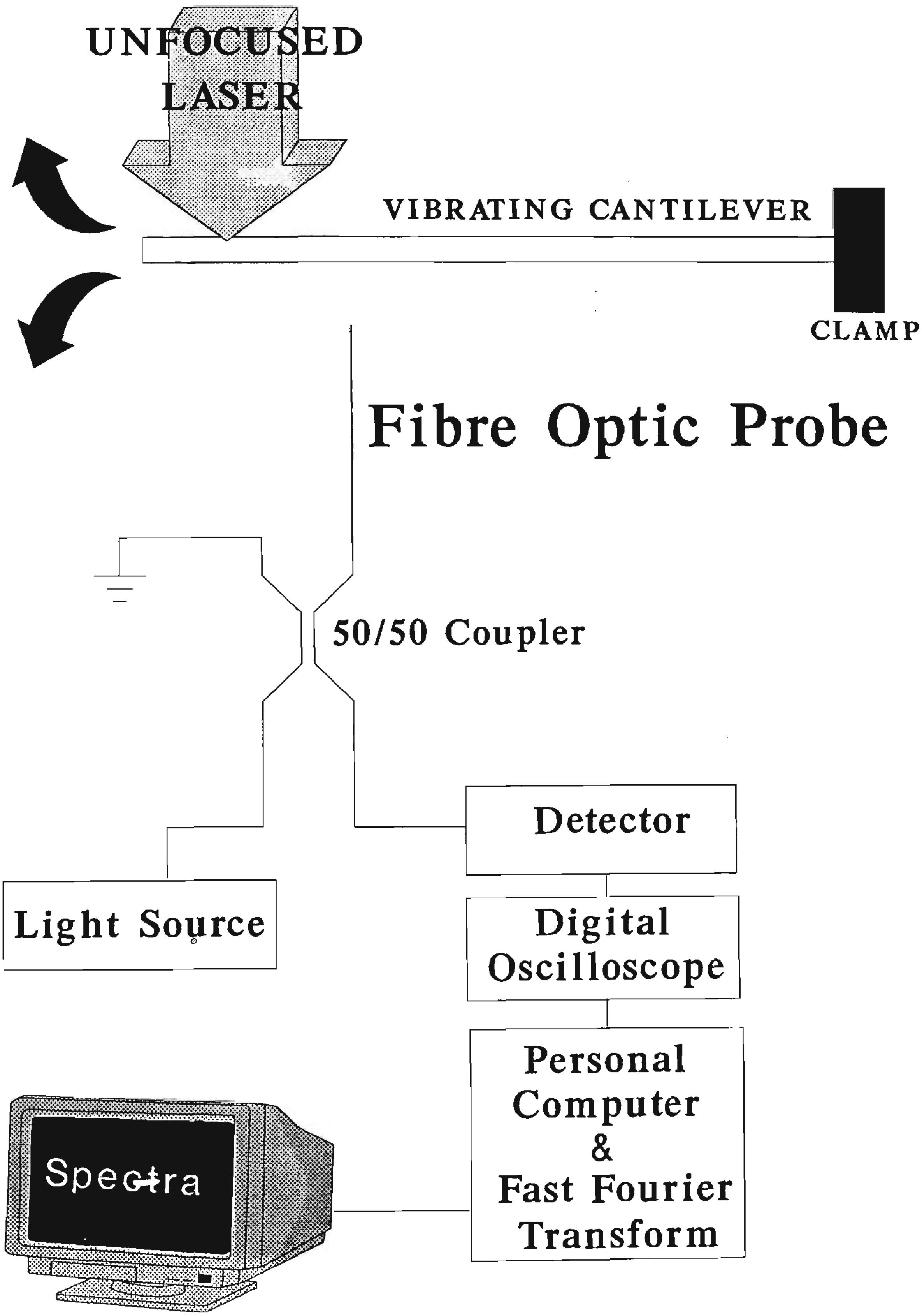

Figure 3.3.2.2 Experimental arrangement

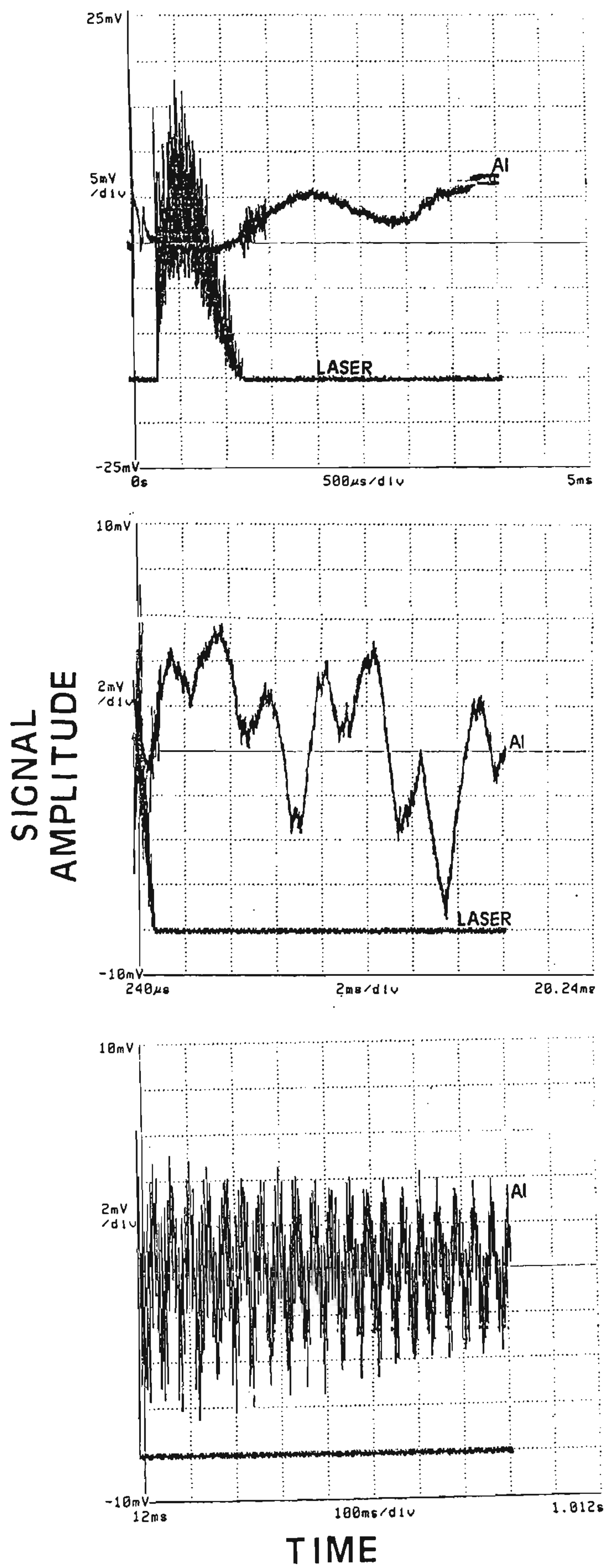

Figure 3.3.2.3 Displacement behaviour of the aluminium cantilever during and after the laser irradiation. In each record, the lower trace is that of the laser pulse.

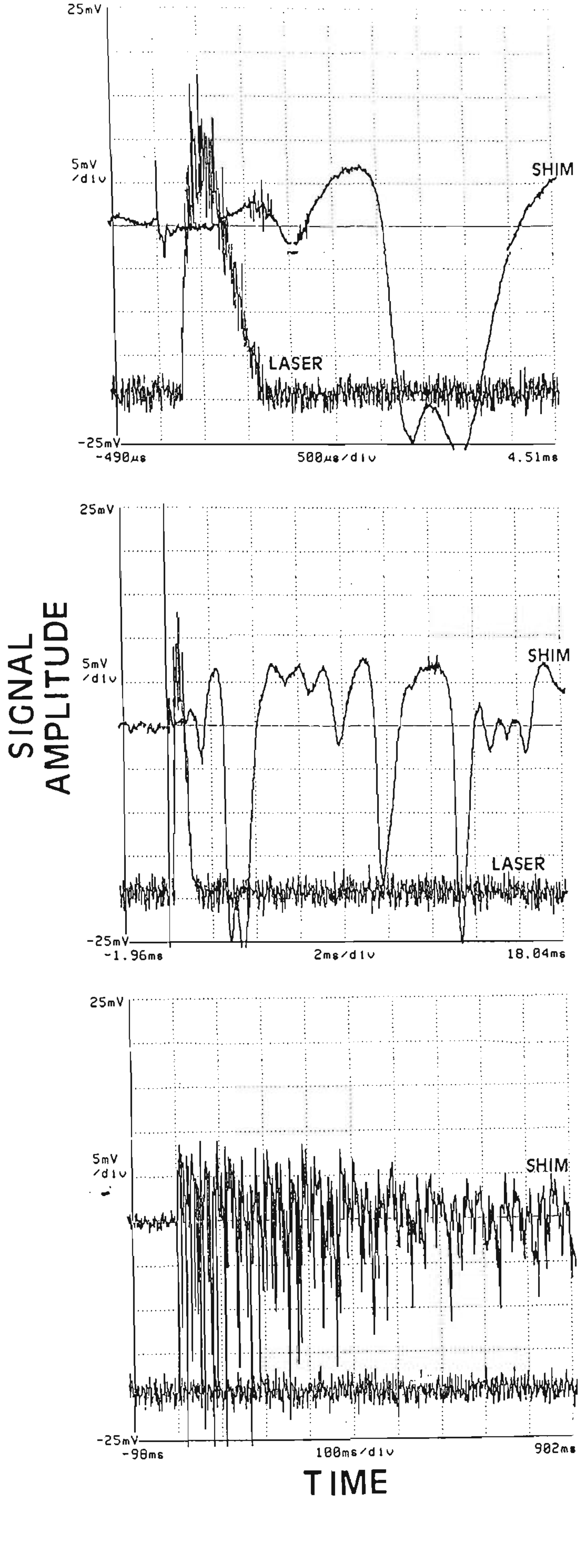

Figure 3.3.2.4 Displacement behaviour of the stainless steel cantilever during and after the laser irradiation. In each record, the lower trace is that of the laser pulse.

3.3.3 Mode suppression using ablation and photo-thermoelastic flexing techniques

The irradiation sites for efficient modal enhancement and suppression using a single laser pulse, both above and below the ablation threshold, were examined to help elucidate the mechanism of excitation. The experimental arrangement used for this investigation is the same as that shown schematically in the previous section (figure 3.3.2.2).

Cantilevers A and S were irradiated with a single pulse from the Nd:glass laser. Two forms of laser pulse were used; namely, an unfocused pulse (8.0 mm spot diameter incident upon a blackened surface) and a focused pulse (0.5 mm spot diameter incident upon a small solder target mass (~1g) attached to the surface, which facilitated ablation in a manner similar to Wood's alloy). Solder was used as it was easy to attach to the cantilevers and ensured that the aluminium cantilever received an impulsive reaction with the focused laser irradiation. This is because the maximum power density achieved by the Nd:glass laser and lens system bordered on the ablation threshold for aluminium (see figure 3.2.2). The solder target was also attached to the steel shim cantilever because direct irradiation of the steel shim had previously blown a hole in the strip and this, aside from the obvious damage, significantly reduced the excitation.

In both the focused and unfocused cases, transverse flexural vibration of each cantilever resulted. The vibrations were recorded by placing the proximity sensor close to the unpolished surfaces, at 0.20L. The sensor location enabled the first four modes of vibration to be investigated for all the selected irradiation sites. The Tektronix DSA 602 was used to store the vibration signals and FFT frequency spectra were obtained, both in real time from the DSA 602, and by processing the stored signals using a HP-Basic routine. The laser was directed as a focused pulse on a solder target at the position of all the computed nodes for the first four modes of the cantilevers' displacement profiles, and also at the position of nodes for the first, second and third derivatives of their displacement profiles. The experiments were then repeated, using the unfocused laser pulse on a blackened surface.

When vibration is due to a focused pulse, excitation directed at the nodes of the displacement profile for a particular mode of vibration should result in preferential suppression of that mode with respect to the other vibrational modes. On the other hand, when an unfocused pulse is used to excite the cantilevers, the relevant nodes for preferential mode suppression should be those of the bending moment profile (second derivative of the displacement profile). Frequency analysis of the vibration data should enable the focused and the unfocused excitation mechanisms to be distinguished.

Because there was substantial shot-to-shot variation in the absolute amplitudes of the individual peaks of the frequency spectrum, a simple criterion was used to assess whether or not mode suppression had been successful at the chosen site of irradiation. If the mode selected for suppression had less relative power than the other three modes examined, the mode was judged to be effectively suppressed. The results of excitation at various nodes for the aluminium cantilever are given for the focused pulse in figure 3.3.3.1 and for the unfocused pulse in figure 3.3.3.2. Likewise, modal amplitudes of vibration in the steel shim are presented for the focused and unfocused pulses in figures 3.3.3.3 and 3.3.3.4 respectively. In figures 3.3.3.1 to 3.3.3.4, a "tick" directly below a mode bar diagram indicates that the selected mode had the least amplitude of the four modes examined.

The spectral density (height of the peaks) of each vibrational mode in the FFT spectrum was dependent on the proximity of the fibre-optic sensor to the cantilever surface, however the

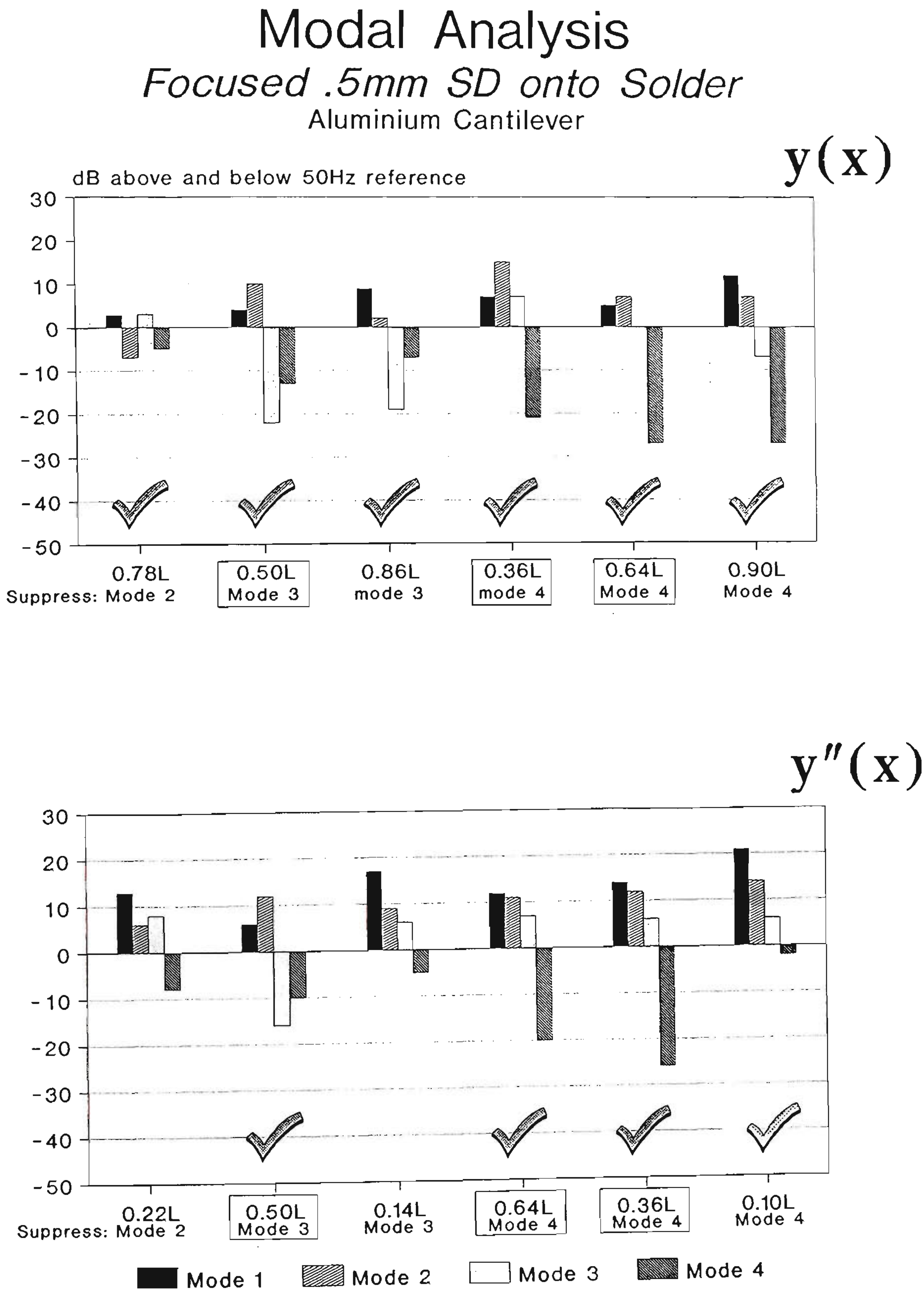

Figure 3.3.3.1. Modal analysis of the aluminium cantilever following excitation at nodal points for the first four modes of vibration by a focused laser pulse incident upon solder.

Modal Analysis

Unfocused 1cm SD

Aluminium Cantilever

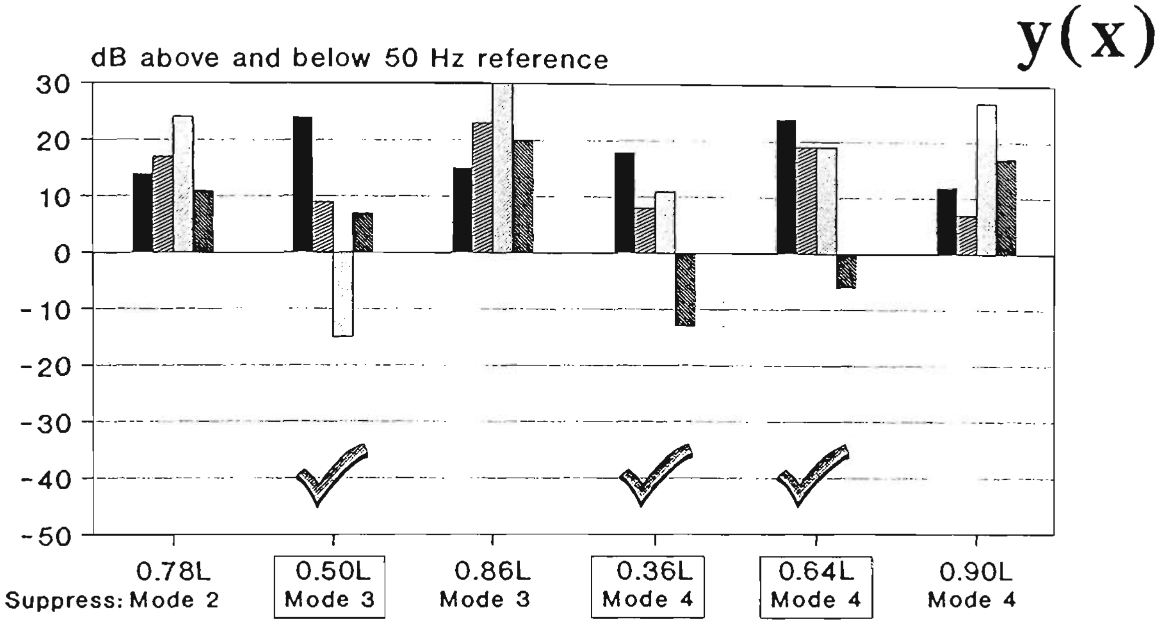

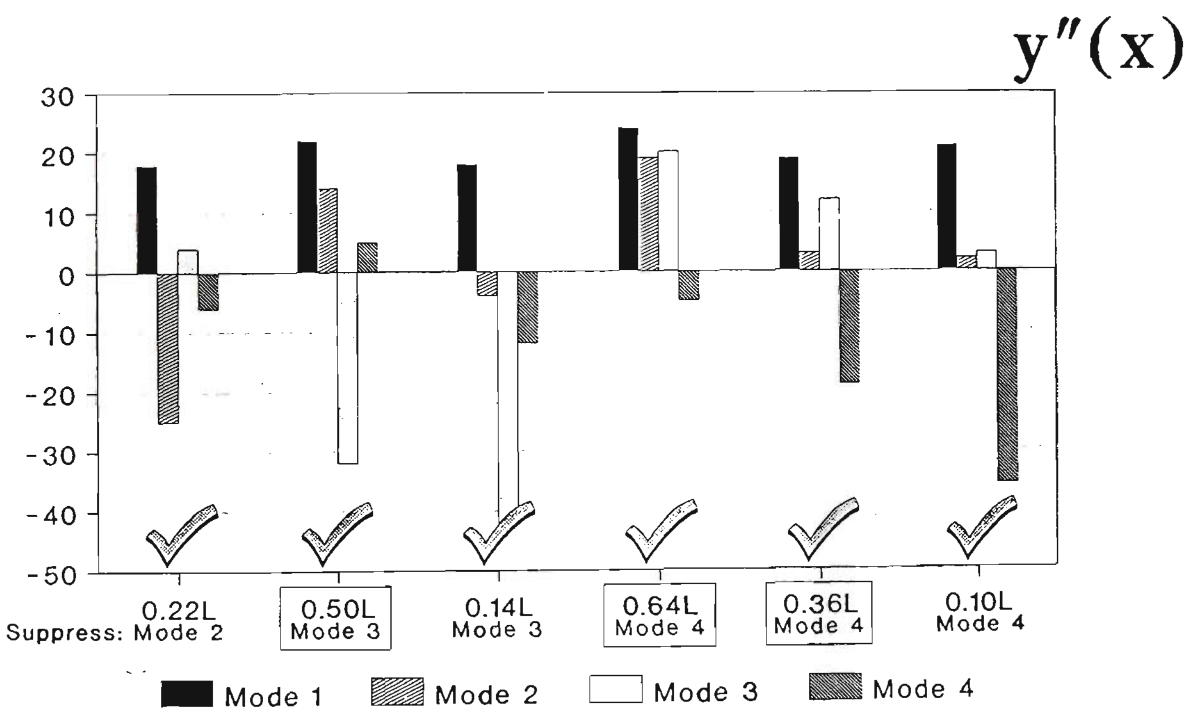

Figure 3.3.3.2. Modal analysis of the aluminium cantilever following excitation at nodal points for the first four modes of vibration by an unfocused laser pulse.

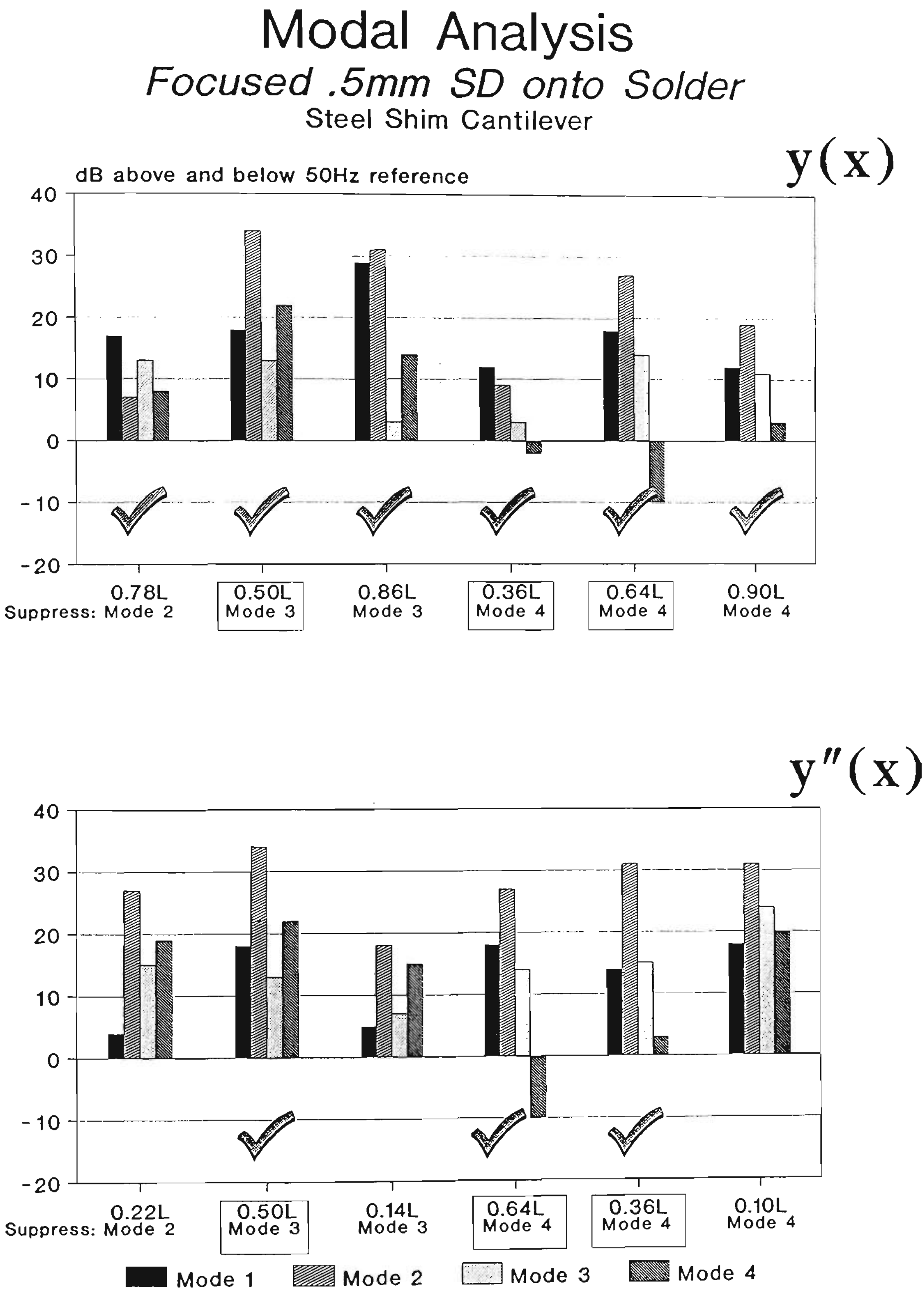

Figure 3.3.3.3. Modal analysis of the steel shim cantilever following excitation at nodal points for the first four modes of vibration by a focused laser pulse incident upon solder.

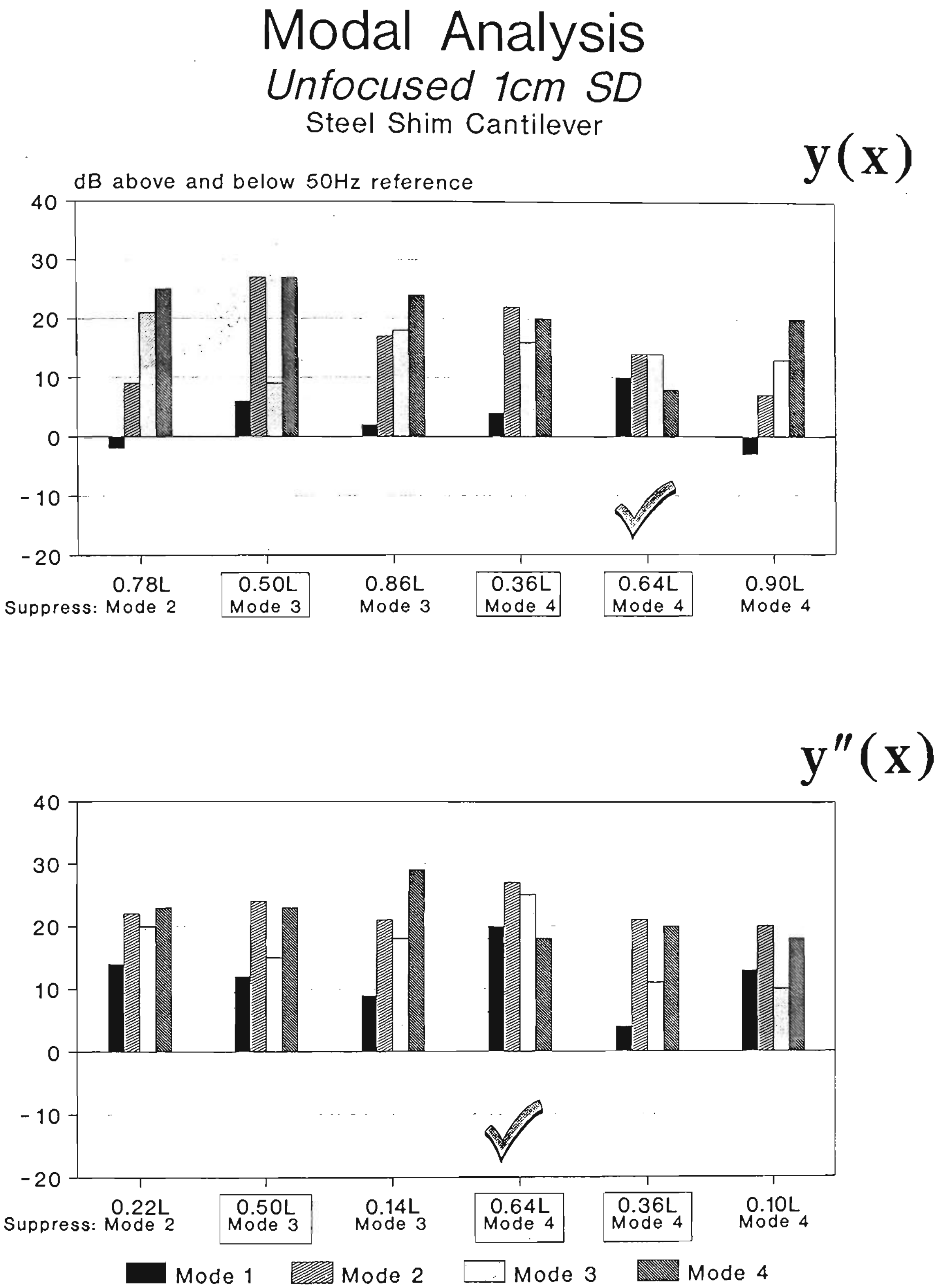

Figure 3.3.3.4. Modal analysis of the steel shim cantilever following excitation at nodal points for the first four modes of vibration by an unfocused laser pulse.

relative spectral density of one vibrational mode to another remained approximately constant for a given set of irradiation conditions. In order to remove the shot-to-shot variations, the amplitudes shown were referenced to the recorded level of residual 50 Hz modulation from the LED light source used in the sensor. This 50 Hz peak also varied with the distance of the sensor from the vibrating surface. The important distinction here is that relative, rather than absolute, spectral densities of the various vibrational modes are being considered. The nominal reference merely enabled figures 3.3.3.1 to 3.3.3.4 to be drawn with a common vertical axis. That is, the vertical axes are the amplitudes of the peaks in the FFT spectrum (in electrical dB) as measured relative to the residual 50 Hz modulation peak. It is also important to note that the displacement profile and the bending moment profile share three points in common (x = 0.5L, 0.36L and 0.64L). These common points are shown using a box surrounding the caption below the mode bar diagram.

Impulsive reactions, caused by ablation of the solder target at nodes of the modal displacement profiles, suppressed all selected modes of vibration (according to the previously mentioned criteria), in both the steel and aluminium cantilevers. Unfocused irradiation, delivered at node locations of the bending moment profile, suppressed all selected modes of vibration in the aluminium cantilever, but was very much less effective for most cases with the steel shim. The one exception for the steel shim was unfocused irradiation at 0.64L. This single case for suppression of mode 4 may be considered a poor example since all four modes were well excited and have much the same amplitude (10 ± 3 dB [upper] and 22 ± 5 dB [lower] in figure 3.3.3.4). Neither focused nor unfocused irradiation directed at nodes of the first and third derivative profiles, or indeed at any other location, were found to definitely suppress the selected modes in either cantilevers A or S. As discussed in the previous section, the laser pulse caused both cantilevers to begin bending during the latter part of the irradiation and relax shortly after the pulse was finished. The duration of the initial flexing was measured directly. Since both cantilevers were clearly well-excited by the laser pulse, it was not clear why the mode suppression techniques using the unfocused laser pulse were successful for cantilever A, but not for cantilever S.

It is evident from figures 3.3.2.4 that, for times beyond about one second after the laser pulse, the lower order modes of vibration tended to dominate the free vibration of cantilever S; yet, energy was initially coupled into much higher-order modes. A direct measurement of the initial oscillations (top trace shown in figure 3.3.2.4), suggests a frequency of around 600 Hz (approximately mode 11). Either energy was being gradually transferred from higher to lower-order modes of vibration through some non-linear process, or the higher-order modes were just more strongly damped. In either case, the failure to observe selective mode suppression in the modal signatures of cantilever S could have been due to taking the Fourier transform of the vibration data over the time during which the mode profile was still developing.

To check the time development of the vibration spectra, the vibration records were sectioned and Fourier transforms taken for each of ten incremental 100 ms intervals over one second. The process was repeated for two 500 ms intervals over 1 s. These are presented in figures 3.3.3.5 (cantilever A) and 3.3.3.6 (cantilever S). There is no evidence of energy transfer between modes, in that none of the modes are observed to significantly increase beyond their initial amplitude with time. The modal data for the first and second vibrational modes in cantilever S are not evident from the Fourier transforms over the 100 ms intervals (and also in the case of mode 1 for the 500 ms interval) because the period of these modes (500 ms in the case of mode 1 (2 Hz) and 83 ms for mode 2 (12 Hz)) were outside, or close to, the total transform sample duration. What is seen in the data is a greater attenuation at higher frequencies, which would contribute to the dominance of lower order-modes at later times. This will be discussed in greater detail in section 3.4.1.

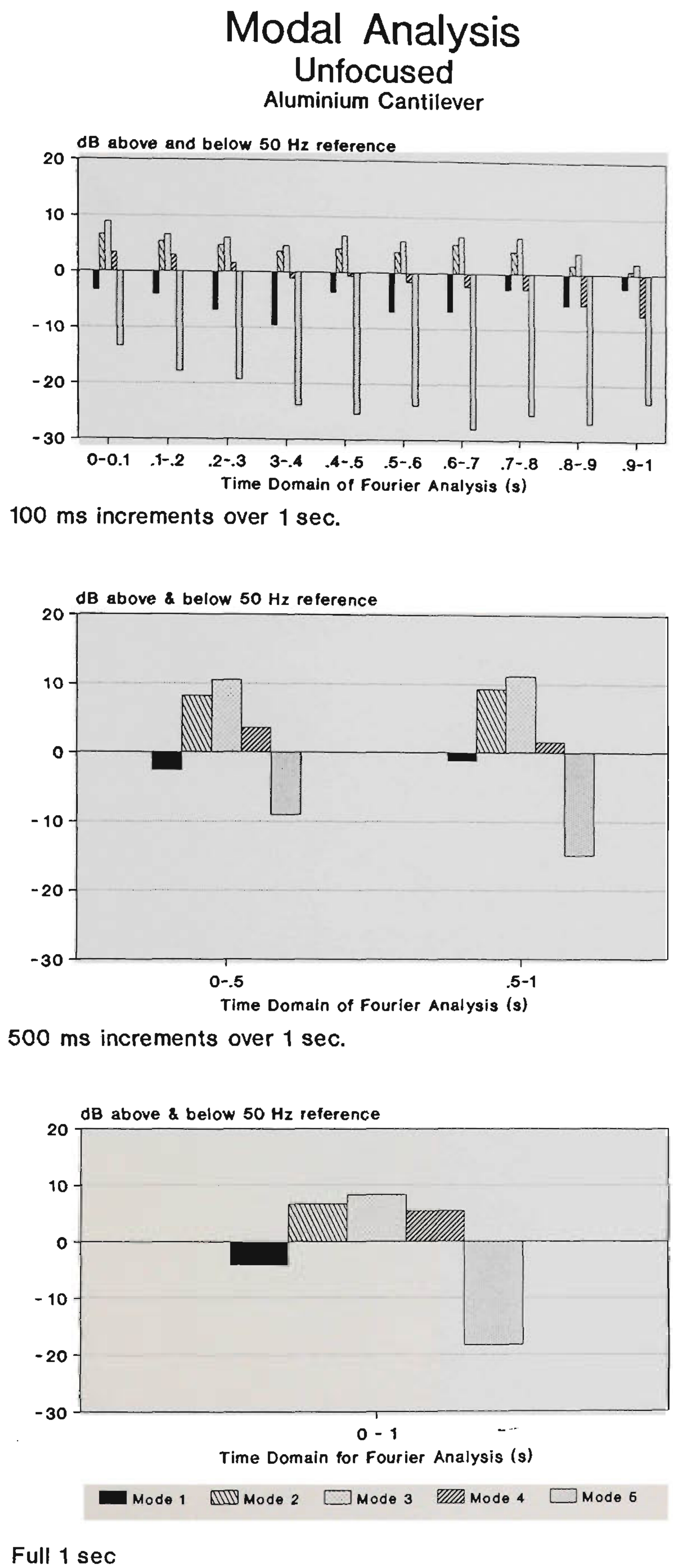

Figure 3.3.3.5 Modal amplitudes of consecutive samples within the vibration profile for cantilever A

Modal Analysis

Unfocused

Shim Steel Cantilever

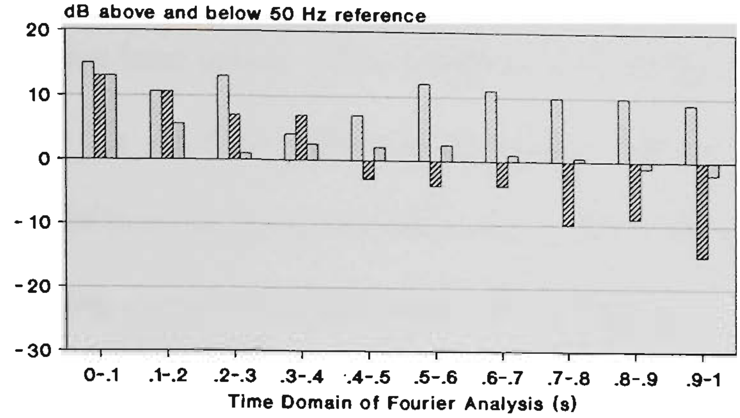

100 ms increments over 1 sec.

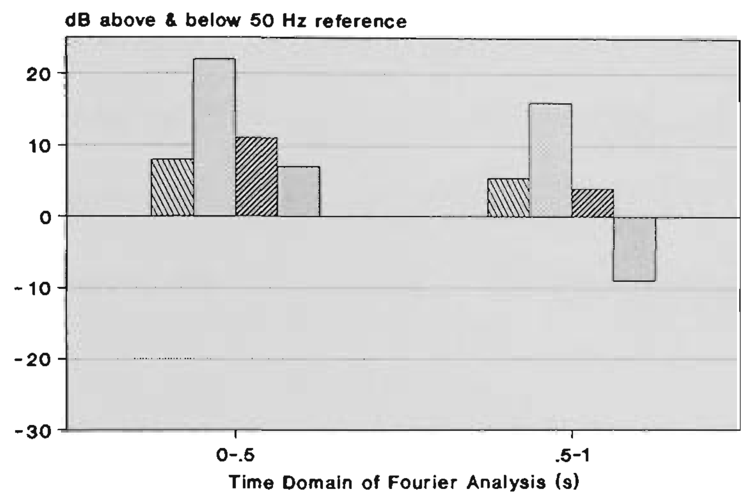

500 ms increments over 1 sec.

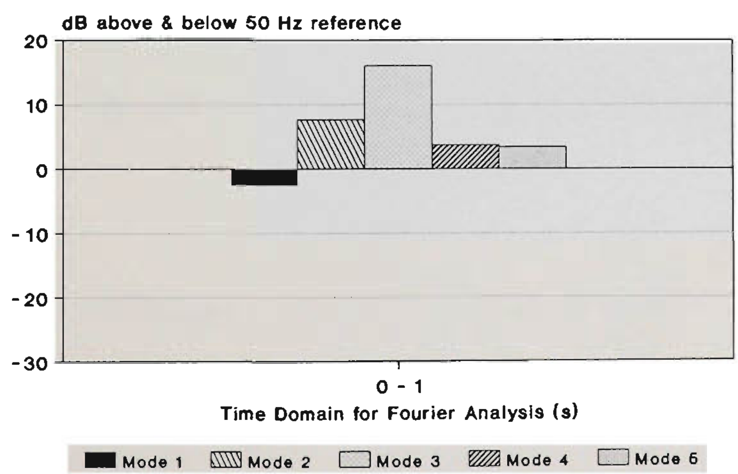

Full 1 sec.

Figure 3.3.3.6 Modal amplitudes of consecutive samples within the vibration profile for cantilever S.

3.4 A photo-thermoelastic model of laser-induced structural flexing

A theoretical model is now presented to explain the observed excitation and vibration of the cantilevers by sub-ablative laser pulses. This model involves the heating of the material surface by the laser pulse and the rapid production of a transient thermal gradient in the irradiated material, which causes differential expansion and bending. Thus, the laser pulse produces a rapid thermally-induced bending moment, and this acts as the driving term in the differential equation describing the vibrational motion. This driving term stimulates vibrational frequencies close to the dominant frequency in the Fourier spectrum of the induced bending moment, as well as at the modal frequencies of the structure. The sections which follow contain calculations (which must necessarily involve a number of simplifying assumptions to make them practicable) for the laser-induced temperature distribution in the irradiated structure and the bending moment that this creates. Where possible quantitative comparisons are made between calculations and experimental measurements.

The heat transfer within a solid, as a result of high-power laser radiation absorbed at the surface, may be calculated approximately using the equation for heat conduction in a semi-infinite solid. [Carslaw and Jaeger 1946, Ready 1971] The differential equation for the three-dimensional heat flow in a semi-infinite slab is

$$\nabla^2 T(x,y,z,t) - \frac{1}{\kappa}\frac{\partial T(x,y,z,t)}{\partial t} = -\frac{Q(x,y,z,t)}{K}, \qquad \text{eq. 3.4.1}$$

where T is the temperature rise as a function of position (planar co-ordinates (x,y) and depth (z)) and time, κ is the thermal diffusivity, K the thermal conductivity, and Q(x,y,z,t) is the rate of heat production per unit volume. If the rate of heat production in the surface material is high enough, the temperature at the surface of the material will exceed the boiling temperature and vaporise. This is the ablation regime (discussed in section 3.2), in which material is ejected from the surface and an impulsive reaction is provided to the irradiated body. However, if the rate of heat production is low, and the temperature rise at the surface is below the ablation threshold, only localised thermal expansion will occur (the thermoelastic regime).

The pulse shape of a normal mode Nd:glass laser, which is shown in figure 2.1.1, is rather complicated due to the presence of relaxation oscillations. In order to simplify the calculations, the pulse shape was approximated by fitting straight lines to the rising and falling edges of the pulse. In so doing, the value of the power profile (P(t)), for a laser of any given total pulse duration (t_p) can be easily evaluated for $t/t_p \leq 1$. $P(t) = 0$ for $t/t_p > 1$. The triangular approximation to the power profile and actual laser profile are superimposed in figure 3.4.1.

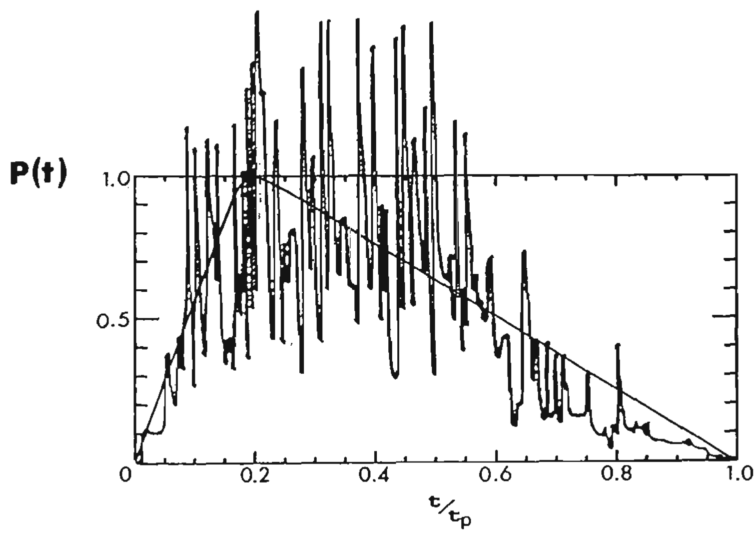

Figure 3.4.1. Laser profile superimposed with a triangular approximation.

The temperature distribution in an isotropic material after irradiation by a laser pulse of Gaussian radius, d, has been described in terms of a number of dimensionless parameters as[Ready, 1971]

$$\Theta(\zeta,\eta,\Upsilon) = \int_0^{\Upsilon} \frac{P(\Upsilon-\Upsilon')\exp[-\zeta^2/(\Upsilon'+1)]\exp[-\eta^2/\Upsilon']}{\sqrt{\Upsilon'}\ (\Upsilon'+1)}\, d\Upsilon' , \qquad \text{eq. 3.4.2}$$

where $\Upsilon = 4\kappa t/d^2$, $\Upsilon_p = 4\kappa t_p/d^2$, $\zeta = r/d$, $\eta = z/d$ and $\Theta = 2\sqrt{\pi}\ KT/(d\ F_{max})$ are the dimensionless temperature (Θ), radius (ζ), depth (η) and time (Υ) parameters involving the temperature difference above the ambient temperature (T), the radial distance from the centre of the laser irradiation (r), and the depth in the material (z). F_{max} is the maximum power density absorbed at the centre of the Gaussian laser spot which is the maximum power density in the laser pulse multiplied by an absorption coefficient (1-R(T)). This relationship was formulated for a semi-infinite solid and so holds true, in this application, until the heat reaches the rear surface of the irradiated sample.

If the surface of a semi-infinite solid (z = 0) is instantly heated to, and maintained at, a constant temperature difference (T_0) above the ambient temperature, then the temperature difference (T(z)) between the ambient temperature at $z = \infty$ and that at a specific depth (z) is simply[Carslaw and Jaeger, 1946]

$$T(z, t) = T_0 \; erfc \frac{z}{2\sqrt{\kappa t}} . \qquad \text{eq. 3.4.3}$$

The complement of the error function (erfc) is zero when $z/\, 2\sqrt{(\kappa t)} = 2$. Values of z(t) and t(z) satisfying this condition give the depth of heat penetration within the material for a particular time or the time taken for the heat to reach a particular depth. Thus, the time taken for heat to propagate from the front surface, which is maintained at a steady temperature, to the rear surface of a plate (z = h, where h is the thickness of the material) is simply

$$t = \frac{h^2}{16\kappa} . \qquad \text{eq. 3.4.4}$$

Hence equation 3.4.2 can be considered valid, in our application, for $t < h^2/16\kappa$ seconds. This condition is rather conservative as it treats the breakdown of equation 3.4.2 as being when the temperature of the rear surface begins to rise above ambient. Ready (1971) used the conditions $z/\, 2\sqrt{(\kappa t)} = 1$ and $t = h^2/4\kappa$, which correspond to the temperature of the rear surface reaching T_o/e, as the limiting conditions for validity of equation 3.4.2.

Equation 3.4.2 was solved numerically and then converted, using the relationship

$$T(r,z,t) = \Theta(\zeta,\eta,\Upsilon)\cdot d\ F_{max}\ /(2\sqrt{\pi}\ K), \qquad \text{eq. 3.4.5}$$

to obtain the temperature variation with time at any radius or depth in the cantilevers A and S during, and after, the laser irradiation. These results should give a reasonable description of the thermal behaviour for the aluminium sample over the first 2.5 ms ($h^2/16\kappa$ ~ 6.5 ms), but are less accurate for the thin steel ($h^2/16\kappa$ ~ 0.3 ms). Table 3.4.1 gives the values and constants used in the calculations. Profiles giving the temperature as a function of time in the front, middle and rear planes below a surface point at the centre of the laser irradiation are shown in figure 3.4.2. These were calculated from equations 3.4.2 and 3.4.5 for 3 mm aluminium and 254 μm stainless steel.

SYMBOL	STAINLESS STEEL	ALUMINIUM
κ	121×10^{-7} m^2.s^{-1}	860×10^{-7} m^2.s^{-1}
K	25 W.m^{-1}.K^{-1}	236 W.m^{-1}.K^{-1}
α	16×10^{-6} K^{-1}	23×10^{-6} K^{-1}
E	2.15×10^{11} N.m^{-2}	7.3×10^{10} N.m^{-2}
I	1.6×10^{-14} m^4	2.7×10^{-11} m^4
ρ	7.8×10^3 kg.m^{-3}	2.7×10^3 kg.m^{-3}
R(T)	~ 0.6 [Ready 1971]	~ 0.8 [Ready 1971]
$d = 0.5$ cm, $\zeta = 0$, $t_p = 1$ ms, $F_{max} = 1.3 \times 10^9$ W.m^{-2}		

Table 3.4.1. Material constants and laser parameters used in the temperature calculations

(a)

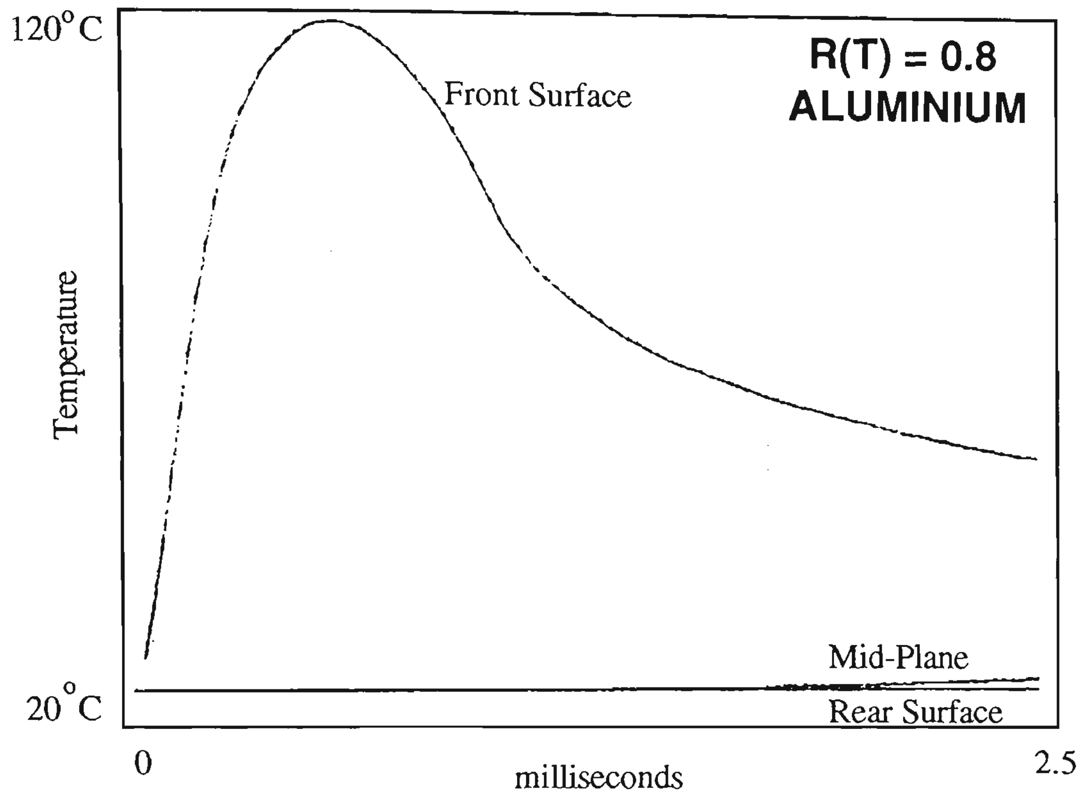

(b)

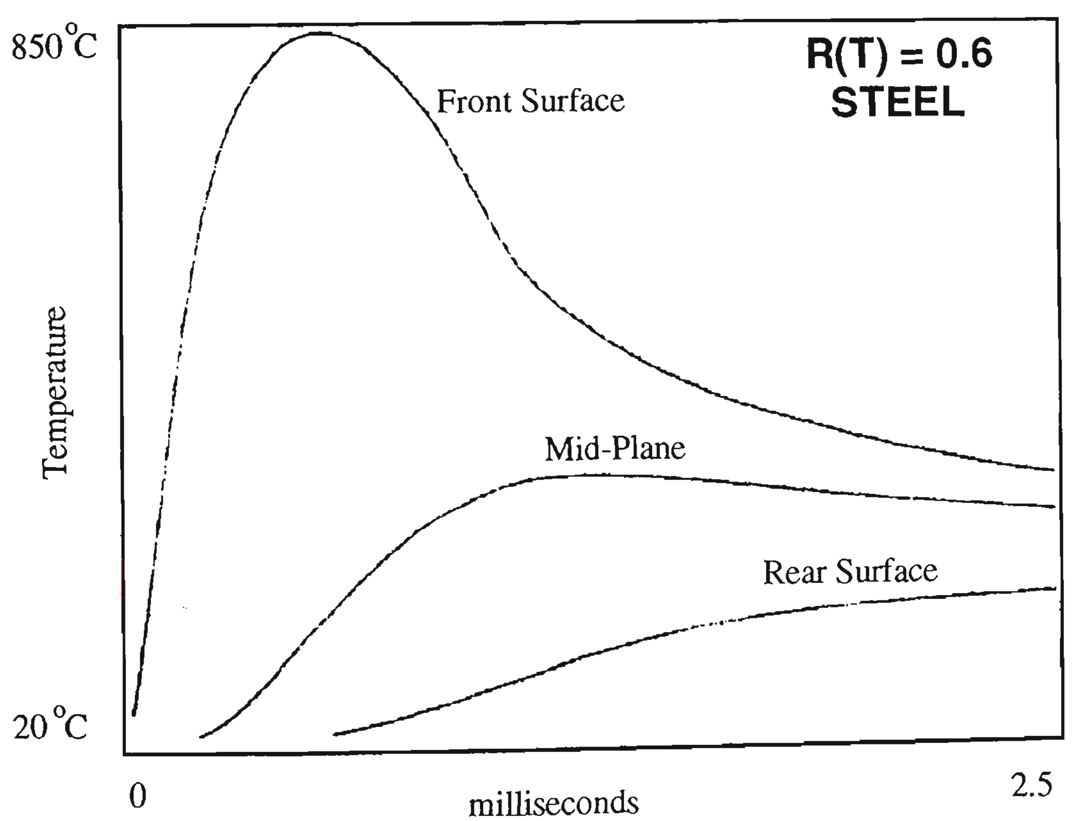

Figure 3.4.2. Temperature profiles, T(z,t), following laser irradiation of (a) 3 mm thick aluminium and (b) 254 μm stainless steel.

These temperature profiles were then used to predict the bending behaviour due to the time dependent thermal expansion of the irradiated cantilevers. The mechanical effect due to heating the front surface of a small element of length (L) within a simple beam of given width (b) and thickness (h) can be readily calculated by dividing the beam into a number of thin layers as shown in figure 3.4.3. If the position of an individual layer is described by a distance (χ) from the centre of that layer to the mid-plane of the cantilever, and the thickness of each layer is δh, then the mean temperature of the layer ($T(\chi,t)$) is given by

$$T(\chi, t) = \frac{1}{\delta h} \int_{\chi - \frac{\delta h}{2}}^{\chi + \frac{\delta h}{2}} T(z, t)\, dz \,. \qquad \text{eq. 3.4.6}$$

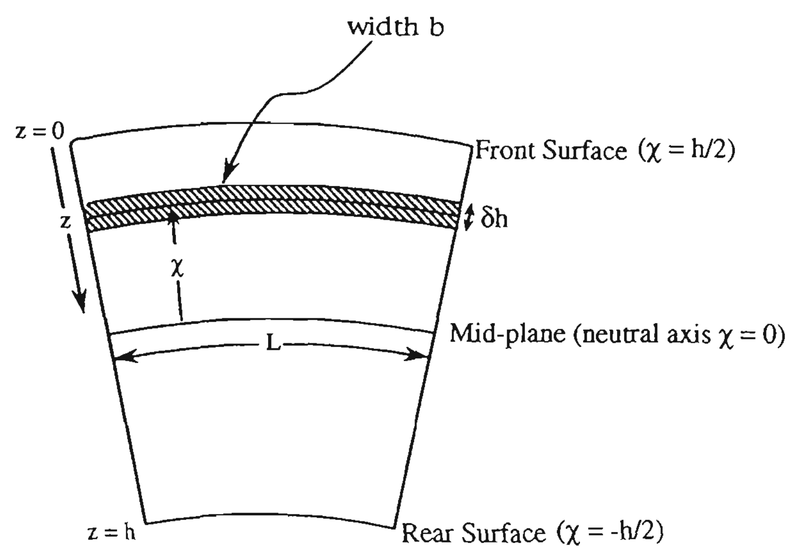

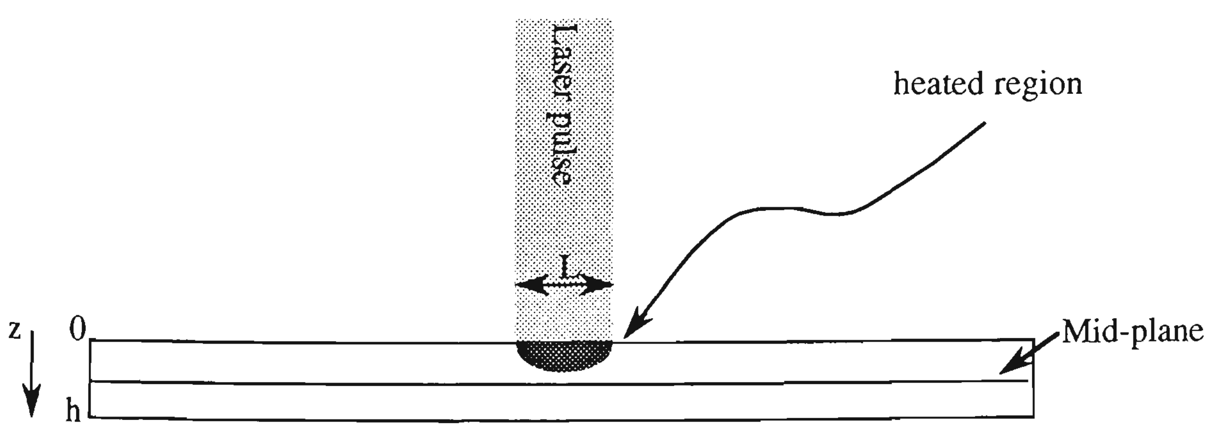

Figure 3.4.3. Diagram showing a thermally-bent cantilever as viewed from above with the laser beam horizontal.

If the temperature of each layer is $\Delta T(\chi)$ above the temperature of the rear surface, then the linear thermal expansion (ΔL) of the layer relative to the rear surface is $\alpha\, L\, \Delta T(\chi)$, where α is the thermal expansion co-efficient. This expansion produces a thermal strain ($\varepsilon(\chi)$) given by

$$\varepsilon(\chi) = \Delta L/L = \alpha\, \Delta T(\chi).$$

The equivalent force ($H(\chi)$) which would produce the same bend and strain as this thermal expansion is

$$H(\chi) = \text{stress} \times \text{area} = E\, \varepsilon(\chi)\, b\, \delta h \ ,$$

where E is the Young's modulus. The moment of this force ($M(\chi,t)$) about the mid-plane is

$$M(\chi,\, t) = \chi\, H(\chi) = b\, E\, \chi\, \delta h\, \varepsilon(\chi,\, t) = \alpha b E \chi\, \delta h\, \Delta T(\chi,\, t)\ . \qquad \text{eq. 3.4.7}$$

The total thermally-induced bending moment for the entire beam is therefore

$$M(t) = \alpha b E \int_{-\frac{h}{2}}^{\frac{h}{2}} \Delta T(\chi,\, t)\, \chi\, d\chi\ . \qquad \text{eq. 3.4.8}$$

This result is in agreement with those obtained by other workers using more complex methods of derivation.[Parkus 1968, Hane et al. 1988a&b, Hane and Hattori 1990] Equation 3.4.8 has been evaluated for 1000 time intervals between the start of the laser pulse and 50 ms, using the thermal data calculated by equation 3.4.5 with 100 layers over the depth of cantilevers S and A. The results of this calculation, over 2.5 ms, are shown in figure 3.4.4. These bending moment profiles were then used to predict the flexing rise times ($1/e\times M_{max}$ to M_{max}, where M_{max} is the maximum bending moment) and fall times (M_{max} to $1/e\times M_{max}$) for both cantilevers.

The predicted rise and fall times of thermal flexing can now be compared to the experimental flexing times measured from the vibration records shown in figures 3.3.2.3 and 3.3.2.4. These times are presented in table 3.4.2. The rise times are in reasonable agreement for both samples, despite the limitations of the calculations. However, there is clearly a marked difference in the

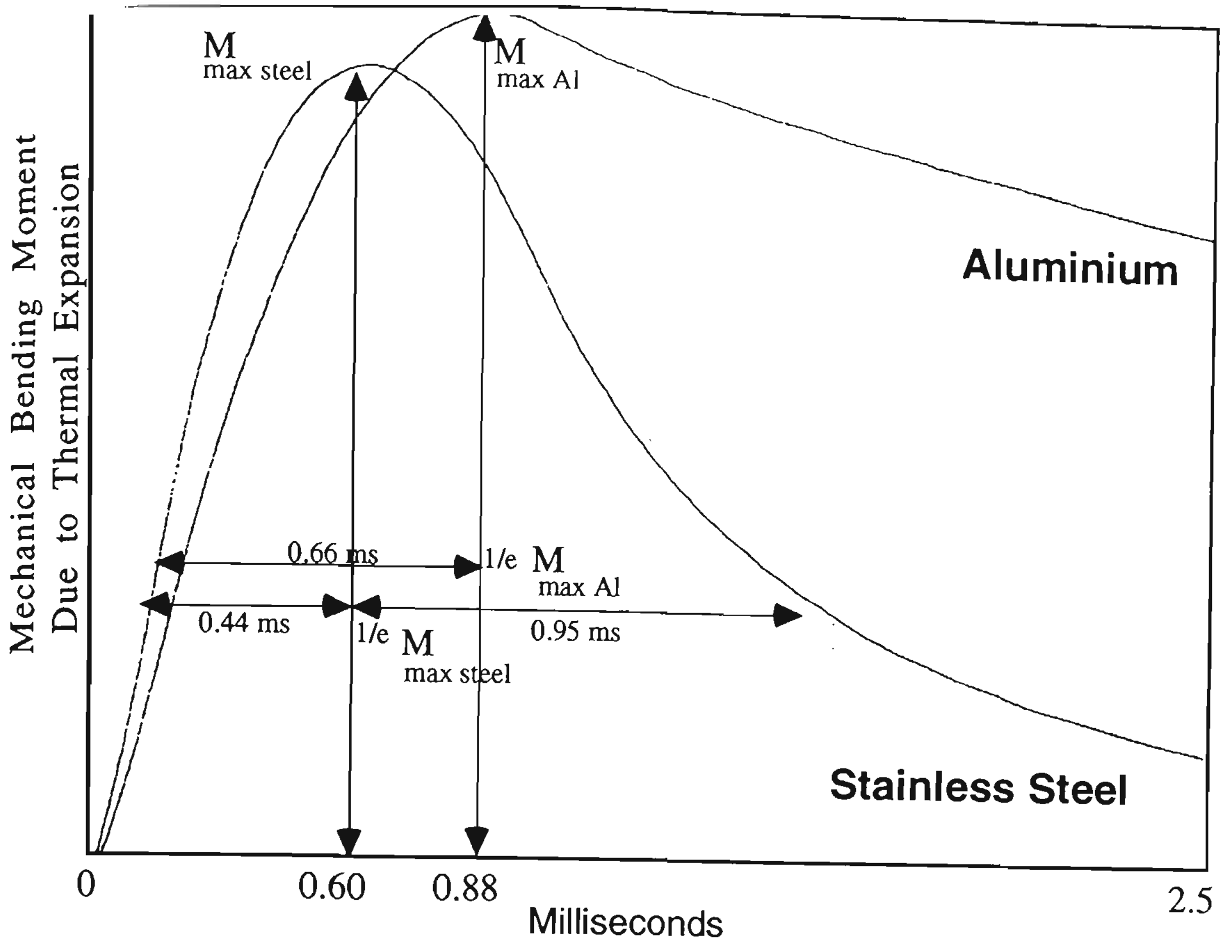

Figure 3.4.4. Moment profiles for 3 mm thick aluminium and 254 μm thick stainless steel beams after thermal excitation.

fall times, since the measured fall times are much shorter than those calculated. Indeed, the fall times are quite close to the rise times. This discrepancy is simply because mechanical vibration has been initiated by the thermal bending. The cantilever's return to mechanical equilibrium is not just controlled by the relaxation of the non-uniform temperature distribution by thermal diffusion, as is the case with the induced bending moment, but also on the flexural rigidity of the cantilever and its mechanical response to the thermal bending moment. This accounts for the different flexing behaviour of the two cantilevers and the difference between calculated and experimental fall times. The matter is discussed in more detail in the next section.

		ALUMINIUM	STAINLESS STEEL
CALCULATION	Rise time Fall time	0.66 ms 11.5 ms	0.44 ms 0.95 ms
EXPERIMENT	Rise time Fall time	0.50 ms 0.45 ms	0.35 ms 0.26 ms

Table 3.4.2 Calculated and experimental rise and fall times of the flexing cantilevers.

3.4.1 Damped harmonic oscillation under the influence of an over-damped bending moment

The purpose of this discussion is to explain the behaviour of a clamped-free cantilever during and after the period of photo-thermoelastic flexing. The actual thermal flexing has been observed directly (figures 3.3.2.3 and 3.3.2.4) and previously compared to the bending moment predicted by the thermal model shown in figure 3.4.4. It was found that only the rise times were in good agreement. To understand the origin of the difference in relaxation times, the differential equations describing the vibrations induced by a time-dependent applied bending moment are presented. The thermal driving term in this differential equation will be approximated by an over-damped harmonic bending moment. The action of this moment on the clamped-free cantilever is similar to that of an applied transient harmonic force.[Bishop and Johnson, 1960] However, whereas a linear displacement of the cantilever is produced by an applied force, this applied moment will produce an angular displacement as shown in figure 3.4.1.1.

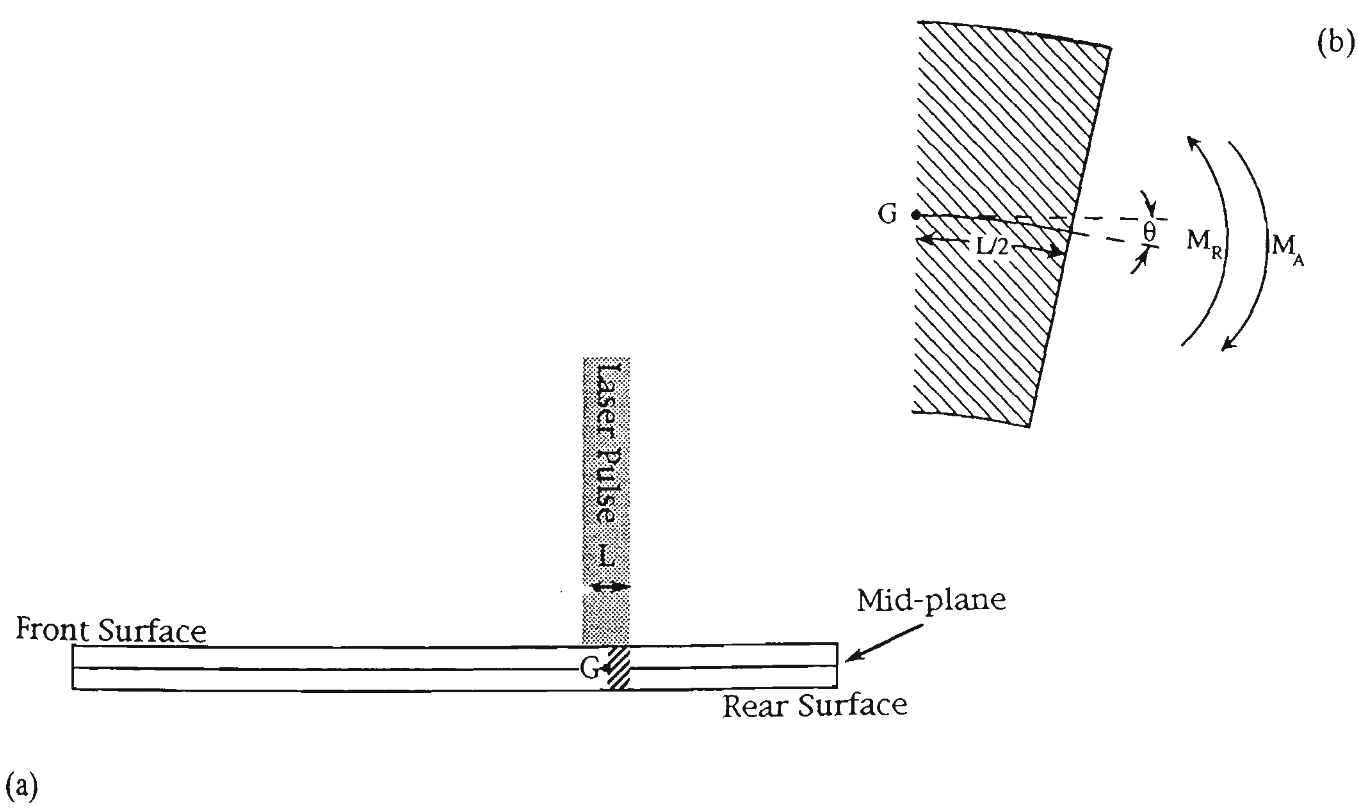

Figure 3.4.1.1 Schematic diagram of (a) a laser heated cantilever (heating symmetric about plane through G) and (b) an expanded section (hatched) directly below the irradiated surface which has been thermally bent.

Consider a cantilever which vibrates in a horizontal plane (so that weight forces can be ignored) after its surface has been heated by a laser pulse. The laser pulse is directed at the centre of the front surface. The excitation is symmetric about the mid-plane passing through G, where G is the centre of mass of the heated element located directly behind the centre of the laser spot. The dynamic equation of rotation of the half-section about an axis through G (the shaded region shown in figure 3.4.1.1) may be analysed in terms of the angular displacement of the mid-plane (θ) as a function of time. Figure 3.4.1.1(b) shows two moments; M_A is the applied moment due to laser heating as described in section 3.4, and M_R is the restoring moment which is taken as being directly proportional to θ (equation 3.1.4). If $\mathbf{I}_G$ is the moment of inertia of the shaded section about the mid-plane axis through G, then the resultant moment acting on this section (clockwise positive) can be equated to the product of $\mathbf{I}_G$ and the angular acceleration. Hence,

$$\mathbf{I}_G \ \partial^2\theta/\partial t^2 = M_A(t) - M_R(t) \qquad \text{eq. 3.4.1.1}$$

or

$$\mathbf{I}_G \ \partial^2\theta/\partial t^2 + M_R(t) = M_A(t). \qquad \text{eq. 3.4.1.2}$$

The applied moment has been calculated using the thermal model developed in the previous section (figure 3.4.4). This applied moment can be approximated by an equation of the form

$$M_A(t) = C\, e^{\frac{-t}{\tau}} \sin\omega_d t \equiv C_1\, e^{-(\frac{1}{\tau} + i\,\omega_d)t} + C_2\, e^{-(\frac{1}{\tau} - i\,\omega_d)t}, \qquad \text{eq. 3.4.1.3}$$

and this function is shown in figure 3.4.1.2. By varying C, τ and ω_d this equation can be used to fit the curves of figure 3.4.4 as shown in figure 3.4.1.3. The values of τ and ω_d used to fit the thermal moments are shown in the legend of figure 3.4.1.3 ($\omega_d/2\pi$ is about 400 Hz for aluminium and 600 Hz for steel). In equation 3.4.1.3, $C_2 = -C_1^*$ (* denotes the complex conjugate) and so C is equal to $i\ 2C_1$. ω_d is the driving frequency and τ is the time constant of the over-damped thermal relaxation. The applied moment has been framed in this manner to allow for complex terms and to introduce a driving frequency term (ω_d) which may excite a specific frequency of oscillation within the cantilever. When the applied moment has decayed away, the cantilever will vibrate freely.

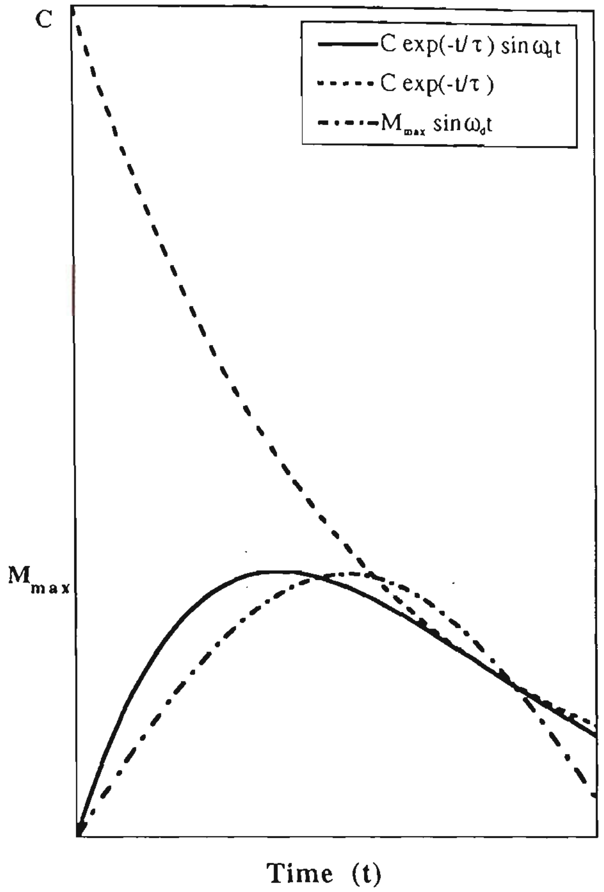

Figure 3.4.1.2. The applied driving moment of equation 3.4.1.3. The exponential and harmonic terms are also shown separately.

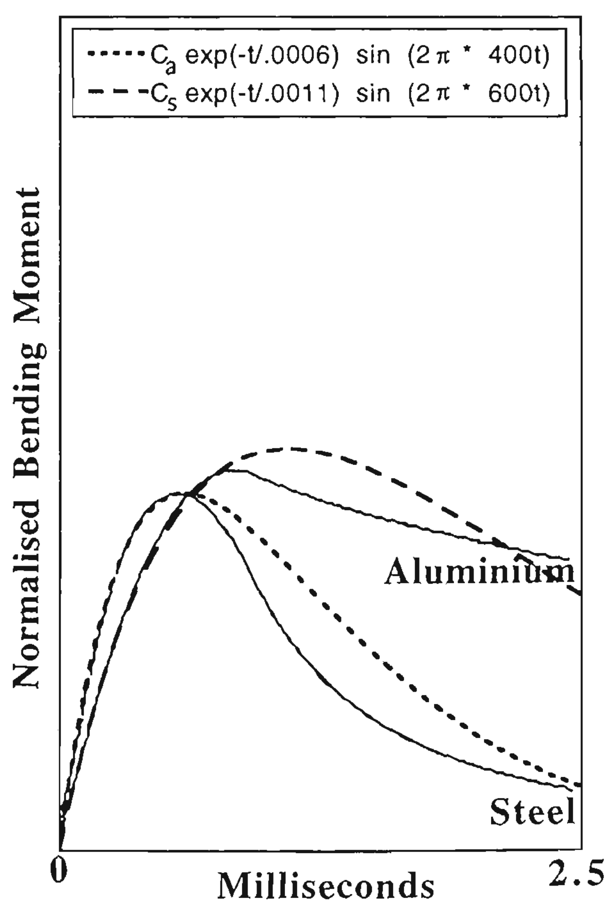

Figure 3.4.1.3. The calculated thermal moments and their approximations. The values of τ and ω_d used to fit these curves are shown in the legend.

The differential equation governing the damped free oscillation of any point on the mid-plane of the cantilever can be written as

$$\frac{\partial^2\theta}{\partial t^2} + \frac{B_n}{I_G}\frac{\partial\theta}{\partial t} + \frac{A_n}{I_G}\theta = 0 , \qquad \text{eq. 3.4.1.4}$$

where B_n is a positive co-efficient describing modal damping and A_n is a mode dependent constant determined by the elasticity, mass and physical dimensions of the cantilever. If B_n is small (so that non-linear effects are negligible) and $1/\gamma = B_n/2I_G$, then the general solution to this equation is that of damped angular simple harmonic motion;

$$\theta(t) = \sum_n (X_1 e^{-(\frac{1}{\gamma} + i\omega_n')t} + X_2 e^{-(\frac{1}{\gamma} - i\omega_n')t}) , \qquad \text{eq. 3.4.1.5}$$

where X_1 and X_2 are amplitude constants and ω_n' are the damped modal frequencies of free vibration (which are, in turn, determined by the boundary conditions). The natural (undamped) angular frequencies of the cantilever (ω_n) are given by $\sqrt{(A_n / I_G)}$. The natural frequencies of oscillation are the same for both angular and linear displacements of the cantilever and were discussed in section 3.1. The natural frequencies are reduced by the internal mechanical damping to give the modal frequencies of damped oscillation (ω_n'):

$$\omega_n'^2 = \omega_n^2 - \frac{1}{\gamma^2} . \qquad \text{eq. 3.4.1.6}$$

The response of the cantilever to the laser pulse can be described by the driven oscillation:

$$\frac{\partial^2\theta}{\partial t^2} + \frac{2}{\gamma}\frac{\partial\theta}{\partial t} + (\omega_n'^2 + \frac{1}{\gamma^2})\theta = C_1 e^{-(\frac{1}{\tau} + i\omega_d)t} + C_2 e^{-(\frac{1}{\tau} - i\omega_d)t} . \qquad \text{eq. 3.4.1.7}$$

The solution to this equation is the sum of two parts; (a) the homogeneous solution and (b) the particular solution. The homogeneous solution is given in equation 3.4.1.5, and the particular solution may be found by substituting a trial function of the form

$$\theta = Y_1 e^{-(\frac{1}{\tau} + i\,\omega_d)t} + Y_2 e^{-(\frac{1}{\tau} - i\,\omega_d)t} \qquad \text{eq. 3.4.1.8}$$

into equation 3.4.1.7.

After collecting like terms, Y_1 and Y_2 have values

$$Y_1 = \frac{C_1}{(\omega_n'^2 - \omega_d^2 + \frac{1}{q^2}) - \frac{i\,2\omega_d}{q}}\,, \qquad Y_2 = \frac{C_2}{(\omega_n'^2 - \omega_d^2 + \frac{1}{q^2}) + \frac{i\,2\omega_d}{q}}\,,$$

eq. 3.4.1.9

where $1/q = 1/\gamma - 1/\tau$. Clearly, $Y_2 = -Y_1^*$. Each term in ω_n' for the homogeneous solution has an associated particular solution term since Y_1 and Y_2 depend on ω_n'. The co-efficients X_1 and X_2 of the homogeneous part of the general solution can be found on application of the boundary conditions $\theta(0) = 0$ and $\partial\theta(0)/\partial t = 0$. These boundary conditions were applied to each term in the series solution. If Y_1 is written in polar form as $Y\,e^{i\,\phi}$, where ϕ is the phase of Y_1, the magnitude, Y, is equal to

$$Y = \frac{|C_1|}{\sqrt{(\omega_n'^2 - \omega_d^2 + \frac{1}{q^2})^2 + \frac{4\omega_d^2}{q^2}}}\,.$$

eq. 3.4.1.10

The general solution (homogeneous and particular parts) can then be written as

$$\theta = \sum_n Y\,[(\frac{1}{\omega_n'}\,(\frac{1}{q}\sin\phi - \omega_d\cos\phi) - i\,\sin\phi)\,e^{-(\frac{1}{\gamma} + i\,\omega_n')t} + (-\frac{1}{\omega_n'}\,(\frac{1}{q}\sin\phi - \omega_d\cos\phi) - i\,\sin\phi)\,e^{-(\frac{1}{\gamma} - i\,\omega_n')t} - i\,2e^{-\frac{t}{\tau}}\sin(\omega_d t - \phi)]$$

eq. 3.4.1.11

The real parts of this solution cancel leaving just an imaginary term, which is consistent with the condition $C_2 = -C_1^*$. Equation 3.4.1.11 is simplified to

$$\theta = -2\sum_n Y\,[\,e^{-\frac{t}{\gamma}}\,(\frac{\sin\omega_n' t}{\omega_n'}\,(\frac{1}{q}\sin\phi - \omega_d\cos\phi) + \sin\phi\cos\omega_n' t) + e^{-\frac{t}{\tau}}\sin(\omega_d t - \phi)]\,.$$

eq. 3.4.1.12

The dominant factor in the magnitude of each of the frequency terms in this series is the magnitude of Y (equation 3.4.10). To a first approximation, the frequency dependence of the solution is given by Y/ω_n'. The dependence of equation 3.4.1.12 on the modal frequencies can now be discussed for three specific cases; (a) for modal frequencies much less than the driving frequency ($\omega_n' \ll \omega_d$), (b) for modal frequencies approximately equal to the driving frequency ($\omega_n' \approx \omega_d$) and (c) for modal frequencies much greater than the driving frequency ($\omega_n' \gg \omega_d$).

(a) When the driving frequency is significantly greater than the modal frequency:

$$Y \simeq \frac{|C|}{\sqrt{(\frac{1}{q^2} - \omega_d^2)^2 + \frac{4\omega_d^2}{q^2}}} . \qquad \text{eq. 3.4.1.13}$$

In this case all modes have approximately the same amplitude of vibration.

(b) For modal frequencies close to the driving frequency:

$$Y \simeq \frac{q\ |C|}{\sqrt{(\frac{1}{q^2} + 4\omega_d^2)}} . \qquad \text{eq. 3.4.1.14}$$

(c) For modal frequencies significantly greater than the driving frequency:

$$Y \simeq \frac{|C|}{(\omega_n'^2 + \frac{1}{q^2})} . \qquad \text{eq. 3.4.1.15}$$

The behaviour of the cantilever can thus be seen to depend on the relationship between the driving frequency of the thermal bending moment and the natural frequencies of the vibrational modes. When the driving frequency is significantly less than the fundamental frequency of oscillation, equation 3.4.1.15 applies. The applied moment will preferentially excite the fundamental mode of vibration and the solution to equation 3.4.1.12 can be approximated by just a single term at the fundamental frequency:

$$2\sin\phi\ Y\, [e^{-\frac{t}{\tau}} - e^{-\frac{t}{Y}} (\cos\omega_1' t + \frac{1}{\omega_1' q} \sin\omega_1' t)] . \qquad \text{eq. 3.4.1.16}$$

Additionally, if the mechanical damping is large or the thermal relaxation time constant is long so that $1/\gamma$ is large in comparison to $1/\tau$, the above equation is dominated by the $e^{-t/\tau}$ term (thermal relaxation). This condition is known as quasistatic thermoelastic bending.[Parkus, 1968]

When the driving frequency is close to one of the modal frequencies of oscillation, comparison of equations 3.4.1.10 and 3.4.1.14 shows that this mode will have the greatest amplitude (the resonant condition). In such a case, the solution to equation 3.4.1.12 can again be approximated by just a single term at the resonant frequency;

$$-2\,Y\,[\,e^{-\frac{t}{\gamma}}\,(\,\frac{\sin\omega_d t}{\omega_d}\,(\frac{1}{q}\sin\phi\;-\;\omega_d\cos\phi)\;+\;\sin\phi\cos\omega_d t)\;+\;e^{-\frac{t}{\tau}}\,\sin(\omega_d t\;-\;\phi)]\;.$$

eq. 3.4.1.17

The solution is therefore a damped oscillation at a single frequency equal to the driving frequency.

Only lower-order modes of oscillation need to be considered in the case where the driving frequency is large with respect to the fundamental frequency, because of the proportionality of the solution in equation 3.4.1.12 to $1/\omega_n'$. For modes of oscillation significantly less than the driving frequency, equation 3.4.1.13 indicates that all modes have approximately the same amplitude. The solution in this case does not simplify, but only the sum of a small number of lower-order modes need to be considered. Furthermore, since the higher frequency modes dissipate energy at a greater rate, the contribution of these modes to the amplitude of the vibrating cantilever will decrease more rapidly than that of the lower frequency modes.

So far, only the temporal behaviour of the cantilever has been discussed. It takes time for the travelling waves produced by the thermal excitation of some arbitrary point along the cantilever to reflect from both ends of the cantilever and then superpose to form a standing wave pattern in the cantilever. The profile of an arbitrary travelling wave can be treated as the Fourier sum of waves at the frequencies which correspond to the modes of free vibration in the cantilever. The propagation velocity (v) of such a transverse travelling wave of angular frequency, ω, on a cantilever of thickness, h, is given by[Elmore and Heald, 1969]

$$v = \sqrt[4]{\frac{Eh^2 \omega^2}{12\rho}}, \qquad \text{eq. 3.4.1.18}$$

and therefore varies with the square root of the angular frequency (this equation can also be derived from the value of, a, in equation 3.1.8). The time taken to establish a standing wave pattern for a particular frequency is then approximately given by the time required for the travelling wave to transit twice the length of the cantilever ($2L/v$).

The resultant standing wave pattern is obtained from the superposition of the two travelling waves reflected from the cantilever ends and the distortion of the cantilever produced by the initial driven oscillation. For the case of free vibration, the bending moment characteristic profile can be obtained using equations 3.1.4, 3.1.9 and 3.1.10(c) and is given by

$$M(x,t) = EI \sum_n \beta_n^2 \left(A\sinh\beta_n x + B\cosh\beta_n x - C\sin\beta_n x - D\cos\beta_n x\right) \left(\alpha_{1n}\sin\omega_n t + \alpha_{2n}\cos\omega_n t\right) .$$

eq. 3.4.1.19

If the location chosen for laser irradiation, and therefore the site of the thermal bending moment, corresponds to an antinode of the bending moment profile for a particular frequency of vibration in the above equation, then energy can easily be supplied to that particular mode. Similarly, if the site of excitation corresponds to a node of a particular frequency in the bending moment profile, then that frequency of vibration cannot be driven by the excitation. This assumes however, that the distortion of the cantilever by the excitation has not relaxed (thermally or mechanically) before the time required for the establishment of the standing wave pattern.

In order to excite as many vibrational modes as possible upon irradiation by a single unfocused laser pulse, the initial excitation must be at a position along the cantilever which is close to as many modal antinodes as possible. Inspection of the bending moment profile for the first five modes of vibration (figure 3.1.7(a)), indicates that thermal excitation of the region between 0.75 and 0.90 of the cantilever length will excite each of those five modes. An optimum position of 0.85L can be chosen which is the same as that found empirically in section 3.3.1.

The temporal excitation of cantilever A is best described by case (b), for which the driving frequency was close to specific mode(s) of vibration ($\omega_n' \approx \omega_d$). The laser-induced thermal moment is applied to cantilever A for a period of about 12 ms (the sum of rise and fall times given in table 3.4.2). The driving frequency was approximated from both the rise time of this moment (also table 3.4.2) and the fitted curve (figure 3.4.1.3) to be about 400 Hz (2.5×10^3 rad.s^{-1}). The second and third vibrational modes of cantilever A have frequencies of 161 Hz and 454 Hz respectively. These modes are therefore well-driven by the laser pulse. Hence, the vibration of cantilever A is determined by the driving frequency ω_d as described by equation 3.4.1.17. These effects can be easily seen in the vibration profile of the cantilever following laser irradiation at 0.85L (figure 3.3.2.3) in which the third mode of vibration is clearly evident immediately following the laser pulse, and also in the sectioned modal analysis of these vibrations (figure 3.3.3.5) in which modes 2 and 3 are clearly dominant during the first 100 ms following the laser irradiation.

Using the material constants given in table 3.4.1, the thickness and modal frequencies of cantilever A, the propagation velocities of modes 2 to 5 were calculated from equation 3.4.1.18 to be 68, 113, 160 and 205 m.s^{-1} respectively. For a cantilever of length 30 cm, the time taken for all of these modes to establish a standing wave pattern is less than the duration of the applied thermal moment (about 12 ms). Therefore, the amplitude of vibration for modal frequencies which had nodes at the irradiation site were suppressed with respect to the amplitudes of the other modes of free vibration. The effectiveness of mode suppression in cantilever A, using the unfocused laser pulse, was shown in figure 3.3.3.2.

The thermal moment generated by the laser in the 254 μm steel shim was calculated to have a duration of about 1.4 ms and a driving frequency of about 600 Hz or 3.8×10^3 rad.s^{-1} (figure 3.4.4, table 3.4.2 and figure 3.4.1.3). The driving frequency was close to the eleventh mode of vibration (about 650 Hz), and cantilever S was observed to oscillate significantly at around this frequency for the first 10 to 20 milliseconds following the laser irradiation (figure 3.3.2.4). However, this high frequency of oscillation was well away from the lower-order modes (between 2 Hz and 60 Hz for modes 1 to 4) and the driving frequency was rapidly damped. Because the frequencies of the lower-order modes of vibration were much less than the driving frequency, as in case (a), the lower-order modes each received about the same excitation from the laser irradiation (as is clearly evident in the FFT of the first 100 ms of vibration shown in figure 3.3.3.6). Figures 3.3.3.5 (progressive FFT for cantilever A) and 3.3.3.6 (progressive FFT for cantilever S) both clearly show the more rapid attenuation of higher-order modes of free vibration with time.

Again, from the modal frequencies, thickness and material constants of cantilever S, the modal propagation velocities for modes 2, 3 and 4 are 5.3, 8.2 and 11.8 m.s^{-1} respectively. For a cantilever of length 31.5 cm, the time taken for these modes to establish a standing wave pattern is significantly greater than the life-time of the applied thermal moment (which in the case of the steel shim is only about 1.4 ms). Consequently, standing waves were not formed at these frequencies of vibration before the laser excitation had finished, and after which the cantilever vibrated freely in all its vibrational modes. The inability of the unfocused laser pulse to suppress selected modes of vibration in the steel cantilever by targeting nodes of the bending moment profile is evident in figure 3.3.3.4.

The experiments discussed in this chapter have supported the conclusion that the mechanism for single laser pulse excitation of structures is the rapid production of a localised photo-thermoelastic bending moment at the irradiation site. This form of excitation has been shown to be most efficient when the laser pulse length is chosen so that the period of the initial thermal flexing is well-matched to the lower-order modal frequencies of the irradiated structure. In addition, suppression of selected vibrational modes is only possible when the duration of the photo-thermoelastic bending moment is long enough to allow a standing wave to be formed before it has relaxed.

Chapter 4

Photo-thermoelastic excitation for modal analysis

4.1 Photo-thermoelastic excitation and modal analysis of a large structure using a single laser pulse

Photo-thermoelastic excitation by a single laser pulse of power density below the surface ablation threshold of the irradiated material has been demonstrated for clamped-free aluminium and steel cantilevers. It is possible to apply this excitation technique to larger and more practical structures for the purpose of modal analysis and non-destructive testing. As an example of how the photothermal flexing can be used to efficiently excite much larger structures, the unfocused laser pulse was used to excite the same 57 kg Mercedes-Benz steel truck-wheel rim that had been previously excited by ablative laser techniques (see section 3.2).

The truck rim was suspended by twelve springs (attached to the inner rim) from a vertical mount. A Brüel & Kjaer Type 8200 calibrated accelerometer was used to monitor the surface vibration of the rim since, being a contact sensor, it was not subject to the problems experienced with the optical proximity sensor due to "sway" (a millimetre or so), in the mounting arrangement. The inherent sway of the spring mounted system after laser irradiation (although quite small with respect to the size of the structure) made the use of the fibre optic proximity sensor impractical since this sensor had to be mounted within 0.5 mm of the vibrating surface. The experimental set-up is shown in plate 4.1.

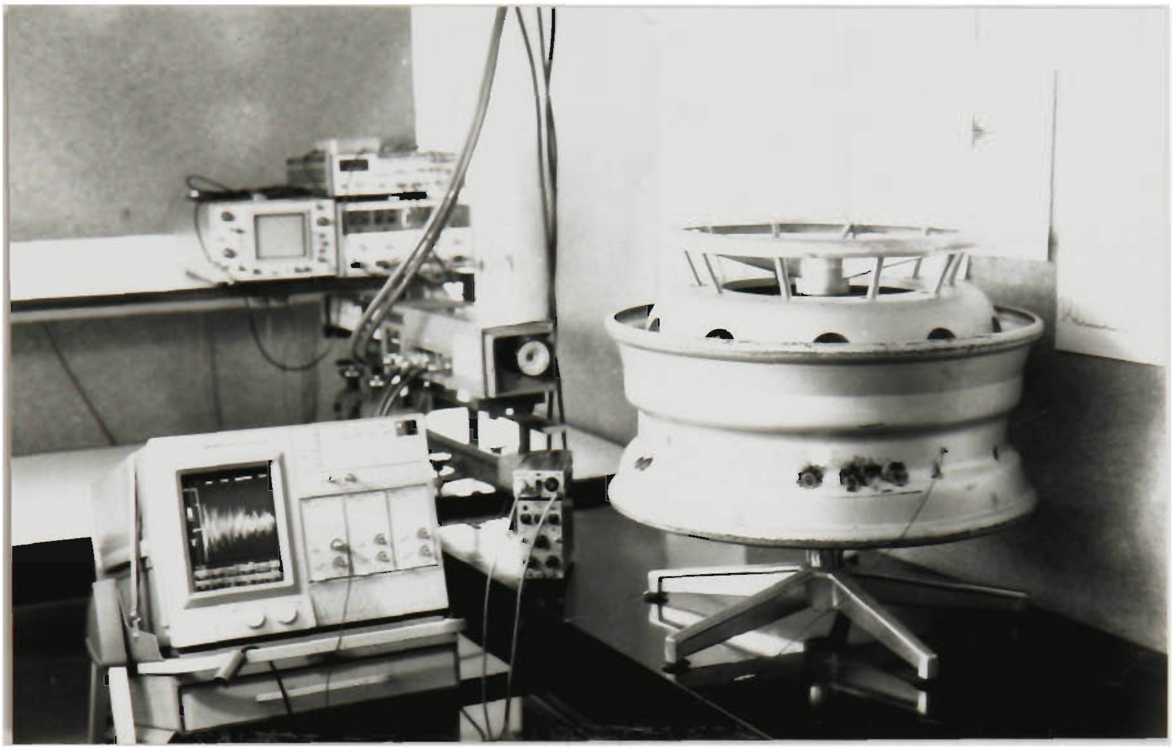

Plate 4.1. Laser-induced structural vibration and vibration analysis of a 57 kg truck wheel rim.

The truck rim was mounted in this fashion so that experimental values for the first nine modes of flexural vibration could be compared with those calculated by finite element analysis using commercial software for modal simulation. The first nine vibrational modes were calculated to have frequencies lying between 200 Hz and 1300 Hz and these are shown in figure 4.1.1.

The unfocused laser pulse was used to irradiate the truck rim at positions around its circumference. The excitation positions can be seen from the circular black marks on the rim (see plate 4.1).

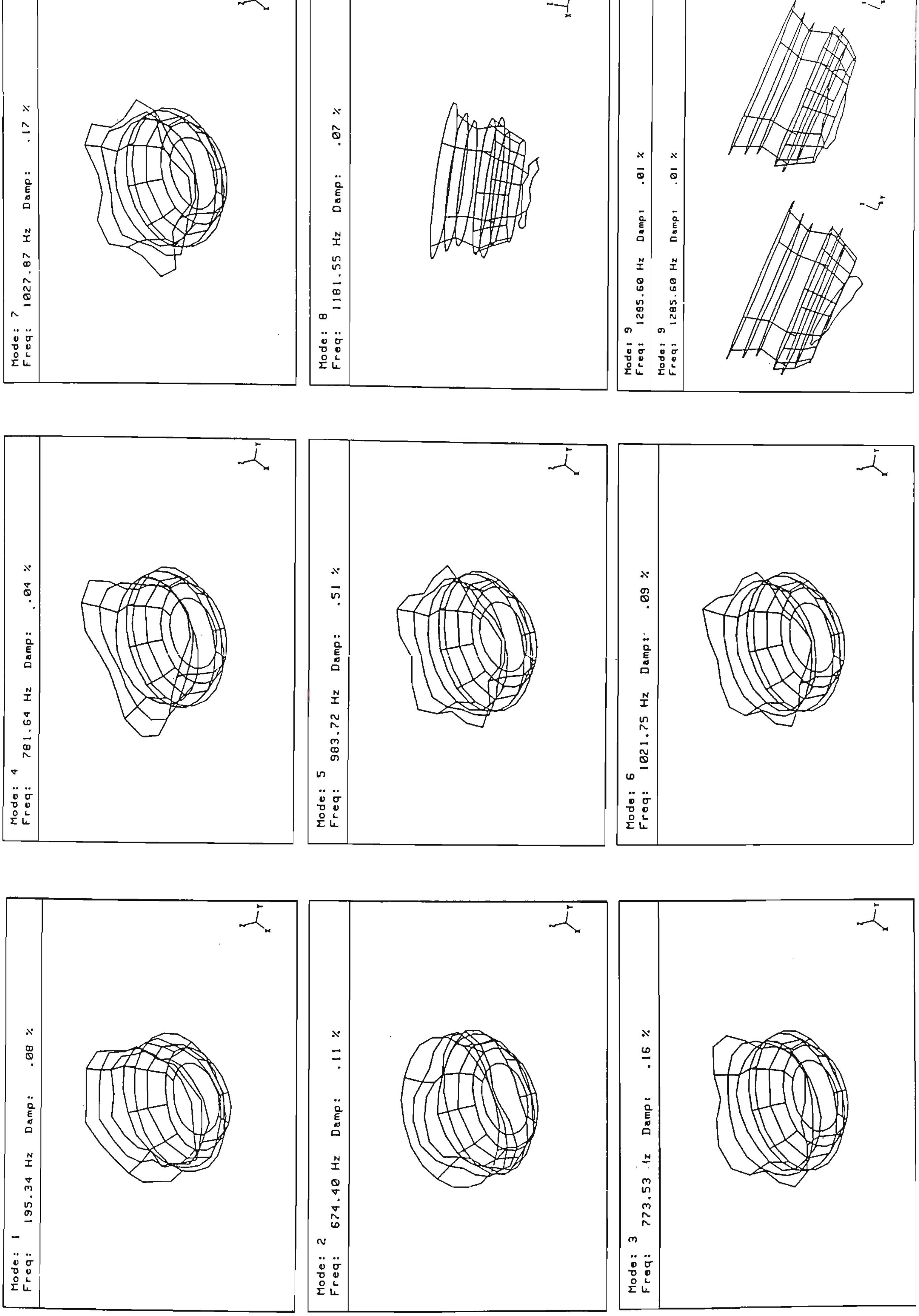

Figure 4.1.1. The calculated first nine vibrational modes for the vertically suspended truck rim. The rim is depicted with the outer lip uppermost and radial contours are used to schematically indicate surface deformations caused by each mode.

These marks were caused by burning the paint on the rim, which was generally not removed prior to irradiation. The paint did not significantly affect the excitation, as there was no noticeable difference when excited at similar positions where the paint had been removed. The rim was very effectively excited by the laser-induced photothermal flexing since an audible ring could be heard after the laser pulse. The vibration profile of the rim was recorded using the Tektronix DSA 602 and translated to the frequency domain using both the real-time FFT display and the HP-Basic routine. The modal signature and the frequency of each mode is shown in figure 4.1.2.

The measured frequencies for the modes of vibration were in good agreement with those calculated by the finite element method. These measured and calculated frequencies are given in table 4.1.1. The modal profile also exhibited several higher-order modes of oscillation which were outside the spectral range used in the finite element analysis.

	MODE 1	MODE 2	MODE 3	MODE 4	MODE 5	MODE 6	MODE 7	MODE 8	MODE 9
CALCULATED	195	674	774	782	984	1022	1028	1182	1285
OBSERVED	188	637	772	839	952	1032	1054	not detected	1255
% DIFF	4	5	½	7	3	1	2		2

Table 4.1.1 Calculated and observed modal frequencies for the truck rim.

It should be noted that free vibration was readily initiated by the single laser pulse, since the principal driving frequency of the thermally-induced bending moment (about 500 to 600 Hz for the 5 mm thick steel plate of the truck rim), was well-matched to the frequencies of the rim's lower-order modes of vibration. Although this rim had several cooling holes (plate 4.1), it had mainly cylindrical geometry. Because of the circular symmetry, there were many equivalent irradiation sites on the surface which were equally efficient in exciting any given mode of free vibration.

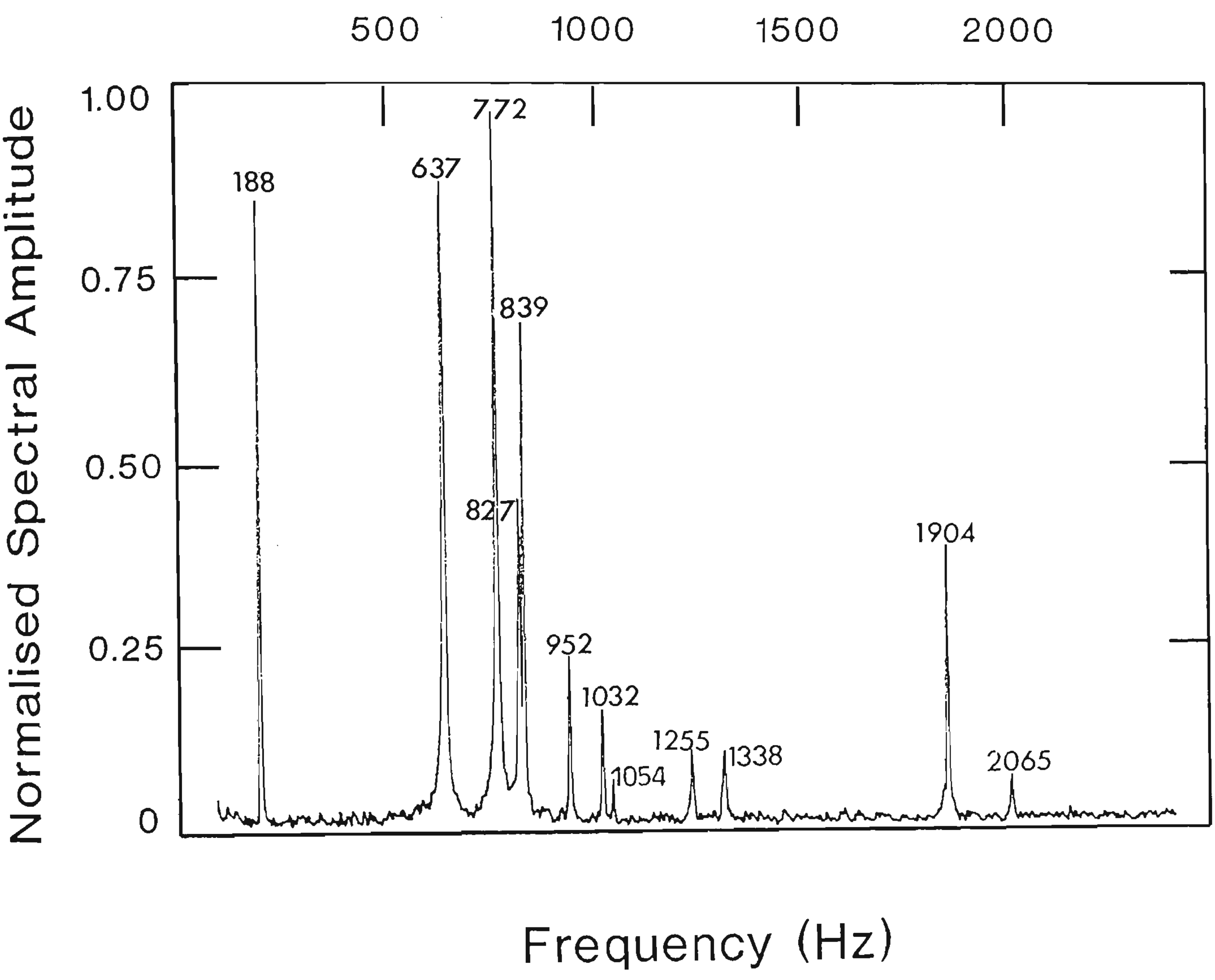

Figure 4.1.2. Modal signature of a 57 kg truck wheel rim excited by a single laser pulse. The frequencies of the various vibrational modes are indicated above the spectral peaks.

4.2 Techniques for suppression and enhancement of vibrational modes using single and dual pulse excitation

Simultaneous irradiation of more than one location on a structure is possible when beam splitting techniques are used to divide and separate the laser pulse. The effectiveness of dual pulse excitation for mode enhancement and suppression has been compared to that of the single pulse technique described in section 3.3.3. Cantilever targets were again used for these measurements because of the ease with which the positions of nodes and antinodes for the various modes could be identified (table 3.1.2). The proximity sensor was used to detect the cantilever displacements. The laser beam paths used in this investigation are shown in figure 4.2.1.

The mirrors (M_1, M_2 and M_3) had a reflectivity of 87% at 1.06 μm when used at an incidence angle of 45°. A 60/40 beam splitting mirror (B_1) was constructed by coating a glass plate with a MgF_2/ZnS stack and glass microscope slides (A_1) were used, when required, to attenuate either branch of the laser pulse to ensure that the optical energy in each pulse was reasonably equal. The pulse energy in each branch was averaged over several laser pulses using an EG&G model 581 radiometer, although shot-to-shot variations were generally less than about 1 J. These beam splitting techniques caused significant loss in the total energy delivered by the laser to the cantilever. When using the arrangement for dual pulse irradiation on the same side, 80% of the total laser energy was delivered to the cantilever (16 J per pulse), whereas dual pulses delivered to opposite sides provided only 60% (12 J per pulse) of the initial laser energy to the structure. The total energy used to excite the cantilever must be taken into consideration when vibrational modes are compared for different irradiation conditions. The efficiency of mode suppression or enhancement may be gauged from changes in the relative amplitudes of individual spectral peaks in any given Fourier spectrum (relative spectral densities) and by comparing whole spectra (modal signatures) for different irradiation sites.

(a)

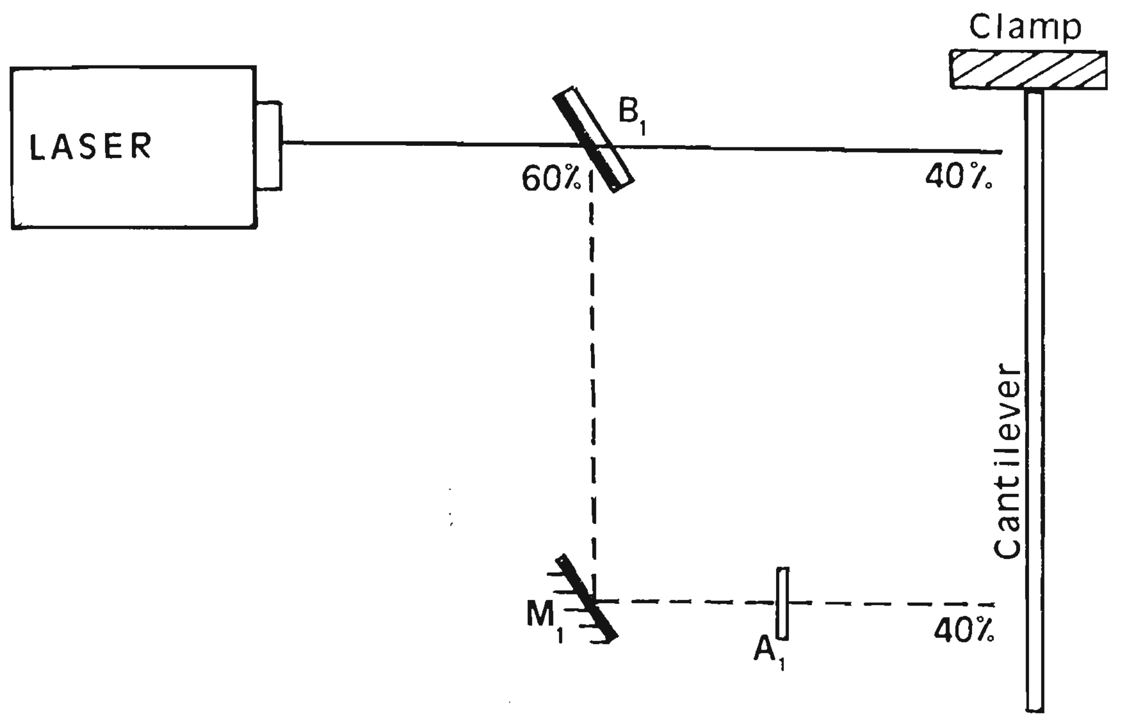

(b)

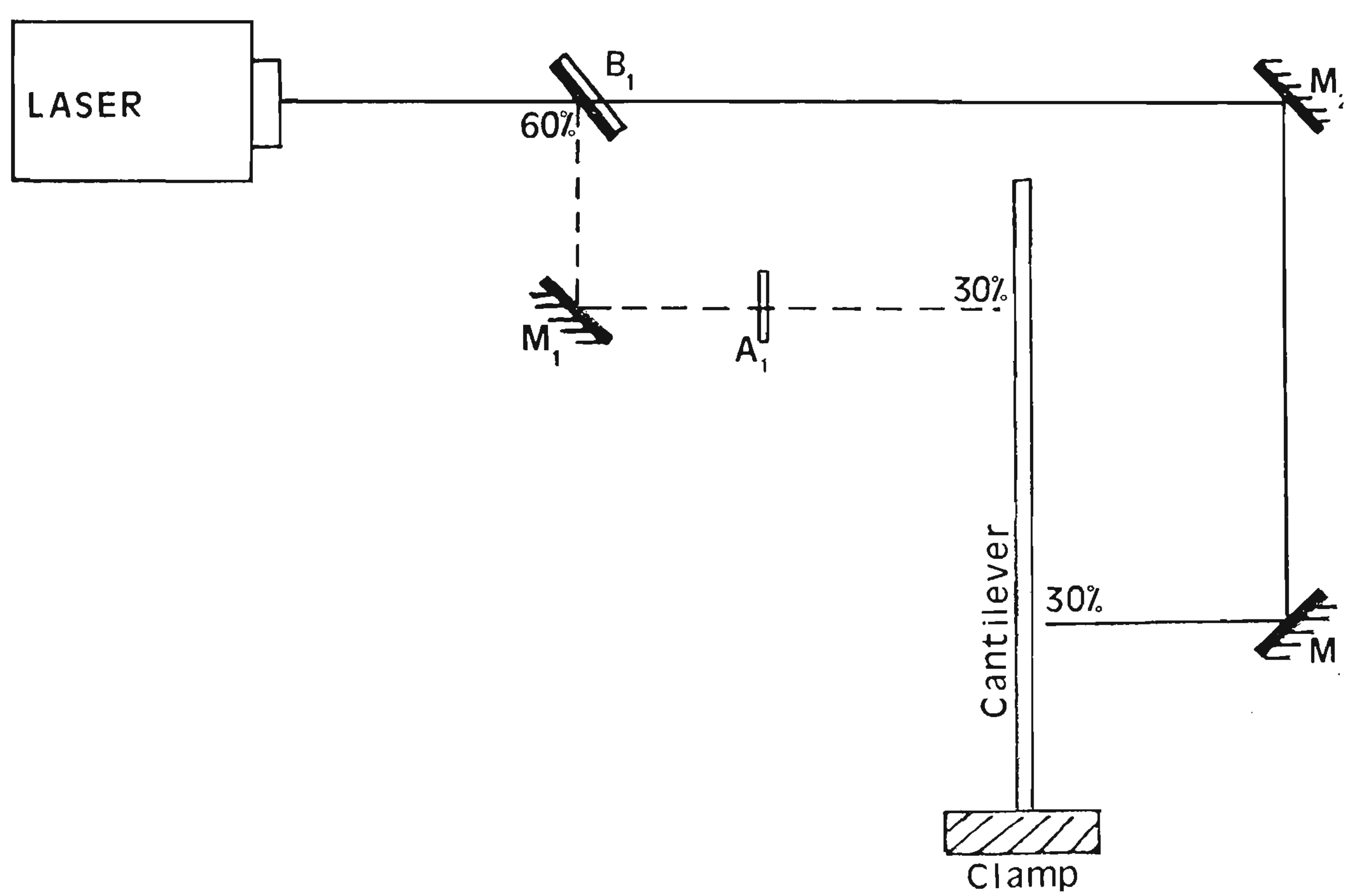

Figure 4.2.1. Beam splitting arrangements for dual excitation on (a) the same side and (b) opposite sides of the cantilever. M = Mirror, B = Beam splitter and A = Attenuator

Irradiation of the cantilever with a single laser pulse directed at a node of the bending moment profile of a particular mode of vibration, so as to suppress that mode with respect to the other modes of vibration, has been discussed in section 3.3.3. In a similar manner, laser-induced flexing at the site of one or more antinodes of the bending moment profile for a particular mode may possibly enhance that mode of vibration.

A detailed modal survey of cantilever A was conducted by irradiating the blackened surface of the cantilever with a single unfocused 40 J pulse at positions between 5 mm (0.016L) and 295 mm (0.98L) from the clamp using intervals of 5 mm (slightly greater than the radius of the unfocused laser spot). The proximity sensor remained at 0.20L throughout this investigation. The proximity of the sensing fibre to the cantilever surface was finely adjusted so that the spectral density of the 50 Hz peak (residual 50 Hz modulation in the LED source) measured a constant -55 dBm on the vertical axis of the Tektronix DSA 602 real-time FFT display. These adjustments were relatively minor, but without them, the relative spectral densities varied by up to about 5 dB as the excitation site was moved progressively further from the clamp. The spectral density of the 50 Hz peak was used as a reference, since it was an artefact of the sensor and not directly affected by variation in the cantilever's modes of vibration The amplitude of the 50 Hz peak depended only on the reflected light intensity at the photodetector and so was determined only by the mean fibre-surface separation and the average power of the LED source. Since the source power was kept constant, this 50 Hz peak could be used as an indicator of the fibre-surface separation. The dBm value (-55 dBm) refers to the electrical power only ($[1\mathrm{mV}]^2/50\Omega$) and does not refer to the optical signal power at the detector. Electrical dBm was chosen as a convenient scale by which to gauge relative gain or loss in the signal amplitude.

The relative spectral densities (the spectral densities, in dB, as measured above or below the 50 Hz reference) of the first four vibrational modes for the 58 irradiation sites along cantilever A are shown in figure 4.2.2. Mode suppression is evident in the figure following irradiation of the cantilever at bending moment nodes of a particular mode (see table 3.1.2 for node positions). Clearly, mode 2 was suppressed by laser irradiation at 0.22L, mode 3 at 0.14L & 0.50L, and mode 4 at 0.10L, 0.36L & 0.64L (as previously discussed in section 3.3.3).

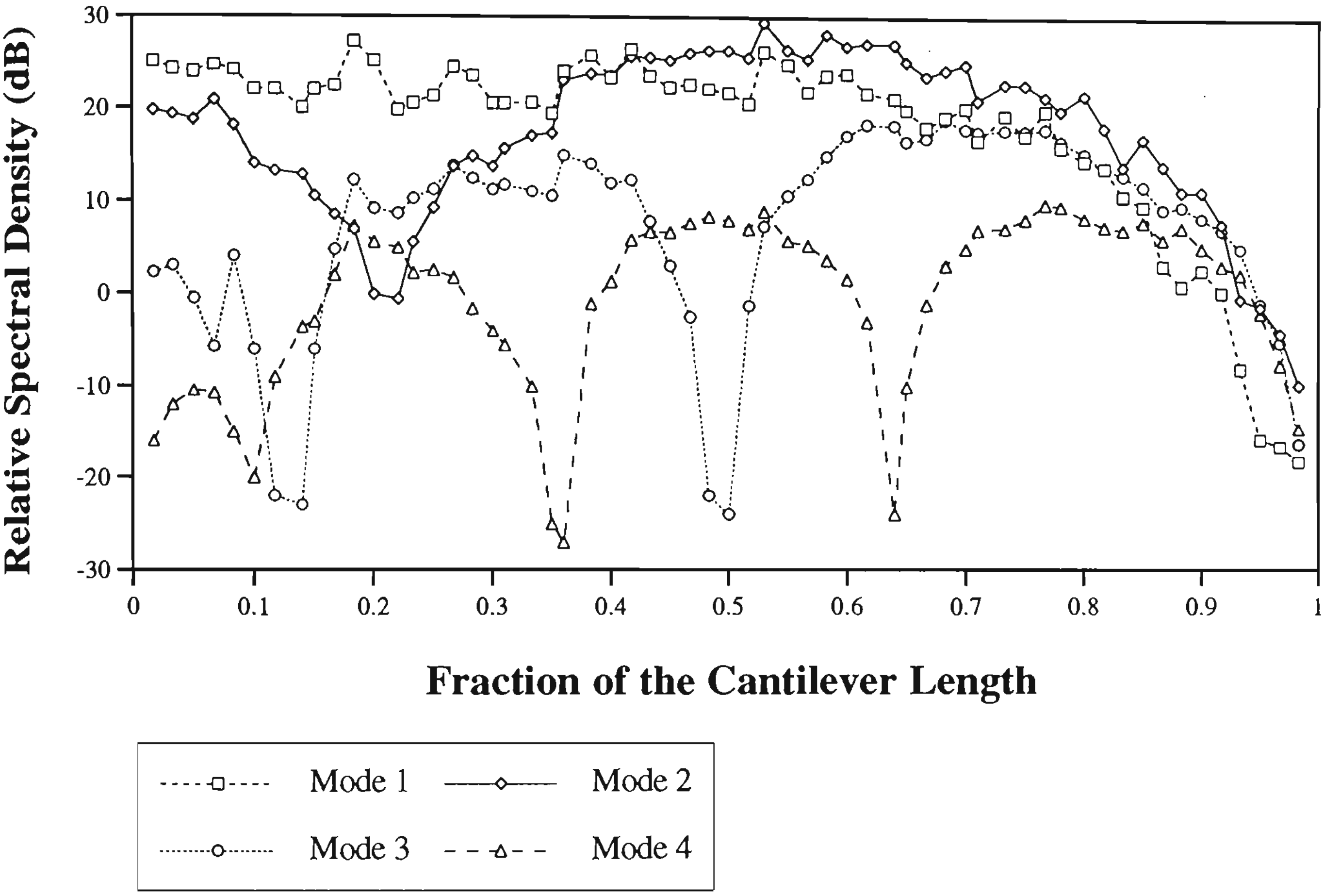

Figure 4.2.2. The relative spectral densities (in dB relative to the 50 Hz reference peak) of the first four modes of vibration for cantilever A using a single 40 J laser pulse to irradiate 58 locations along the cantilever length.

The relative spectral densities within the modal signature following irradiation at 0.85L (the optimum irradiation site discussed in section 3.3.1) may also be compared to those measured from the modal signatures following irradiation at other sites. Enhancement of the selected mode of vibration (the spectral density of a particular mode increased with respect to the spectral density of the same mode after laser irradiation at 0.85L) is also indicated from figure 4.2.2 for; mode 1 at any irradiation site closer to the clamp than 0.85L; mode 2 at 0.53L, and mode 3 at 0.71L. There is no marked enhancement of mode 4 at other irradiation sites since 0.85L is close to a bending moment antinode of mode 4 at 0.78L. The enhancements obtained, while they can be significant, represent the maxima of fairly broad features in figure 4.2.2. In contrast to this, the modal suppression can be seen to be far more localised, giving rise to relatively narrow minima in the figure. Modal suppression is clearly far more efficient than modal enhancement, since the decrease in modal amplitude after irradiation at nodes can often be 30 dB or more. Figure 4.2.2 can also be used to select the most efficient locations for excitation of a specific mode of vibration. This is used in subsequent sections where maximum resonant amplitudes are required.

The beam splitting arrangements shown in figure 4.2.1 were used to irradiate the cantilever at two locations simultaneously. The efficiency of dual laser pulse irradiation for the enhancement or suppression of selected vibrational modes was gauged by comparing the relative spectral densities obtained following dual pulse irradiation of cantilever A, to those obtained after irradiation by a single pulse. Since dual pulse suppression or enhancement techniques apply to modal geometries with two or more nodes (or antinodes), modes 1 and 2 are not considered. This dual pulse investigation excited vibrations within the cantilever using surface irradiation with laser pulse energies of 40 J, 32 J, 24 J, 16 J and 12 J. For valid comparisons to be made between spectral densities obtained under these varied irradiation conditions, the effect of variation of laser pulse energy on these spectral densities was taken into account.

The Nd:glass laser energy can be simply changed by varying the flashtube pump energy. This allowed any output energy to be selected between about 1 J and 40 J. In order to assess the effect of changes in laser energy on the relative spectral densities of the first four modes of vibration (measured with reference to the 50 Hz peak), the laser was used to irradiate the cantilever at 0.85L and the pulse energy was varied from 1 J to 5 J in 1 J steps and then from 5 J to 40 J in 5 J steps. In addition, single pulses of 12 J, 16 J, 24 J and 32 J were also used for comparison with the total energies used in the dual pulse experiments. These results are plotted in figure 4.2.3. As expected, decreasing the laser energy decreases the amplitude of the modal peaks. The changes amounted to a little more than 10 dB for a change in laser energy from 40 J to 10 J. Even at 1 J, where the total decrease in amplitude was about 30 dB, the laser was still very effective in exciting vibration. This is consistent with the results reported by Koss and Tobin [Koss and Tobin, 1983] who used energies of about this magnitude.

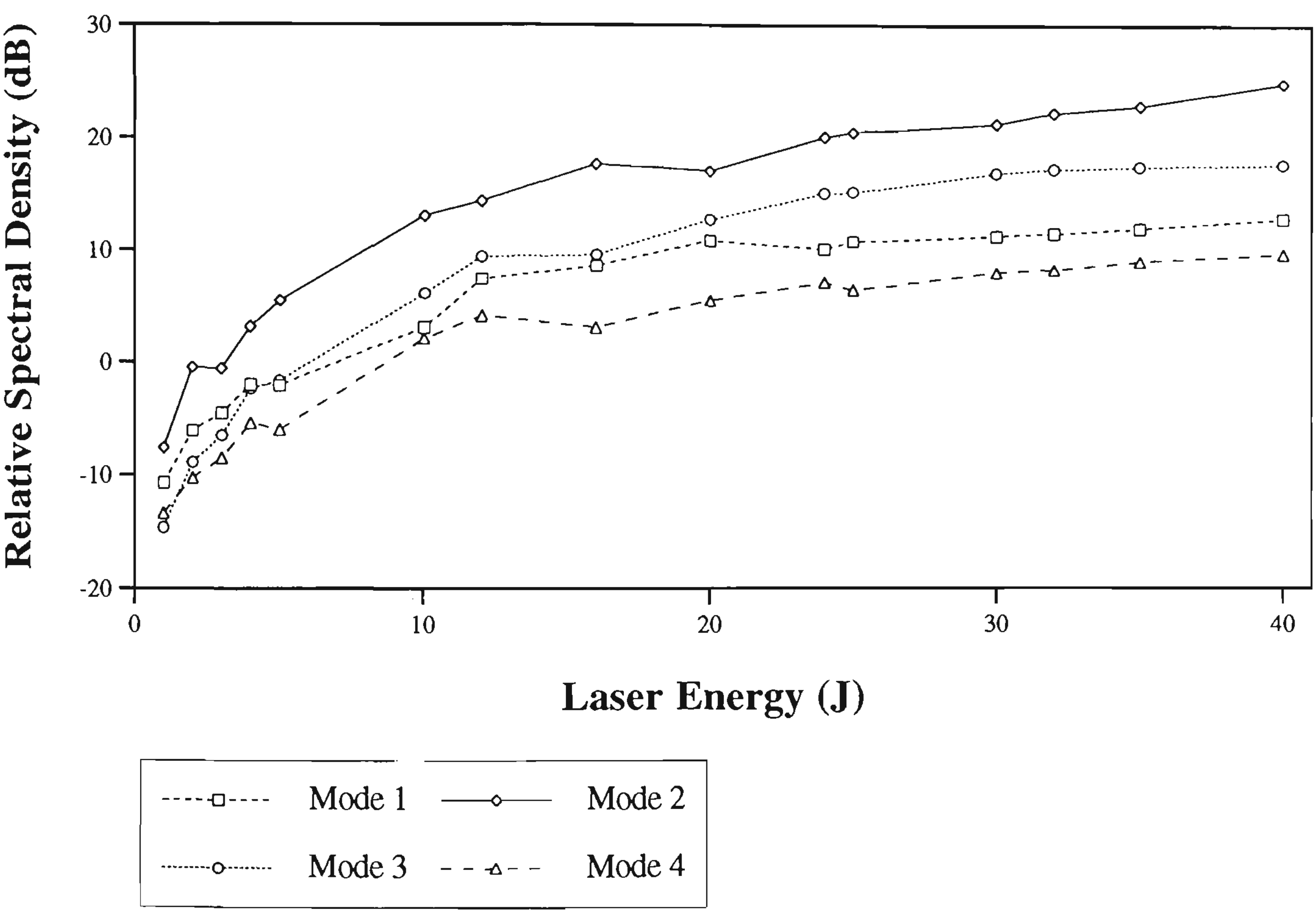

Figure 4.2.3. The relative spectral densities (measured in dB with reference to the 50 Hz peak) of the first four vibrational modes of cantilever A for varied laser pulse energy using a single pulse at 0.85L.

The relative spectral densities of modes 3 and 4, obtained following laser irradiation by two pulses at separate locations, can now be compared with the spectral densities of those modes following single 12 J, 16 J, 24 J, 32 J and 40 J irradiation at 0.85L. The spectral densities following single pulse irradiation at these energies for modes 3 and 4 (taken from figure 4.2.3) are displayed as two mode bar diagrams on the left hand side of figure 4.2.4. The other mode bar diagrams in figure 4.2.4 show the spectral densities obtained following both single and dual pulse excitation at locations (nodes or antinodes) chosen to either suppress or enhance mode 3 or mode 4. The irradiation sites are annotated beside each mode bar diagram. The numerical values of the spectral densities obtained following dual site irradiation at 0.85L, and the various node and antinode combinations, are given in table 4.2. In interpreting this data, it is important to understand that there was considerably more variability in the spectral densities of the strongly suppressed peaks than was the case for normal data. For normal data the spectral densities vary by only about ± 1 dB from shot-to-shot, however the variations observed in the strongly suppressed modes was about ± 2 to 3 dB. The data given represent typical modal signatures with about average spectral densities rather than the numerical average of a set of modal profiles.

	DUAL 16 J PULSES @ 0.85L (32 J total)	DUAL 16 J PULSE SUPPRESSION (Same Side)	DUAL 12 J PULSE ENHANCEMENT (Opposite Sides)	DUAL 16 J PULSE ENHANCEMENT (Same Side)
MODE 3	15	-11 (0.14L & 0.50L)	15 (0.31L & 0.71L)	
MODE 4	10	-18 (0.10L & 0.36L) -19 (0.36L & 0.64L) -15 (0.10L & 0.64L)	8 (0.22L & 0.50L) 7 (0.50L & 0.78L)	7 (0.22L & 0.78L)

( ) The location of the laser irradiation sites

Table 4.2. The spectral densities (in dB relative to the 50 Hz reference peak) for dual pulse excitation at 0.85L and at locations chosen for mode suppression or enhancement.

Comparison of Single and Dual Unfocused Laser Pulses

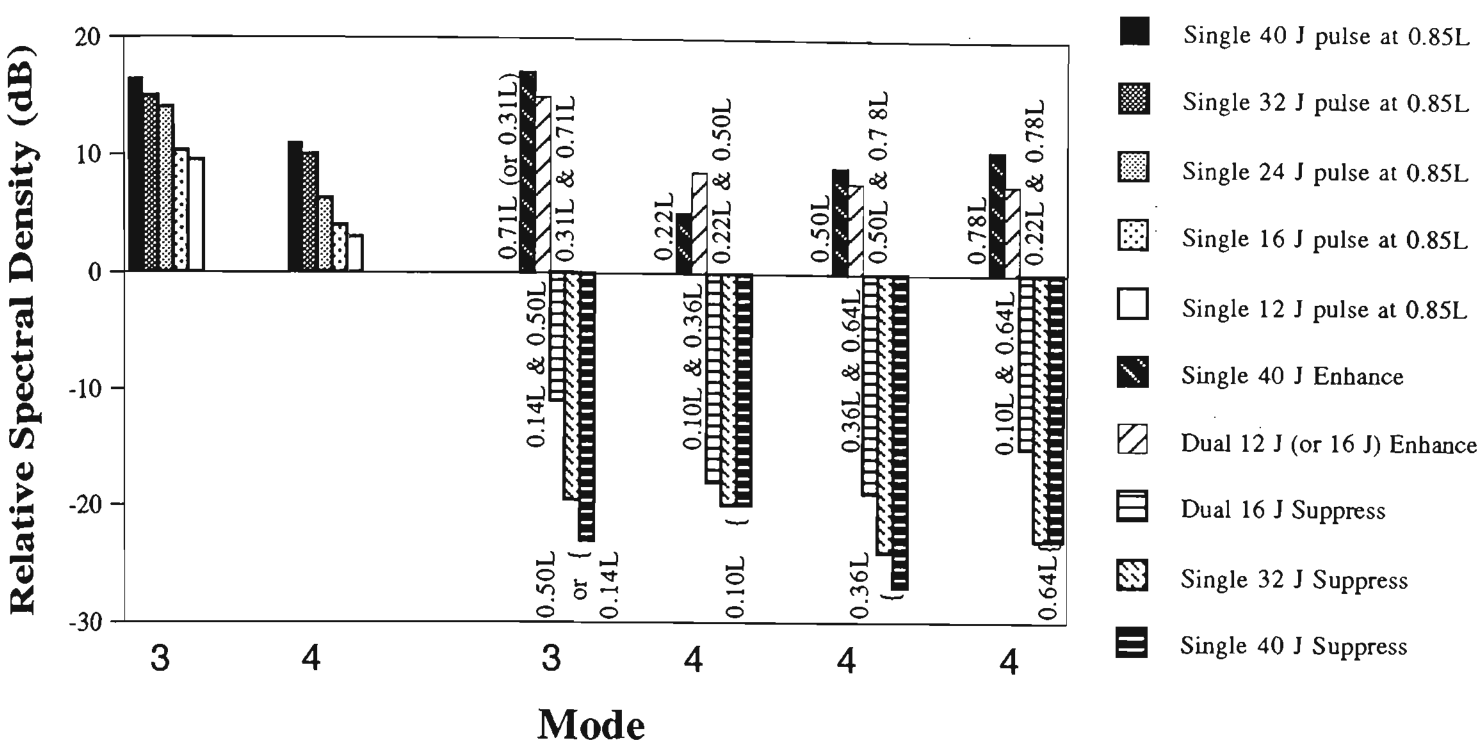

Figure 4.2.4. The relative spectral densities for modes 3 and 4 of Cantilever A using single and dual pulses of various energies in attempts to selectively enhance and suppress particular modes. The irradiation sites and energies are indicated in the diagram and legend.

These measurements show that dual pulse irradiation at two nodes simultaneously (2 × 16 J pulses) suppressed the selected mode of vibration by at least 25 dB when compared to irradiation with the same total energy (32 J) at 0.85L. However, it can been seen that a single laser pulse directed at a node is also very effective in suppressing a selected mode. In fact it is marginally better than two pulses. The improvement of between about 2 dB and 10 dB is not very significant when the shot-to-shot fluctuations of 2 to 3 dB are taken into account. It is also worth noting that there is little difference in the effectiveness of the suppression with 32 J and 40 J single pulses. It is clear from these results, that any significant excitation at a node is very efficient at suppressing that particular mode in the vibration profile, and it appears that a large excitation at one node is more effective than dual excitation (at half the laser energy) at two nodes. Thus, there is nothing to be gained in this situation from more complex experimental arrangements using beam splitting techniques.

Likewise, dual pulses directed at antinodes for enhancement of a specific mode (12 J pulses when irradiating consecutive antinodes or 16 J per pulses when irradiating the first and third antinodes) were found to be slightly less efficient than a single pulse of the same total energy at 0.85L. In fact, maximum excitation for a particular mode is achieved by directing the maximum amount of laser energy available to a single antinode of that particular mode. It has not been possible to selectively couple the bulk of the excitation energy into a particular mode by using multiple-point excitation techniques. The amplitude of a selected mode is not further enhanced (beyond that obtained using a single pulse of energy equal to the sum of the multiple beam energies) by using multiple irradiation sites and the other modes are still evident in the vibration profile.

It is also clear from figure 4.2.4 that dual pulse enhancement (two 12 J or 16 J pulses) were more effective than a single 12 J or 16 J pulse. This is to be expected, since the total energy available for excitation is doubled. In the next section, forced oscillation of a selected mode is achieved using repetitive low-power diode laser pulses which are tuned to match the resonant frequency of that mode. In this case multiple sources and irradiation points have been found to be effective as they increase the total energy available for excitation.

4.3 Photo-thermoelastic excitation of aluminium cantilevers using repetitive pulses from single and multiple low-power diode lasers

The theory of chapter 3 predicts that even small laser energies should produce some vibrational excitation of the target structures. It was decided to try to assess the feasibility of using optical excitation with very much smaller and simpler lasers. AlGaAs laser diodes, with powers measuring tens of milliwatt, are now readily available at reasonable prices and so it was decided to try to excite the cantilever structures using these sources. However, as seen from figure 4.2.3, a decrease in laser energy by something less than two orders of magnitude produced a decrease in the amplitude of the peaks in the vibration spectrum of two to three orders of magnitude. Hence, it was clear that a much more sensitive vibration detector would be required and so the interferometric sensor (described in section 2.2.2) was constructed. This provided an increase of about three orders of magnitude in detection sensitivity (micrometres to nanometres) even without narrow tuning of the bandwidth for the detection circuitry. On its own, this was not likely to provide sufficient sensitivity. However, at these low powers the bending moments could also be enhanced by reducing the diameter of the laser spot on the target without fear of reaching the ablation threshold. In addition, the vibration amplitudes could be increased by up to several orders of magnitude by using repetitive pulses to force oscillation at the resonant frequencies of the target structure.[Bishop and Johnson, 1960] Such repetitive pulsing, with any desired mark-to-space ratio, is very easy to achieve with diode lasers.

Experiments were carried out using one or more Sharp LT016MD, 15 mW (r.m.s), 810 nm laser diodes (maximum CW power ~ 40 mW) focused to a spot size of 0.5 mm at the surface of cantilever A. The unpolished aluminium cantilever, interferometric sensor and bulk optics were mounted on a vibration isolated table. Three diode lasers were mounted so they could slide along either side of the full length of the cantilever at a distance of 10 cm from the surface. Objective lenses (×20), placed close to the diode lasers, were used to focus the laser irradiation onto the cantilever surface. The irradiation sites were selected along both sides of the cantilever length to match the antinode locations of the cantilever's bending moment profile (table 3.1.2 and figure 3.1.7(a)). A schematic diagram of the cantilever, interferometer and diode laser arrangement is shown in figure 4.3.1.

Drive circuits were constructed to digitally modulate the laser diodes when triggered by a TTL square wave (section 2.2.1). One or more laser diodes were then synchronously pulsed, with a repetition-rate determined by the TTL modulation frequency, and swept through a frequency range which was known to contain one of the modes of vibration. The pulse-repetition-rate was gradually increased from 2 Hz below a known modal frequency for cantilever A to 2 Hz above. The cantilever was thereby driven to resonance when the laser-induced photo-thermoelastic flexing of the cantilever matched a mode of vibration. Cantilever displacements greater than a few nanometres were detected using the interferometric sensor, and the driving frequency of the laser diode was recorded for the peak displacement amplitude detected (gauged from the peak spectral density of that mode in the real-time FFT display of the Tektronix DSA 602). The driving frequency of the forced resonance indicated the frequency of the selected mode of vibration to an accuracy of ± 0.5 Hz; the resolution being limited by the stability of the square wave oscillator. In this manner, the first five resonant modes of vibration were excited and studied. Greater resonant displacement amplitudes for a particular mode were achieved using two or three synchronously pulsed laser diodes focused onto sites along opposite sides of the cantilever corresponding to the consecutive antinodes of the bending moment profile.

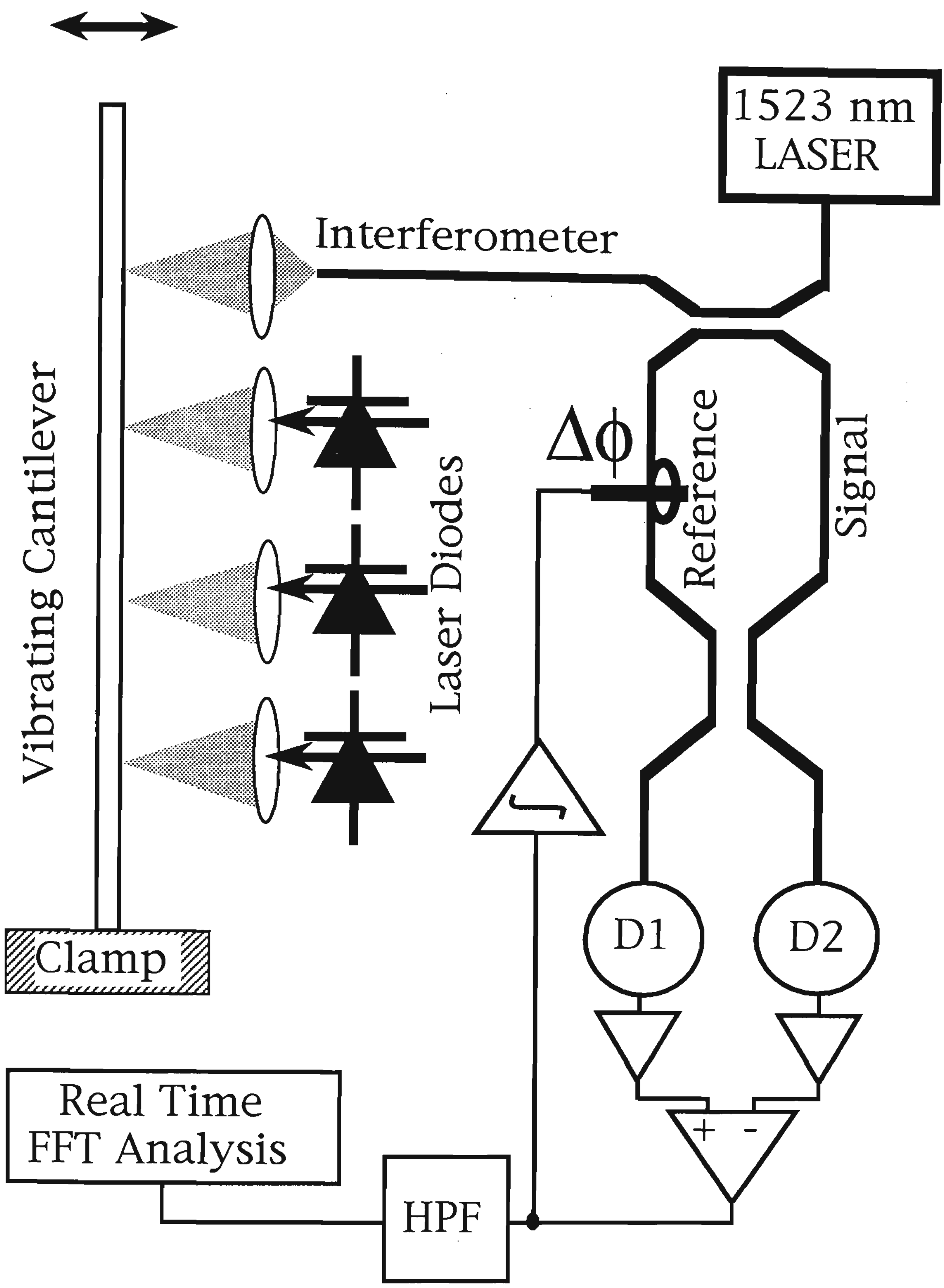

Figure 4.3.1. Schematic diagram of the cantilever, interferometer and laser diode arrangement used for repetitive pulse experiments.

In order to efficiently excite a particular mode of vibration, the characteristic thermal properties of the cantilever must also be considered. The rate of heat dissipation within the material is determined solely, in the simple case of a semi-infinite solid, by the thermal diffusivity constant and the thickness of the material.[Carslaw and Jaeger, 1946] The thermal bending moment, and hence the efficiency of excitation, is determined by the temperature difference between the front and rear surfaces (section 3.4). When a constant laser power is incident on the surface, the temperature difference begins to rise and will reach a maximum before decreasing as the rear surface begins to heat-up. Hane et al. (1988)[a] has shown that the efficiency of the excitation is maximised (using a 50% duty cycle) by choosing a laser pulse repetition frequency such that the temperature difference just reaches its maximum value when the laser power is on and just relaxes to zero during the time that the laser is off. This frequency is called the characteristic frequency for the structure (f_c).[Charpentier et al. 1982, Hane et al. (1988)a&b, Hane and Hattori 1990] At frequencies well below this value, the temperature difference peaks before the laser power is turned off and the average temperature of the structure will rise. For frequencies well above f_c, the amplitude of thermal modulation will decrease, varying approximately inversely with modulation frequency (f_m).[Hane and Hattori, 1990] It can be shown that the characteristic frequency for a thin plate of thickness, h, and thermal diffusivity, κ, is given by[Ibid.]

eq. 4.3.1

$$f_c = \frac{\kappa}{h^2} .$$

The characteristic frequency of cantilever A ($\kappa = 8.60 \times 10^{-5}$ $m^2.s^{-1}$, h = 3 mm) was calculated from equation 4.3.1 to be approximately 10 Hz. Therefore, when the sample is pulsed at 10 Hz, the optimum heat transfer and thermoelastic moment is achieved. However, the laser pulse repetition frequencies necessary for forced oscillation of cantilever A are all greater than 10 Hz and so the amplitude of the thermoelastic moments induced in the target will vary approximately as $[1 + (f_m/f_c)^2]^{-1/2}$; in inverse proportion to the frequency of the resonant mode excited.

Consequently, the peak thermal moment achieved when exciting mode 2 (26 Hz) was around 100 times greater than that of mode 5 (1496 Hz). This frequency dependent attenuation of the bending moment amplitude, combined with the increased difficulty of exciting higher-order modes, limited the number of modes which could be excited and measured using this technique. The spectral densities of the first five resonant modes for single, dual and triple 15 mW (r.m.s) diode laser excitation are presented in table 4.3.1.

MODE (Frequency)	DETECTED ELECTRICAL SIGNAL POWER (dB) ABOVE NOISE		
	Single Diode Laser	Two Diode Lasers	Three Diode Lasers
Mode 1 (26 Hz)	**45** [32]		
Mode 2 (162 Hz)	**39** [37] (0.53L)		
Mode 3 (454 Hz) Mode 3 (454 Hz)	**26** [18] (0.31L) **24** [19] (0.71L)	**45** (0.31L 0.71L)	
Mode 4 (889 Hz) Mode 4 (889 Hz) Mode 4 (889 Hz)	**13** [9] (0.22L) **13** [11] (0.50L) **13** [11] (0.79L)	**17** (0.22L 0.50L) **20** (0.22L 0.79L) **18** (0.50L 0.79L)	**25** (0.22L 0.50L 0.79L)
Mode 5 (1469 Hz) Mode 5 (1469 Hz) Mode 5 (1469 Hz) Mode 5 (1469 Hz)	**5** [*] (0.17L) **5** [*] (0.39L) **6** [*] (0.61L) **7** [*] (0.84L)	**12** (0.17L 0.39L) **13** (0.17L 0.61L) **12** (0.17L 0.84L) **10** (0.39L 0.61L) **10** (0.39L 0.84L) **12** (0.61L 0.84L)	**17** (0.17L 0.39L 0.61L) **16** (0.39L 0.61L 0.84L) **19** (0.17L 0.39L 0.84L)

Table 4.3.1. Resonant vibration signal power levels (**bold**) from the interferometric sensor for single, dual and triple 15 mW diode laser forced oscillation.
[ ] denotes remote excitation and sensing at 1 m through glass sheet;
( ) the point of excitation, and
* not detected

The remote application of this excitation technique was also demonstrated by using a single diode laser to optically excite the cantilever surface at a range of one metre through an intervening 3 mm thick glass window. For these measurements, the interferometric sensor was also placed at a range of 1 m, behind the glass window. This data is also given in table 4.3.1 inside the square brackets.

,Simultaneous excitation at multiple antinode sites significantly increased the resonant amplitudes (unlike section 4.2, the laser pulse energy is not reduced with multiple sources). In the case of the third mode, dual excitation provided an improvement of 15 dB over the signal power gained by the single diode laser. The electrical dBm scale on the Tektronix DSA 602 ($[1mV]^2/50\Omega$), although not a true measure of the power spectral density, was again used as a convenient scale by which to gauge the relative gain or loss in the signal amplitudes. The noise-floor of the interferometer over the 2 kHz spectral range, for unpolished aluminium, was -60 dBm and the minimum signal which could be reliably detected was -55 dBm. A signal power of 5 dB above noise indicated a vibrational amplitude of approximately 1 nm (see section 2.2.2).

The photo-thermoelastic structural excitation of an aluminium cantilever has therefore been demonstrated using low-power diode lasers pulsed at a frequency matching a resonant mode of vibration. Simultaneous irradiation of more than one antinode on the cantilever's bending moment profile has been shown to significantly increase the amplitude of the vibration (signal increased by 10 to 20 dB). Furthermore, the remote capabilities of this technique have been demonstrated by the optical excitation and sensing of the cantilever from behind a glass window.

The use of diode lasers and the fibre interferometer to excite and measure vibrations in such a large structure has been remarkably effective. The system did not require complicated alignment as the interferometer operated by coupling some of the scattered light back into the fibre, and this was not particularly sensitive to small variations in the angle of incidence of the interferometer beam on the irradiated surface. It was only necessary that the vibrating surface be approximately perpendicular to the open-air path of the interferometer. It should be noted that a further improvement in the detection sensitivity of the interferometer by about two orders of magnitude is possible by reducing the bandwidth of the detector electronics from approximately 30 kHz to around 1 Hz (thus reducing the noise).

The diode laser system was briefly used to try to detect the resonant modes of vibration of the 57 kg truck rim (section 4.1). This was unsuccessful since no signals were detected above the noise. Forced oscillation of the truck rim could have been made possible by reducing the detector bandwidth, but further efforts to achieve this were not attempted in this work.

Non-destructive laser excitation and non-contact optical sensing of structural vibration has now been demonstrated using single and multiple high-power laser pulses as well as repetitive low-power diode laser pulses. Modal frequencies have been measured to within 0.5 Hz. The modal analysis of a laser vibrated structure may now be used to non-destructively test for changes in that structure. That is, comparison of the modal signature of a given structure to that of a reference spectrum may be used to detect physical variations such as size, shape, elasticity or homogeneity, and/or defect in the integrity of the structure due to cracks and flaws. The following chapter reports a series of experiments which used these non-destructive optical excitation and sensing techniques to obtain modal signatures from fatigued and cracked structures. In comparing the modal signatures of damaged and undamaged structures, it may be possible to identify the damaged structures directly.

Chapter 5

Modal analysis of laser-excited structures for non-destructive testing

5.1 Detection of stress fatigue in an aluminium cantilever

The following investigation sought to detect damage in a structure which had been stress fatigued by multiple stretching cycles. The intention was to try to produce internal cracks by the fatigue process and show that these cracks may be detected by measuring the modal frequency shifts. The only fatiguing equipment available was relatively slow in achieving each tension cycle, and so allowed for only a limited number of stretching cycles (thousands) and thus large stresses were applied in order to try to produce significant damage within this number of cycles. For most of this work, cantilevers have been used as test-structures because of the simplicity of their modal vibrations. Investigations using these simple structures have helped to clarify the physics of the processes involved. Since the dynamic characteristics of clamped-free cantilevers have been very well-defined, the following experiments continued to use this type of structure.

An aluminium strip was stretched to about 95% of its ultimate tensile stress (2 GN/m^2) and then relaxed to about 20% of UTS (0.4 GN/m^2). Each stretching cycle was intended to damage the aluminium's polycrystalline structure by causing dislocations and micro-cracks. With each repeated cycle of stretching, these dislocations and micro-cracks should both increase in number and merge as they propagate throughout the material. After many such cycles the strip would eventually fracture. Fatigue damage within the aluminium strip should decrease the elasticity of the metal and thus alter the value of Young's modulus. Therefore, if the strip were to be mounted as a clamped-free cantilever and excited to free vibration, the fatigue damage should decrease the modulus of elasticity, slow the propagation velocities of individual frequencies (equation 3.4.1.18) and thus reduce the modal frequencies. Furthermore, the mechanical damping of the cantilever's vibrations should also be affected.

An Instron 1195, 100 kN Universal Testing Machine (screw-thread controlled), was used to provide repeated cycles of varied tensile stress to an aluminium strip between 20% and 95% of the strip's UTS (2.2 GN/m^2). Fairly large loads (16 - 76 kN) were used to fatigue the aluminium strip within a limited number of cycles (10,000). The 400 mm × 12 mm × 3 mm strip was clamped over a length of 50 mm at each end and stretched using the screw thread mechanism to strain the strip uniformly along its exposed length of 300 mm. The strip was stretched for 200, 400, 800, 2000 and 10000 cycles. Visible damage was observed as surface striations after 2000 cycles. After the selected number of cycles, the aluminium strip was removed from the Testing Machine and mounted as cantilever A. The cantilever was excited with an unfocused 40 J Nd:glass laser pulse on a blackened surface at 0.85L and the vibrations were detected using the proximity sensor placed at 0.20L. Since this investigation was conducted during the development of the proximity sensor, the modal frequencies derived using the proximity sensor were checked with those obtained using a conventional strain gauge bridge (section 2.1.3). The vibration profiles were digitally recorded over one second on a Philips 250 MS/s oscilloscope (4096 data points) and transformed to the frequency domain using a HP-Basic FFT routine on a personal computer.

Two sets of fatigue trials were conducted independently, the first providing progressive fatigue damage to a single aluminium strip attached with a strain gauge bridge, the other using a set of six identical aluminium strips which were individually fatigued for the appropriate number of cycles and then monitored by the proximity sensor. The strain gauge bridges were damaged in the fatiguing process and so were replaced after each stage of progressive fatigue. The need to replace the strain gauges (for those tests involving strain gauges) could have caused additional frequency shifts, since it was very difficult to ensure that the gauges were replaced under exactly the same conditions. Therefore, the accuracy and repeatability of the strain gauge frequency measurements were not expected to be as good as those obtained using the non-contact optical sensor. The measured modal frequencies for modes 1 to 5 are shown after each number of stretching cycles in table 5.1. These frequency values were averaged from three modal signatures after each stage of fatigue. The frequency resolution is restricted to ± 2 Hz because there were only 1024 spectral data points over the selected 2 kHz range of the FFT.

Clearly, the modal frequencies decrease as the number of stretching cycles increase. As anticipated, it appeared that the modal frequencies were reduced with increased stress fatigue damage. However, there were significant problems associated with this data; the need to replace damaged strain gauges after each period of fatigue varied the mass loading on the cantilever due to adhesive and wiring, the cantilevers were clamped and reclamped under slightly different tension conditions, and the major problem, the samples stretched about 15 mm in length (about 4% of the total length) after 10,000 cycles.

MODE	UNFATIGUED	200 Cycle	400 Cycle	800 Cycle	2000 Cycle	10000 Cycle	& % SHIFT
STRAIN GAUGE SERIES							
1	26	25	25	25	25	25	4
2	164	162	160	158	158	158	4
3	455	446	443	438	438	438	4
4	873	857	846	838	831	844	5
5	1484	1460	1457	1430	1435	1426	3
FIBRE OPTIC SENSOR SERIES							
1	26	25	25	25	25	25	4
2	163	161	158	159	157	158	4
3	458	446	438	441	435	437	4
4	896	879	863	854	848	847	5
5	1481	1462	1453	1460	1440	1437	3

Table 5.1. Modal frequencies (in Hertz) for cantilever A after selected numbers of stretching cycles.

The 3 to 5% frequency shifts in all modes of vibration associated with the 10,000 stretching cycles (table 5.1) were about same as the percentage increase in the cantilever length (4%). The change in length did not however explain the measured frequency shifts, as each time the aluminium strip was clamped to form a cantilever, the free length was adjusted to be 300 mm. The reduction in the cantilever thickness with extension (Poisson's ratio for aluminium = 0.16) and the decrease in density due to dimensional changes together account for about a 2% decrease in frequency. After allowance is made for the experimental uncertainty in determining these frequencies (± 2 Hz), it would appear that there may be a small frequency shift which is not explained by dimensional changes and experimental uncertainties for modes 3, 4 and 5. This matter is examined in more detail in the following sections.

5.1.1 Corrections for physical deformation in the modal analysis of a fatigued cantilever

The observed reduction in mean thickness, mean width and mass of the vibrated section after each stage of stress fatigue, was taken into account in an attempt to isolate any modal frequency shifts caused by changes in the elastic modulus of the aluminium. Each 400 mm aluminium strip was carefully weighed (± 10 mg) and measured across its width and thickness (± 2 μm), at 10 mm intervals along its length. The mean thicknesses were calculated for the exposed 300 mm of each vibrating strip and then the frequencies of free vibration were calculated using equation 3.1.17 and standard values of E and ρ. These calculated frequencies and the observed frequencies (using the proximity sensor), are given in table 5.1.1.1.

MODE	ORIGINAL	200 Cycles	400 Cycles	800 Cycles	2000 Cycles	10000 Cycles
1	27:26	27:25	26:25	26:25	26:25	26:25
2	172:163	170:161	168:158	168:159	168:157	168:158
3	483:458	476:446	470:438	471:441	470:435	470:437
4	947:896	934:879	922:863	824:854	922:848	922:847
5	1566:1481	1544:1462	1525:1453	1528:1460	1524:1440	1525:1437

Table 5.1.1.1. Calculated and observed modal frequencies (Hz) for cantilever A. The first figure shown is that calculated by Euler's Equation, the second value is the observed frequency.

The calculated modal frequencies for the original (unfatigued) strip are consistently high. However, the calculations assumed standard values for the Young's modulus and the density of aluminium and also that the observed frequencies were the natural frequencies (ω_n) and not the reduced damped modal frequencies (ω_n') as described by equation 3.4.1.6. To account for this, an experimental value of E/ρ was calculated from the observed modal frequencies of the unfatigued cantilever using equation 3.1.17. Then, using the total mass and the unstretched physical dimensions of the 400 mm unfatigued strip, the actual density was calculated and an effective value of 6.27×10^{10} obtained for Young's modulus (standard value 7×10^{10}). Using this experimental value of Young's modulus for the unfatigued cantilever, and the measured mass and mean dimensions of each stress fatigued strip, the modal frequencies of the 300 mm long vibrating fatigued sections were recalculated as shown in table 5.1.1.2. The relative uncertainty in the theoretical calculations was calculated from the parameters used in equation 3.1.17 to be about 1%.

MODE	ORIGINAL	200 Cycles	400 Cycles	800 Cycles	2000 Cycles	10000 Cycles
1	26:26	25:25	25:25	25:25	25:25	25:25
2	164:163	161:161	159:158	159:159	159:157	159:158
3	458:458	451:446	445:438	446:441	445:435	445:437
4	896:896	884:879	873:863	875:854	872:848	873:847
5	1482:1481	1461:1462	1443:1453	1447:1460	1443:1440	1443:1437

Table 5.1.1.2. Calculated (revised) and observed modal frequencies (Hz) for cantilever A.

The observed and theoretical values of the 10,000 cycle cantilever are well within experimental error for modes 1 and 2 and differ by 8 Hz (1.8%), 26 Hz (3%) and 6 Hz (0.5%) for modes 3, 4 and 5 respectively. After consideration of the uncertainties in the both the calculated and experimental values, only mode 4 showed a definite frequency shift (at least 1.5% which cannot be attributed to uncertainties or dimensional changes) with an increased number of stretching cycles. In the case of mode 4, it appeared that there may be a shift which was due to a change in the Young's modulus of the sample.

In an attempt to verify this, the 10,000 cycle fatigued strip was annealed. Aluminium Standards and Data for the annealing and age-hardening of wrought and extruded aluminium products[Aluminium Development Council of Aust., 1988] indicated that fatigue damage could be alleviated within 6060 T5 aluminium (the aluminium sample used) by heating at 345°C for 2-3 hours, followed by simple cooling.

Another 400 mm aluminium strip was fatigued between 20% and 95% UTS for 10,000 cycles. The modal signatures of this 10,000 cycle strip, and also of an unfatigued control strip of the same aluminium, mass and dimensions, were recorded and then the two strips were heated at 345°C for three hours. Some residual fatigue stress within the 10,000 cycle strip should have been relieved during the annealing process. The temper grading (T5) of the aluminium would be equally effected for both the fatigued strip and the control. If the elasticity of the cantilever had been reduced by the stress damage, then the annealing process should partly restore the elastic modulus of the fatigued aluminium strip and show a significantly greater change in the measured value of Young's modulus to that of the control strip. The shift in Young's modulus due to the change in temper would be the same for both the strips. The measured modal frequencies and the comparisons in elastic modulus are shown in table 5.1.1.3.

SAMPLE	OBSERVED FREQUENCIES	E (GPa)	SHIFT IN E (GPa)
Control Before	26: 163: 458: 896: 1481	62.7	
Control After	26: 165: 461: 903: 1437	63.7	1.0
10000 CY Before	25: 158: 443: 869: 1437	62.2	
10000 CY After	25: 159: 446: 875: 1449	63.1	0.9

Table 5.1.1.3. Observed frequency shifts (in Hertz), due to annealing in the 10,000 cycle and control strips.

The observed shift in Young's Modulus was found to be very similar in both strips (to within 0.1 GPa). The annealing process had therefore nearly the same effect on both strips. It was concluded that the increase in frequency observed in the 10,000 cycle cantilever could not be attributed to the relief of fatigue damage, but simply to the change in temper of the aluminium. These experiments could not provide conclusive evidence that there had been a change in Young's modulus during the stretching process. However, there still remains the apparently significant frequency shift observed for mode 4. If there had been a structural change produced in the sample, then there may also be an observable change in the damping of the vibrational modes. Changes in damping were investigated in the next section.

5.1.2 Damping effects in a fatigued cantilever

As the fatigue of the vibrating aluminium cantilever increases, the mechanical damping, $e^{-t/\gamma}$, should also increase. Any increase in the modal damping co-efficient ($1/\gamma$) would both reduce the modal frequencies and increase the full width at half the maximum height (FWHM) of the modal peaks in the Fourier spectrum.[Bishop and Johnson, 1960]

The FFT computer analysis was modified to indicate the number of data points spanning the width of each modal peak at half the maximum amplitude of each modal peak. Modal peaks were typically 2 to 6 data points at FWHM (the bandwidth at FWHM depends on the frequency range of the spectrum and the number of data points used in the FFT). There was no significant variation observed in the number of data points at FWHM whilst stretching the strips over 10,000 cycles. Small variations in the FWHM were not detected because the 2 Hz resolution of these FWHM measurements was rather poor; therefore, further measurements of FWHM values were not attempted.

The damping decay constant ($1/\gamma$) in equation 3.4.1.6 was approximately found by fitting the curve

$$y(t) = C\,e^{-\frac{t}{\gamma}}, \qquad \text{eq. 5.1.2}$$

to the observed decay of the recorded vibration profiles for the fatigued cantilevers. Due to the dominance of the fundamental mode in these profiles, this process could only determine the damping constant for the fundamental mode. Higher-order modes should be more heavily damped. The vibration amplitude of the heavily fatigued strips were clearly more rapidly attenuated than for those with lesser stretching cycles when the vibration profiles for those cantilevers were compared. The values of $1/\gamma$ obtained by this process would account for a frequency difference between free and damped vibration in the fundamental mode of only about 0.5%. This is negligible. However the fact that changes are observed in the damping does suggest that the observed frequency shifts (at least in mode 4) may well have been partly due to some form of structural damage in the cantilevers. In fact, the changes in damping may well be a more sensitive measure of fatigue damage than shifts in the modal frequencies (at least at low frequencies).

This investigation of the modal frequency shifts in cyclically stretched cantilevers showed at least a 1.5% frequency shift in mode 4 of the 10,000 cycle cantilever which was not explained by experimental uncertainties or dimensional change. Stress fatigue is a likely cause of this frequency shift, however it has not been possible to confirm this directly (although the increased mechanical damping of the fundamental mode with greater number of stretching cycles is consistent with this interpretation). This investigation as a whole, has highlighted the fact that it is not easy to conclusively identify the cause of frequency changes as these depend on a number of parameters. Changes in length, thickness, density and elasticity all produce frequency changes. However, this technique was most successful in identifying the fact that some change had occurred, particularly at higher frequencies.

This conclusion applies equally to the proposed fatigue analysis of the Mercedes-Benz truck rims. If the truck rims were to experience any deformation or change in shape during the periods of in-service fatigue, the modal signatures would shift in an unpredictable fashion. This would make any further interpretation of the differences in modal signatures very difficult. It is sufficient to conclude that modal analysis cannot be used to quantify changes in elasticity due to fatigue damage in practical structures when those structures are subjected to unspecified wear and tear, and hence variation in shape and size.

5.2 A cracked Macchi aircraft test-sample

It was found in the previous experiment, that elongation of the aluminium sample resulted in significant changes to the modal characteristics of that sample. It was concluded that it was very difficult to identify any small frequency shifts due to fatigue damage when the physical geometry of the structure had undergone unknown change. The solution to this problem is to avoid permanent dimensional changes in the test-sample by subjecting it to a much larger number of fatigue cycles at significantly reduced stress. Unfortunately, as previously mentioned, the only available testing machine (an Instron 1195) was not designed for this type of use. The only other possibility therefore was to obtain suitably fatigued samples by other means.

A cracked sample of 7073 T6 aluminium, obtained from Hawker De Havilland Ltd., was examined to test the photothermal excitation and modal analysis techniques on a fatigued structure showing an extensive crack. The sample was unique in that it had been subjected to accelerated structural fatigue over a million or so cycles under stress conditions normally experienced by a Macchi jet whilst in routine service. The sample had been cut from a Macchi jet at 3000 flying hours and then further fatigued within the laboratory until it cracked. The cracked sample had dimensions

100.06 mm × 25.00 mm × 5.00 mm and mass 34.28 g. The sample displayed a bisecting lateral fatigue crack extending to within 2 mm of both sides from a hole and crack starter (small slots), at its centre. The sample also had two support holes located near each end. Two more samples of 7073 T6 Aluminium, obtained from two Hercules aircraft struts, were machined to duplicate the Macchi sample and thereby provide a controlled reference of the same aluminium type. Photographs of the damaged and duplicated plates are shown in plate 5.2.1.

The samples were supported as 90 mm long clamped-free cantilevers and were excited by an unfocused laser pulse at 0.85L, using the proximity sensor at 0.20L to detect the vibrations. The physical dimensions of the samples resulted in a high flexural rigidity and so the vibrations excited in the samples were of a much higher frequency than those previously examined and resulted in only slight displacements of the cantilever surface. Only the fundamental mode of vibration was detected as shown in figure 5.2.1. The two control samples presented single peaks at 433 Hz and 448 Hz and the cracked sample also showed a lone peak at 414 Hz. The frequency differences between the cracked sample and the control samples were 19 Hz and 34 Hz. Taking the average value of these frequency differences to about 25 Hz, this difference is attributed to the induced fatigue and the crack, and so represents a frequency shift due to damage of about 5½%. Because the two control samples were carefully machined to have very nearly identical dimensions and weights to that of the cracked sample, the variation in the first vibrational mode for the two control samples must be due to slight material differences between the two Hercules struts from which the controls were taken.

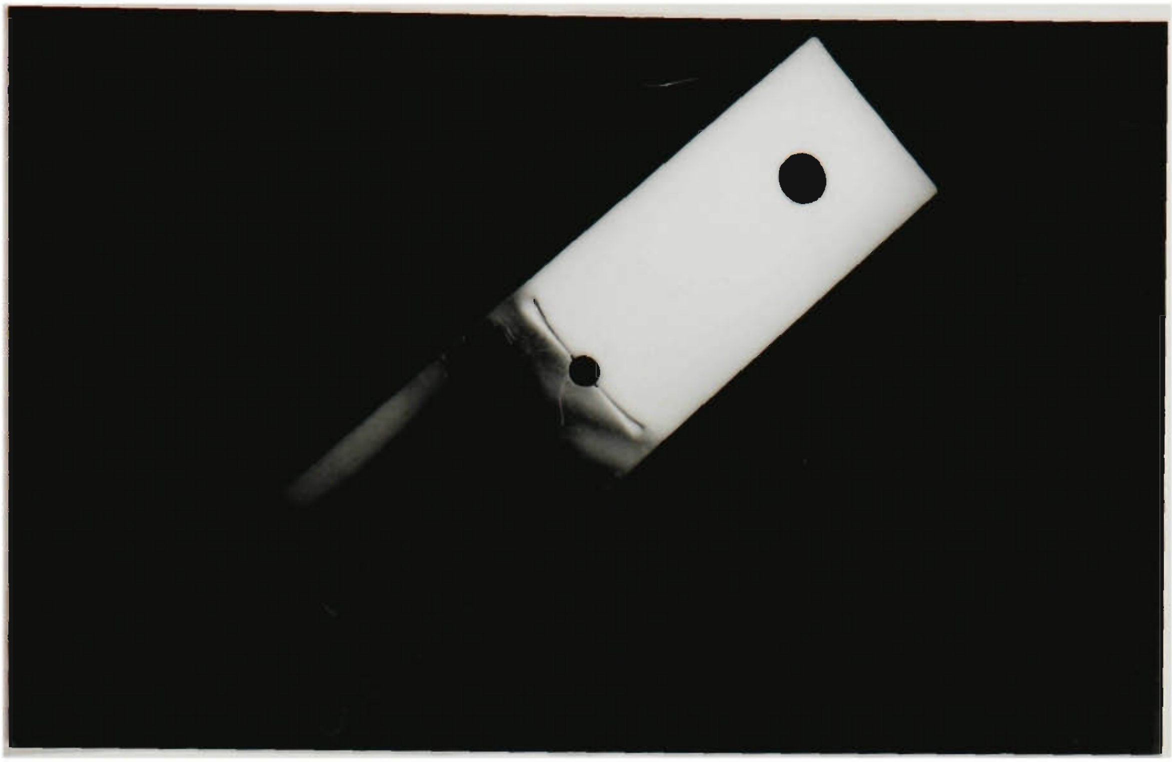

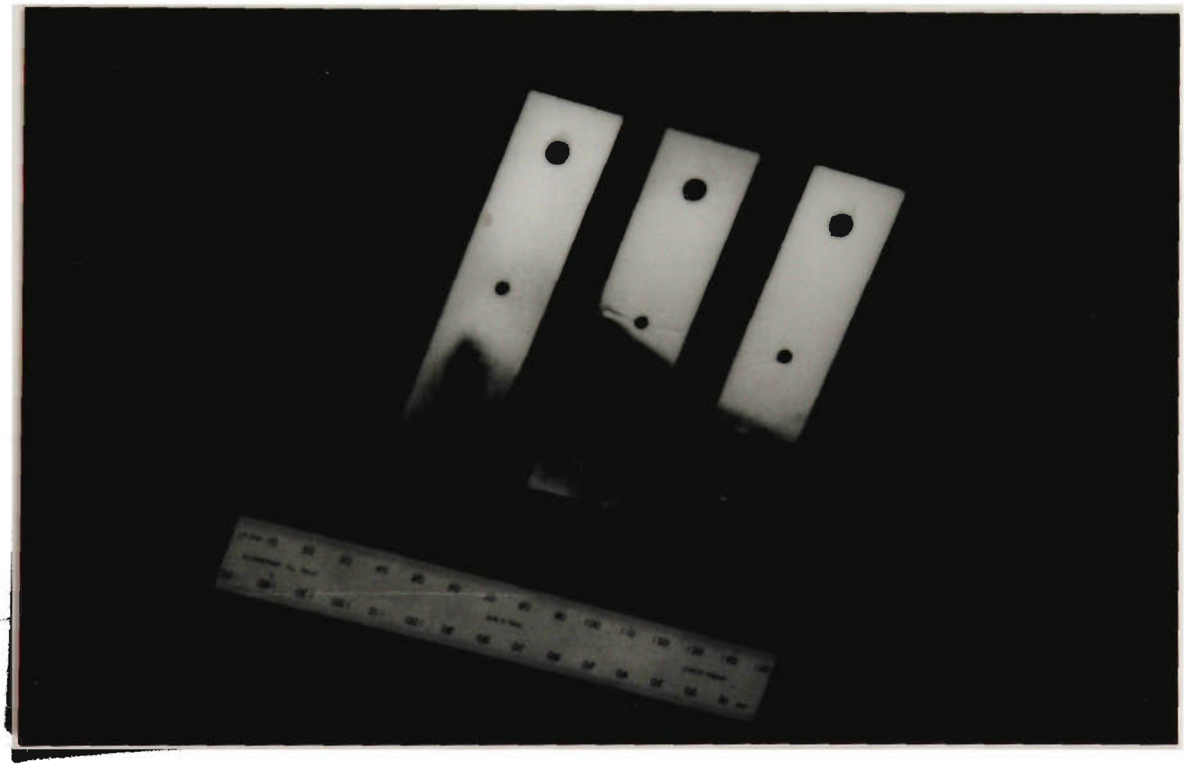

Plate 5.2.1 The upper plate shows a Macchi jet aluminium wing span sample with a bisecting lateral crack extending to within 2 mm of both sides. In the lower plate, the two control samples are shown either side of the damaged test-sample .

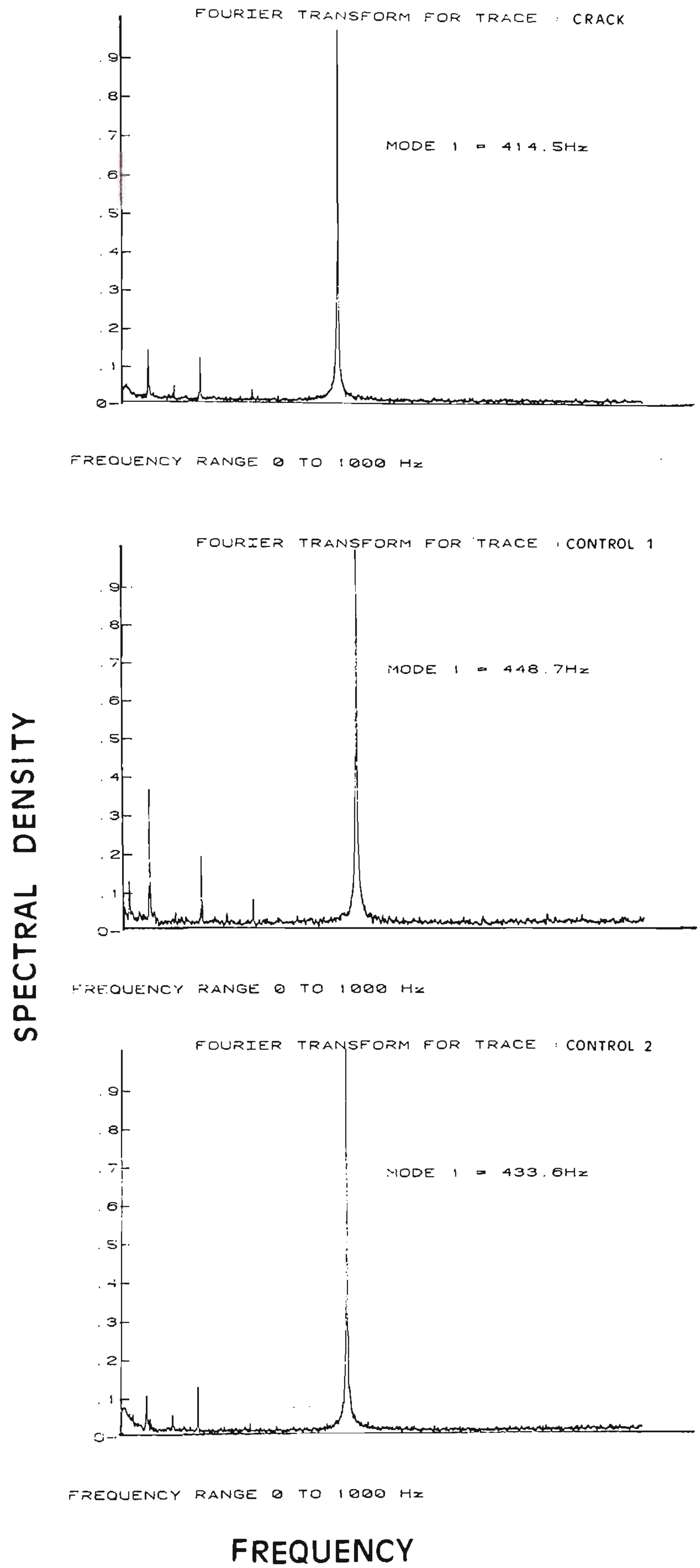

Figure 5.2.1 Frequency spectra of the cracked Macchi sample (upper) and the two control samples using single pulse laser excitation and optical detection.

This investigation highlighted one of the limitations of this method using photothermal excitation. The frequencies of the first four modes of vibration for the control samples, when mounted as cantilevers, were calculated from equation 3.1.17 (damping was assumed to be negligible) to be: 460 Hz, 2.6 kHz, 7.1 kHz and 13.9 kHz. In section 4.3.1, the unfocused Nd:glass laser pulse on 3 mm aluminium produced a rise time of approximately 0.6 ms and hence a driving frequency of about 400 Hz. The rise time for the 5 mm thick aluminium Macchi sample should be approximately the same. The period of the excitation was therefore slightly less than, but still well matched to, the fundamental mode of the clamped-free Macchi cantilever. The test-sample was therefore easily excited at the fundamental frequency. However, the higher-order modes were well outside the flexing cycle initiated by the laser irradiation and so these did not significantly contribute to the resultant vibration (equations 3.4.1.15 and 3.4.1.16}. Thus, the fact that only the first mode could be easily excited or detected, is consistent with the predictions of the analysis presented in section 3.4.1.

To investigate the modal signatures of the cracked and control samples over a greater frequency range, the samples were mounted as free-free plates on stretched rubber mounts (much like an xylophone). Three diode lasers, as described in section 4.2, were positioned above one of the plates so that their outputs were jointly focused to a single point located midway between the centre and end hole (an antinode for the even modes of vibration). The interferometric sensor monitored the reflective surface of the sample and the sensor output signal, which was clear and strong, was recorded and displayed in the frequency domain using the real-time FFT function of the Tektronix DSA 602 analyser. Despite several careful attempts, the laser diodes were unable to induce flexural motion at any of the known vibrational modes, that is, within the displacement sensitivity (1½ nm) of the interferometric sensor, in any of these plates.

The failure of the diode lasers and interferometric sensor to excite and detect vibrations in these samples can be understood by considering the characteristic frequency (f_c) described in section 4.3. The repeated pulses from the laser diodes are an efficient means of excitation when the pulse-repetition-rate is close to the characteristic frequency of the irradiated plate. f_c for the Macchi sample was calculated, using equation 4.3.1, to be 3.4 Hz. Since the effectiveness of the excitation deceases as $[1 + (f_m/f_c)^2]^{-1/4}$, when the modulation frequency (f_m) increases beyond f_c, the diode lasers were ineffective in exciting even the first mode of resonance within the free-free cantilever. The modal frequencies were calculated from equation 3.1.17, using values of $(\beta_n L)^2$ for free-free cantilever boundary conditions, [Bishop and Johnson, 1960] to be: 2.6 kHz, 7.1 kHz, 13.9 kHz and 22.7 kHz.

Having been faced with the limitations of both single and repetitive laser excitation techniques, a more conventional technique was employed, using the free-free mounting set-up described above. The plates were tapped lightly, but sharply, on their front surfaces with a small hammer to excite transverse flexural vibrations. Like an xylophone, the plates produced a sharp, clear audible ring. The sound produced from the cracked sample was qualitatively "duller" and higher pitched than that from both control samples. The frequency spectra were recorded and analysed on the DSA 602 oscilloscope using a simple microphone for a transducer and the modal frequencies were averaged over a series of 10 trials. Three modes of free-free vibration were clearly evident in the FFT spectra of the vibration profiles as shown in figures 5.2.2 and 5.2.3. Comparison of the decay rates in the vibration profiles given in these two figures, clearly shows increased damping of the fundamental mode for the cracked sample. The measured frequencies of the first three vibrational modes for both the cracked and control samples and the percentage difference between the cracked plate frequency and the average of those for the control samples, are given in table 5.2.1.

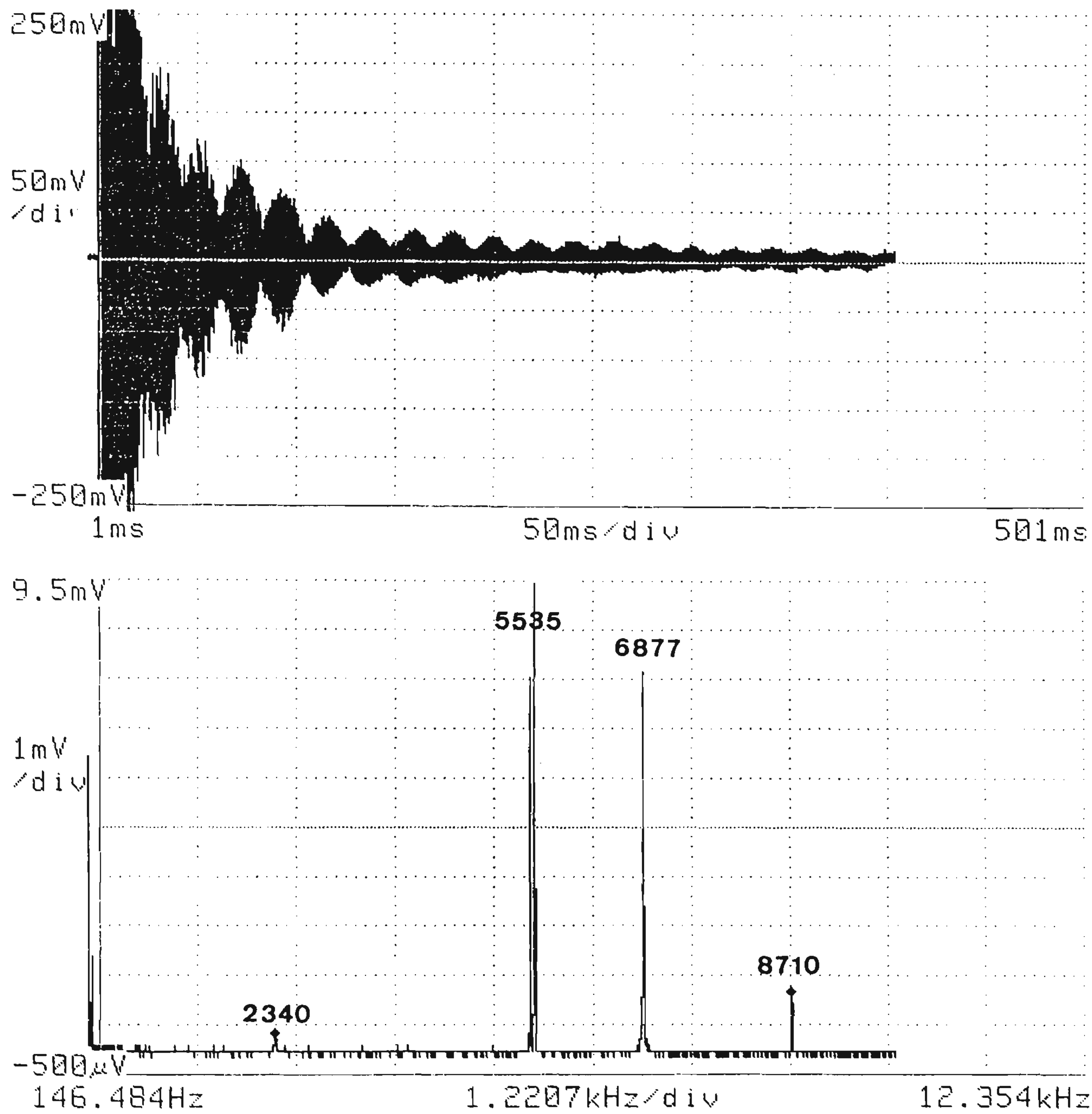

Figure 5.2.2. Vibration profile and frequency spectrum of the cracked Macchi jet test-sample using a simple hammer to excite the free-free cantilever and microphone detection.

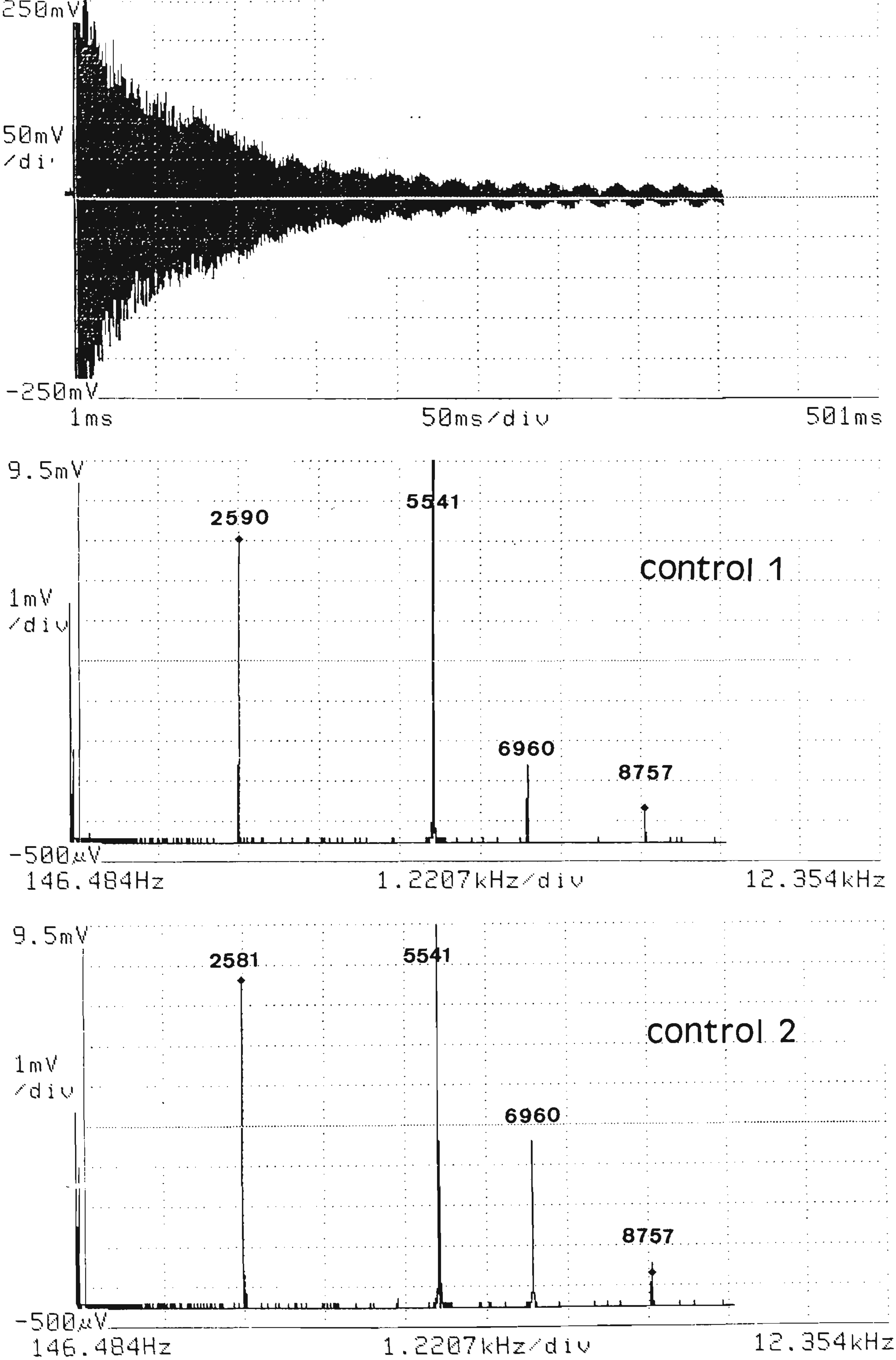

Figure 5.2.3. Typical vibration profile and the frequency spectra for the two control samples using a simple hammer to excite the free-free cantilever and microphone detection.

	CONTROL 1	CONTROL 2	CRACKED SAMPLE	Δ
Mode 1	2590 ± 1 Hz	2581 ± 3 Hz	2340 ± 3 Hz	- 9.4 %
Mode 2	6960 ± 1 Hz	6960 ± 1 Hz	6877 ± 3 Hz	- 1.2 %
Mode 3	13160 ± 10 Hz	13140 ± 10 Hz	12340 ± 10 Hz	- 6.2 %

Table 5.2.1 Modal frequencies of the cracked and control samples. Δ represents the difference between the average of the control sample frequencies and the frequency of the cracked sample.

The modal frequencies of the cracked and control samples were then calculated using finite element analysis. Finite element analysis was used since the holes and the lateral crack precluded accurate analysis by simple beam theory. The finite element analysis predicted the natural frequencies given in table 5.2.2. The predicted frequencies were consistently high in comparison with those observed (probably due to errors in the assumed values of E and ρ) and the frequency shifts less significant (approximately half); however, in both calculations and measurements the frequency shift for mode 3 was about 70% of that for mode 1.

	Mode 1	Mode 2	Mode 3	Mode 4
PREDICTED FREQUENCY (Hz)				
Simple beam	2690	7376	14370	23580
Beam with holes	2706		14190	
Beam with crack	2493	7352	13620	23350
Beam with holes and crack	2587		13760	
PREDICTED FREQUENCY SHIFT (%)				
Crack in beam with holes	- 4.4		- 3.03	

Table 5.2.2. Modal frequency predictions based on finite element analysis. Note, even modes are not calculated for holes due to half beam boundary conditions used in FE analysis.

These simple experiments with the Macchi aluminium sample have helped to demonstrate some of the practical limitations of using photothermal techniques to excite a structure for the purpose of modal analysis. The effectiveness of the single laser pulse techniques (for the Nd:glass system used) in exciting a simple aluminium structure is limited to low frequencies (< 1 kHz), where the lower-order modes of flexural vibration are close to the driving frequency of the laser excitation. For efficient low-power repetitive laser pulse excitation, the characteristic frequency must also be close to the lower-order modes of vibration.

Thus, for single-pulse excitation, the dominant driving frequency in the Fourier spectrum of the thermal bending moment in the material must be approximately matched to the frequencies of the lower-order modes of vibration. For repetitive pulse excitation, the characteristic frequency must be considered for the type and thickness of material irradiated. If these conditions cannot be satisfied, remote optical excitation methods cannot generally be used and more conventional techniques for exciting vibrations are required.

5.3 Frequency shifts due to slots and cracks

In this chapter, attempts have been made to measure modal frequency shifts produced by fatigue and cracks in samples. To simplify the experimental procedure, and to readily control the severity and location of structural damage, very thin machined slots were used to create discontinuities in a structure which simulated the presence of cracks.[Wellman 1978, Sato 1983, Cawley and Ray 1988] In this section, results are reported for the application of the non-contact optical excitation and sensing techniques to the modal analysis of cantilevers containing thin machined slot damage. The effect of this damage on modal frequencies was examined for cantilever A using unfocused single pulse irradiation. Cantilever A was subjected to damage without significant alteration to the dimensions of the structure. Although a little mass was lost through cutting slots, this would increase the modal frequencies rather than decrease them. The modal frequencies of the slotted aluminium cantilevers could equally well have been measured using low-power diode laser excitation and the interferometric sensor described in section 4.3.

Slots of constant width and varying depth were cut laterally across the face of the aluminium cantilevers to simulate flaws and cracks in the cantilevers. The modal signatures were examined and modal frequencies observed to shift, after each increment in damage, in a similar manner to that reported by other authors.[Spain et al. 1964, Nagy et al. 1978, Cawley 1985, Cawley and Ray 1988] The damage to the cantilever could be readily identified when its modal signature was compared with a standard modal signature from an undamaged sample. This technique may be used to assess the extent and location of damage in metal and composite structures,[Adams et al. 1978, Chrondros and Diamargonas 1980, Ju and Mimovich 1988] since the effect of the damage on specific modes of vibration is dependent on the location of the damage with respect to the nodal points of the vibration profile. The frequency shift for a given mode is dependent not only on the presence of damage, but also on the location of that damage with respect to the nodal points of the vibration. For example, a vibrational mode with a node at the site of damage will not contribute to the displacement of the structure at that point, and as such, that mode of vibration will not be affected by the discontinuity in flexural rigidity at that point. Conversely, the shift in a particular modal frequency will be greatest when the damage site is at an antinode of that mode. A minimum of two consecutive modal frequencies, or one odd and one even mode, are therefore required to test for the presence of damage or structural variations in a "go/no go" evaluation. The measurement of three modal frequencies can sometimes be used to determine the approximate location of the damage in simple structures.[Akgün et al. 1984, Ju and Mimovich 1988] However, as the cantilever is damaged, the mode shapes and therefore the position of the nodes and antinodes of a specific mode of vibration also change.

In this experiment, changes were detected and measured in four of the modal frequencies of two identical aluminium cantilevers as a result of thin slots of width 0.4 mm cut across their breadth. One cantilever was damaged at a location which did not correspond to a node for any of the first four vibration modes (200 mm from the clamp; 0.67L) and hence damage at this location affected all of these modes. The other cantilever was damaged at a position corresponding to a node for all odd modes except the fundamental (150 mm from the clamp; 0.50L). In the latter case, it was expected that the damage would not produce modal frequency shifts for odd modes (other than the first). Measurements were made of the modal frequencies of the first four modes as the cantilevers were subjected to increasing damage by increasing the depth of the slots. The cantilevers were slotted laterally, by depth increments of 0.3 mm, until 80% of the cross-sectional area had been removed, and the modal signature was recorded after each increment in slot depth with a precision of ± 0.6 Hz. The enhanced precision of this experiment, in comparison to the ± 2 Hz reported in section 5.1, was achieved by using the Tektronix DSA 602 in enhanced accuracy mode for 16,368 vibration data points.

Numerical results, showing reductions in modal frequencies with damage to the cross-sectional area, are given in table 5.3 and figure 5.3.1. Figure 5.3.2 presents the data of figure 5.3.1 in a manner which shows the magnitudes of the shifts rather than the absolute frequencies of the various modes. Slot damage at x = 0.50L caused frequency reduction in the 1st, 2nd and 4th modes. The 3rd mode remained unaffected. Slot damage at 0.67L caused a reduction in the frequency of all modes. In the latter case, a node for the 4th mode was only 10 mm away from the slot location and this mode had the least frequency reduction. These results clearly demonstrate the potential of this technique for non-destructive testing, although the frequency shifts are relatively small for the low-order modes unless there is significant damage to the structure.

(a) Slot at 0.50L:

DEPTH (mm)	DAMAGE (%)	MODE 1:SHIFT (Hz)	MODE 2:SHIFT (Hz)	MODE 3:SHIFT (Hz)	MODE 4:SHIFT (Hz)
0	0	25.63 : 0	163.6 : 0	456.5 : 0	896.0 : 0
0.3	10.07	25.63 : 0	163.6 : 0	456.5 : 0	896.0 : 0
0.6	20.13	25.63 : 0	162.4 : 1.2	456.5 : 0	888.7 : 7.3
0.9	30.20	25.63 : 0	161.1 : 2.5	456.5 : 0	882.6 : 13.4
1.2	40.27	25.63 : 0	158.7 : 4.9	456.5 : 0	871.6 : 24.4
1.5	50.34	25.63 : 0	155.0 : 8.6	456.5 : 0	854.5 : 41.5
1.8	60.40	25.63 : 0	146.5 : 17.1	456.5 : 0	817.9 : 78.1
2.1	70.47	24.41 : 1.22	134.3 : 29.3	456.5 : 0	775.1 : 120.9
2.4	80.54	23.19 : 2.44	116.0 : 47.6	456.5 : 0	725.1 : 170.9

(b) Slot at 0.67L:

DEPTH (mm)	DAMAGE (%)	MODE 1:SHIFT (Hz)	MODE 2:SHIFT (Hz)	MODE 3:SHIFT (Hz)	MODE 4:SHIFT (Hz)
0	0	25.63 : 0	163.6 : 0	456.5 : 0	896.0 : 0
0.3	10.07	25.63 : 0	163.6 : 0	456.5 : 0	896.0 : 0
0.6	20.13	25.63 : 0	162.4 : 1.2	454.1 : 2.4	894.8 : 1.2
0.9	30.20	25.63 : 0	161.1 : 2.5	449.2 : 7.3	893.6 : 2.4
1.2	40.27	25.63 : 0	159.9 : 3.7	441.9 : 14.6	893.6 : 2.4
1.5	50.34	25.63 : 0	157.5 : 6.1	434.6 : 21.9	891.1 : 4.9
1.8	60.40	25.63 : 0	150.1 : 13.5	412.6 : 43.9	889.9 : 6.1
2.1	70.47	25.63 : 0	133.1 : 30.5	376.0 : 80.5	883.8 : 12.2
2.4	80.54	24.41 :1.22	116.0 : 47.6	338.1 : 118.4	875.2 : 20.8

Table 5.3 Modal frequency shift with cross-sectional slot damage at (a) 0.50L and (b) 0.67L for a 3 mm thick aluminium cantilever.

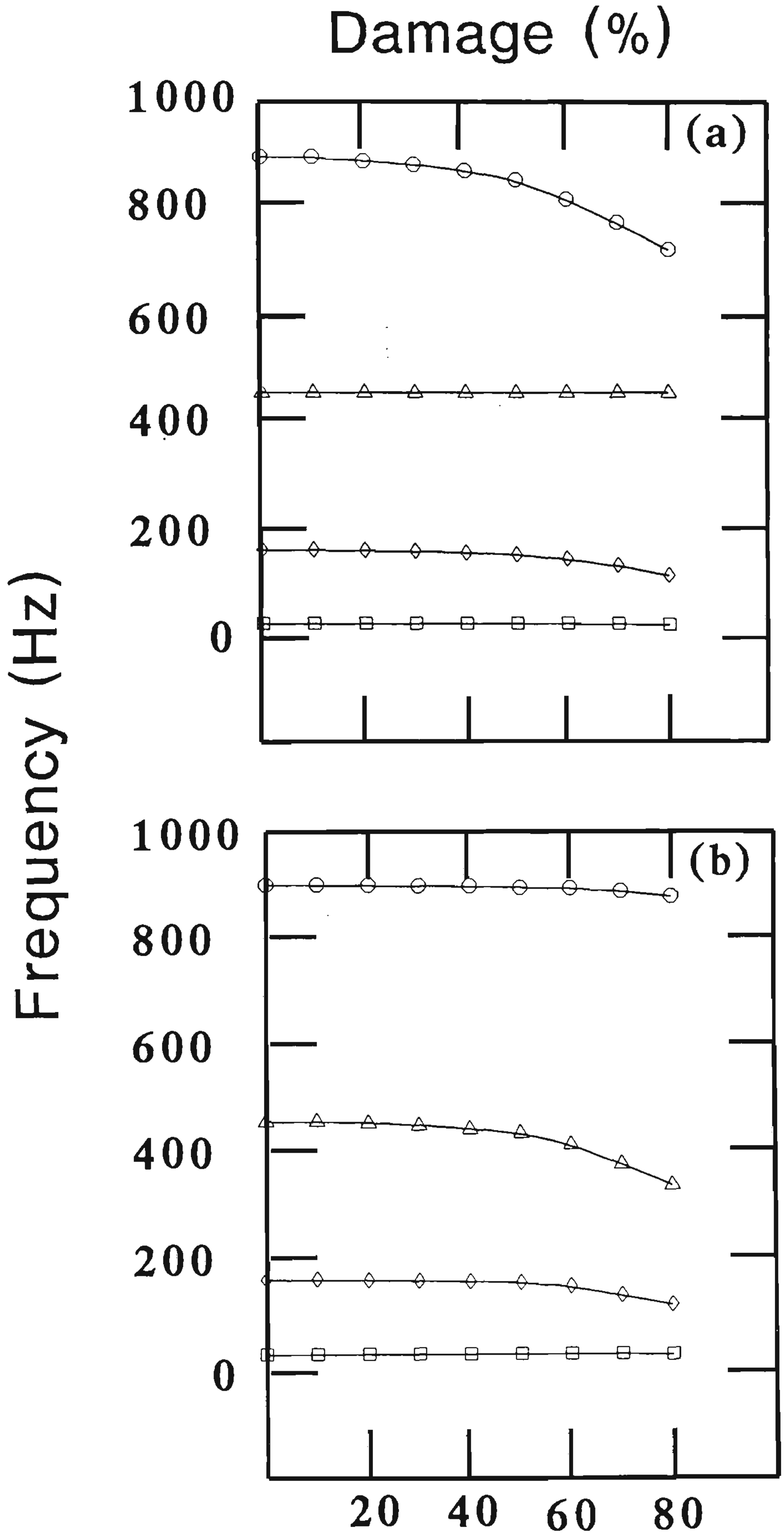

Figure 5.3.1 Modal frequency variation with percentage of cross-sectional damage for the first four modes of vibration of an aluminium cantilever. (a) Slot at 0.50L; (b) slot at 0.67L. □ , Mode 1; ◇ , Mode 2; Δ , Mode 3; ○ , Mode 4.

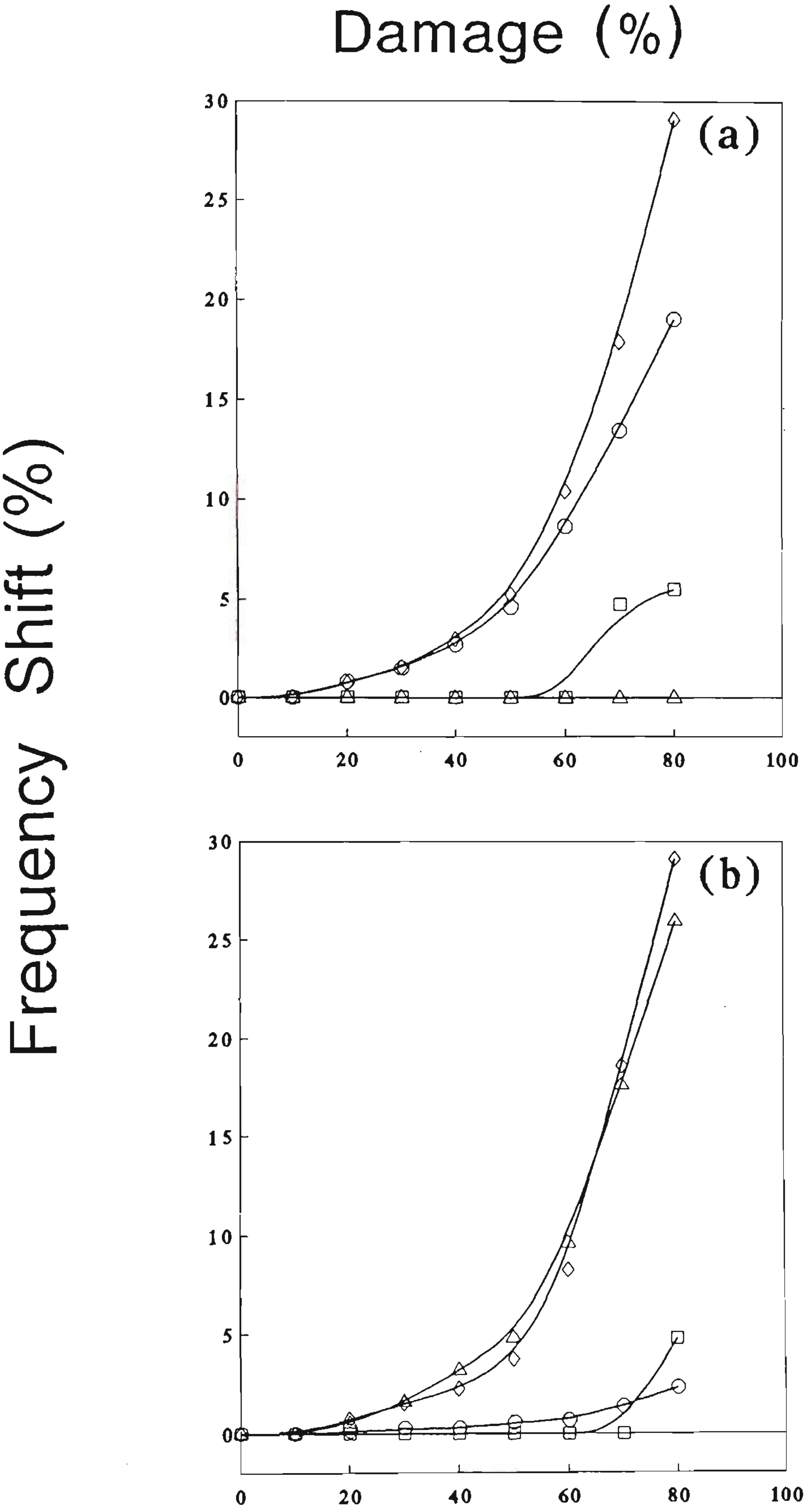

Figure 5.3.2. The percentage shift in modal frequency with percentage of cross-sectional damage for the first four modes of vibration of an aluminium cantilever. (a) Slot at 0.50L; (b) slot at 0.67L. □ , Mode 1; ◇ , Mode 2; Δ , Mode 3; ○ , Mode 4.

Chapter 6

Conclusion

A new technique for the non-contact laser excitation and optical detection of mechanical vibrations in structures has been described in this thesis. This technique does not damage the surface of the structure. Experiments have been conducted and models have been developed, which show that the physical mechanism of the laser excitation, using a single high-energy pulse with a power density below the ablation threshold of the irradiated material, is consistent with a rapidly-produced thermal bending moment at the site of the laser irradiation. The differential equation for the motion of the structure during, and after, this excitation has been formulated. The solutions of this have been used to explain the variations observed in the efficiency of the process for different structures and irradiation conditions.

It was found that heating the front surface of a structure with a single sub-ablative laser pulse resulted in a bending moment being rapidly applied by differential expansion of the front and rear surfaces. The laser-induced moment produced an angular displacement of the structure at the irradiation site and the structure's consequent motion was described by a dynamic equation for angular displacement of the mid-plane axis as a function of time. The laser-induced flexing initiated vibration at the natural frequencies of the structure, as well as at frequencies determined by the driving term. The excitation was most effective when the dominant frequency in the spectral profile of the thermally-induced bending moment was matched, or was close to, one of the lower-order modes of free vibration. Immediately after laser-excitation of the structure, travelling waves propagate away from the irradiation site and flexural modes of vibration are not produced until reflections of these waves have generated standing wave patterns. The location of the laser irradiation site is only important if the time taken to establish a standing wave pattern for a particular frequency is less than the total duration of the laser-induced moment. When this is the case, if the laser irradiation site is chosen at the node of a specific mode in the bending moment profile, then that mode will be preferentially suppressed with respect to other vibrational modes. Similarly, if an antinode of a specific mode is targeted, the amplitude of that mode of vibration will be maximised. When the duration of the applied moment is less than the time required to establish a standing wave pattern, the position of the irradiation site has little effect on the modal amplitudes of free vibration.

Experiments, which attempted to enhance or suppress a particular mode of vibration, showed that there was little to be gained by using complex beam-splitting arrangements with a single laser pulse. A single high-energy pulse was more effective than dual pulses at half the laser energy.

The single laser pulse excitation process has been shown to be remarkably effective at exciting free vibration in even very large structures. Although most experiments have been conducted using cantilevers (because of the simplicity of the modal characteristics and the frequency calculations), it has been shown that even a steel truck wheel rim was well-excited using this method.

A very effective optical fibre proximity sensor was developed for non-contact measurement of the modal spectra of the vibrating structures. The proximity sensor was a simple and easily constructed intensity-modulated device, which detected small variations in proximity between a vibrating surface and the sensor tip. Vibrational amplitudes up to about 0.2 mm were detected with reasonable linearity and the minimum vibration amplitude which could be detected was approximately 1 μm when the sensor tip was 50 μm from the vibrating surface. When combined with laser excitation, this allowed for totally remote modal analysis of the laser vibrated structure.

The modal frequencies of the vibrating structure depend on the size, shape and structural integrity of the sample being investigated. A change in any of these parameters will give rise to shifts in the frequencies of the vibrational modes. A number of investigations, using periodically-stretched cantilevers, cracked test-samples and cantilevers with machined slots, applied these new techniques to detect damage and/or dimensional change in these structures. The results reported for the stretched and slotted cantilevers are for quite significant damage rather than very small cracks because of the difficulty of preparing slightly damaged samples with available equipment. The technique thus appears relatively insensitive to minor cross-sectional damage. In fact this is the case as damage of the order of 20% is required to produce frequency shifts of the order of 1 to 7 Hz in the various modes. It should be noted, however, that greater sensitivity would be achieved under conditions which allowed better resolution of the modal frequencies (longer sampling records). The low sensitivity is mainly due to the small changes in frequency of the resonant modes with damage. This is thus a limitation of the technique of modal analysis using any method of excitation and sensing. In fact the optical sensing technique developed in this thesis has been shown to have better resolution than contact sensors such as strain gauges. The optical excitation and sensing techniques developed in this thesis will find application in any situation in which conventional modal analysis techniques are suitable and particularly in situations in which the non-contact non-damaging advantages are relevant.

The low-power limit for the modal analysis of structures using optical excitation techniques has also been investigated. Repetitively pulsed diode lasers, tuned to a resonance of a structure, have been used to measure the resonant frequencies of forced oscillation which are the same as the modal frequencies of free vibration. Simultaneous excitation of more than one antinode on the structure's bending moment profile significantly increased the amplitude of the resonant flexural oscillations. This diode laser technique was most efficient when the thermal characteristic frequency of the irradiated structure was close to the lower-order modes of structural vibration. It has been shown that this technique can also be used to both excite and detect structural resonance from behind a glass window at a range of 1 metre; provided that a very sensitive method is available for measurement of the small vibrations. An optical fibre interferometer was developed for this purpose. This could be used at a large range without need for complicated alignment and had a minimum amplitude sensitivity of 0.3 nm (MDPS of 2.4 mrad) for a practical signal-to-noise ratio of 2. Both the vibration sensors described in this work are relatively simple and cost-effective alternatives to many of the established contact vibration detection techniques commonly used for high resolution frequency analysis.

To the knowledge of this author, neither the mechanism nor the demonstration of photo-thermoelastic structural excitation, using single laser pulses (single or multiple irradiation sites) below the surface ablation threshold of the irradiated structure, have been previously reported. Similarly, no previous work has been reported on the use of repetitive low-power diode laser pulses to excite structural resonances in large structures, such as the cantilevers described in this thesis.

Symbols used in the thesis

a	general constant
A	cross-sectional area
A	general constant
A_n	mode dependent constant for angular harmonic oscillation
b	width of a rectangular cross-section or cantilever
B	general constant
B_n	mode dependent damping decay constant
c	velocity of light
c	specific heat
C, C_1, C_2	general constants
C1, C2	50:50, 2×2 directional couplers
d	Gaussian radius of the laser profile
D	general constant
D1, D2	Germanium photo-detectors
E	energy
E	Young's modulus of elasticity
$\tilde{E}_0(t)$	time varying electric field vector of the source
$\tilde{E}_i(t)$	time varying electric field vector at the i^{th} detector
f	frequency
f_c	characteristic frequency
f_d	driving frequency
f_m	modulation frequency
f_n	frequency of a specific mode of vibration

$F(t)$	absorbed power density at the centre of a laser spot as a function of time
F_{max}	maximum absorbed power density at the centre of a laser spot
G	a specific point on the mid-plane of a cantilever (immediately below centre of a laser spot) which represents the centre-of-mass of the surrounding section
G-N	mid-plane of a cantilever
$\mathbf{h}$	Planck's constant
h	thickness
$H(t)$	force as a function of time
$\mathbf{I}_G$	moment of inertia of the rotating section about G
I	second moment of area
J	reduction factor
$\mathbf{k}$	specific momentum transfer co-efficient
k	an integer
$k_{i(t\ or\ c)}$	the complex amplitude co-efficients for the i^{th} directional coupler, t denotes the transmitted beam, c the coupled beam
$k'_{i(t\ or\ c)}$	the real amplitude co-efficients for the i^{th} directional coupler
K	thermal conductivity
l_f	latent heat of fusion
l_v	latent heat of vaporisation
L	length of a section or a cantilever
m	mass
m_g	mass of gas
m_w	molecular weight
$M(x,t)$	bending moment as a function of position and time
$M(\chi)$	bending moment of a layer at a measured distance from the mid-plane
M_A	applied moment

M_R	restoring moment
M_{max}	maximum bending moment
n	an integer called the "mode number"
N	power loss per unit area due to thermal diffusion
O	origin
p	momentum
P(t)	normalised laser power profile as a function of time
Q	rate of heat production
Q(x,y,z,t)	rate of heat production per unit volume
$\mathbf{R}_g$	universal gas constant
R(T)	reflectivity as a function of temperature
s	displacement
S	shear force
t	time
t_p	laser pulse duration
T_0	temperature difference above ambient temperature
T_b	boiling temperature
T(x,y,z,t)	temperature as a function of planar position, depth and time
$T(\chi)$	mean temperature of a layer at a given distance from the mid-plane
v	the propagation velocity of a travelling transverse wave on a cantilever
v_{ss}	steady state gas velocity
U	mode dependent constant
V(t)	amplitude of the signal voltage and a function of time
V_{max}	maximum signal amplitude
W	mode dependent constant

x	position
$y(x,t)$	cantilever displacement as a function of position and time
y_L	initial displacement of a clamped-free cantilever at $x = L$
z	depth
α	surface expansion co-efficient
α_{1n}, α_{2n}	general constants pertaining to the nth mode
β_n	mode dependent characteristic number
γ	mechanical damping decay constant
Γ	degree of coherence (complex number)
δ	total strain (also used to indicate a small change in......)
Δ	a change in ....
ε	strain
$\varepsilon(\chi)$	strain in a layer at a given distance from the mid-plane
ζ	dimensionless depth related variable
η	dimensionless radius related variable
$\Theta(\zeta,\eta,\tau)$	dimensionless temperature function
$\theta(t)$	angular displacement as a function of time
κ	thermal diffusivity
λ	optical wavelength
Π_0	irradiance at the source
Π_i	irradiance at the i^{th} detector
ρ	density
σ	stress
$\sigma(\chi)$	stress in a layer at a given distance from the mid-plane
Υ	dimensionless time related variable.

Υ'	dimensionless variable related to the propagation time of a thermal source
Υ_p	dimensionless variable related to the duration of a laser pulse
τ	time constant.
$\tau_{a \text{ or } b}$	propagation time in the signal arm (a) or reference arm (b)
ϕ	phase angle
$\phi_{a \text{ or } b}$	phase of the signal arm (a) or reference arm (b) at C2. Coupler phase shifts are not included.
$\phi(t)$	phase as a function of time
χ	distance from the mid-plane
ω	angular frequency
ω'	angular frequency of a damped system
ω_d	angular frequency of the driving term
ω_n	angular frequency of an undamped vibrational mode
ω'_n	angular frequency of an damped vibrational mode
$\odot$	centre of curvature
i	$\sqrt{-1}$
e	exponential constant 2.718
$\Re e$	real part of a complex number
$\mid \ \mid$	modulus
$< >$	time average
*	complex conjugate

References

Adams R.D. and Bacon D.G.C. (1973)
Measurement of flexural damping capacity and dynamic Young's modulus of metals and reinforced plastics
Journal of Physics D: Applied Physics 6: 27-41

Adams R.D. and Cawley P. (1988)
Defect types and non-destructive testing techniques for composites and bonded joints
NDT International 21: 208-222

Adams R.D., Cawley P., Pye C.J. and Stone B.J. (1978)
A vibration technique for non-destructively assessing the integrity of structures.
Journal of Mechanical Engineering Science 20(2): 93-100.

Adams R.D. and Coppendale J. (1976)
Measurement of elastic moduli of structural adhesives by a resonant bar technique
Journal of Mechanical Engineering Science 18(3): 149-158

Adams R.D., Walton D., Flitcroft J.E. and Short D. (1975)
Vibration testing as a non-destructive test tool for composite materials
Composite Reliability, American Society for Testing and Materials STP 580: 159-175

Aindow A.M., Cooper J.A., Dewhurst R.J. and Palmer S.B. (1983)
Crack depth estimation using wide-band laser generated surface acoustic waves
Proceedings of the 1983 Ultrasonics International Conference, Butterworth Scientific, London, 1983 pp.20-24

Aindow A.M., Dewhurst R.J., Hutchins D.A. and Palmer S.B. (1979)
The efficient production of acoustic pulses at free metal surfaces by Q-switched lasers
Proceedings of the IEEE 4th Quantum and Electronics Conference, Edinburgh 1979, pp. 255-258

Aindow A.M., Dewhurst R.J., Hutchins D.A. and Palmer S.B. (1980)
Characteristics of a laser-generated acoustic pulse in metals
Society of Photo-optical Instrumentation Engineers: 1980 European Conference on Optical Systems and Applications, Utrecht 236: 478-485

Aindow A.M., Dewhurst R.J., Hutchins D.A. and Palmer S.B. (1981)
Laser-generated ultrasonic pulses at free metal surfaces
Journal of the Acoustical Society of America 69(2): 449-455

Aindow A.M., Dewhurst R.J. and Palmer S.B. (1982)
Laser-generation of directional surface acoustic wave pulses in metal
Optics Communications 42(2): 116-120

Aindow A.M., Dewhurst R.J., Palmer S.B. and Scruby C.B. (1984)
Laser-based non-destructive testing techniques for the ultrasonic characterisation of sub-surface flaws
NDT International 17(6): 329-335

Akgün M., Ju F.D. and Paez T.L. (1984)
A general theory of circuit analogy in fracture diagnosis
University of New Mexico, Bureau of Engineering Research ME124(84)AFOSR-993-1, AFOSR-TR-84-0910

Alexander J.C. and Nurmikko A.V. (1973)
Excitation of thin elastic membranes by momentum transfer of laser light
Optics Communications 9(4): 404-406

Aluminium Development Council of Australia (1988)
Aluminium standards and data for the annealing and age-hardening of wrought aluminium products
Australian Government Publications, 1988.

Anderholm N.C. (1970)
Laser generated stress waves
Applied Physics Letters 16(3): 113-115

Andres M.V., Foulds J.W.H. and Tudor M.J. (1986)
Optical activation of a silicon vibrating sensor
Electronic Letters 22(21): 1097-1099

Aprahamian R. and Evensen D.A. (1970)
Applications of holography to dynamics: high frequency vibration of plates
Transactions of the ASME: Journal of Applied Mechanics December: 1083-1090

Ash E.A., Dieulesaint E. and Rakouth H. (1990)
Generation of surface acoustic waves by means of a C.W. laser
Electronics Letters 16(12): 470-472

Askar'yan G.A., Prokhorov A.M., Chanturiya G.F. and Shipulo G.P. (1963)
The effects of a laser beam in liquid
Soviet Journal of Experimental and theoretical Physics 17(6): 1463-1465

Bar-Cohen Y. (1979)
Non-destructive testing of microwelds using laser-induced shock waves
British Journal of NDT, March: 76-78

Bell A.G. (1880)
On the production and reproduction of sound by light
American Journal of Science 20(118): 305-324

Bentham J.P. and Koiter W.T. (1973)
Asymptotic approximation to crack problems
in Mechanics of Fracture I, Methods of analysis and solutions of crack problems,ed. Sih G.C., Noordhoff International,Leyden,1973, pp.155-158

Bishop R.E.D. and Johnson D.C. (1960)
The Mechanics of Vibration
Cambridge University Press, Melbourne 1979

Bondarenko A.N., Drobot Yu.B. and Kruglov S.V. (1976)
Optical excitation and detection of nanosecond acoustic pulses in non-destructive testing
Soviet Journal of Non-destructive Testing 12: 655-658

Bourkoff E. and Palmer C.H. (1985)
Low-energy optical generation and detection of acoustic pulses in metals and non-metals
Applied Physics Letters 46(2): 143-145

Bowers J.E. (1982)
Fiber-optical sensor for surface acoustic waves
Applied Physics Letters 41(3): 231-233

Bray D.E., Dalvi N.G. and Finch R.D. (1973)
Ultrasonic flaw detection in model railway wheels
Ultrasonics, March: 66-72

Brienza M.J. and DeMaria A.J. (1967)
Laser-induced microwave sound by surface heating
Applied Physics Letters 11(2): 44-46

Brown D.A., Cameron C.B., Keolian R.M., Gardner D.L. and Garrett S.L. (1991)
A symmetric 3×3 coupler based demodulator for fiber optic interferometric sensors
Society of Photo-optical Instrumentation Engineers: Fiber Optic and Laser Sensors IX, 1584: 328-335

Bruinsma A.J.A. (1987)
Non-contact detection of pulsed acoustic displacements for the evaluation of sub-surface defects
Society of Photo-optical Instrumentation Engineers: Fiber Optic Sensors II, 798: 76-81

Bryant L.E. and McIntire P. eds. (1985)
Nondestructive testing Handbook
American Society for Nondestructive Testing, Columbus, OH, 2 edn. 1985

Bruinsma A.J.A. and Jongeling T.J.M. (1989)
Some other applications for fibre optic sensors
Optical Fibre Sensors: Systems and Applications Volume 2, Culshaw B. and Dakin J. eds., Artech House, USA 1989, pp. 721-765

Buchhave P. (1975)
Laser doppler vibration measurements using variable frequency shift
DISA Information Bulletin 18: 15-20

Budenkov G.A. and Kaunov A.D. (1979)
The excitation of elastic waves in solids by means of a laser beam due to the thermoelastic effect
Ninth World Conference on Non-destructive Testing, Melbourne, PAPER #4A-14

Burger C.P., Dudderar T.D., Gilbert J.A., Peters B.R. and Smith J.A. (1987)
Laser excitation through fiber optics for NDE
Journal of Non-destructive Evaluation 7(1): 57-64

Bushnell J.C. and McCloskey D.J. (1968)
Thermoelastic stress production in solids
Journal of Applied Physics 39(12): 5541-5546

Carome E.F., Clark N.A. and Moeller C.E. (1964)
Generation of acoustic Signals in liquids by ruby laser-induced thermal stress transients
Applied Physics Letters 4(6): 95-97

Carslaw H.S. and Jaeger J.C. (1946)
Conduction of Heat in Solids
Oxford University Press 2nd edition, London 1959

Cawley P. (1985)
Non-destructive testing of mass produced components by natural frequency measurements
Proceedings of the Institution of Mechanical Engineers 199(B3): 161-168

Cawley P. (1987)
Rapid production quality control by vibration measurements
Materials Evaluation 45: 564-568

Cawley P. and Adams R.D. (1978)
The predicted and experimental natural modes of free-free CFRP plates
Journal of Composite Materials 12: 336-347

Cawley P. and Adams R.D. (1979)[a]
The location of defects in structures from measurements of natural frequencies
Journal of Strain Analysis 14(2): 49-57

Cawley P. and Adams R.D. (1979)[b]
A vibration technique for non-destructive testing of fibre composite structures
Journal of Composite Materials 13: 161-175

Cawley P. and Ray R. (1988)
A comparison of natural frequency changes produced by cracks and slots
Transactions of the ASME: Journal of Vibration, Acoustics, Stress, and Reliability in Design 110: 366-370

Cawley P., Woolfrey A.M. and Adams R.D. (1985)
Natural frequency measurements for production quality control of fibre composites
Composites 16(1): 23-27

Charpentier P., Lepoutre F. and Bertrand L. (1982)
Photoacoustic measurements of thermal diffusivity description of the "drum effect"
Journal of Applied Physics 53(1): 608-614

Chitnis V.T., Kumar S. and Sen D. (1989)
Optical fiber sensor for vibration amplitude measurement
Journal of Lightwave Technology 7(4): 687-691

Chondros T.G. and Dimarogonas A.D. (1980)
Identification of cracks in welded joints of complex structures
Journal of Sound and Vibration 69(4): 531-538

Cielo P., Nadeau F. and Lamontagne (1985)
Laser generation of convergent acoustic waves for materials inspection
Ultrasonics 23: 55-62

Clark S.E. and Emmony E.C. (1989)
The early detection of laser-induced damage
Journal of Physics E: Scientific Instruments 22:466-475

Cook R.O. and Hamm C.W. (1979)
Fiber optic lever displacement transducer
Applied Optics 18(19): 3230-3241

Cookson R.A. and Bandyopadhyay P. (1978)
Mechanical vibration measurements using a fibre optic laser-doppler probe
Optics and Laser Technology February: 33-36

Cooper J.A.,Crosbie R.A.,Dewhurst R.J.,McKie A.D.W. and Palmer S.B. (1986)
Surface acoustic wave interactions with cracks and slots: a non-contacting study using lasers
IEEE Transactions: Ultrasonics, Ferroelectrics, and Frequency Control 33(5): 462-470

Crosbie R.A., Dewhurst R.J. and Palmer S.B. (1986)
Flexural resonance measurements of clamped and partially clamped disks excited by nanosecond laser pulses
Journal of Applied Physics 59(6): 1843-1848

Dakin J. and Culshaw B. eds. (1989)
Optical Fibre Sensors: Volumes I & II
Artech House, USA 1989

Davies D.E.N. and Kingsley S.A. (1974)
Method of phase-modulating signals in optical fibres: application to optical-telemetry systems
Electronics Letters 10(2): 21-22

Davis R., Henshell R.D. and Warburton G.B. (1972)
A Timoshenko beam element
Journal of sound and vibration 22(4): 475-487

Deferrari H.A., Darby R.A. and Andrews F.A. (1967)
Vibrational displacement and mode-shape measurement by laser interferometer
Journal of the Acoustical Society of America 42(5): 982-985

Dewhurst R.J. (1983)
A hand-held laser-generator of ultrasonic pulses
Non-destructive Testing Communications 1: 93-103

Dewhurst R.J. Hutchins D.A. and Palmer S.B. (1982)
Quantitative measurements of laser-generated acoustic waveforms
Journal of Applied Physics 53(6): 4064-4071

Dimarogonas A.D. and Papadopoulos C.A. (1983)
Vibration of cracked shafts in bending
Journal of Sound and Vibration 91(4): 583-593

Drain L.E., Speake J.H. and Moss B.C. (1977)
Displacement and vibration measurement by laser interferometry
Society of Photo-optic Instrumentation Engineers: 1st European Congress on Optics Applied to Metrology 136: 52-57

Eastep F.E. and Hemmig F.G. (1982)
Natural frequencies of circular plates with partially free, partially clamped edges
Journal of Sound and Vibration 84(3): 359-370

Edwards K.A., Tobin R.C. and Koss L.L. (1983)
Selective excitation of modes of vibration by means of a laser
Journal of Sound and Vibration 90(3): 452-455

Ellis R. (1988)
Digital signal processing in AmigaBasic
Amazing Computing 3(10): 65-72

Elmore W.C. and Heald M.A. (1969)
The Physics of Waves
McGraw-Hill Book Company, New York, 1969

Falconer J.E. (1987)
Micromachining of silicon for sensor devices
GEC Journal of Research 5(3): 189-191

Felix M.P. (1974)
Laser-generated ultrasonic beams
Review of Scientific Instruments 45(9): 1106-1108

Fox J.A. (1974)
Effect of water and paint coatings on laser irradiated targets
Applied Physics Letters 24(10): 461-464

Fox J.A. and Barr D.N. (1973)
Laser-induced shock effects in plexiglass and 6061-T6 aluminium
Applied Physics Letters 22(11): 594-596

Frost H.M. (1979)
Electromagnetic-ultrasound transducers: principles, practice and applications
Physical Acoustics, Mason W.P. and Thurston R.N. eds., Academic Press, New York 1979, 14: 179-275

Gaukroger D.R., Heron K.H. and Skingle C.W. (1974)
The processing of response data to obtain modal frequencies and damping ratios
Journal of Sound and Vibration 35(4): 559-571

Gournay L.S. (1966)
Conversion of electromagnetic to acoustic energy by surface heating
Journal of the Acoustical Society of America 40(6): 1322-1330

Green R.E. Jr. (1985)
Ultrasonic materials characterisation
Proceedings of the Ultrasonics International 1985 Conference,Brighton U.K. pp. 11-13

Green R.E. Jr. (1987)
Ultrasonic non-destructive materials characterisation
Materials Analysis by Ultrasonics:Metals,Ceramics,Composites. Vary A. ed., Noyes Data Corporation, New Jersey U.S.A. pp. 1-29

Halliwell N.A. (1979)
Laser-doppler measurement of vibrating surfaces: a portable instrument
Journal of Sound and Vibration 62(2): 312-315

Halstead H.J., Harris D.A. and Peckham I.A. (1969)
A Course in Pure and Applied mathematics
Macmillan, Australia 2nd Ed.,1967

Hane K. and Hattori S. (1990)
Photothermal bending of a layered sample in plate form
Applied Optics 29(1): 145-150

Hane K., Kanie T. and Hattori S. (1988)[a]
Photothermoelastic probing for a clamped plate sample
Applied Optics 27(2): 386-392

Hane K., Kanie T. and Hattori S. (1988)[b]
Photothermoelastic imaging at a flexural resonance frequency of a clamped plate sample
Journal of Applied Physics 64(4): 2229-2232

Hartman W.F., Forrestal M.J. and Bushnell J.C. (1972)
An experiment on laser-generated stress waves in a circular elastic ring
Transactions of the ASME: Journal of Applied Mechanics March: 119-123

Heritier J.M. and Seigman A.E. (1983)
Picosecond measurements using photoacoustic detection
IEEE: Journal of Quantum Electronics 19(10): 1551-1558

Hettche L.R., Schriempf J.T. and Stegman R.L. (1973)
Impulse reaction resulting from the in-air irradiation of aluminium by a pulsed CO2 laser
Journal of Applied Physics 44(9): 4079-4085

Hockaday B.D., Walters J.P. and Leonberger F.L. (1990)
All-optical pressure transducer with low temperature sensitivity
Presented at the 7th Optical Fibre Sensors Conf., Sydney, Dec.2-6, 1990 as a post-deadline paper

Hora H. (1973)
Momentum transfer to laser-irradiated targets, indicating the nonlinear interaction force
Applied Physics Letters 23(1): 39-40

Hull J.B. and John V.B (1988)
Non-destructive Testing
Macmillan Education, London U.K. 1988

Hutchins D.A. (1988)
Ultrasonic generation by pulsed lasers
Physical Acoustics, Mason W.P.and Thurston R.N. eds., Academic Press, New York 1988 18: 21-123

Hutchins D.A., Dewhurst R.J. and Palmer S.B. (1981)[a]
Mechanisms of laser-generated ultrasound by directivity pattern measurements
Proceedings of the 1981 Ultrasonics International Conference, Brighton U.K. pp.20-25

Hutchins D.A., Dewhurst R.J. and Palmer S.B. (1981)[b]
Directivity patterns of laser-generated ultrasound in aluminium
Journal of the Acoustical Society of America 70(5): 1362-1369

Hutchins D.A., Dewhurst R.J. and Palmer S.B. (1981)[c]
Laser generated ultrasound at modified metal surfaces
Ultrasonics 19: 103-108

Hutchins D.A., Dewhurst R.J., Palmer S.B. and Scruby C.B. (1981)[d]
Laser generation as a standard acoustic source in metals
Applied Physics Letters 38(9):677-679

Hutchins D.A., Hauser F. and Goetz T. (1986)
Surface waves using laser generation and electromagnetic acoustic transducer detection
IEEE Transactions: Ultrasonics, Ferroelectrics, and Frequency Control 33(5): 478-483

Hutchins D.A. and Macphail J.D. (1985)
A new design of capacitance transducer for ultrasonic displacement detection
Journal of Physics E: Scientific Instruments 18: 69-73

Hutchins D.A. and Nadeau F. (1983)
Non-contact ultrasonic waveforms in metals using laser generation and interferometric detection
Proceedings of the 1983 IEEE Ultrasonics Symposium, pp. 1175-1177

Hutchins D.A. and Tam A.C. (1986)
Pulsed photoacoustic materials characterisation
IEEE Transactions : Ultrasonics, Ferroelectrics and Frequency Control 33(5): 429-449

Ing R.K. and Monchalin J.P. (1991)
Broadband optical detection of ultrasound by two-wave mixing in a photorefractive crystal
Applied Physics Letters 59(25): 3233-3235

Jackson D.A., Priest R., Dandridge A. and Tveten A.B. (1980)
Elimination of drift in a single-mode optical fiber interferometer using piezoelectrically stretched coiled fiber
Applied Optics 19(17): 2926-2929

Jackson D.A. and Jones D.C. (1989)
Interferometers
Optical Fiber Sensors: Systems and Applications Volume II, Culshaw B. and Dakin J. eds., Artech House USA 1989, Chapter 10, pp. 329-380

Jacob P.G., Griffin R.A. and Elias M.C. (1988)
Interferometric fibre-optic sensing systems
IREE: Proceedings of the 13th Australian Conference on Optical Fibre Technology, Hobart 1988, pp. 109-112

Jing J. (1992)
Remote ultrasound by laser optical generation and reception
Presented at the 10th National Australian Institute of Physics Conference, Melbourne, 10-14 Feb. 1992

Jones B.E., Medlock R.S. and Spooncer R.C. (1989)
Intensity and wavelength-based sensors and optical actuators
Optical Fiber Sensors: Systems and Applications Volume II, Culshaw B. and Dakin J. eds., Artech House USA 1989, Chapter 12, pp. 431-473

Jones E.D. (1971)
Ultrafast laser-induced stress waves in solids
Applied Physics Letters 18(1): 33-35

Jones R.E., Naden J.M. and Neat R.C. (1988)
Optical-fibre sensors using micromachined silicon resonant elements
IEE Proceedings 135(D5): 353-358

Ju F.D. (1986)
Modal frequency theory of fracture damage diagnosis in structures
Mechanical Engineering Department, University of New Mexico, Albuquerque, NM 87131 pp. 103-111

Ju F.D., Akgün M. and Paez T.L. (1983)
Fracture diagnosis in beam-frame structures using circuit-analogy
Recent Advances in Engineering Mechanics 2: 767-769

Ju F.D., Akgün M., Wong E.T. and Lopez T.L. (1982)
Modal method in diagnosis of fracture damage in simple structures
American Society of Mechanical Engineers:Productive Applications of Mechanical Vibrations, Merchant H.C.& Gears T.L.AMD-53 pp.113-126

Ju F.D. and Mimovich M.E. (1988)
Experimental diagnosis of fracture damage in structures by the modal frequency method
Transactions of the ASME: Journal of Vibration, Acoustics, Stress and Reliability in Design 110: 456-463

Karner C., Mandel A. and Träger F. (1985)
Pulsed laser photothermal displacement spectroscopy for surface studies
Applied Physics A: Solids and Surfaces 38: 19-21

Keller J.B. and Karal F.C. Jr. (1960)
Surface wave excitation and propagation
Journal of Applied Physics 31(6): 1039-1045

Kingsley S.A. (1975)
Optical-fibre phase modulator
Electronics Letters 11(19): 453-454

Kingsley S.A. (1978)
Fibredyne systems for passive or semipassive fibre-optic sensors
Electronics Letters 14(14): 419-422

Kino G.S. and Stearns R.G. (1985)
Acoustic wave generation by thermal excitation of small regions
Applied Physics Letters 47(9): 926-928

Kitching R., Sanderson N. and Hinduja S. (1975)
Flexibility of rectangular beams with abrupt changes of section
International Journal of Mechanical Sciences 17: 403-410

Kobayashi T. and Shodong J. (1988)
Optical fm heterodyne interferometry for range and displacement measurements
CPEM '88 Digest, 1988 Conference on Precision Electromagnetic Measurements Suematsu Y. ed., Ibaraki Japan pp. 133-134

Koch A. and Ulrich R. (1990)
Fibre-optic displacement measurement of rough surfaces
Technische Universität Hamburg-Harburg, Germany

Kohanzadeh Y., Whinnery J.R. and Carrol M.M. (1975)
Thermoelastic waves generated by laser beams of low power
Journal of the Acoustical Society of America 57(1): 67-71

Konstantinov L., Neubrand A. and Hess P. (1989)
Surface acoustic waves in solid-state investigations
Photoacoustic, Photothermal & Photochemical Processes at Surfaces & in Thin Films. Hess P. ed. Springer-Verlag, Heidelberg 1989 pp. 273-301

Koo K.P., Tveten A.B. and Dandbridge A. (1982)
Passive stabilisation scheme for fiber interferometers using (3×3) fiber directional couplers
Applied Physics Letters, 41(7): 616-618

Koo K.P., Dandridge A. and Tveten A.B. (1983)
Performance characteristics of a passively stabilised fiber interferometer using a (3×3) fiber directional coupler.
Proc. of Electronics Division of the Institution of Electrical Engineers 1st International Conf. on Optical Fibre Sensors, London, April 1983; 200-204

Koss L.L. (1980)
Laser ring
Tenth International Congress on Acoustics, Sydney, 9-16 July, 1980 Paper G10.5

Koss L.L. and Tobin R.C. (1983)
Laser induced structural vibration
Journal of Sound and Vibration 86(1): 1-7

Kozel S.M., Listvin V.N. and Churenkov A.V. (1990)
Photothermal self-excitation of mechanical microresonators
Optical Spectroscopy (USSR) 69(3): 401-402

Krautkrämer J. (1979)
Unconventional methods of generating, coupling and receiving ultrasound in non-destructive testing
Proceedings of the Ninth World Conference on Non-destructive Testing, Melbourne 1979

Krautkrämer J. and Krautkrämer H. (1990)
Ultrasonic Testing of Materials
Springer-Verlag, Berlin 4th Ed. 1990

Kubota K. and Nakatani Y. (1973)
Optical excitation of acoustic pulse in solids
Japanese Journal of Applied Physics 12(6): 888-894

Lai H.M. and Young K. (1982)
Theory of the pulsed optoacoustic technique
Journal of the Acoustical Society of America 72(6): 2000-2007

Laming R.I., Gold M.P., Payne D.N. and Halliwell N.A. (1986)
Fibre-optic vibration probe
Electronics Letters 22(3): 167-168

Langdon R.M. and Lynch B.J. (1988)
Photoacoustics in optical sensors
GEC Journal or Research 6(1): 55-62

Le Brun A. and Pons F. (1987)
Non-contact ultrasonic testing: applications to metrology and non-destructive testing
Non-destructive Testing Volume IV, Farely J.M. and Nichols R.W. eds., Pergamon Press, Oxford 1979 pp. 1593-1602

Ledbetter H.M. and Moulder J.C. (1979)
Laser induced Rayleigh waves in aluminium
Journal of the Acoustical Society of America 65(3): 840-842

Lee R.E. and White R.M. (1968)
Excitation of surface waves by transient surface heating
Applied Physics letters 12(1): 12-14

Legace L.J. and Kissinger C.D. (1977)
Non-contact displacement and vibration measurement systems employing fiber optic and capacitance transducers
Proceedings of the 23rd Annual International Instrumentation Society of America Conference, Las Vegas 1977

Lehfeldt E. and Höller P. (1967)
Lamb waves in lamination detection
Ultrasonics October: 255-257

Lewin A.C., Kersey A.D. and Jackson D.A. (1985)
Non-contact surface vibration analysis using a momomode fibre optic interferometer incorporating an open air path
Journal of Physics E: Scientific Instruments 18: 604-608

Liebowitz H. (1969)
Fracture, an Advanced Treatise
Liebowitz H. ed., Academic Press, New York 1969

Liu G. (1982)
Theory of the photoacoustic effect in condensed matter
Applied Optics 21(5): 955-960

Lowder J.E., Lencioni D.E., Hilton T.W. and Hull R.J. (1973)
High-energy pulsed CO2-laser-target interactions in air
Journal of Applied Physics 44(6): 2759-2762

Lowder J.E. and Pettingill L.C. (1974)
Measurement of CO2-laser-generated impulse and pressure
Applied Physics Letters 24(4): 204-207

Matthias E. and Dreyfus R.W. (1989)
From laser-induced desorption to surface damage
Photoacoustic, Photothermal & Photochemical Processes at Surfaces & in Thin Films. Hess P. ed., Springer-Verlag, Heidelberg 1989 pp. 89-128

Monchalin J.P. (1985)
Optical detection of ultrasound at a distance using a confocal Faby-Perot interferometer
Applied Physics Letters 47(1): 14-16

Monchalin J.P., Héon R., Bouchard P. and Padioleau C. (1989)
Broadband optical detection of ultrasound by optical sideband stripping with a confocal Fabry-Perot
Applied Physics Letters 55(16): 1612-1614

Mortimore D.B. (1990)
Theory and fabrication of 4 × 4 single-mode fused optical fiber couplers
Applied Optics 29(3): 371-374

McDonald F.A. and Wetsel G.C. Jr. (1988)
Theory of photothermal and photoacoustic effects in condensed matter
Physical Acoustics, Mason W.P. and Thurston R.N. eds., Academic Press New York 1988 18: 167-27

McLachlan N.W. (1951)
Theory of Vibrations
Dover Publications, New York 1966

Nadeau F. and Hutchins D.A. (1984)
A study of the interaction of surface waves with slots using non-contact laser generation and detection of ultrasound
Proceedings of the 1984 IEEE Ultrasonics Symposium, group on Sonics and Ultrasonics, Dallas, Paper #9082.810 pp 921-925

Nagy K., Dousis D.A., and Finch R.D. (1978)
Detection of flaws in railroad wheels using acoustic signatures
Transactions of the ASME: Journal of Engineering for Industry 100: 459-467

Niemeier Th. and Ulrich R. (1986)
Quadrature outputs from fiber interferometer with 4 × 4 coupler
Optics Letters 11(10): 677-679

O'Keefe J.D. and Skeen C.H. (1972)
Laser-induced stress-wave and impulse augmentation
Applied Physics Letters 21(10): 464-466

Palmer C.H. (1973)
Ultrasonic surface wave detection by optical interferometry
Journal of the Acoustical Society of America 53(3): 948-949

Palmer C.H., Claus R.O. and Fick S.E. (1977)
Ultrasonic wave measurement by differential interferometry
Applied Optics 16(7): 1849-1856

Parker B., Jensen A. and Chenoweth H. (1974)
Applied Strength of Materials
McGraw-Hill, Sydney, 1974

Parkus H. (1968)
Thermoelasticity
Blaisdell Publishing Company, USA 1968

Peercy P.S., Jones E.D., Bushnell J.C. and Gobeli G.W. (1970)
Ultrafast rise time laser-induced stress waves
Applied Physics Letters 16(3): 120-122

Perlin A.R. (1989)
Single optical fiber transducers: a technical overview
Presented at Interopto'89, International Optoelectronic Exhibition, Tokyo

Philp W.R. and Booth D.J. (1991)
Laser excitation of transverse mechanical vibrations in structures.
Proc. NDT '91, Australian Institute of Non-destructive Testing National Conf.(Melb.) August 1991.
Reprinted by the Publishers in Non-Destructive Testing Australia 30(4), August 1993, pp. 104-108

Philp W.R., Booth D.J., Shelamoff A. and Linthwaite M.J. (1992)
A simple fibre optic sensor for measurement of vibrational frequencies.
Journal of Measurement Science and Technology 3: 603-606.
Reprinted by the Publishers in Engineering Optics 5(3), August 1992, pp. 375-378.

Philp W.R., Booth D.J. and Perry N.D. (1993)
A model for laser-induced excitation of vibration in structures using intensities below the surface ablation threshold.
Abstract published in the Proc. Australian Conference on Lasers Optics and Spectroscopy, (Melb.) December 1993, p 76

Philp W.R. and Booth D.J. (1994)
Remote excitation and sensing of mechanical resonances in structures using laser diodes and an optical fibre interferometer.
Accepted for publication Journal of Measurement Science and Technology

Philp W.R., Booth D.J. and Perry N.D. (1994)
Single-pulse laser stimulation of structural vibration using power densities below the surface ablation threshold.
Submitted to the Journal of Sound and Vibration.

Pickelmann L. (1987)
Piezomechanical actuators; principles and applications
Piezomechanik-Optik (Gmbh), St-Cajetan-Straße 13-8000 München 80, September.

Pickelmann L. (1990)
Piezoelectrical and electrostrictive actuators; what's the difference ?
Piezomechanik-Optik (Gmbh), St-Cajetan-Straße 13-8000 München 80, September.

Pirri A.N., Schlier R. and Northam D. (1972)
Momentum transfer and plasma formation above a surface with a high power CO2 laser
Applied Physics Letters 21(3): 79-81

Prescott J. (1924)
Applied Elasticity
Dover Publications, New York 1961.

Ready J.F. (1965)
Effects due to absorption of laser radiation
Journal of Applied Physics 36(2): 462-468

Ready J.F. (1971)
Effects of High-Power Laser Radiation
Academic Press, New York 1971

Ready J.F. (1974)
Impulse produced by the interaction of CO2 TEA laser pulses
Applied Physics Letters 25(10): 558-560

Ready J.F. (1982)
Laser processing - the first 20 years
Laser Institute of America, Industrial and Engineering Laser Applications, Honeywell Systems and Research Centre, Minneapolis pp193-204

Rogers L.M. (1987)
Monitoring fatigue in offshore structures
Reliability in Non-destructive Testing, Brook C. and Hamstead P.D. eds. Pergamon Press Oxford pp. 2961-2977

Romberg T.M., Cassar A.G. and Harris R.W. (1984)
A comparison of traditional fourier and maximum entropy spectral methods for vibration analysis
Transactions of the ASME: Journal of Vibration, Acoustics, Stress, and Reliability in Design 106: 36-39

Rosencwaig A. and Gersho A. (1976)
Theory of the photoacoustic effect with solids
Journal of Applied Physics 47(1): 64-69

Rousset G., Bertrand L. and Cielo P. (1985)
A pulsed thermoelastic analysis of photothermal surface displacements in layered materials
Journal of Applied Physics 57(9): 4396-4405

Rousset G., Charbonnier F. and Lepoutre F. (1983)[a]
Calculation of thermoelastic bendings of thin plates application to thermal diffusivities measurements
Journal de Physique Colloque C6, supplement au #10, tome 44: 39-42

Rousset G., Lepoutre F. and Bertrand L. (1983)[b]
Influence of thermoelastic bending on photoacoustic experiments related to measurements of thermal diffusivity of metals
Journal of Applied Physics 54(5): 2383-2391

Sachse W. and Hsu N.N. (1979)
Ultrasonic transducers for materials testing and their characterisation
Physical Acoustics, Mason W.P. and Thurston R.N. eds., Academic Press New York 1979, 14: 277-406

Sanderson N. and Kitching R. (1978)
Flexibility of shafts with abrupt changes of section
International Journal of Mechanical Sciences 20: 189-199

Sanderson N. and Reid S.R. (1976)
Photoelastic approach to the determination of the flexural rigidity of rectangular beams with abrupt changes of section.
International Journal of Mechanical Sciences 18: 341-346

Sato H. (1983)
Free vibration of beams with abrupt changes in cross section
Journal of Sound and Vibration 89(1): 59-64

Scala C.M. and Doyle P.A. (1991)
Characterization of composite overlays by laser ultrasonics
Proc. NDT '91, Australian Institute of Non-destructive Testing National Conf. (Melbourne) August 1991

Scruby C.B. and Drain L.E. (1990)
Laser Ultrasonics: Techniques and Applications
A. Hilger Bristol, England, Philadelphia 1990

Scruby C.B., Dewhurst R.J., Hutchins D.A. and Palmer S.B. (1980)
Quantitative studies of thermally generated elastic waves in laser-irradiated metals
Journal of Applied Physics 51(12): 6210-6216

Sontag H. and Tam A.C. (1986)
Optical detection of nanosecond acoustic pulses
IEEE Transactions: Ultrasonics, Ferroelectrics, and Frequency Control 33(5): 500-506

Spain R.F., Schubring N.W. and Diamond M.J. (1964)
An electronic ear for certifying reliability
Materials Evaluation 22: 113-117

Sudarshanam V.S. (1992)
Minimum detectable phase shift in spectrum-analysis techniques of optical interferometric vibration detection
Applied Optics 31(28): 5997-6002

Takada K., Kobayashi M. and Noda J. (1990)
Fiber optic Fourier transform spectrometer with a coherent interferogram averaging scheme
Applied Optics 29(34): 5170-5176

Tam A.C. (1986)
Applications of photoacoustic sensing techniques
Reviews of Modern Physics 58(2): 381-431

Tam A.C. (1989)
Photothermal characterisation of surfaces and interfaces
Photoacoustic, Photothermal & Photochemical Processes at Surfaces & in Thin Films. Hess P. ed. Springer-Verlag Heidelberg 1989 pp. 157-170

Tam A.C. and Coufal H. (1983)
Photoacoustic generation and detection of 10-ns acoustic pulses in solids
Applied Physics Letters 42(1): 33-35

Tam A.C. and Sullivan B. (1983)
Remote sensing of pulsed photothermal radiometry
Applied Physics Letters 43(4): 333-335

Temple J.A.G. (1988)
NDT and structural integrity from pyramids to power stations
Reliability in Non-destructive Testing, Brook C. and Hamstead P.D. eds. Pergamon Press Oxford pp. 135-154

Tippur H.V. (1992)
Coherent gradient sensing: a Fourier optics analysis and application to fracture
Applied Optics 31(22): 4428-4439

Thomson W.T. (1966)
Vibration Theory and Applications
George Allen and Unwin, London 1966

Uttamchandani D., Thornton K.E.B., Nixon J. and Culshaw B. (1987)
Optically excited resonant diaphragm pressure sensor
Electronics Letters 23(4): 152-153

Vandiver J.K. (1977)
Detection of structural failure on fixed platforms by measurement of dynamic response
Journal of Petroleum Technology 29: 305-310

Vierck R.K. (1979)
Vibration Analysis
Harper and Row, New York 2nd ed. 1979

Vogel J.A. and Bruinsma A.J.A. (1987)
Contactless ultrasonic inspection with fiber-optics
Non-destructive Testing Volume IV, Farely J.M. and Nichols R.W. eds., Pergamon Press, Oxford 1987 pp. 2267-2278

Vogel J.A., Bruinsma A.J.A. and Berkhout A.J. (1987)
Beamsteering of laser generated ultrasound
Proceedings of the 1987 Ultrasonics International Conference pp. 141-152

Von Gutfeld R.J. (1980)
Thermoelastic generation of elastic waves for non-destructive testing and medical diagnostics
Ultrasonics 18: 175-181

Von Gutfeld R.J. and Melcher R.L. (1977)[a]
MHz acoustic waves from pulsed thermoelastic expansions and their application to flaw detection
Materials Evaluation October: 97-99

Von Gutfeld R.J. and Melcher R.L. (1977)[b]
20-MHz acoustic waves from pulsed thermoelastic expansions of constrained surfaces
Applied Physics Letters 30(6): 257-259

Von Gutfeld R.J. and Vigliotti D.R. (1983)
Thermoelastic hologram for focused ultrasound
Applied Physics Letters 42(12): 1018-1020

Wang M.L., Paez T.L. and Ju F.D. (1984)
Identification of inelastic MDF systems
American Society of Civil Engineers: Proceedings of the 5th Engineering Mechanics Division Specialty Conference. pp. 1005-1008

Waters J.P. and Mottier F.M. (1986)
Fiber optic laser vibration sensor
Transactions of the Instrumentation Society of America 25(1): 63-70

Wellman R.J. (1978)
Laser system for the remote sensing of flaws in solids
Conference on Laser and Electro-optic Systems, San Diego #THKK2: 106-107

White R.M. (1963)
Generation of elastic waves by transient surface heating
Journal of Applied Physics 34: 3559-3567

White R.G. (1971)
Evaluation of the dynamic characteristics of structures by transient testing
Journal of Sound and Vibration 15(2): 147-161

Williams C.C. (1984)
High resolution photothermal laser probe
Applied Physics letters 44(12): 1115-1117

Yang J.C.S., Dagalakis N. and Hirt M. (1974)
Application of the random decrement technique in the detection of an induced crack on an offshore platform model
American Society of Mechanical Engineers Publication AMD-37 pp. 55-68

Yang L.C. (1974)
Stress waves generated in thin metallic films by a Q-switched ruby laser
Journal of Applied Physics 45(6): 2601-2608

Yoneda K., Tawata M. and Hatorri S. (1980)
Laser probe for surface acoustic wave measurements
Japanese Journal of Applied Physics: Proc. 1st Symposium on Ultrasonic Electronics, Tokyo, 1980: 20(Sup. 20-3): 61-64

Yoshino T. (1989)
Heterodyne-type optic sensors
Anritsu News 8(40): 4-10

Yuen M.M.F. (1985)
A numerical study of the eigenparameters of a damaged cantilever
Journal of Sound and Vibration 103(3): 301-310

Publications resulting from the research described in this thesis

Philp W.R. and Booth D.J. (1991)
Laser excitation of transverse mechanical vibrations in structures.
Proc. NDT '91, Australian Institute of Non-destructive Testing National Conf.(Melb.) August 1991.
Reprinted by the Publishers in Non-Destructive Testing Australia 30(4), August 1993, pp. 104-108

Philp W.R., Booth D.J., Shelamoff A. and Linthwaite M.J. (1992)
A simple fibre optic sensor for measurement of vibrational frequencies.
Journal of Measurement Science and Technology 3: 603-606.
Reprinted by the Publishers in Engineering Optics 5(3), August 1992, pp. 375-378.

Philp W.R., Booth D.J. and Perry N.D. (1993)
A model for laser-induced excitation of vibration in structures using intensities below the surface ablation threshold.
Abstract published in the Proc. Australian Conference on Lasers Optics and Spectroscopy, (Melb.) December 1993, p 76

Philp W.R. and Booth D.J. (1994)
Remote excitation and sensing of mechanical resonances in structures using laser diodes and an optical fibre interferometer.
Accepted for publication Journal of Measurement Science and Technology

Philp W.R., Booth D.J. and Perry N.D. (1994)
Single-pulse laser stimulation of structural vibration using power densities below the surface ablation threshold.
Submitted to the Journal of Sound and Vibration.

Meas. Sci. Technol. 3 (1992) 603–606. Printed in the UK

A simple fibre optic sensor for measurement of vibrational frequencies

W R Philp, D J Booth, A Shelamoff and M J Linthwaite

Department of Applied Physics, Victoria University of Technology, PO Box 64, Footscray, Victoria 3011, Australia

Received 23 September 1991, in final form 30 January 1992, accepted for publication 17 February 1992

Abstract. A non-contact non-interferometric fibre optic vibration sensor is described which is constructed from a 50/125 μm multimode communication grade directional coupler, a modulated 820 nm LED and a PIN photodiode module. The sensing fibre is one arm of the directional coupler. The sensor is designed to detect small proximity variations between an unprepared reflective surface and the end of the sensing fibre. Vibrations of amplitude 1 μm for mirrored surfaces and 4 μm for unpolished aluminium can be detected for a sensor located approximately 50 μm from the vibrating surface. The sensor output is reasonably linear for vibration amplitudes up to about 0.2 mm. The sensor uses synchronous detection circuitry based on common, low cost integrated circuits to improve the output signal-to-noise ratio by a factor of ten. The design of the vibration sensor is described in sufficient detail for it to be easily reconstructed at minimum expense.

1. Introduction

Vibration analysis is an important and frequently used technique for a wide range of scientific and industrial applications. Standard vibration sensors include strain gauges, microphones, accelerometers and optical detectors – all of which have their specific uses. Fibre optic sensors may be used in applications requiring point sensing for accurate spatial resolution, or non-contact detection where one does not wish to load or obstruct the object under investigation.

The fibre optic vibration sensor was developed to investigate the modal resonant frequencies of a variety of large and small mechanical structures under laser excitation [1]. The fibre optic system enabled ready access to awkward locations and operated reliably in an environment with high electromagnetic interference. The non-contact nature of the sensor eliminated problems experienced with structures of small mass, where strain gauge or accelerometer transducers loaded the structure and modified natural resonances.

Interferometric fibre and bulk optic sensors suitable for vibration frequency measurements have been described by a number of authors [2, 3]. Others [4–7] have discussed non-interferometric, multimode fibre optic vibration sensors which are suitable for vibration detection and measurement of displacement. This paper presents details of a sensitive non-interferometric fibre optic vibration sensor which is simple, inexpensive and readily constructed from the description given.

2. The fibre optic sensor

A schematic diagram of the fibre optic sensor used for vibration frequency measurements is shown in figure 1. A Hewlett Packard HFBR-1404 820 nm LED source was square-wave modulated at a frequency of 1 MHz and launched into an optical fibre at a power level of

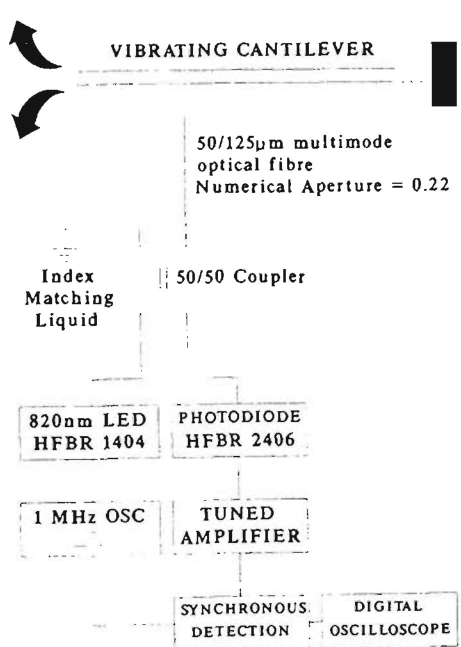

Figure 1. Schematic diagram of the fibre optic sensor.

0957-0233/92/060603 + 04 $04.50 © 1992 IOP Publishing Ltd

−17.6 dB m. The modulated light was passed through a 50:50 multimode directional coupler and illuminated a vibrating structure. Some reflected light from the structure was coupled back into the fibre and detected by a Hewlett Packard HFBR-2406 PIN photodiode receiver module. Changes in the separation between the fibre tip and the vibrating surface caused a change in the intensity of the light re-entering the fibre. Intensity variation in the reflected light produced amplitude modulation of the optical square wave signal at the oscillation frequencies of the structure.

The circuit diagram for the synchronous detector is shown in figure 2. The amplitude modulated signal was amplified by an LM733 amplifier tuned to 1 MHz and then synchronously detected using a CD4010 quad bilateral switch operated as a balanced mixer. The reference signal for the synchronous detection was supplied by the same signal generator used to modulate the LED. No phase compensation was necessary in the synchronous detection as phase shifts were negligible for modulation frequencies below 1 MHz, provided that optical and electrical paths were kept under a few metres. The output from the synchronous circuit was filtered using a low pass filter with a cut-off frequency of 20 kHz. The output noise level was 1.8 mV peak-to-peak. The signal-to-noise ratio (SNR) of the PIN photodiode module was improved with the synchronous detection circuit by a factor of ten, from about 3:1 to 30:1.

The physical parameters which determine the optical power coupled back into the fibre have been outlined by Perlin [7]. The major parameters which influence the detected power are the reflectivity of the reflecting surface, the proximity of the surface, the angle of incidence of the light and the numerical aperture of the sensing fibre. For vibration frequency measurements, the cause of the signal variation is not important as long as it varies at the vibration frequency. For the cantilever structures and exprimental arrangement described in this paper, the variations in power coupled back into the fibre are principally due to variations in the probe-to-target distance caused by the vibration. For the small amplitudes of vibrations excited, the variation in angle of incidence of the probe beam on the target is negligible. Figure 3 shows the output signal from the optical fibre sensor as a function of proximity for normal incidence on a variety of reflective surfaces. These data were obtained by mounting the reflective surface on a micrometer and varying the distance between the fibre tip and the surface. A front surfaced mirror, a polished steel surface and a clean unpolished aluminium surface were examined. The reflected light intensity from the surface of the object under investigation decreased rapidly with distance from the sensor, hence the sensor

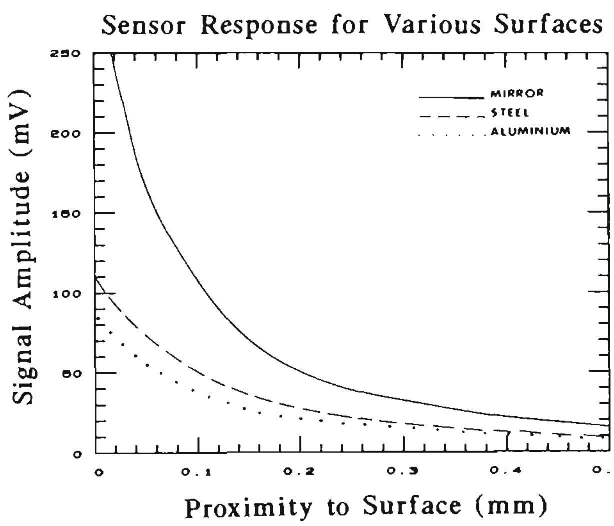

Figure 3. Sensor output for various reflective surfaces.

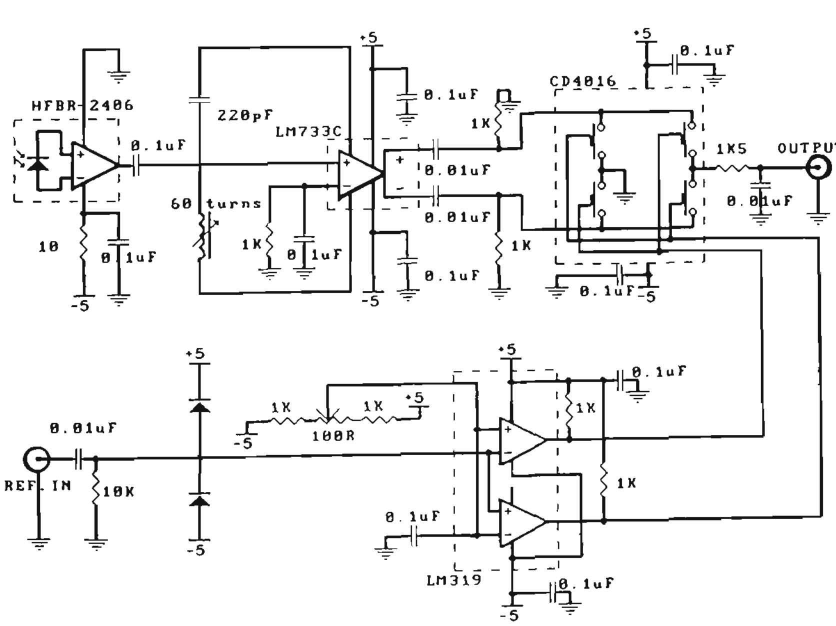

Figure 2. Circuit diagram of the synchronous detector.

signal did not vary linearly with displacement. The sensor could detect vibrations with amplitudes up to about 0.2 mm with reasonable linearity from an unprepared aluminium surface. Amplitudes in excess of this produced signal distortion. Asymmetry in the optical signal due to the large amplitude of vibration was evident in figure 5. These nonlinear effects produced additional harmonics in the acoustic frequency spectrum but did not affect the frequencies of the resonant modes. Vibrations of amplitude 1 μm for mirrored surfaces and 4 μm for unpolished aluminium were detected for a sensor located approximately 50 μm from the vibrating surface. The above figures for the minimum detected amplitude were determined from the measured signal noise and the slope of the curves in figure 3.

Figures 4 and 5 illustrate the vibration profiles and the resonant vibration frequencies for a 300 mm × 12 mm × 3 mm aluminium clamped-free cantilever using a standard strain gauge bridge (4 × TML PL-10-11; length 10 mm, resistance 120 Ω and gauge factor 2.07) and an identical cantilever (without the strain gauge) using the fibre optic sensor located 60 mm from the clamped end of the cantilever. The difference between the vertical scales in figures 4 and 5 is not significant as this is merely due to the difference in signal output levels from the two sensors. The first five resonant frequencies for the aluminium cantilever were calculated to be 26. 163, 457, 896 and 1482 Hz. A comparison of the frequency profiles gained from the two transducers clearly demonstrates the enhanced precision and resolution gained with the optical sensor as the agreement between measured and calculated frequencies is better and the spectral peaks are much narrower. The area illuminated by the fibre optic sensor was approximately 7×10^{-3} mm^2 which is very much smaller than that of the strain gauge bridge (effective area approximately 100 mm^2). Hence the fibre sensor allowed much greater spatial resolution and more accurate resonant frequency determination than was possible with the strain gauges. Loading effects due to the mass of the wiring and the adhesive further compounded errors in the resonant frequencies determined by the strain gauge transducer.

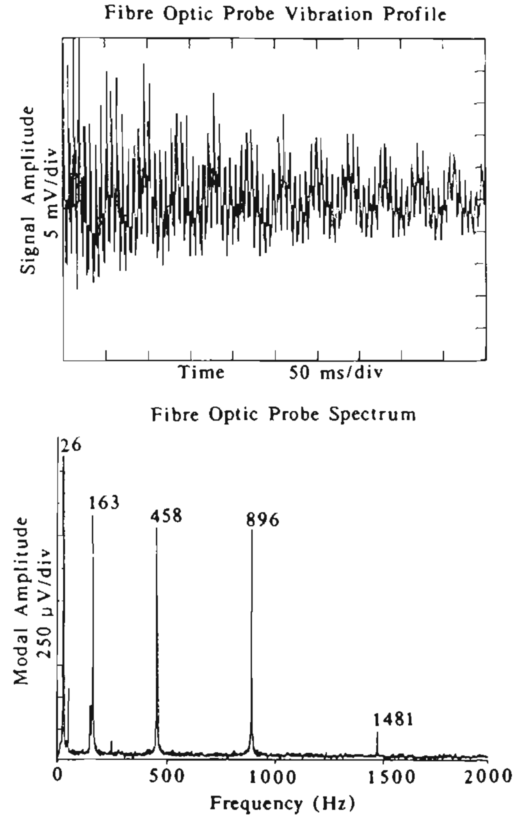

Figure 5. Vibration profile and frequency spectrum of a laser-excited aluminum cantilever as detected by the fibre optic sensor at a distance of 0.2 mm from the cantilever surface.

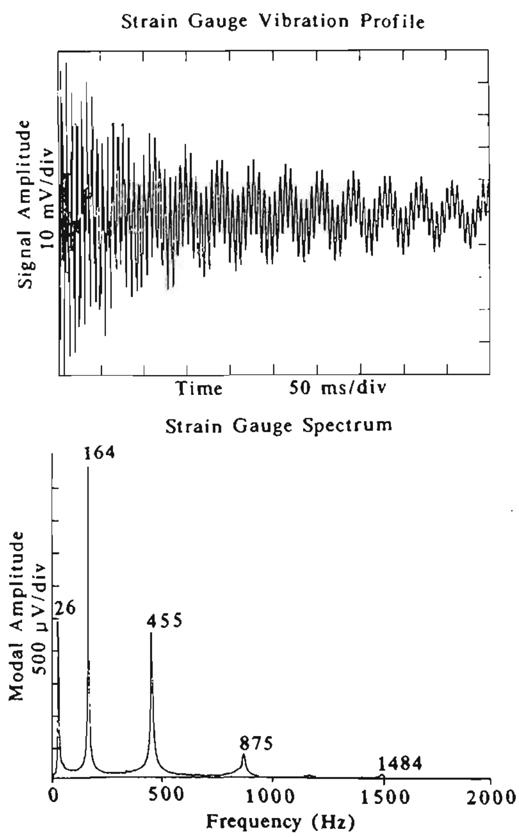

Figure 4. Vibration profile and frequency spectrum of a laser-excited aluminium cantilever as detected by a strain gauge full bridge.

3. Conclusion

A simple and easily constructed fibre optic sensor was developed to detect small variations in proximity between a vibrating surface and the sensor tip. Vibrational amplitudes up to about 0.2 mm were detected with reasonable linearity. The minimum vibration amplitude which could be detected was approximately 1 μm when the sensor tip was 50 μm from the vibrating surface. This vibration sensor is a reliable and cost effective alternative for non-contact vibration detection and high-resolution frequency analysis.

References

[1] Philp W R and Booth D J 1991 Laser excitation of transverse mechanical vibrations in structures *Proc. NDT '91, Australian Institute of Non-destructive Testing National Conf. (Melbourne) August 1991*

[2] Jackson D A and Jones J D C 1989 Interferometers *Optical Fiber Sensors: Systems and Applications* Vol 2 eds B Culshaw and J Dakin (Boston: Artech House)

[3] Waters J P and Mottier F M 1986 Fibre optic laser vibration sensor *ISA Trans.* **25** 63–70

[4] Cook R O and Hamm C W 1979 Fibre optic lever displacement transducer *Appl. Opt.* **20** 3230–41

[5] Chitnis V T, Kumar S and Sen D 1989 Optical fibre sensor for vibration amplitude measurement *J. Lightwave Technol.* **7** 687–91

[6] Culshaw B and Dakin J (eds) 1989 *Optical Fiber Sensors: Systems and Applications* Vol 2 (Boston: Artech House)

[7] Perlin A R 1989 Single optical fiber transducers: a technical overview on the subject *Interopto '89 Int. Optoelectronic Exhib. (Tokyo) 1989*